ČESKÉ VYSOKÉ UČENÍ TECHNICKÉ V PRAZE
Fakulta jaderná a fyzikálně inženýrská

DIZERTAČNÁ PRÁCA

Meranie excitačných funkcií jadrových reakcií na cyklotróne U-120M

Praha 2020 Jaroslav Červenák

Bibliografický záznam

Autor: Ing. Jaroslav Červenák
České vysoké učení technické v Praze
Fakulta jaderná a fyzikálně inženýrská
Katedra jaderné chemie

Název práce: Meranie excitačných funkcií jadrových reakcií na cyklotróne U-120M

Študijný program: Aplikace přírodních věd

Študijný odbor: Jaderná chemie

Školiteľ: prof. Ing. Ondřej Lebeda, Ph.D.
Ústav jaderné fyziky AV ČR, v. v. i
odd. radiofarmak

Akademický rok: 2019/2020

Počet strán: 119

Kľúčové slová: excitačné funkcie, účinné prierezy, cyklotrón U-120M, protóny, deuteróny, príprava rádionuklidov, nukleárna medicína, monitorovacie reakcie

Bibliographic Entry

Author:	Jaroslav Červenák, MSc. Czech Technical University in Prague Faculty of Nuclear Sciences and Physical Engineering Department of Nuclear Chemistry

Title of Dissertation:	Measurement of Excitation Functions of Nuclear Reactions on Cyclotron U-120M
Degree Programme:	Application of Natural Sciences
Field of Study:	Nuclear Chemistry

Supervisor:	Prof. Dr. Ondřej Lebeda Nuclear Physics Institute of the CAS Department of Radiopharmaceuticals

Academic Year:	2019/2020
Number of Pages:	119
Keywords:	excitation functions, cross-sections, cyclotron U-120M, protons, deuterons, preparation of radionuclides, nuclear medicine, monitoring reactions

Poďakovanie

Na tomto mieste by som veľmi rád poďakoval všetkým, bez koho by táto práca nevznikla. V prvom rade patrí veľká vďaka môjmu školiteľovi prof. Ing. Ondřejovi Lebedovi, Ph.D. za to, že ma naučil všetko, čo o excitačných funkciách viem a zároveň mi ukázal, že ani ten Mozart vlastne nie je až taká zlá hudba.

Ďalej by som sa chcel poďakovať svojim rodičom za to, že kedysi vyslovili názor, že mám najprv vyštudovať niečo poriadne, a potom si môžem študovať tie svoje operné rážie (stále dúfam, že jadrová chémia patrí do kategórie *„niečo poriadne“*). Ďakujem aj svojim súrodencom, ktorí ma od malička viedli k tomu byť trpezlivým pedagógom.

Túto prácu venujem dedkovi, ktorý mi bol vždy veľkým vzorom a starkej, ktorá ma tajne podozrievala, že som doktorské štúdium ukončil už pred niekoľkými rokmi.

Abstrakt

Excitačné funkcie jadrových reakcií majú nezastupiteľný význam v mnohých vedecko-priemyselných aplikáciách. Hrajú zásadnú úlohu pri plánovaní prípravy rádionuklidov z dôvodu optimalizácie parametrov ožarovania kvôli výťažkom pripravovaného rádionuklidu a rádionuklidovým nečistotám. Ďalším využitím excitačných funkcií je monitorovanie cyklotrónového zväzku nabitých častíc, kde sa na dôslednosť a presnosť pri meraní excitačných funkcií kladú obzvlášť vysoké nároky. Excitačné funkcie sa využívajú aj pri tzv. TLA (Thin Layer Analysis). Je to analytická metóda založená na aktivácii tenkých vrstiev ťažkými nabitými časticami, ktorá dovoľuje stanoviť úbytok materiálu napr. mechanickým oterom či koróznym opotrebovaním. Meranie excitačných funkcií slúži aj ako spätná väzba pre tvorcov teoretických predpovedí účinných prierezov jadrových reakcií či ako podnet pre opätovné meranie jadrových dát (intenzity gama liniek, polčasy premeny) v prípade odhalenia systematických chýb vo výpočtoch aktivít.

Táto práca ponúka popis experimentálneho stanovenia excitačných funkcií protónov na ^{nat}Mo, ^{197}Au, ^{nat}Ti a ^{nat}Cu pri energiách do 36 MeV a deuterónov na ^{197}Au a ^{nat}Cu pri energiách do 20 MeV. Podrobne analyzuje možnosti prípravy rádionuklidov s potenciálnym využitím v nukleárnej medicíne (hlavne ^{99m}Tc, ^{99}Mo, ^{197m,g}Hg) vrátane ich teoretických výťažkov a tiež sa venuje excitačným funkciám využiteľným pre monitoring zväzku nabitých častíc na cyklotróne. Štyri excitačné funkcie boli v rámci tejto práce zmerané vôbec po prvýkrát. Experimenty dali podnet na prepočítanie intenzít rozpadovej schémy a intenzít gama liniek rádionuklidu ^{197m}Hg, z ktorého vzišla jedna z publikácií, ktoré túto prácu tvoria.

Abstract

Excitation functions of nuclear reactions play an irreplaceable role in a lot of scientific or industrial applications. They are of major importance in production of radionuclides as inevitable for optimizing incident beam energy and its loss in a target in order to maximize the yield of desired radionuclide and to minimize content of radionuclidic impurities. Another application of excitation functions represents the field of charged particles beam monitoring. In this case, high precision measurement of such excitation functions is desirable. Another application is so-called Thin Layer Analysis (TLA), a method based on the activation of thin layers with heavy charged particles. This method permits to quantify the decrease in material caused by wear or corrosion, e.g. during engines operation. Experimentally determined excitation functions are an inevitable feedback for improvement of theoretical nuclear reaction model codes. As the measurements are usually closely related to precise activity quantification, it may sometimes uncover inconsistency in the published decay data and initiate their revision.

This work describes measurement of excitation functions of protons on ^{nat}Mo, ^{197}Au, ^{nat}Ti and ^{nat}Cu in the energy interval up to 36 MeV and deuterons on ^{197}Au and ^{nat}Cu with energies up to 20 MeV. In-detail analysis of production routes resulting in production of medically relevant radionuclides (^{99m}Tc, ^{99}Mo, ^{197m,g}Hg) is provided. Attention is paid to excitation functions of beam monitoring reactions of protons and deuterons. Four excitation functions were measured for the first time in our work. The experiments focused on production of ^{197m,g}Hg revealed inconsistencies in the decay scheme of ^{197m}Hg that was subsequently thoroughly revised. It allowed us to correct our cross-sections accordingly, as well as significant part of the previously published data.

OBSAH

1 Teoretický úvod a prehľad súčasného stavu študovanej problematiky

V tejto kapitole sú zavedené základné pojmy a definície potrebné k štúdiu jadrových reakcií, ich energetiky, mechanizmov a výťažkov. Tento prehľad sa opiera o práce [1,2], kde je táto problematika rozoberaná detailne. Kapitola taktiež podáva stručný prehľad vývoja a súčasného stavu merania excitačných funkcií jadrových reakcií.

1.1 Energetika jadrových reakcií

Majme všeobecnú jadrovú reakciu X + x → Y + y resp. v skrátenom zápise X(x,y)Y, kde X je *terčové jadro*, x je *projektil*, Y je *výsledné jadro* a y *emitovaná častica*. Ak treba v rovnici reakcie vyznačiť energetické pomery, reakcia sa zapisuje v tvare X + x → Y + y + *Q*, kde *Q* je energia danej reakcie. Pri jadrových reakciách platí opačný úzus ako pri chemických reakciách, tj. ak je $Q > 0$, je reakcia *exoergická* a energia sa v reakcii uvoľňuje, ak je $Q < 0$, ide o *endoergickú* reakciu a energia sa v reakcii spotrebúva. Hodnotu *Q* je možné vypočítať ako energetický ekvivalent rozdielu súčtu pokojových hmotností častíc pred reakciou a súčtu pokojových hmotností častíc po reakcii:

$$Q = [m_X + m_x - (m_Y + m_y)]c^2 \tag{1}$$

Časť energie projektilu sa premení na kinetickú energiu produktov reakcie (predpokladáme, že je terčové jadro v pokoji), ktorá je rovná kinetickej energii ťažiska sústavy. Zo zákona zachovania hybnosti potom vyplýva, že energia projektilu, ktorý vyvoláva endoergickú reakciu, musí byť minimálne rovná súčtu *Q* a kinetickej energie unášanej ťažiskom. Ide o tzv. *prahovú energiu* E_{thr} a platí pre ňu vzťah:

$$E_{thr} = -Q\frac{m_x + m_X}{m_X} \tag{2}.$$

Endoergické jadrové reakcie ťažkých nabitých častíc neprebiehajú bezprahovo, aj napriek tomu, že $Q < 0$. Dôvodom je odpudzovanie kladne nabitého projektilu a kladne nabitého terčového jadra, ide o tzv. *Coulombovskú bariéru*, ktorú musí projektil prekonať, aby vyvolal danú reakciu. Výšku tejto bariéry je možné odhadnúť zo vzťahu:

$$B_C \doteq \frac{Z_x Z_X}{A_x^{1/3} + A_X^{1/3}} \ [MeV] \tag{3},$$

kde Z je protonové číslo projektilu, resp. terčového jadra a A je jeho nukleónové číslo.

Ani Coulombovská bariéra však nie je jedinou prekážkou pri prieniku projektilu do terčového jadra. Pri zrážkach, ktoré nie sú centrálne, sa uplatňuje ešte tzv. *odstredivá potenciálová bariéra*, ktorú je možné interpretovať ako rotačnú energiu, ktorú udelí projektil terčovému jadru v prípade necentrálnej zrážky. Platí pre ňu približný vzťah:

$$B_S \doteq 20\frac{A_x + A_X}{A_x A_X\left(A_x^{1/3} + A_X^{1/3}\right)^2} \ [MeV] \tag{4},$$

kde symboly majú vyššie uvedený význam. Dôsledné odvodenia presných vzťahov na výpočet Coulombovskej a odstredivej potenciálovej bariéry sú uvedené napr. v [1].

1.2 Mechanizmy jadrových reakcií

Mechanizmy jadrových reakcií ťažkých nabitých častíc sa popisujú dvomi krajnými prípadmi alebo ich kombináciou (pre účely tejto práce nebude spomínaný popis pružného a nepružného rozptylu). Ide o reakcie, ktoré prebiehajú *priamo* alebo *nepriamo*.

V prípade priamých reakcií projektil po vstupe do jadra interaguje s jednotlivými nukleónmi, ktorým odovzdáva časť svojej energie. Nukleón s novonadobudnutou kinetickou energiou môže opustiť terčové jadro alebo svoju energiu opäť stratiť v ďalších nukleón-nukleónových zrážkach, rovnako ako projektil. Priame reakcie prebiehajú v čase porovnateľnom s časom, ktorý projektil potrebuje na preletenie priemeru jadra (10^{-20}–10^{-23} s). Emisia výsledných častíc z jadra v tomto prípade nie je izotropná. Ku priamym reakciám patria aj tzv. *prenosové reakcie*, pri ktorých jadro z projektilu alebo projektil z jadra „vytrhne“ jeden alebo viac nukleónov. Prvý prípad je ozvačovaný za tzv. *stripping reakciu* (napr. (d,p) reakcia), druhý za tzv. *pick-up reakciu* (napr. (p,d) reakcia).

Nepriame reakcie prebiehajú za vzniku *zloženého jadra*. Ide o útvar, ktorý vznikne po vstupe projektilu do terčového jadra. Energia prinesená projektilom sa v jadre rozptýli a projektil po určitom čase nie je odlíšiteľný od ostatných nukleónov. V dôsledku štatistických fluktuácií sa na jednom či viacerých nukleónoch sústredí taká časť prinesenej energie, ktorá daným nukleónom dovolí opustiť zložené jadro. Časť energie takto excitovaného jadra sa môže vyžiariť aj ako γ kvantum. Tieto procesy sa opakujú, až kým jadro nezostane vo svojom základnom energetickom stave. Doba života zloženého jadra je rádovo vyššia (10^{-14}–10^{-19} s) ako čas, za ktorý preletí projektil priemerom jadra. V tomto prípade sú výsledné častice emitované izotropne. Môže sa stať, že zložené jadro emituje nukleón, resp. nukleóny skôr, ako sa projektil stihne energeticky integrovať medzi ostatné nukleóny. V tomto prípade ide o tzv. *precompound decay*.

So zvyšujúcou sa energiou projektilu sa zväčšuje spektrum emitovaných nukleónov či ich zhlukov. Môže dochádzať k trieštivým reakciám a pri energiách rádovo GeV a vyšších sú možné reakcie ako fragmentácia, multipartícia a štepenie jadier. V prípade emisie zhluku nukleónov sa prahová energia reakcie znižuje o väzbovú energiu zhluku častíc (d = np + 2,225 MeV, t = p2n + 8,482 MeV, ^{3}He = 2pn + 7,718 MeV, α = 2p2n + 28,296 MeV atď.).

1.3 Účinné prierezy a excitačné funkcie jadrových reakcií

Účinný prierez jadrovej reakcie je miera pravdepodobnosti jej priebehu za daných podmienok. Označuje sa σ a názorne sa interpretuje ako zdanlivá plocha jadra resp. jeho priemet, ktorou keď projektil prejde, vyvolá danú jadrovú reakciu. Z tejto predstavy vychádzajú aj jednotky pre účinný prierez – ide o jednotky plochy. Najčastejšie sa používa jednotka *barn* (1 b = 10^{-24} cm^2) a z nej odvodená jednotka *milibarn* (mb). Najvyššie účinné prierezy majú všeobecne záchytné reakcie tepelných neutrónov, jeden z najvyšších doposiaľ známych účinných prierezov má reakcia ^{135}Xe(n,γ), kde σ dosahuje až 2,6.10^6 b. Naopak najmenšie účinné prierezy majú interakcie neutrín s hmotou, pri ktorých sa ich hodnoty pohybujú rádovo len okolo 10^{-19} b [1].

Hodnota účinného prierezu závisí od vlastností jadra a častice, ktorá reakciu vyvoláva. Ide hlavne o energiu projektilu a terčového jadra, ich veľkosť resp. náboj, spin či hybnosť a ďalšie vlastnosti. Účinný prierez závisí aj od charakteru výsledného jadra a emitovanej častice. Závislosť účinného prierezu danej reakcie od energie projektilu sa nazýva *excitačná funkcia* reakcie. Excitačné funkcie môžu nadobúdať rozmanité tvary, napr. majú rôzny priebeh pre reakcie nabitých a nenabitých častíc, už len z toho dôvodu, že exoergické reakcie neutrónov vďaka absencii náboja projektilu prebiehajú bezprahovo.

Excitačné funkcie jadrových reakcií sa merajú prakticky od vynálezu cyklotrónu (dvadsiate a tridsiate roky dvadsiateho storočia). Za tých takmer sto rokov bolo zmerané ohromné množstvo excitačných funkcií, tie najdôležitejšie dokonca niekoľko desiatokrát. Je jasné, že s postupným upresňovaním rozpadových dát a s rozvojom techniky detektorových systémov sa kvalita merania obvykle zvyšuje. S tým je v niektorých prípadoch spojený veľký rozptyl nameraných dát – či už samotných energií projektilu alebo k nim prislúchajúcich účinných prierezov. Relatívne vysoké neistoty pozorujeme aj v prípadoch, kedy sa jedná o excitačné funkcie pre rádionuklidy významné v praxi. To je dôvod, prečo je meranie excitačných funkcií vysoko aktuálne aj dnes a zostane aktuálne aj v najbližšej budúcnosti.

Snáď najvýznamnejším dôvodom pre meranie excitačných funkcií je ich využitie pri príprave rádionuklidov – dajú sa na ich základe vypočítať výťažky pre výsledný produkt rovnako ako aj výťažky potenciálnych rádionuklidových nečistôt, ktoré pri spracovaní terča a separácii produktu môžu prekážať. Výpočtom výťažkov rádionuklidov z excitačných funkcií sa venuje kapitola 4.5. Excitačné funkcie teda umožňujú optimalizáciu prípravy rádionuklidov tým, že prezrádzajú, aká je optimálna vstupná energia zväzku či jeho energetická strata v terčovom materiáli (tj. optimálna hrúbka terča), aby bol výťažok pripravovaného rádionuklidu čo najvyšší a podiel nečistôt ešte prijateľný, hlavne s ohľadom na izotopické nečistoty. Presne zmerané excitačné funkcie pre vznik pripravovaného rádionuklidu a jeho potenciálnych nečistôt sú veľmi dôležitou, avšak určite nie jedinou podmienkou úspešnej optimalizácie jeho prípravy. V praxi do hry vstupuje hlavne vhodne zvolený terč (terčový materiál – obohatený izotop, čistý prvok prírodného zloženia alebo ich zlúčeniny, konštrukcia terča či jeho tepelno-vodivostné vlastnosti) a následne po ožarovaní vhodne zvolený separačný postup vzniknutého rádionuklidu a ďalšia práca s ním (rádionuklidová a rádiochemická čistota výsledného preparátu).

K meraniu excitačných funkcií aktivačnou metódou patrí neodmysliteľne meranie aktivity rádionuklidov vzniknutých v terči. Pri týchto meraniach sa môžu objaviť nekonzistentné intenzity rôznych γ liniek daného rádionuklidu, ktoré sú podnetom na revíziu rozpadových schém rádionuklidov a na upresnenie výpočtu ich aktivít. Meranie excitačných funkcií je v tomto prípade akási spätná väzba, rovnako ako v prípade porovnávania experimentálnych dát s teoretickou predpoveďou účinných prierezov rôznych výpočtových kódov založených na fyzikálnych modeloch. Na základe zmeraných účinných prierezov a miery ich zhody s teoretickou predpoveďou je možné optimalizovať vstupné parametre modelov pre výpočty excitačných funkcií.

Ďalším využitím excitačných funkcií je už spomínaný monitoring energie a prúdu zväzku aktivujúcich častíc. V podstate ide o to, že nastavením vstupných parametrov (energia a prúd) pri výpočte účinných prierezov sa maximalizuje zhoda nameraných a odporúčaných účinných prierezov. Využívajú sa reakcie na kovových terčoch, ktoré majú vhodné vlastnosti (stálosť,

dostupnosť, atď.), a ktorých aktivácia vedie na produkt, ktorého aktivita sa dá veľmi presne stanoviť. Ak sú excitačné funkcie zmerané s vysokou presnosťou, môžu tieto reakcie slúžiť na monitorovanie zväzku. Využívajú sa napr. reakcie $^{nat}Ti(p,x)^{48}V$, $^{nat}Cu(d,x)^{62,63,65}Zn$ a mnoho ďalších. Tejto téme sa venuje kapitola 4.2.

Namerané účinné prierezy zhromažďuje IAEA v databáze EXFOR [3], a pre monitorovacie reakcie a pre tvorbu významných rádionuklidov s uplatnením napr. v nukleárnej medicíne vytvára databázu tzv. *odporúčaných účinných prierezov* [4]. IAEA zadáva aj projekty pracoviskám, ktoré sa dlhodobo zaoberajú problematikou merania excitačných funkcií. Časť dát predkladanej práce je súčasťou jedného z nich: „*Nuclear Data for Charged-Particle Monitor Reactions and Medical Isotope Production*“s výstupom v podobe publikácie [5].

2 Ciele práce

Cieľom predkladanej práce je meranie excitačných funkcií jadrových reakcií ťažkých nabitých častíc na rôznych terčových materiáloch na cyklotróne U-120M Ústavu jaderné fyziky Akademie věd České republiky, v. v. i. Cieľ práce je možné kvôli lepšej prehľadnosti rozdeliť na čiastočné, dobre definované celky:

A) Meranie excitačných funkcií reakcií ^{nat}Mo(p,x) s dôrazom na reakcie ^{nat}Mo(p,x)^{99m}Tc, ^{nat}Mo(p,x)^{99}Mo a ^{nat}Mo(p,x)$^{96m+g}$Tc. Dôkladne zmerané excitačné funkcie reakcií ^{nat}Mo(p,x)^{99m}Tc a ^{nat}Mo(p,x)^{99}Mo sú kľúčové pre prípravu *cyklotrónového technécia-99m*, ktoré je možné využiť v nukleárnej medicíne ako alternatívu *generátorového technécia-99m*. Reakcia ^{nat}Mo(p,x)$^{96m+g}$Tc je monitorovacou reakciou protónového zväzku pri ožarovaní na urýchľovačoch častíc.

B) Meranie excitačných funkcií reakcií prirodzene monoizotopického zlata ^{197}Au(p,x) s dôrazom na reakcie ^{197}Au(p,x)^{197m}Hg a ^{197}Au(p,x)^{197g}Hg. Tieto excitačné funkcie sú dôležité pre prípravu uvedených nuklidov a ich využitie v nukleárnej medicíne ako potenciálneho nového teranostického izomérneho páru.

C) Meranie excitačných funkcií reakcií ^{197}Au(d,x) s dôrazom na reakcie ^{197}Au(d,x)^{197m}Hg a ^{197}Au(d,x)^{197g}Hg. Tieto excitačné funkcie sú dôležitou alternatívou ku príprave ^{197m,g}Hg aktiváciou zlata protónmi.

D) Meranie excitačných funkcií reakcií ^{nat}Cu(d,x).

E) Meranie excitačných funkcií reakcií ^{nat}Ti(p,x) s dôrazom na reakciu ^{nat}Ti(p,x)^{48}V ako jednu z najdôležitejších monitorovacích reakcií protónového zväzku pri ožarovaní na urýchľovačoch častíc.

F) Meranie excitačných funkcií reakcií ^{nat}Cu(p,x) s dôrazom na reakcie ^{nat}Cu(p,x)^{62}Zn, ^{nat}Cu(p,x)^{63}Zn a ^{nat}Cu(p,x)^{65}Zn, ktoré slúžia ako monitorovacie reakcie protónového zväzku pri ožarovaní na urýchľovačoch častíc.

3 Zoznam publikácií

V tejto kapitole je uvedený zoznam publikácií, z ktorých dizertačná práca vychádza. Prehlásenie spoluautorov o podiele na danej publikácii je uvedené v kapitole 7.2 Prehlásenie spoluautorov.

Publikácia I

Červenák J., Lebeda O., *Experimental cross-sections for proton-induced nuclear reactions on ^{nat}Mo*, Nucl. Instrum. Methods Phys. Res. B 380 (2016) 32-49 doi: doi.org/10.1016/j.nimb.2016.05.006

Publikácia II

Červenák J., Lebeda O., *Measurement of cross-sections of proton-induced nuclear reactions on ^{197}Au focused on the production of the theranostic pair $^{197m,g}Hg$*, Nucl. Instrum. Methods Phys. Res. B 458 (2019) 118-125 doi: 10.1016/j.nimb.2019.08.006

Publikácia III

Lebeda O., Červenák J., *Measurement of deuteron-induced nuclear reactions cross-sections on ^{197}Au and on ^{nat}Cu focused on the theranostic $^{197m,g}Hg$*, Nucl. Instrum. Methods Phys. Res. B 461 (2019) 105–113 doi: 10.1016/j.nimb.2019.09.034

Publikácia IV

Lebeda O., Červenák J., *Revised cross-sections for formation of theranostic $^{197m,g}Hg$ in proton- and deuteron-induced reactions on ^{197}Au.* Nuclear Instruments and Methods in Physics Research B 478 (2020), 85–91. doi: 10.1016/j.nimb.2020.05.014

Publikácia V

Lebeda O., Kondev F. G., Červenák J., *Branching ratio and γ-ray emission probabilities in the decay of the $J^{\pi}=13/2^{+}$ isomer in ^{197}Hg*, Nucl. Instrum. Methods Phys. Res. A 959 (2020) 163481 doi: 10.1016/j.nima.2020.163481

Publikácia VI

Červenák J., Lebeda O., *New cross-section data for proton-induced reactions on ^{nat}Ti and ^{nat}Cu with special regard to the beam monitoring*, Submitted into: Nucl. Instrum. Methods Phys. Res. B, submitted manuscript NIMB-S-20-00521

4 Komentár k súboru publikovaných prác

Táto kapitola podáva výklad k experimentálnemu stanoveniu účinných prierezov, resp. excitačných funkcií jadrových reakcií ťažkých nabitých častíc. Pozornosť je venovaná metodike experimentov, rovnako ako aj prehľadu veličín a vzťahov potrebných na spracovanie a vyhodnotenie dát.

Text v nasledujúcich kapitolách zjednocuje publikácie, z ktorých práca vychádza, uvádza ich do súvislosti s cieľom práce a venuje sa praktickému dopadu výsledkov.

4.1 Terče a terčová technika

Pri experimentálnom stanovení excitačných funkcií sa s výhodou používa, ak to povaha experimentu dovoľuje, tzv. *stacked foil*, resp. *gas chamber technique* (metóda sendvičového terča), ktorá je schematicky znázornená na **OBR. 1**. Tenké kovové fólie sa poskladajú na seba, medzi ne sa vložia fólie na monitorovanie energie a prúdu aktivujúceho zväzku a fólie, ktoré slúžia iba na zníženie energie zväzku (tzv. degradéry). Hrúbka terčovej fólie sa volí tak, aby energetická strata zväzku vo fólii bola maximálne 1 MeV (ideálne však do niekoľko desatín MeV). V takomto prípade sa potom s vyhovujúcou presnosťou dá priradiť vypočítaný účinný prierez energii projektilu v strede hrúbky fólie.

Pre meranie excitačných funkcií na plynových terčových materiáloch sa miesto fólií používajú za sebou poskladané komôrky plnené natlakovaným plynom a platí všetko ostatné, čo bolo spomenuté pri meraní excitačných funkcií na kovových fóliách. Tlak plynu v komôrkach musí byť nastavený tak, aby rádionuklidy vznikali v dostatočnom množstve (spodný limit pre tlak), a na druhej strane tak, aby stopa zväzku v plyne lokálne neznížila jeho plošnú hustotu, ktorá by skreslila účinné prierezy v danej komôrke. V tom hrá úlohu aj rozmer zväzku – fokusovanejší zväzok predstavuje väčšie riziko zriedenia plynu.

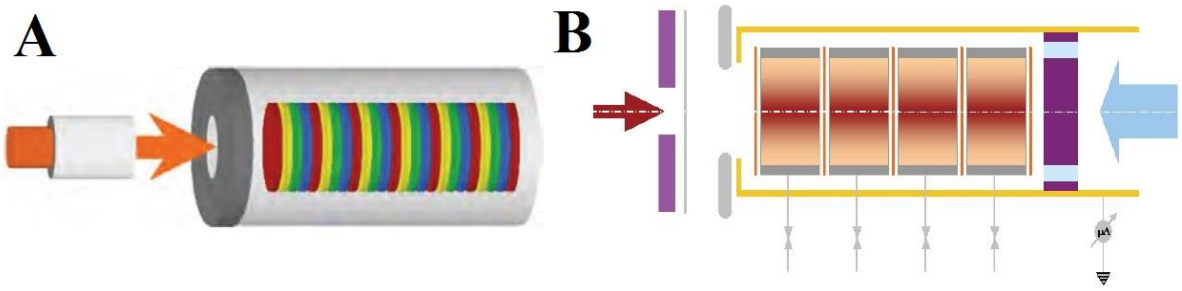

OBRÁZOK 1 Schématické znázornenie metódy sendvičového terča
pre A) kovové fólie a B) plynové komôrky [7]

Pri použití tejto metódy je možné zmerať viac bodov excitačnej funkcie v rámci jedného ožarovania, čo je výhodné z časového aj ekonomického hľadiska. Pred ožarovaním sa pripraví model terča v závislosti od vstupnej energie zväzku nabitých častíc. Straty energie zväzku sa vypočítaú zo závislosti lineárnej brzdnej schopnosti materiálu, ktorým zväzok daných častíc prechádza, od energie tejto častice (dáta prebraté z kódu SRIM [6]). Pozícia fólií a ich hrúbka (predovšetkým degradérov energie) sa volí tak, aby boli body excitačných funkcií približne rovnomerne rozdelené, a aby ich bolo dostatočne veľa. Obvykle sa používajú rozostupy bodov cca 1,0–2,0 MeV.

Okrem zmienených výhod prináša táto metóda aj určité nevýhody. Jednou z nich je zvyšujúca sa neistota hodnoty energie zväzku so zvyšujúcou sa vzdialenosťou fólií od vstupu zväzku do terča. Toto je dané neistotami pri meraní hrúbky fólií, neistotou energie zväzku na vstupe do terča a rozmytím energie zväzku pri priechode sendvičom (tzv. straggling). Znížiť túto neistotu je teda nielen v záujme presnosti určenia energie zväzku v danej fólii, ale aj presnosti výpočtu účinných prierezov. K zníženiu neistoty hodnoty energie vo fóliách jednoznačne prispieva aj zníženie neistoty energie zväzku na vstupe do terča.

Druhou nevýhodou použitia tejto metódy je problém s meraním aktivít rádionuklidov s krátkym polčasom premeny vo väčšom počte fólií bezprostredne po ukončení ožarovania. Toto sa dá vyriešiť znížením počtu fólií v terči a meraním ich aktivít na viacerých detektoroch. V tejto práci bolo pristúpené k obidvom opatreniam – pri ožarovaní protónmi sa vždy ožarovali dva sendvičové terče (vyššie a nižšie energie) a následné merania aktivity prebiehali na dvoch až troch HPGe detektoroch.

4.2 Stanovenie energie a prúdu zväzku

Energiu zväzku vstupujúceho do terča je možné pomerne presne zmerať rôznymi metódami. Na cyklotróne U-120M, na ktorom boli namerané všetky experimentálne dáta, z ktorých táto práca vychádza, je energia zväzku stanovovaná z presného merania polomeru orbity zväzku v mieste jeho vývodu. Stredná energia zväzku je následne stanovená z matematického modelu urýchľovacích režimov pre cyklotrón U-120M [8].

Prúd zväzku sa stanovuje absolútne meraním deponovaného náboja v elektricky izolovanom terči. Pri priamom meraní celkového náboja zväzku treba obmedziť javy, ktoré môžu jeho hodnotu skresľovať. Ide napr. o emisiu sekundárnych elektrónov alebo zvody chladiacim médiom, obvykle deionizovanou vodou. V prípade, že treba skorigovať kolísanie prúdu od priemernej hodnoty, môže sa záznam prúdu numericky zintegrovať kvôli presnej korekcii na rozpad počas ožarovania. Toto má praktický význam len pre rádionuklidy s krátkym polčasom premeny a v prípadoch, kedy sú výkyvy prúdu výrazné. V prípade všetkých rádionuklidov meraných v predkladanej práci bola na výpočet účinných prierezov použitá, s ohľadom na minimálne kolísanie prúdu počas ožarovania, priemerná hodnota prúdu, ktorá bola prakticky identická s výpočtom na základe presnej korekcie na rozpad určenej zo záznamu prúdu. Pri všetkých experimentoch, z ktorých táto práca vychádza, bolo od obsluhy cyklotrónu požadované, aby mal prúd častíc pri ožarovaní konštantnú hodnotu a bol zaznamenávaný každú sekundu.

Pri stanovení excitačných funkcií by mal byť prúd dostatočne nízky na to, aby počas ožarovania nedochádzalo k tepelnému poškodeniu terča v dôsledku brzdenia zväzku. Natavenie fólie totiž väčšinou znehodnotí celý experiment. Zároveň ale musí byť prúd dostatočne vysoký na to, aby bolo možné bez väčších problémov zmerať aktivitu vzniknutých, hlavne dlhodobejších, rádionuklidov. Tieto požiadavky väčšinou spĺňajú prúdy v intervale 0,1–1,0 μA. Použitie zväzku v tomto rozsahu prúdov je výhodné aj z toho dôvodu, že je dostatočne stabilný a jeho stanovenie na cyklotróne je zaťažené relatívne malou neistotou.

Overiť alebo spresniť energiu a prúd zväzku je možné aj s využitím tzv. monitorovacích reakcií. Ide o reakcie na dobre dostupných prírodných kovoch, z ktorých sa dajú ľahko vyrobiť veľmi tenké fólie s homogénnou hrúbkou. Použiteľné sú len tie reakcie, ktoré vedú na precízne merateľné rádionuklidy, ktorých excitačné funkcie sú známe s vysokou presnosťou. Na tieto excitačné funkcie sa po vyhodnotení experimentálnych dát „nafituje“

daná zmeraná excitačná funkcia drobnými úpravami hodnôt vstupnej energie a prúdu zväzku v rámci ich neistôt.

Monitoring zväzku nemá nijako komplikovať priebeh experimentu. Monitorovacie fólie sú z materiálov s veľmi dobrými fyzikálnymi a chemickými vlastnosťami (tepelná vodivosť, stálosť na vzduchu atď.). Monitorovacie excitačné funkcie by mali mať relatívne vysoké účinné prierezy kvôli rýchlemu a spoľahlivému stanoveniu aktivity vznikajúceho rádionuklidu aj pri relatívne krátkych ožarovaniach a nemali by byť ovplyvnené problematickými interferenciami. Rádionuklid vznikajúci v takejto reakcii by mal mať dostatočne dlhý polčas premeny, aby mohlo byť meranie monitorovacích fólií realizované s odstupom a nenarušovalo meranie aktivít terčových fólií s rádionuklidmi s krátkym polčasom premeny. Okrem požiadavky na polčas premeny je dôležité, aby mal monitorovací rádionuklid dostatočne vysoké intenzity γ liniek, ktoré sú známe s vysokou presnosťou. IAEA vo svojej databáze [4] zverejňuje vhodné reakcie pre monitoring protónového, deuterónového, ^{3}He a zväzku α častíc a z vybraných nameraných publikovaných dát odvodzuje odporúčané účinné prierezy pre tieto reakcie, ktoré slúžia ako referenčné hodnoty pre ďalších užívateľov. V **TABUĽKE 1** sú uvedené reakcie zo spomínanej databázy.

TABUĽKA 1 Reakcie vhodné pre monitoring energie a prúdu ťažkých nabitých častíc [4]

protóny	deuteróny	^{3}He častice	α častice
^{27}Al(p,x)^{22}Na	^{27}Al(d,x)^{22}Na	^{27}Al(^{3}He,x)^{22}Na	^{27}Al(α,x)^{22}Na
^{27}Al(p,x) ^{24}Na	^{27}Al(d,x) ^{24}Na	^{27}Al(^{3}He,x) ^{24}Na	^{27}Al(α,x) ^{24}Na
^{nat}Ti(p,x)^{48}V	^{nat}Ti(d,x)^{48}V	^{nat}Ti(^{3}He,x)^{48}V	^{nat}Ti(α,x)^{51}Cr
^{nat}Ti(p,x)^{46}Sc	^{nat}Ti(d,x)^{46}Sc	^{nat}Cu(^{3}He,x)^{66}Ga	^{nat}Cu(α,x)^{66}Ga
^{nat}Ni(p,x)^{57}Ni	^{nat}Fe(d,x)^{56}Co	^{nat}Cu(^{3}He,x)^{63}Zn	^{nat}Cu(α,x)^{67}Ga
^{nat}Cu(p,x)^{62}Zn	^{nat}Ni(d,x)^{61}Cu	^{nat}Cu(^{3}He,x)^{65}Zn	^{nat}Cu(α,x)^{65}Zn
^{nat}Cu(p,x)^{63}Zn	^{nat}Ni(d,x)^{56}Co		
^{nat}Cu(p,x)^{65}Zn	^{nat}Ni(d,x)^{58}Co		
^{nat}Cu(p,x)^{56}Co	^{nat}Cu(d,x)^{62}Zn		
^{nat}Cu(p,x)^{58}Co	^{nat}Cu(d,x)^{63}Zn		
^{nat}Mo(p,x)$^{96m+g}$Tc	^{nat}Cu(d,x)^{65}Zn		

Pri výbere vhodnej monitorovacej reakcie pre experiment je dôležité zistiť, pre aký energetický rozsah sa daná reakcia dá použiť. Hlavnú úlohu tu hrá prah najmenej energeticky náročnej reakcie, ktorá v danom terči pri ožarovaní prebieha. Tak napr. reakcia ^{nat}Cu(p,x)^{56}Co sa dá použiť pre energie vyššie ako 45 MeV, reakcia ^{nat}Cu(p,x)^{62}Zn od cca 14 MeV a reakcie ^{nat}Cu(p,x)^{65}Zn a ^{nat}Ti(p,x)^{48}V sa dajú použiť už pre energie od asi 5 MeV. Pre stanovenie hodnoty prúdu je vhodná nevýrazná závislosť účinného prierezu od energie, pri stanovení energie je to naopak. Niektoré neistoty sa pri stanovení energie a prúdu dajú eliminovať, ak pri aktivácii fólie vznikajú dva nezávislé, dobre merateľné rádionuklidy súčasne. Pomer ich aktivít R je totiž daný iba účinnými prierezmi reakcií, v ktorých vznikajú (σ_1, σ_2) a ich rozpadovými konštantami λ_1 a λ_2. Pomer R je teda daný vzťahom 5 [9]:

$$R = \frac{A_1^{EOB}}{A_2^{EOB}} = \frac{\sigma_1\left(1 - e^{\lambda_1 t_b}\right)}{\sigma_2(1 - e^{\lambda_2 t_b})} \quad (5),$$

kde A^{EOB} je aktivita ku koncu ožarovania [Bq] a t_b je doba ožarovania [h, resp. konzistentné jednotky s λ]. Tento prístup sa dá napríklad využiť, ak sa pri ožarovaní protónmi použijú medené fólie ako monitory. Pri ožarovaní ^{nat}Cu protónmi totiž vznikajú až tri dobre merateľné izotopy zinku ^{62,63,65}Zn a pri vyšších energiách aj dva izotopy kobaltu ^{56,58}Co.

4.3 Meranie aktivity a korekcie interferencií

Po ukončení ožarovania bol sendvičový terč rozobratý na jednotlivé fólie, ktoré boli následne merané na dvoch až troch HPGe detektoroch (GMX45-Plus, Ortec; GC2019, Canberra a GEM40P4-83-SMP, Ortec). Všetky detektory použité v tejto práci boli skalibrované na energiu a na účinnosť detekcie η v závislosti od energie γ kvanta. Kalibračné závislosti boli merané pomocou komerčne dostupných etalónov typu EG 3 (^{241}Am, ^{133}Ba, ^{60}Co, ^{137}Cs a ^{152}Eu), ktoré vyrobil Český metrologický institut (ČMI), Inspektorát pro ionizující záření. Použité rádionuklidy poskytujú dostatočný počet γ liniek pokrývajúcich energetickú oblasť 26–1408 keV. Na **OBR. 2** je príklad kalibračnej krivky detekčnej účinnosti pre HPGe detektor Ortec GMX45Plus pre vzdialenosť etalón-detektor 1000 mm. Preloženie nameraných bodov v škále $\ln(\eta)/\ln(E_\gamma)$ polynómom piateho stupňa vo všetkých kalibrovaných vzdialenostiach etalón-detektor má štvorec korelačného koeficientu vyšší ako 0,999. Pre energie žiarenia γ vyššie ako 240 keV je vyhovujúci lineárny fit tejto závislosti ($\ln(240) \approx 5{,}5$).

Polčasy rádionuklidov a intenzity ich γ liniek boli prebraté buď z knižnice NuDat2 [10] alebo ENSDF [11], hodnoty Q a prahy reakcií boli vypočítané pomocou Q-value calculator [12]. Zmerané γ spektrá boli vyhodnotené programom DEIMOS32 [13].

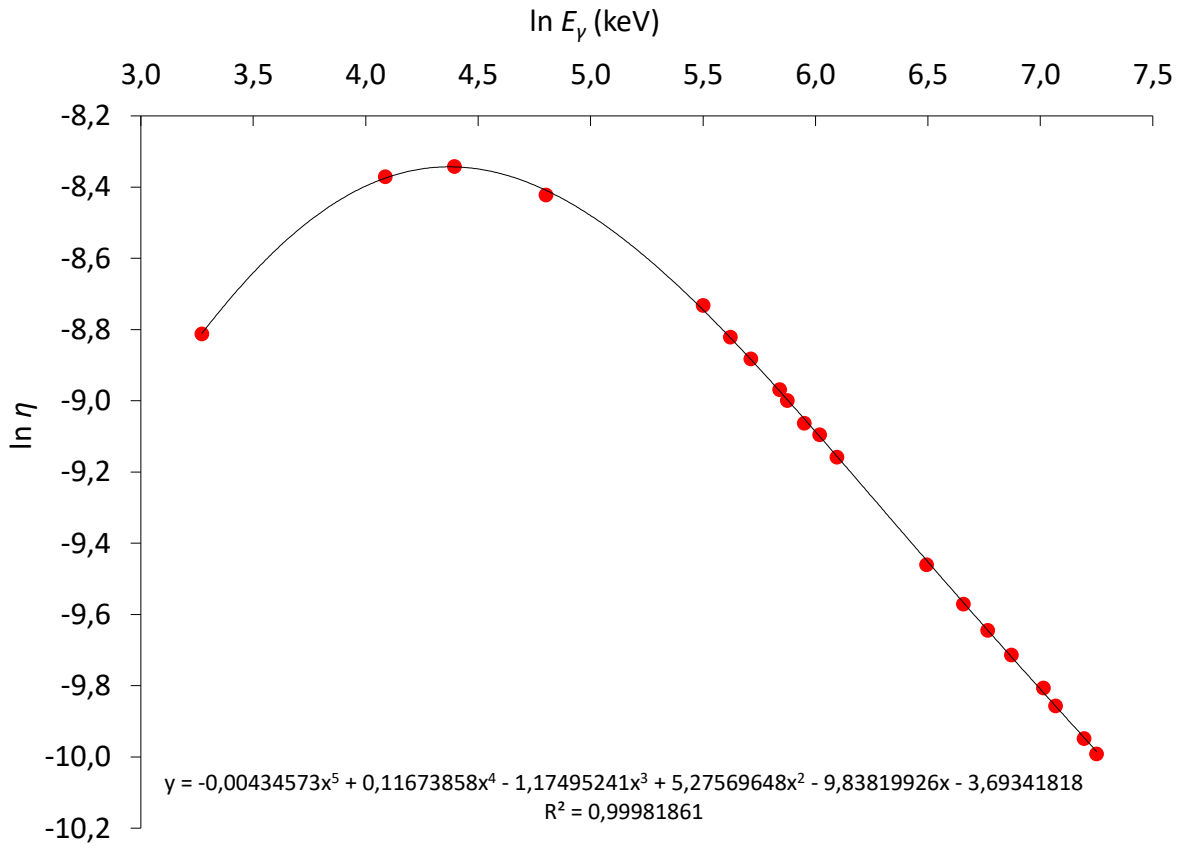

OBRÁZOK. 2 Závislosť účinnosti detekcie η žiarenia γ na jeho energii E_γ pre HPGe detektor Ortec GMX45Plus, vzdialenosť etalón-detektor 1000 mm

Každá fólia bola meraná niekoľkokrát v rôznych geometriách vzorka-detektor, aby bolo možné vyhodnotiť aktivitu rádionuklidov s rôznymi polčasmi rozpadu, prípadne rôznymi intenzitami gama liniek. Z nameraných γ spektier sa vypočítala aktivita ku koncu ožarovania A^{EOB} (End Of Bombardment) podľa vzťahu:

$$A^{EOB} = \frac{P_\gamma}{I_\gamma \eta t_m} \frac{\lambda t_r}{1 - e^{-\lambda t_r}} e^{\lambda t_c} \quad (6),$$

kde P_γ je zmeraná čistá plocha fotopíku danej linky žiarenia γ, I_γ je intenzita danej γ linky, η je účinnosť jej detekcie, t_m expozícia („live time"), λ rozpadová konštanta daného rádionuklidu, t_r celková doba merania („real time") a t_c doba, ktorá uplynula od konca ožarovania po začiatok merania („cooling time").

Pri ožarovaní tenkých fólií zväzkom ťažkých nabitých častíc pozorujeme zvyčajne jav vyrazenia malého (ale merateľného) podielu vzniknutých rádionuklidov na nasledujúcu fóliu v sendvičovom terči. Pomer vyrazenej a celkovej aktivity vzniknutého rádionuklidu závisí od rôznych podmienok (atómová hmotnosť terčového materiálu, hrúbka fólie, energia zväzku, energetické pomery pri reakcii samotnej atď.). Jav je výrazný predovšetkým pri použití ľahkých materiálov (hliník, titan). Tieto vyrazené aktivity sa dajú presne zmerať v prípadoch, kedy signál aktivity vyrazenej časti nezaniká v spektre fólie, na ktorú odrazený rádionuklid dopadne. V praxi sa jedná o dva prípady, kedy je možné vyrazené aktivity jednoducho zmerať:

- Polčas stanovovaného rádionuklidu je dostatočne dlhý na to, aby bolo možné počkať s meraním jeho vyrazenej aktivity, kým klesne „pozadie" fólie na prijateľnú úroveň.
- Aktivity v danej fólii sú tak nízke, že umožňujú pristúpiť k meraniu vyrazených aktivít daného rádionuklidu bezprostredne po ožarovaní.

Ako príklad je na **OBR. 3** znázornená závislosť percenta vyrazenej aktivity ^{48}V vzniknutej v reakcii ^{nat}Ti(p,x) od energie protónov v strede hrúbky tejto Ti fólie. Podiel vyrazenej aktivity sa pohybuje v rozmedzí od 0,8 do 2,6 %.

Pri vyhodnocovaní aktivity rádionuklidov treba brať do úvahy tiež zoslabenie γ liniek s nízkou energiou pre fólie, ktoré majú nezanedbateľnú hrúbku oproti polvrstve danej energie γ linky v danom materiáli. V týchto prípadoch treba zmeranú plochu píku korigovať na stredné zoslabenie γ linky v materiáli fólie podľa nasledujúceho vzťahu:

$$P = P_0 \frac{1}{d} \int_0^d e^{-\mu\rho x} dx = P_0 \frac{1 - e^{-\mu\rho d}}{\mu\rho d} \quad (7),$$

kde P_0 je korigovaná čistá plocha píku, d je hrúbka materiálu, μ je hmotnostný zoslabovací koeficient danej energie γ linky v danom materiáli a ρ hustota materiálu, všetko dosadené v konzistentných jednotkách. V prípade dostatočných vzdialeností vzorky od detektoru treba použiť hmotnostný zoslabovací koeficient, ktorý nezahŕňa koherentne rozptýlene fotóny [14].

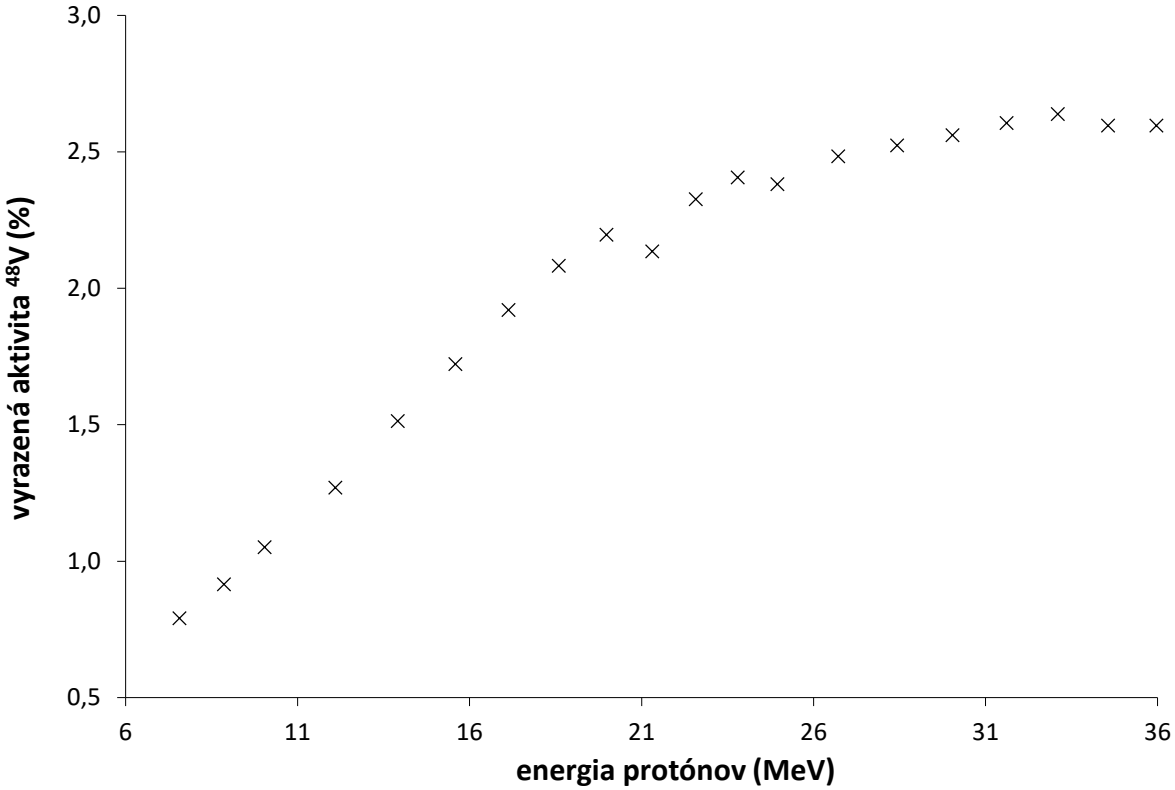

OBRÁZOK 3 Závislosť percenta vyrazenej aktivity ^{48}V pri reakciách ^{nat}Ti(p,x) od energie zväzku protónov

Ďalšie korekcie, ktoré treba v mnohých prípadoch pri spracovaní dát urobiť, sú korekcie interferencií v rámci stanovenia aktivít, resp. účinných prierezov. Dajú sa rozdeliť do dvoch kategórií:

1. Interferencia píkov rovnakých alebo blízkych energií, ktoré nie je možné na danom detektore rozlíšiť. K tomuto môže dochádzať z rôznych dôvodov, napr. náhodná blízkosť píkov podobných energií, pozaďové píky zasahujúce do píku skúmaného rádionuklidu alebo píky s rovnakou energiou v prípadoch, kedy sa dve izobarické jadrá rozpadajú na rovnaké stabilné jadro, ktoré pri deexcitácii vyžaruje γ kvantá tých istých energií. Interferencie tohto typu je možné vyriešiť, resp. obísť dvomi spôsobmi:
   A) Použiť na vyhodnotenie aktivity jedného z rádionuklidov inú, neinterferujúcu γ linku, ak existuje. Aktivitu druhého rádionuklidu potom vypočítať z plochy píku výpočtom korigovanej na príspevok kontaminujúceho rádionuklidu.
   B) V prípade dostatočne veľkého rozdielu v polčasoch rozpadu rádionuklidov je možné počkať na prakticky úplný rozpad kratšie žijúceho rádionuklidu a aktivitu dlhšie žijúceho rádionuklidu potom vypočítať zo spektra bez príspevku kontaminujúceho píku.
2. Príspevok k aktivite priamo vznikajúceho rádionuklidu rozpadom iného rádionuklidu prítomného v terči. Tieto prípady sa korigujú výpočtom v dvoch krokoch:
   A) do úvahy sa berie príspevok aktivity dcérskeho rádionuklidu vzniknutého z materského rádionuklidu počas ožarovania.
   B) do úvahy sa berie príspevok aktivity dcérskeho rádionuklidu vzniknutého z materského rádionuklidu po ožarovaní.

   Za určitých podmienok sa dajú prípady 2.A a 2.B riešiť aj jednoduchšie, ich podrobnejší popis je v kapitole 4.4, rovnica 13.

Prípady 2.A a 2.B sa popisujú rovnicami:

$$A_2^{EOB} = f\frac{d\rho N_A \sigma I}{Aze}\left(1 - \frac{\lambda_2}{\lambda_2 - \lambda_1}e^{-\lambda_1 t_b} + \frac{\lambda_1}{\lambda_2 - \lambda_1}e^{-\lambda_2 t_b}\right) \quad (8),$$

$$A_2 = f\frac{\lambda_2}{\lambda_2 - \lambda_1}A_1^{EOB}\left(e^{-\lambda_1 t} - e^{-\lambda_2 t}\right) + A_2^{EOB}e^{-\lambda_2 t} \quad (9),$$

kde index *1* označuje veličiny patriace materskému rádionuklidu a index *2* veličiny patriace dcérskemu rádionuklidu, *f* je pravdepodobnosť, s ktorou sa materský rádionuklid premieňa na dcérsky, *d* je hrúbka fólie, *σ* je účinný prierez pre vznik daného rádionuklidu pri energii v strede hrúbky fólie, *I* je intenzita prúdu zväzku, *A* je molová hmotnosť materiálu terčovej fólie, *z* je náboj projektilu, *e* je elementárny náboj, t_b je čas ožarovania („time of bombardment“) a *t* je čas uplynutý od okamihu ukončenia ožarovania do okamihu zahájenia merania („cooling time“).

Pri korekciách príspevku aktivity z rozpadu materského rádionuklidu k aktivite dcérskeho, treba brať do úvahy aj ich rozpad, resp. prírastok počas merania. Z tohto dôvodu boli vypočítané stredné aktivity materského a dcérskeho rádionuklidu počas merania (vzťah 10 a 11) a z nich odvodené počty impulzov príspevku aktivity materského rádionuklidu k aktivite dcérskeho.

$$\bar{A}_1 = A_1^{EOB}e^{-\lambda_1 t_c}\frac{1 - e^{-\lambda_1 t_m}}{\lambda_1 t_m} \quad (10),$$

$$\bar{A}_2 = \frac{\lambda_2 f A_1^0}{(\lambda_2 - \lambda_1)t_m}\left(\frac{1 - e^{-\lambda_1 t_m}}{\lambda_1} + \frac{1 - e^{-\lambda_2 t_m}}{\lambda_2}\right) + \frac{A_2^0}{\lambda_1 t_m}\left(1 - e^{-\lambda_2 t_m}\right) \quad (11),$$

kde $\bar{A}_i$ je stredná aktivita materského, resp. dcérskeho rádionuklidu a A_i^0 je aktivita materského rádionuklidu, resp dcérskeho rádionuklidu vzniknutého z materského rádionuklidu. Aktivita A_2^0 sa vypočíta zo vzťahu 9.

4.4 Výpočet účinných prierezov a excitačné funkcie

Zo zmeranej aktivity rádionuklidu korigovanej k EOB sa vypočíta účinný prierez reakcií vedúcich k jeho vzniku podľa vzťahu:

$$\sigma = \frac{P_\gamma}{I_\gamma \eta t_m}\frac{\lambda t_r}{1 - e^{-\lambda t_r}}e^{\lambda t_c}\frac{Aze}{d\rho N_A I(1 - e^{-\lambda t_b})} = A^{EOB}\frac{Aze}{d\rho N_A I(1 - e^{-\lambda t_b})} \quad (12),$$

kde symboly majú vyššie uvedený význam.

V predchádzajúcej kapitole boli popísané korekcie pre možné prípady interferencií píkov v γ spektrách. Prípad 2.A a 2.B pre geneticky zviazané rádionuklidy, kde sú splnené podmienky:

- $\lambda_1 >> \lambda_2$
- bola zmeraná aktivita A_1 materského rádionuklidu z neinterferujúceho píku
- bola zmeraná aktivita A_2^{cum} dcérskeho rádionuklidu po úplnom rozpade materského rádionuklidu,

sa dá vyriešiť priamo pre účinný prierez, bez nutnosti výpočtom korigovať aktivitu ku koncu ožarovania. Vyššie uvedené podmienky totiž dovoľujú zjednodušiť vzťahy 8 a 9, z ktorých po úpravách pre účinný prierez platí:

$$\sigma_{cum} = f\frac{\lambda_2}{\lambda_2 - \lambda_1}\sigma_1 + \sigma_2 \qquad (13),$$

kde σ_{cum} je tzv. *kumulatívny účinný prierez* (tj. účinný prierez vypočítaný z kumulatívnej aktivity dcérskeho rádionuklidu po úplnom rozpade materského rádionuklidu extrapolovanej k času ukončenia ožarovania), ostatné symboly majú vyššie uvedený význam.

K nameraným účinným prierezom boli zo zákona o šírení chýb vypočítané neistoty, ktoré pozostávali z neistôt hodnôt jednotlivých veličín z rovnice 8. Jednalo sa o:

- detekčnú účinnosť γ linky pre výpočet aktivity (< 3 %)
- intenzitu γ linky (väčšinou < 5 %)
- čistú plochu píku pre γ linku (< 10 %, väčšinou však < 2%)
- prúd (cca 6 %)
- hrúbka fólie (< 2 %)

Neistota polčasu premeny rádionuklidu nebola do výpočtu zahrnutá, pretože sa polčas vo vzťahu 12 vyskytuje v exponenciálnych členoch. Celková relatívna neistota účinných prierezov sa pohybovala od 6,9 % pre prípady, kedy sa neistota pri vyhodnocovaní plochy píku γ linky blížila nule (dôležité, precízne zmerané rádionuklidy) až po desiatky percent, kedy pri malých plochách píkov bola neistota ich vyhodnotenia výrazne väčšia (nízke aktivity rádionuklidov, eventuálne píky na vysokom či komplikovanom pozadí, komplikované korekcie aktivít).

Vypočítané účinné prierezy boli aj s ich neistotami porovnané so všetkými dostupnými publikovanými experimentálnymi dátami a s teoretickou predpoveďou výpočtového kódu TALYS [15]. Týmto krokom sa podrobnejšie venujú nasledujúce podkapitoly.

4.4.1 Porovnanie excitačných funkcií s ostatnými experimentálnymi dátami

Ťažisko rešeršnej časti práce zameranej na meranie excitačných funkcií tkvie prakticky vždy v získavaní nameraných opublikovaných účinných prierezov študovaných reakcií a ich následné porovnanie medzi sebou a s novonameranými dátami. Experimentálne dáta boli väčšinou prebraté z databázy EXFOR [3], ktorá obsahuje veľké množstvo publikovaných účinných prierezov a s nimi súvisiacich dát. V niektorých prípadoch však bolo treba vyhľadať dáta v pôvodnej publikácii (keďže ich databáza EXFOR neobsahovala) alebo kontaktovať autora osobne.

Ako bolo spomínané v úvode tejto práce, excitačné funkcie sa merajú už takmer sto rokov. Za ten čas sa vstupné rozpadové dáta pre výpočet účinných prierezov menili (veľakrát dosť výrazne). To je jeden z dôvodov, prečo sa experimentálne dáta merané v rôznych obdobiach môžu až dramaticky líšiť. Ako vyplýva z rovnice 12, je korekcia zmeny niektorých parametrov triviálna (intenzita γ liniek, prúd), no korekcia iných parametrov prakticky nemožná bez prístupu k vtupným dátam výpočtov (polčas premeny). Databáza EXFOR okrem nameraných účinných prierezov ponúka vo väčšine prípadov aj dáta, na základe ktorých boli dané účinné prierezy počítané. Tieto dáta je taktiež možné dohľadať v pôvodných

publikáciách. Predtým, ako sa teda pristúpilo k porovnávaniu dátových radov medzi sebou, boli všetky experimentálne stanovené účinné prierezy, pokiaľ to bolo možné, korigované na aktuálne rozpadové dáta.

V prípade experimentu ožarovania molybdénu protónmi boli z elementárnych účinných prierezov odvodené izotopové účinné prierezy niektorých reakcií (^{100}Mo(p,x)^{99m}Tc, ^{99}Mo) a publikované dáta boli skorigované na aktuálne známe izotopické zloženie prírodného molybdénu, ktoré sa nedávno menilo.

4.4.2 Porovnanie excitačných funkcií s ich teoretickými predpoveďami

Väčšina výpočtových kódov teoretických predpovedí účinných prierezov funguje na kombinácii viacerých modelov binukleárnych jadrových reakcií (hlavne kombinácia simulácií mechanizmov zloženého jadra a priamej reakcie). Tieto kódy dokážu predikovať častokrát veľmi spoľahlivo účinné prierezy reakcií protónov na stredne ťažkých jadrách, predovšetkým v prípade emisie jedného či viacerých neutrónov. V prípade reakcií ľahkých jadier je teoretická predpoveď limitovaná. Toto je spôsobené silnou individualitou v „jadrovom charaktere“ ľahkých prvkov. Ďalšie rozdiely oproti experimentu môžu nastať v prípadoch, kedy reakcia prebieha aj mechanizmom, s ktorým výpočtový kód nepracuje alebo ho nevie dobre popísať. Ide napr. o (d,p) reakcie, ktoré prebiehajú ako tzv. *stripping reakcie* a prebiehajú aj hlboko pod úrovňou coulombickej bariéry resp. prahu reakcie, viď kapitola 1.2. Toto je dobre vidieť napr. v **Publikácii III** pri reakciách ^{197}Au(d,p)^{198m,g}Au.

V tejto práci boli experimentálne dáta porovnávané s predpoveďou kódu TALYS, prevzatej z online databázy TENDL [15]. TALYS je kód, ktorý poskytuje dáta pre reakcie neutrónov, protónov, deuterónov, tritónov, ^{3}He, α častíc a γ kvánt s energiou do 200 MeV na jadrách so strednou dobou života dlhšou ako 1 sekunda od Z = 1 (^{1}H), do Z = 115 (^{291}Mc).

Treba však zdôrazniť, že teoretické predpovede nemôžu nahradiť experimentálne dáta (aspoň zatiaľ) tiež preto, že všetky kódy, ktoré počítajú účinné prierezy, potrebujú dáta z experimentov na doladenie vstupných parametrov.

4.5 Výpočet výťažkov rádionuklidov v hrubých terčoch

Pri meraní excitačných funkcií jadrových reakcií je cieľom zmerať účinný prierez pre danú, čo najpresnejšie definovanú energiu projektilu. To je docielené, ako už bolo spomínané v kapitole 4.1, použitím tenkých terčových fólií, ktoré zaručia nízku stratu energie projektilu pri jeho priechode fóliou. Pri príprave rádionuklidov je však na terč kladená opačná požiadavka – terč má byť dostatočne hrubý na to, aby zabrzdil projektil o požadovaný energetický rozsah (až jednotky mm v závislosti od terčového materiálu a projektilu). Energia projektilu sa v takomto hrubom terči výrazne mení v závislosti od jeho polohy v terči. Tejto zmene energie zodpovedá aj zmena účinného prierezu pre danú reakciu, a tým aj množstvo vzniknutého rádionuklidu. Pri výpočte výťažkov v hrubých terčoch sa teda s výhodou používa aproximácia nameraných excitačných funkcií ich fitovaním jedným alebo viacerými polynómami (rovnica 14) a závislosť lineárnej brzdnej schopnosti projektilu od energie sa v danom terčovom materiáli aproximuje mocninou funkciou (rovnica 15).

$$\sigma_{(E)} = \sum_{i=0}^{n} a_i E^i \tag{14},$$

$$-\frac{dE}{dx} = pE^q \tag{15},$$

kde a_i, p a q sú koeficienty danej funkcie.

Veličina, ktorá sa používa pre kvantifikáciu aktivity rádionuklidu v okamihu ukončenia ožarovania, je tzv. *saturačný výťažok rádionuklidu v hrubom terči*. Je to aktivita rádionuklidu vzniknutého v terči hrúbky d pri nekonečne dlhom ožarovaní (v praxi $t_{irr} >> T_{½}$) zväzkom častíc s prúdom 1 μA. Saturačný výťažok Y_{sat} je definovaný nasledujúcim vzťahom:

$$Y_{sat} = \frac{\rho f N_A}{Aze10^6} \int_0^d \sigma_{(E)}\, dx \tag{16},$$

$$resp.\ Y_{sat} = \frac{\rho f N_A}{Aze10^6} \int_{E_{in}}^{E_{out}} \frac{-\sigma_{(E)} dE}{(-dE/dx)} = \frac{\rho f N_A}{Aze10^6} \int_{E_{out}}^{E_{in}} \frac{\sigma_{(E)}}{(-dE/dx)} dE \tag{17}.$$

Po dosadení rovnice 14 a 15 do rovnice 17 bude pre saturačný výťažok platiť vzťah 18, ktorý sa dá jednoducho zintegrovať analyticky, preto sa s výhodou používa pre výpočet výťažku rádionuklidu v hrubom terči z fitovaných účinných prierezov.

$$Y_{sat} = \frac{\rho f N_A}{Aze10^6} \frac{1}{p} \int_{E_{in}}^{E_{out}} \left(-\sum_{i=0}^{n} a_i E^{i-q} \right) dE = \frac{\rho f N_A}{Aze10^6} \frac{1}{p} \int_{E_{out}}^{E_{in}} \left(\sum_{i=0}^{n} a_i E^{i-q} \right) dE \tag{18}.$$

Zo vzťahu (18) vyplýva aj to, že pre saturačný výťažok rádionuklidu v hrubom terči, v ktorom projektil stratil energiu $(E_{in} - E_{out})$, kde $E_{out} > E_{thr}$, platí:

$$Y = Y_{sat}^{E_{in}} - Y_{sat}^{E_{out}} \tag{19}.$$

Pomocou vyššie uvedených vzťahov boli vypočítané saturačné výťažky pre všetky rádionuklidy identifikované a kvantifikované v ožiarených terčoch.

5 Súhrn

Cieľom práce bolo meranie excitačných funkcií jadrových reakcií ťažkých nabitých častíc na rôznych terčových materiáloch na cyklotróne U-120M Ústavu jaderné fyziky Akademie věd České republiky, v. v. i. Boli zmerané excitačné funkcie ^{nat}Mo(p,x), ^{197}Au(p,x), ^{nat}Ti(p,x) a ^{nat}Cu(p,x) v intervale energií do 36 MeV a ^{197}Au(d,x) a ^{nat}Cu(d,x) pre energie deuterónov do 20 MeV. Zmerané a opublikované výsledky sú zhrnuté v nasledujúcich bodoch:

- Excitačné funkcie reakcií ^{nat}Mo(p,x)^{93g}Tc, ^{93m}Tc, $^{93m+g}$Tc, ^{94g}Tc, ^{94m}Tc, ^{95g}Tc, ^{95m}Tc, $^{96m+g}$Tc, ^{97m}Tc, ^{99m}Tc, ^{90}Mo, ^{93m}Mo, ^{99}Mo, ^{88g}Nb, ^{88m}Nb, ^{89g}Nb, ^{89m}Nb, $^{90m+g}$Nb, $^{90m+g}$Nb^{cum}, ^{91m}Nb, ^{92m}Nb, ^{95g}Nb, ^{95m}Nb, $^{95m+g}$Nb, ^{96}Nb, $^{97m+g}$Nb, $^{88m+g}$Zr^{cum} a $^{89m+g}$Zr^{cum} boli zmerané v intervale energií 6,9–35,8 MeV. Hlavná pozornosť bola venovaná tvorbe ^{99m}Tc a ^{99}Mo, ktoré majú význam pri príprave ^{99m}Tc a $^{96m+g}$Tc pre monitoring protónového zväzku. Vôbec po prvýkrát boli zmerané excitačné funkcie reakcií pre vznik ^{97m}Tc, ^{88g}Nb, ^{88m}Nb a ^{89m}Nb. V prípade ^{97m}Tc ide o veľmi hodnotné dáta, keďže tento rádionuklid je významným dlhodobým izotopickým kontaminantom ^{99m}Tc pri jeho cyklotrónovej príprave reakciou ^{100}Mo(p,2n) na vysoko obohatenom ^{100}Mo. Excitačné funkcie boli porovnané s dostupnými publikovanými dátami a s teoretickou predpoveďou kódu TALYS. Ku všetkým spomínaným rádionuklidom boli napočítané výťažky v hrubých terčoch. V **Publikácii I** k týmto dátam boli navrhnuté odporúčané účinné prierezy pre reakcie ^{100}Mo(p,2n)^{99m}Tc, ^{100}Mo(p,x)^{99}Mo a ^{nat}Mo(p,x)$^{96m+g}$Tc na základe vybraných experimentálnych dát. V publikácii je taktiež podaný detailný rozbor možností prípravy cyklotrónového technécia-99m a napočítané jeho teoretické výťažky za rôznych ožarovacích podmienok aj s príspevkom aktivity z rozpadu molybdénu-99.

- Excitačné funkcie reakcií ^{197}Au(p,x)^{197m}Hg, ^{197g}Hg, ^{195m}Hg, ^{195g}Hg, ^{196m2}Au, $^{196m1+g}$Au, $^{194m+g}$Au boli zmerané v intervale energií 6,4–35,3 MeV. Excitačné funkcie boli porovnané s dostupnými publikovanými dátami a s teoretickou predpoveďou kódu TALYS. Ku všetkým spomínaným rádionuklidom boli napočítané výťažky v hrubých terčoch. Ku všetkým izomérnym párom boli napočítané izomérne pomery ich účinných prierezov vrátanie ich neistôt. V **Publikácii II** k týmto dátam je dopodrobna rozobraná optimalizácia prípravy teranostického izomerného páru ^{197m,g}Hg nielen s ohľadom na výťažky, ale aj na pomer obidvoch izomérov v produkte.

- Excitačné funkcie reakcií ^{197}Au(d,x)^{197m}Hg, ^{197g}Hg, ^{198m}Au, ^{198g}Au, $^{196m1+g}$Au a ^{196m2}Au boli zmerané v intervale energií 8,3–19,7 MeV. Excitačné funkcie boli porovnané s dostupnými publikovanými dátami a s teoretickou predpoveďou kódu TALYS. Ku všetkým spomínaným rádionuklidom boli napočítané výťažky v hrubých terčoch. Ku všetkým izomérnym párom boli napočítané izomérne pomery ich účinných prierezov vrátanie ich neistôt. V **Publikácii III** k týmto dátam je dopodrobna rozobraná možnosť prípravy teranostického izoméreho páru ^{197m,g}Hg a porovnanie metód jeho prípravy a výťažkov pri príprave reakciami ^{197}Au(p,x) a ^{197}Au(d,x). Relatívne výnimočne aktivácia deuterónmi vedie nielen na výhodnejší izomérny pomer, ale aj na vyšší výťažok ^{197m,g}Hg.

- Pri vyhodnocovaní posledných dvoch spomínaných experimentov bola odhalená nekonzistencia vo výpočte aktivity rádionuklidu ^{197m}Hg z rôznych γ liniek. Toto dalo podnet na dôkladné zmeranie γ spektier a rozpadových kriviek rádionuklidov ^{197m,g}Hg. Pre tieto experimenty bol pripravený bodový zdroj ^{197m,g}Hg ožarovaním hrubého

zlatého terča deuterónmi s následnou separáciou vzniknutej ortuti extrakčnou chromatografiou pomocou LN-resin. Na základe týchto dát bola prehodnotená rozpadová schéma, hlavne pravdepodobnosť vetvenia IT vs. EC izoméru ^{197}Hg so spinom $J^{\pi} = 13/2^{+}$. Nové dáta sú zhrnuté v **Publikácii V**, na základe ktorej boli znovu vyhodnotené dáta z experimentov ^{197}Au(p,x) a ^{197}Au(d,x). Ich zhrnutím vznikla **Publikácia IV**.

- V rámci experimentov ^{197}Au(d,x) boli vyhodnotené aktivity produktov aktivácie medených degradérov a opublikované excitačné funkcie reakcií ^{nat}Cu(d,x)^{63}Zn, resp. v danom rozsahu energií reakcie ^{63}Cu(d,2n)^{63}Zn a sú súčasťou **Publikácie III**.

- Excitačné funkcie reakcií ^{nat}Ti(p,x)^{48}V, ^{43}Sc, ^{44g}Sc, ^{44m}Sc, $^{46m+g}$Sc, ^{47}Sc a ^{48}Sc boli zmerané v intervale energií 6,4–36,0 MeV. V týchto experimentoch bol kladený obzvlášť veľký dôraz na správnosť a presnosť stanovenia účinných prierezov, a preto, kde to bolo možné, bola zmeraná aj aktivita odrazených atómov na nasledujúcej terčovej fólii a táto aktivita bola započítaná do celkovej aktivity daného rádionuklidu v terčovej fólii. Po porovnaní vypočítaných dát s už publikovanými dátami a teoretickou predpoveďou kódu TALYS bol urobený ich výber, z ktorého boli navrhnuté účinné prierezy pre reakciu ^{nat}Ti(p,x)^{48}V. Následne bola diskutovaná diskrepancia medzi nami navrhovanými účinnými prierezmi a účinnými prierezmi odporúčanými IAEA v databáze [4] v oblasti maxima tejto excitačnej funkcie. Ku všetkým zmeraným rádionuklidom boli napočítané výťažky v hrubých terčoch.

- Excitačné funkcie reakcií ^{nat}Cu(p,x)^{62}Zn, ^{63}Zn, ^{65}Zn, ^{61}Cu a $^{58m+g}$Co boli zmerané v intervale energií 7,3–35,9 MeV. Excitačné funkcie boli porovnané s dostupnými publikovanými dátami a s teoretickou predpoveďou kódu TALYS. Ku všetkým spomínaným rádionuklidom boli napočítané výťažky v hrubých terčoch. Po kritickom zhodnotení experimentálnych dát bol urobený ich výber, na základe ktorého boli navrhnuté odporúčané účinné prierezy reakcií ^{nat}Cu(p,x)^{62}Zn, ^{63}Zn a ^{65}Zn. Tieto excitačné funkcie boli porovnané s excitačnými funkciami odporúčanými IAEA v databáze [4] a prípadné rozdiely boli v publikácii k týmto dátam diskutované. Výsledky experimentov ^{nat}Ti(p,x) a ^{nat}Cu(p,x) sú zhrnuté v **Publikácii VI**.

6 Referencie

[1] V. Majer, L. Drška, B. Chutný, V. Kačena, J. Malý, A. Zeman: *Základy jaderné chemie*. Státní nakladatelství technické literatury, Praha, 1961.

[2] W.D. Loveland, D.J. Morrissey, G.T. Seaborg: *Modern Nuclear Chemistry*, John Wiley & Sons, 2006. (ISBN 0-471-11532-0)

[3] N. Otuka, E. Dupont, V. Semkova, B. Pritychenko, A.I. Blokhin, M. Aikawa, S. Babykina, M. Bossant, G. Chen, S. Dunaeva, R.A. Forrest, T. Fukahori, N. Furutachi, S. Ganesan, Z. Ge, O.O. Gritzay, M. Herman, S. Hlavač, K. Katō, B. Lalremruata, Y.O. Lee, A. Makinaga, K. Matsumoto, M. Mikhaylyukova, G. Pikulina, V.G. Pronyaev, A. Saxena, O. Schwerer, S.P. Simakov, N. Soppera, R. Suzuki, S. Takács, X. Tao, S. Taova, F. Tárkányi, V.V. Varlamov, J. Wang, S.C. Yang, V. Zerkin, Y. Zhuang: *Towards a More Complete and Accurate Experimental Nuclear Reaction Data Library (EXFOR): International Collaboration Between Nuclear Reaction Data Centres (NRDC)*, Nucl. Data Sheets 120, 272, 2014. https://doi.org/10.1016/j.nds.2014.07.065.

[4] IAEA TEC-DOC-1211: *Charged particles cross-sections database for medical radioisotope production*. IAEA, Vienna, 2001. Dostupné online na: <http://www-nds.iaea.org/medical>.

[5] A. Hermanne, A.V. Ignatyuk, R. Capote, B.V. Carlson, J.W. Engle, M.A. Kellett, T. Kibedi, G. Kim, F.G. Kondev, M. Hussain, O. Lebeda, A. Luca, Y. Nagai, H. Naik, A.L. Nichols, F.M. Nortier, S.V. Suryanarayana, S. Takács, F. Tárkányi, M. Verpelli. *Reference Cross Sections for Charged-particle Monitor Reactions*. Nuclear Data Sheets 148 (special issue), pp. 338–382, 2018. https://doi.org/10.1016/j.nds.2018.02.009

[6] J.F. Ziegler, M.D. Ziegler, J.P. Biersack: SRIM2010 Code. Dostupné online na: <http://www.srim.org/>.

[7] F. Tarkanyi, A. Hermanne, F. Ditroi, S. Takacs, B.Kiraly, J. Csikai, M. Baba, H. Yamazaki, M.S. Uddin, A.V. Ignatyuk, S.M. Qaim: *Systematic study of activation cross-sections of deuteron induced reactions used in accelerator applications*; Nuclear Measurements, Evaluations and Applications – 6th Workshop Proceedings, 203-214, 2011.

[8] M. Čihák, O. Lebeda, J. Štursa, *Beam dynamic simulation in the isochronous cyclotron U-120M*, in: Proceedings of the eighteenth international conference on cyclotrons and their applications, CYCLOTRONS 2007, Giardini Naxos, Italy, 2007.

[9] P. Kopecký, *Proton beam monitoring via the Cu(p,x)^{58}Cu, ^{63}Cu(p,2n)^{62}Zn and ^{65}Cu(p,n)^{65}Zn Reactions in Copper*, Int. J. Appl. Radiat. Isot. 36 (8), 657–661, 1985.

[10] NuDat 2.6. National Nuclear Data Center, Brookhaven National Laboratory, 2012. Dostupné online na <www.nndc.bnl.gov/nudat2/>.

[11] M.R. Bhat: *Evaluated Nuclear Structure Data File (ENSDF)*, in: Nuclear Data for Science and Technology. Research Reports in Physics. Springer, Berlin, Heidelberg, 1992. https://doi.org/10.1007/978-3-642-58113-7_227.

[12] B. Pritychenko, A. Sonzogni, Q-value calculator, NNDC, Brookhaven National Laboratory. Dostupné online na <http://www.nndc.bnl.gov/qcalc>.

[13] J. Frána: *Program DEIMOS32 for gamma-ray spectra evaluation*. J. Radioanal. Nucl. Chem. 257(3), pp. 583–587, 2003. https://doi.org/10.1023/A:1025448800782.

[14] M.J. Berger, J.H. Hubbell, S.M. Seltzer, J. Chang, J.S. Coursey, R. Sukumar, D.S. Zucker, K. Olsen : *XCOM: Photon Cross Section Database* (version 1.5), National Institute of Standards and Technology, Gaithersburg, MD, 2010. Dostupné online na: <http://physics.nist.gov/xcom>.

[15] A.J. Koning, D. Rochman, S.C. van der Marck, J. Kopecky, J.Ch. Sublet, S. Pomp, H. Sjostrand, R. Forrest, E. Bauge, H. Henriksson, O. Cabellos, S. Goriely, J. Leppanen, H. Leeb, A. Plompen, R. Mills, *TALYS-based evaluated nuclear data library*. Dostupné online na <http://www.talys.eu/tendl-2019>.

7 Prílohy

7.1 Publikácie

Publikácia I

Červenák J., Lebeda O.

Experimental cross-sections for proton-induced nuclear reactions on ^{nat}Mo

Nucl. Instrum. Methods Phys. Res. B 380 (2016) 32-49
http://dx.doi.org/10.1016/j.nimb.2016.05.006

Nuclear Instruments and Methods in Physics Research B 380 (2016) 32–49

Contents lists available at ScienceDirect

Nuclear Instruments and Methods in Physics Research B

journal homepage: www.elsevier.com/locate/nimb

Experimental cross-sections for proton-induced nuclear reactions on ^{nat}Mo

Jaroslav Červenák, Ondřej Lebeda *

Nuclear Physics Institute of the CAS, Husinec-Řež 130, 250 68 Řež, Czech Republic

ARTICLE INFO

Article history:
Received 26 February 2016
Received in revised form 2 May 2016
Accepted 4 May 2016

Keywords:
Cross-sections
Excitation functions
Proton-induced nuclear reactions
Natural molybdenum
^{99}Mo
^{99m}Tc
$^{96m+g}$Tc
^{95m}Tc
Thick target yields
U-120 M cyclotron

ABSTRACT

In the framework of the Co-ordinated Research Project of the IAEA, we measured in detail cross-sections of the nuclear reactions ^{nat}Mo(p,x)^{93g}Tc, ^{93m}Tc, $^{93m+g}$Tc, ^{94g}Tc, ^{94m}Tc, ^{95g}Tc, ^{95m}Tc, $^{96m+g}$Tc, ^{97m}Tc, ^{99m}Tc, ^{90}Mo, ^{93m}Mo, ^{99}Mo, ^{88g}Nb, ^{88m}Nb, ^{89g}Nb, ^{89m}Nb, $^{90m+g}$Nb, $^{90m+g}$Nb^{cum}, ^{91m}Nb, ^{92m}Nb, ^{95g}Nb, ^{95m}Nb, $^{95m+g}$Nb, ^{96}Nb, $^{97m+g}$Nb, $^{88m+g}$Zr^{cum} and $^{89m+g}$Zr^{cum} in the energy range of 6.9–35.8 MeV. The data for formation of ^{97m}Tc, ^{88g}Nb, ^{88m}Nb and ^{89m}Nb are reported for the first time. The obtained results were compared to the prediction of the nuclear reaction model code TALYS adopted from the TENDL-2015 library and to the previously published cross-sections. The thick target yields for all the radionuclides were calculated from the measured data. We suggest recommended cross-sections and thick target yields for the ^{100}Mo(p,2n)^{99m}Tc, ^{100}Mo(p,x)^{99}Mo and ^{nat}Mo(p,x)$^{96m+g}$Tc nuclear reactions deduced from the selected experimental data.

1. Introduction

The current data base contains many experimental data on the proton-induced reactions on natural molybdenum [1–22]. Cross-sections for the ^{100}Mo(p,2n)^{99m}Tc and ^{100}Mo(p,x)^{99}Mo reactions attracted attention of the wider scientific community due to the recent severe crisis in the supply of ^{99}Mo/^{99m}Tc generators [23,24], because direct cyclotron production of ^{99m}Tc represents a promising alternative to reactor-produced ^{99}Mo/^{99m}Tc generators [24–28]. Besides that, elemental cross-sections for the reaction ^{nat}Mo(p,x)$^{96m+g}$Tc are relevant for proton beam monitoring [7,22], the reaction ^{nat}Mo(p,x)^{95m}Tc provides tracer of ^{99g}Tc [29] and data for formation of ^{93g}Tc, ^{93m}Tc, $^{93m+g}$Tc, ^{94g}Tc, ^{94m}Tc, ^{95g}Tc, ^{97m}Tc, ^{90}Mo, ^{93m}Mo, ^{88g}Nb, ^{88m}Nb, ^{89g}Nb, ^{89m}Nb, $^{90m+g}$Nb, ^{91m}Nb, ^{92m}Nb, ^{95g}Nb, ^{95m}Nb, $^{95m+g}$Nb, ^{96}Nb, $^{97m+g}$Nb, $^{88m+g}$Zr^{cum} and $^{89m+g}$Zr^{cum} are of interest for testing the nuclear reaction model codes, estimating activation of parts exposed to proton beams and for the thin layer activation (TLA) [30].

In spite of a large number of experiments focused on proton activation of natural molybdenum, the available data are often scattered and inconsistent. It is true particularly for formation of ^{99m}Tc, but also in the cases, where no problems like interferences or substantial nuclear decay data unreliability occur, e.g. ^{99}Mo [22]. Cross-section data for several relevant radionuclides like ^{97m}Tc are missing at all.

In the framework of the Coordinated Research Project of International Atomic Energy Agency (IAEA) "*Nuclear Data for Charged-Particle Monitor Reactions and Medical Isotope Production*", we were charged with providing new experimental data for formation of ^{99m}Tc and ^{99}Mo on ^{100}Mo, as well as for the ^{nat}Mo(p,x)$^{96m+g}$Tc monitoring reaction. We have, therefore, measured thoroughly elemental activation cross-sections for the ^{nat}Mo(p,x)^{93g}Tc, ^{93m}Tc, $^{93m+g}$Tc, ^{94g}Tc, ^{94m}Tc, ^{95g}Tc, ^{95m}Tc, $^{96m+g}$Tc, ^{97m}Tc, ^{99m}Tc, ^{90}Mo, ^{93m}Mo, ^{99}Mo, ^{88g}Nb, ^{88m}Nb, ^{89g}Nb, ^{89m}Nb, $^{90m+g}$Nb, $^{90m+g}$Nb^{cum}, ^{91m}Nb, ^{92m}Nb, ^{95g}Nb, ^{95m}Nb, $^{95m+g}$Nb, ^{96}Nb, $^{97m+g}$Nb, $^{88m+g}$Zr^{cum} and $^{89m+g}$Zr^{cum} reactions and compared them with the previously published data.

Since new abundances of stable Mo isotopes (^{92}Mo 14.53%, ^{94}Mo 9.15%, ^{95}Mo 15.84%, ^{96}Mo 16.67%, ^{97}Mo 9.60%, ^{98}Mo 24.39% and ^{100}Mo 9.82%) have been recently released [31], we used them for conversion of elemental to isotopic cross-sections for reactions on ^{100}Mo. The converted cross-sections adopted from the publications that used the former abundances (^{92}Mo 14.84%, ^{94}Mo 9.25%, ^{95}Mo 15.92%, ^{96}Mo 16.68%, ^{97}Mo 9.55%, ^{98}Mo 24.13% and ^{100}Mo 9.63% [32]) were also corrected for the new abundance of ^{100}Mo before comparing them with our results.

* Corresponding author.
E-mail address: lebeda@ujf.cas.cz (O. Lebeda).

http://dx.doi.org/10.1016/j.nimb.2016.05.006
0168-583X/

2. Experimental

2.1. Target and irradiation

Two stacks of foils, each consisting of ten ^{nat}Mo foils (99.9%, 19.3 μm thick, Goodfellow, Great Britain) interleaved with ten ^{nat}Cu foils (99.9%, 10.6 μm thick, Goodfellow, Great Britain), eleven ^{nat}Ti foils (99.6%, 11.0 μm thick, Alfa Aesar, USA) and a few Cu degraders (55.9 and/or 10.6 μm thick) were irradiated on the external proton beam of the cyclotron U-120 M in the Nuclear Physics Institute of the CAS. Both stacks were located in a Faraday-cup like target holder and irradiated for one hour. The entrance beam energy was set by positioning of an extracting carbon foil and its value was deduced from the precisely measured beam orbit position [33]. The average beam energy in the center of each foil was calculated using the code SRIM [34]. The current of the collimated beam was kept constant during the irradiation, recorded each second and integrated over the bombardment time t_b.

2.2. Activity measurement

After the end of bombardment (EOB), the stacks were immediately dismounted and the activity of radionuclides in each foil was measured using an energy and efficiency calibrated HPGe detector (GMX45-Plus, Ortec) coupled with the DSPEC jr 2.0 integrated gamma spectrometer (Ortec). The energy and efficiency calibration of the spectrometer was performed using a set of standards (^{241}Am, ^{152}Eu, ^{137}Cs, ^{133}Ba and ^{60}Co) provided by the Czech Institute of Metrology with combined standard uncertainties ranged from 0.4% to 1.0%. Detection efficiency was determined for the sample-detector distances 150, 200, 400, 600, 1000 and 1600 mm. The whole energy range was fitted by a polynomial of the 5th degree:

$$\ln \eta = \sum_{n=0}^{5} a_n \ln E^n, \tag{1}$$

where η is detection efficiency, a_n is polynomial coefficient and E is energy of the photopeak. For the gamma ray energies exceeding 240 keV, a linear fit was used providing practically the same efficiencies as the polynomial fit.

Decay data (half-lives, gamma ray energies and intensities) of the radionuclides were adopted from the data base NuDat2 [35] and for ^{99m}Tc and ^{99}Mo from Ref. [36]. Nuclear reaction energies and thresholds were calculated using Q-calc [37]. The data relevant to the formation and quantification of the activation products are summarized in Table 1.

Each Mo foil was measured five to eight times in order to optimize conditions for quantification of radionuclides with various half-lives and activities, and to see consistency of the applied interference corrections (see Section 2.3). The gamma ray spectra were evaluated in the program DEIMOS32 [38].

2.3. Interference corrections

Table 1 indicates several interferences that affect activity measurement of several radionuclides born in the irradiated target foils. The most complex situation is represented by the set of corrections for determining the ^{99m}Tc activity born directly in the ^{100}Mo(p,2n) reaction. As thoroughly discussed earlier [15,22,28], the 140.51 keV net peak area is to be corrected for:

- Contribution of ^{99m}Tc born from ^{99}Mo during and after irradiation.
- Contribution of the 140.51 keV gamma line emitted directly in ^{99}Mo decay.
- Contribution of 141.18 keV gamma line from the decay of ^{90}Nb produced directly and due to the decay of ^{90}Mo (for E_p > 22 MeV).

The corrections were performed as described in Ref. [15]. We also paid attention to other interferences that occurred in the measurements either due to accidental proximity of the two gamma lines or due to emission of the same energy gamma lines from the nuclei decaying to the same product (^{95}Nb and ^{95}Tc, ^{96}Nb and ^{96g}Tc or ^{94m}Tc and ^{94g}Tc). Activity of the interference-affected radionuclide was then calculated with use of other non-interfering gamma line (if available) or of significant difference in the half-lives or in the gamma line intensities of the interfering radionuclides.

If both cumulative cross-section σ_{cum} of the longer-lived daughter radionuclide and shorter-lived parent cross-section σ_1 could be measured, we deduced the cross-section for the direct formation of the daughter radionuclide σ_2 from the following formula:

$$\sigma_{cum} = \frac{\lambda_1}{\lambda_1 - \lambda_2} f \sigma_1 + \sigma_2, \tag{2}$$

where λ_1 and λ_2 are decay constants of the parent and daughter radionuclides and f is transition probability of the parent to the daughter radionuclide. The same formula was used to derive prediction of the cumulative cross-sections from the cross-sections for the parent and the daughter radionuclide formation in various contributing nuclear reaction channels provided in TENDL-2015.

2.4. Calculation of the cross-sections, their uncertainties, thick target yields and prediction of excitation functions

Elemental and cumulative elemental cross-sections were calculated from the activation formula:

$$\sigma = \frac{P_\gamma}{I_\gamma \eta t_m} \frac{\lambda t_r}{1 - e^{-\lambda t_r}} e^{\lambda t_c} \frac{Aze}{d\rho N_A I (1 - e^{-\lambda t_b})}, \tag{3}$$

where σ is cross-section for formation of a radionuclide at the beam energy in the foil's center (cm^2), P_γ is net peak area of the gamma line selected for the quantification, I_γ is its intensity per decay and η its detection efficiency, t_m is real time of the measurement (h), t_r is live time of the measurement (h), t_c is time elapsed between the EOB and start of the measurement (h), A is atomic weight of the foil's material (g/mol), z is proton charge ($z = 1$), e is elementary charge (1.602177×10^{-19} C), d is thickness of the foil (cm), ρ is density of the foil's material (g/cm^3), N_A is Avogadro's number (6.022137×10^{23} mol^{-1}), I is beam current (A), λ is decay constant of the radionuclide (h^{-1}) and t_b is irradiation time (h).

The total uncertainty of the measured cross-section is obtained by summing up the following uncertainties in quadrature:

- Detection efficiency for a gamma line selected for the activity calculation (ca 3%).
- Emission probability of a gamma line selected for activity calculation (usually < 5%).
- Net peak area of a gamma line selected for activity calculation (< 25%, mostly < 2%).
- Beam current (< 6%).
- Foil's thickness (< 2%).

As ^{99m}Tc and ^{99}Mo are produced solely in the reactions on ^{100}Mo [6], the measured elemental cross-sections were converted to isotopic cross-sections on ^{100}Mo.

Thick target yields for all the radionuclides were deduced from the obtained experimental data by integrating the fitted

Table 1
Data for the investigated radionuclides. *Q*-values for isomeric nuclei have to be lowered by the energy level of the isomer. *Q*-values for reactions where composed particles are emitted have to be increased by binding energy of the particle (d = np + 2.225 MeV, t = p2n + 8.482 MeV, ^{3}He = 2pn + 7.718 MeV, α = 2p2n + 28.296 MeV). Energies of gamma lines used for quantification of each particular radionuclide are in bold. Uncertainties of the half-lives, gamma line energies and their intensities in the last valid digits are given in italics.

RN	Half-life	E_γ (keV)	I_γ (%)	Contributing reactions	Q-value (MeV)	E_{thr} (MeV)
^{93g}Tc	2.75 h *5*	**1362.94 *7***	**66.2**	^{92}Mo(p,γ)	4.087	0
		1477.14 *8*	8.7 *5*	^{94}Mo(p,2n)	−13.661	13.808
		1520.28 *9*	24.4	^{95}Mo(p,3n)	−21.030	21.254
^{93m}Tc	43.5 min *10*	**391.83 *8***	**58.3**	^{96}Mo(p,4n)	−30.185	30.502
^{94g}Tc	293 min *1*	**702.67 *7***	**99.6 *18***			
		849.74 *7*	95.7 *18*	^{94}Mo(p,n)	−5.038	5.092
		871.05 *7*	99.9	^{95}Mo(p,2n)	−12.407	12.539
^{94m}Tc	52.0 min *10*	871.05 *7*	94.2	^{96}Mo(p,3n)	−21.562	21.788
		993.19 *9*	2.21 *3*	^{97}Mo(p,4n)	−28.383	28.678
		1522.1 *2*	4.5 *3*	^{98}Mo(p,5n)	−37.025	37.406
		1868.68 *8*	**5.7 *3***			
^{95g}Tc	20.0 h *1*	**765.789 *9***	**93.8 *3***	^{94}Mo(p,γ)	4.896	0
				^{95}Mo(p,n)	−2.473	2.499
^{95m}Tc	61 d *2*	**204.117 *2***	**63.2 *8***	^{96}Mo(p,2n)	−11.627	11.749
		582.082 *3*	30.0 *4*	^{97}Mo(p,3n)	−18.448	18.64
		835.149 *5*	26.6 *4*	^{98}Mo(p,4n)	−27.091	27.37
^{96g}Tc	4.28 d *7*	568.88 *7*	0.92 *6*	^{95}Mo(p,γ)	5.399	0
		778.22 *4*	**99.76**	^{96}Mo(p,n)	−3.756	3.795
		812.54 *4*	82 *3*	^{97}Mo(p,2n)	−10.577	10.687
		849.86 *4*	98 *4*	^{98}Mo(p,3n)	−19.219	19.417
		1126.85 *6*	15.2 *12*	^{100}Mo(p,5n)	−33.437	33.774
^{97m}Tc	91.0 d *6*	**96.5 *1***	**0.320**	^{96}Mo(p,γ)	5.714	0
				^{97}Mo(p,n)	−1.107	1.119
				^{98}Mo(p,2n)	−9.750	9.85
				^{100}Mo(p,4n)	−23.967	24.209
^{99m}Tc	6.0067 h *10*	**140.511 *1***	**88.5 *2***	^{98}Mo(p,γ)	6.501	0
				^{100}Mo(p,2n)	−7.716	7.794
^{90}Mo	5.67 h *7*	122.370 *22*	64 *3*	^{92}Mo(p,p2n)	−22.778	23.027
		257.34 *4*	**78 *4***	^{94}Mo(p,p4n)	−40.525	40.96
^{93m}Mo	6.85 h *7*	263.049 *13*	57.4 *11*	^{94}Mo(p,pn)	−9.678	9.782
				^{95}Mo(p,p2n)	−17.047	17.228
				^{96}Mo(p,p3n)	−26.201	26.477
		684.693 *21*	**99.9 *8***	^{97}Mo(p,p4n)	−33.023	33.366
		1477.138 *3*	99.1 *11*	^{98}Mo(p,p5n)	−41.665	42.094
^{99}Mo	65.949 h *14*	140.5106 *10*	4.72 *	^{100}Mo(p,pn)	−8.292	8.375
		140.5106 *10*	90.2 *17*			
		181.0938 *11*	6.01 *11*			
		739.500 *17*	**12.12 *14***			
^{88g}Nb	14.55 min *11*	399.4 *1*	31.8 *17*			
		502.9 *1*	60 *5*			
		1057.1 *1*	**100 *6***			
		1082.6 *1*	103 *6*	^{92}Mo(p,2p3n)	−42.135	42.597
^{88m}Nb	7.78 min *1*	399.4 *1*	46.0 *23*	^{94}Mo(p,2p5n)	−59.882	60.525
		450.6 *1*	**26.8 *13***			
		638.0 *1*	26.4 *12*			
		1057.1 *1*	90 *5*			
		1082.6 *1*	54 *3*			
^{89g}Nb	2.03 h *7*	**1627.2 *2***	**3.5**	^{92}Mo(p,2p2n)	−29.614	29.939
^{89m}Nb	66 min *2*	**588.0 *2***	**95.57**	^{94}Mo(p,2p4n)	−47.362	47.87
^{90g}Nb	14.60 h *5*	141.178 *15*	66.8 *7*	^{92}Mo(p,2pn)	−19.506	19.72
				^{94}Mo(p,2p3n)	−37.254	37.653
		1129.224 *15*	**92.7 *5***	^{95}Mo(p,2p4n)	−44.623	45.096
				^{96}Mo(p,2p5n)	−53.777	54.342
				^{97}Mo(p,2p6n)	−60.598	61.228
^{91m}Nb	60.86 d *22*	104.62 *5*	0.574	^{92}Mo(p,2p)	−7.458	7.54
				^{94}Mo(p,2p2n)	−25.206	25.476
				^{95}Mo(p,2p3n)	−32.575	32.921
		1204.67 *8*	**2.0 *3***	^{96}Mo(p,2p4n)	−41.729	42.168
				^{97}Mo(p,2p5n)	−48.551	49.055
^{92m}Nb	10.15 d *2*	**934.44 *10***	**99.15**	^{94}Mo(p,2pn)	−17.319	17.505
				^{95}Mo(p,2p2n)	−24.688	24.951
				^{96}Mo(p,2p3n)	−33.843	34.198
				^{97}Mo(p,2p4n)	−40.664	41.087
				^{98}Mo(p,2p5n)	−49.307	49.814

Table 1 (*continued*)

RN	Half-life	E_γ (keV)	I_γ (%)	Contributing reactions	Q-value (MeV)	E_{thr} (MeV)
^{95g}Nb	34.991 d *6*	**765.803 *6***	**99.808 *7***	^{96}Mo(p,2p)	−9.298	9.395
				^{97}Mo(p,2pn)	−16.119	16.286
	3.61 d *3*	**235.690 *20***	**24.8 *8***	^{98}Mo(p,2p2n)	−24.761	25.016
^{95m}Nb				^{100}Mo(p,2p4n)	−39.979	39.372
^{96}Nb	23.35 h *5*	460.040 *12*	26.62 *19*			
		568.871 *12*	**58.0 *3***	^{97}Mo(p,2p)	−9.226	9.322
		778.224 *15*	96.45 *22*	^{98}Mo(p,2pn)	−17.868	18.052
		849.929 *13*	20.45 *19*	^{100}Mo(p,2p3n)	−32.086	32.409
		1091.349 *12*	48.50 *15*			
^{97g}Nb	72.1 min *7*	**657.94 *9***	**98.23**	^{98}Mo(p,2p)	−9.796	9.897
		1024.4 *3*	1.09 *7*	^{100}Mo(p,2p2n)	−24.013	24.255
^{88g}Zr	83.4 d *3*	**392.87 *9***	**97.29**	^{92}Mo(p,3p2n)	−33.900	34.272
				^{94}Mo(p,3p4n)	−51.648	52.202
^{89g}Zr	78.41 h *12*	**909.15 *15***	**99.04**	^{92}Mo(p,3pn)	−24.581	24.85
				^{94}Mo(p,3p4n)	−42.328	42.783

* This is intensity of the 140.51 keV gamma line emitted in the ^{99}Mo decay itself. The following value (90.2%) is valid for ^{99}Mo in transient equilibrium with ^{99m}Tc.

cross-sections over the measured energy range using the linear energy transfer.

Besides comparison with previously published data, the measured cross-sections were confronted also with excitation functions obtained via the TALYS nuclear reaction model code adopted from the TENDL-2015 library [39]. The excitation functions were calculated as a weighted sum of the predicted cross-sections for those reaction channels on stable molybdenum isotopes that result in a particular radionuclide.

3. Results and discussion

3.1. Beam energy and current

The beam energy deduced from the precisely measured beam orbit position [33] was 36.00 ± 0.30 MeV for the 1st stack of foils and 21.35 ± 0.30 MeV for the 2nd stack of foils. The beam current obtained from continuous monitoring of the beam was 1.230 and 0.5078 μA for the 1st and 2nd stack of foils, respectively. These beam current values were used without any further correction and their estimated uncertainty was 6%. The cross-sections calculated from the activation of the two separately irradiated stacks of foils provided smooth curves without apparent break between the both data sets, as obvious from Figs. 1–27. The data obtained from the ^{nat}Ti and ^{nat}Cu monitors will be published separately in order to compare them with the recommended cross-sections for the monitoring reactions [40] in detail.

3.2. Activity calculations and the cross-sections

All the measured cross-sections are summarized in Tables 2 and 3. Particular excitation functions are discussed in the following paragraphs and displayed in Figs. 1–27. In the case of $^{96m+g}$Tc in the first stack of foil, we quantified its recoil fraction ejected on the following foil in the stack. We found that it decreased from 0.324% at 35.75 MeV to 0.227% at 23.5 MeV. It, therefore, seems that for the molybdenum foils of 20 μm thickness and the proton beam energies used in the experiment, one may neglect this phenomenon in the activity evaluation.

3.2.1. Cross-sections for the $^{nat}Mo(p,x)^{93m}Tc$, $^{nat}Mo(p,x)^{93m+g}Tc$ and $^{nat}Mo(p,x)^{93g}Tc$ reactions

Activity of ^{93m}Tc was calculated via its 391.83 keV gamma line and that of ^{93g}Tc (and $^{93m+g}$Tc) via its 1362.94 keV gamma line. We observed a very good agreement between our data for the formation of isomer ^{93m}Tc and the data provided by Uddin et al. (2008) [14], Lebeda and Pruszyński (2010) [15] and Tárkányi et al. (2012) [20]. The prediction of TENDL-2015 describes well the course of the excitation function, but it suggests somewhat lower values than indicated by the experimental data for E_p = 17–32 MeV, cf. Fig. 1a. Cumulative cross-sections for $^{93m+g}$Tc were published in Refs. [13–15,20]. Our measurement is consistent with them except few points in Refs. [13,14] which are lower (see Fig. 2a). Prediction of the cumulative cross-sections deduced from the data for the formation of the isomer and the ground state in TENDL-2015 according to the formula (2) corresponds very well with the measured cross-sections in the whole energy range (cf. Fig. 2a).

The experimental data for direct formation of the ground state ^{93g}Tc were calculated from the works [14,15,20], which provide formation cross-sections of both the isomer ^{93m}Tc and the cumulative ground state $^{93m+g}$Tc (cf. Figs. 1a and 2a), using the formula (2). The resulting cross-sections are displayed on Fig. 3a. Although the work [20] supplies data for the direct production of ^{93g}Tc, they are surprisingly higher than the cross-sections calculated as described above. The authors of Ref. [20] deduced obviously cross-sections for the direct formation of ^{93g}Tc from the simplified formula $\sigma_{cum} = f\sigma_1 + \sigma_2$. It is, however, applicable only if λ_2 is negligible compared to λ_1, cf. formula (2). Besides that, they used slightly lower value of the factor f (0.766) instead of f = 0.774 we adopted from Ref. [35]. We found exceptionally good agreement among the previously published data, our measurement and the TENDL-2015 prediction, as obvious from Fig. 3a.

Formation of ^{93m}Tc and ^{93g}Tc in measurable amounts was observed below 13 MeV [13,15,20], although the threshold of the ^{94}Mo(p,2n) reaction is 13.8 MeV. For E_p < 13 MeV, both isomers are formed solely in the ^{92}Mo(p,γ) reaction. It is a nice example of relatively high cross-section of the (p,γ) reaction that reaches maximum of ca 7 mb at ca 8.3 MeV (corrected for the abundance of ^{92}Mo in ^{nat}Mo). The measured data for ^{nat}Mo(p,x)^{93m}Tc, $^{93m+g}$Tc, ^{93g}Tc reactions up to 14 MeV are displayed separately on Figs. 1b, 2b and 3b in order to expose their comparison with each other and with the predicted values of TENDL-2015. At maximum, the model predicts two to three times lower cross-sections than observed in the experiment. It is to be noted that at 13.46 MeV, we have not detected any ^{93m}Tc what is in a good agreement with the very low forecast of TENDL-2015 (cf. Fig. 1b).

3.2.2. Cross-sections for the $^{nat}Mo(p,x)^{94g}Tc$ and $^{nat}Mo(p,x)^{94m}Tc$ reactions

Activity of ^{94g}Tc was determined using the 702.67 keV gamma line, while that of ^{94m}Tc was measured using its weaker, but also

Table 2
Measured cross-section data for formation of Tc and Mo radionuclides in the ^{nat}Mo(p,x) reactions.

E_p (MeV)	σ (mb)												
	^{93g}Tc	^{93m}Tc	$^{93m+g}$Tc	^{94g}Tc	^{94m}Tc	^{95g}Tc	^{95m}Tc	$^{96m+g}$Tc	^{97m}Tc	^{99m}Tc	^{90}Mo	^{93m}Mo	^{99}Mo
35.75 ± 0.31	64.7 ± 5.1	7.70 ± 0.53	72.77 ± 5.02	69.1 ± 4.8	34.9 ± 3.1	113.4 ± 7.8	26.8 ± 1.9	106.9 ± 7.3	11.8 ± 1.5	2.61 ± 0.34	37.7 ± 3.2	6.86 ± 0.73	15.4 ± 1.1
34.34 ± 0.33	65.8 ± 5.2	8.19 ± 0.57	74.43 ± 5.13	69.9 ± 4.8	37.6 ± 3.4	105.1 ± 7.3	24.6 ± 1.7	129.7 ± 8.9	11.6 ± 1.6	2.48 ± 0.33	29.4 ± 2.5	6.13 ± 0.66	15.5 ± 1.1
32.87 ± 0.36	67.7 ± 5.4	8.99 ± 0.63	77.17 ± 5.32	70.2 ± 4.8	38.0 ± 3.9	96.3 ± 6.6	22.9 ± 1.6	156 ± 11	12.3 ± 1.5	3.35 ± 0.36	20.1 ± 1.7	5.60 ± 0.60	15.4 ± 1.1
31.37 ± 0.39	72.8 ± 5.8	10.04 ± 0.70	83.38 ± 5.75	70.8 ± 4.9	42.2 ± 3.8	89.8 ± 6.2	22.1 ± 1.6	180 ± 12	12.9 ± 1.6	3.48 ± 0.36	11.31 ± 0.98	4.91 ± 0.53	15.6 ± 1.1
29.80 ± 0.42	75.6 ± 6.1	10.90 ± 0.76	87.10 ± 6.00	71.2 ± 4.9	43.2 ± 3.8	88.3 ± 6.1	22.6 ± 1.6	192 ± 13	11.7 ± 1.8	3.40 ± 0.31	4.59 ± 0.40	3.98 ± 0.43	15.6 ± 1.1
28.17 ± 0.46	77.1 ± 6.2	11.04 ± 0.77	88.74 ± 6.12	71.8 ± 4.9	43.2 ± 3.9	96.3 ± 6.6	25.6 ± 1.8	193 ± 13	10.2 ± 1.4	3.47 ± 0.30	1.31 ± 0.12	3.06 ± 0.33	15.9 ± 1.2
26.45 ± 0.50	74.5 ± 6.0	10.68 ± 0.74	85.74 ± 5.92	71.0 ± 4.9	42.2 ± 3.8	111.9 ± 7.7	30.4 ± 2.1	184 ± 13	12.3 ± 1.5	4.13 ± 0.39	0.284 ± 0.041	2.05 ± 0.22	15.5 ± 1.1
24.66 ± 0.55	65.5 ± 5.3	10.09 ± 0.71	76.13 ± 5.25	69.6 ± 4.8	41.8 ± 3.8	131.0 ± 9.0	37.2 ± 2.6	166 ± 11	19.0 ± 1.7	5.41 ± 0.45	0.113 ± 0.033	1.21 ± 0.14	15.2 ± 1.1
23.50 ± 0.58	56.9 ± 4.7	9.86 ± 0.70	67.28 ± 4.65	67.9 ± 4.7	41.3 ± 3.8	139.1 ± 9.6	40.8 ± 2.9	147 ± 10	25.2 ± 2.3	6.81 ± 0.56	0.082 ± 0.031	0.781 ± 0.093	14.6 ± 1.1
22.27 ± 0.62	48.1 ± 4.2	11.06 ± 0.78	59.72 ± 4.12	67.7 ± 4.7	46.5 ± 4.2	137.9 ± 9.5	42.9 ± 3.0	121.8 ± 8.4	36.3 ± 2.8	9.08 ± 0.74	0.101 ± 0.032	0.521 ± 0.069	13.8 ± 1.0
20.98 ± 0.30	49.4 ± 4.6	12.02 ± 0.83	62.08 ± 4.46	68.0 ± 4.7	53.9 ± 4.8	126.2 ± 8.7	47.2 ± 3.3	99.9 ± 6.9	45.6 ± 3.8	13.7 ± 1.1		0.456 ± 0.063	12.00 ± 0.86
19.64 ± 0.33	47.3 ± 4.5	12.75 ± 0.88	60.67 ± 4.38	67.6 ± 4.7	57.5 ± 5.1	118.7 ± 8.2	47.7 ± 3.4	97.5 ± 6.7	53.8 ± 4.2	18.4 ± 1.5		0.206 ± 0.040	10.20 ± 0.73
18.23 ± 0.36	45.4 ± 4.2	12.12 ± 0.84	58.15 ± 4.08	63.8 ± 4.4	59.1 ± 5.2	115.4 ± 8.0	50.5 ± 3.5	99.6 ± 6.9	51.0 ± 4.2	22.5 ± 1.8		0.168 ± 0.040	8.21 ± 0.60
16.74 ± 0.41	38.1 ± 3.5	9.19 ± 0.64	47.78 ± 3.37	59.9 ± 4.1	64.0 ± 5.7	113.5 ± 7.8	52.8 ± 3.7	102.7 ± 7.1	52.6 ± 4.3	23.9 ± 2.0		0.129 ± 0.039	5.94 ± 0.43
15.18 ± 0.45	19.4 ± 1.7	3.14 ± 0.22	22.68 ± 1.67	50.8 ± 3.5	63.4 ± 5.6	112.7 ± 7.8	51.0 ± 3.6	110.6 ± 7.6	55.3 ± 4.4	24.0 ± 2.0			3.72 ± 0.28
13.46 ± 0.51	0.653 ± 0.046		0.653 ± 0.046	30.6 ± 2.1	54.3 ± 4.8	110.8 ± 7.6	47.5 ± 3.3	134.7 ± 9.3	56.5 ± 4.3	23.7 ± 1.9			1.55 ± 0.12
11.60 ± 0.59	0.217 ± 0.073	0.243 ± 0.059	0.472 ± 0.038	14.6 ± 1.0	44.6 ± 3.9	85.6 ± 5.9	38.6 ± 2.7	144.5 ± 9.9	40.7 ± 3.1	21.4 ± 1.8			0.412 ± 0.047
9.46 ± 0.70	0.567 ± 0.077	0.308 ± 0.041	0.891 ± 0.062	8.17 ± 0.56	36.8 ± 3.2	66.8 ± 4.6	29.3 ± 2.1	99.4 ± 6.8	14.3 ± 1.4	11.05 ± 0.90			
8.23 ± 0.77	0.565 ± 0.088	0.405 ± 0.048	0.991 ± 0.070	4.80 ± 0.33	30.0 ± 2.6	52.3 ± 3.6	22.2 ± 1.6	76.8 ± 5.3	11.3 ± 1.0	2.95 ± 0.24			
6.85 ± 0.88	0.426 ± 0.059	0.262 ± 0.028	0.701 ± 0.049	1.73 ± 0.12	18.2 ± 1.6	31.3 ± 2.2	13.9 ± 1.0	46.7 ± 3.2	6.30 ± 0.68	0.105 ± 0.009			

Table 3
Measured cross-section data for formation of Nb and Zr radionuclides in the ^{nat}Mo(p,x) reactions.

E_p (MeV)	σ (mb)												
	^{88g}Nb	^{89g}Nb	^{89m}Nb	$^{90m+g}$Nb	$^{90m+g}$Nb^{cum}	^{91m}Nb	^{92m}Nb	^{95m}Nb	$^{95m+g}$Nb	^{95g}Nb	^{96}Nb	$^{97m+g}$Nb	$^{88m+g}$Zr^{cum}	$^{89m+g}$Zr^{cum}
35.75 ± 0.31	3.21 ± 0.30	3.73 ± 0.80	0.683 ± 0.082	47.8 ± 4.2	109.5 ± 7.5	11.9 ± 2.0	4.13 ± 0.29	0.62 ± 0.13	4.53 ± 0.34	3.87 ± 0.37	1.39 ± 0.32	0.502 ± 0.054	11.43 ± 0.79	5.19 ± 0.36
34.34 ± 0.33	3.51 ± 0.34		0.67 ± 0.12	43.8 ± 3.8	91.9 ± 6.3	12.2 ± 2.1	3.76 ± 0.26	0.73 ± 0.12	3.93 ± 0.30	3.17 ± 0.33	1.18 ± 0.31	0.476 ± 0.055	11.73 ± 0.81	3.98 ± 0.28
32.87 ± 0.36	2.97 ± 0.33	2.40 ± 0.73	0.296 ± 0.086	36.7 ± 3.0	69.6 ± 4.8	12.9 ± 2.2	3.49 ± 0.24	0.71 ± 0.12	3.70 ± 0.28	2.95 ± 0.31	1.13 ± 0.36	0.468 ± 0.062	11.41 ± 0.79	2.87 ± 0.20
31.37 ± 0.39	2.56 ± 0.39	2.13 ± 0.63	0.258 ± 0.082	26.7 ± 2.2	45.2 ± 3.1	15.6 ± 2.6	3.31 ± 0.23	0.63 ± 0.12	3.42 ± 0.27	2.76 ± 0.30	1.44 ± 0.41	0.452 ± 0.078	10.58 ± 0.73	2.07 ± 0.15
29.80 ± 0.42	1.54 ± 0.37	2.13 ± 0.50	0.38 ± 0.11	15.0 ± 1.3	22.6 ± 1.6	16.1 ± 2.7	3.15 ± 0.22	0.54 ± 0.11	2.95 ± 0.24	2.39 ± 0.27	1.23 ± 0.24	0.370 ± 0.046	9.33 ± 0.64	1.73 ± 0.12
28.17 ± 0.46		2.05 ± 0.50	0.27 ± 0.10	6.96 ± 0.68	9.10 ± 0.63	17.5 ± 2.9	3.10 ± 0.22	0.51 ± 0.11	2.28 ± 0.21	1.74 ± 0.24	1.39 ± 0.25	0.287 ± 0.043	7.73 ± 0.53	1.89 ± 0.13
26.45 ± 0.50		3.41 ± 0.58	0.38 ± 0.11	3.87 ± 0.45	4.34 ± 0.30	17.8 ± 3.0	3.12 ± 0.22	0.39 ± 0.10	1.78 ± 0.21	1.37 ± 0.23	1.31 ± 0.24	0.255 ± 0.046	5.79 ± 0.40	2.53 ± 0.18
24.66 ± 0.55		4.39 ± 0.63	0.67 ± 0.15	2.82 ± 0.38	3.00 ± 0.21	18.6 ± 3.1	3.03 ± 0.21	0.38 ± 0.11	1.38 ± 0.15	0.99 ± 0.18	1.67 ± 0.23	0.324 ± 0.058	3.83 ± 0.26	3.47 ± 0.24
23.50 ± 0.58		4.33 ± 0.70	0.65 ± 0.16	2.06 ± 0.21	2.20 ± 0.16	18.6 ± 3.1	2.78 ± 0.20	0.261 ± 0.088	1.18 ± 0.26	0.91 ± 0.28	1.27 ± 0.28	0.328 ± 0.058	2.49 ± 0.17	4.01 ± 0.28
22.27 ± 0.62		3.77 ± 0.55	0.78 ± 0.16	1.30 ± 0.15	1.47 ± 0.11	18.9 ± 3.2	2.57 ± 0.18	0.288 ± 0.085	1.12 ± 0.18	0.81 ± 0.20	1.22 ± 0.30	0.323 ± 0.065	1.361 ± 0.094	4.23 ± 0.29
20.98 ± 0.30		4.03 ± 0.49	0.954 ± 0.094			18.7 ± 3.1	2.12 ± 0.15	0.312 ± 0.062	1.29 ± 0.24	0.96 ± 0.25	1.23 ± 0.31	0.305 ± 0.042	0.455 ± 0.033	4.07 ± 0.28
19.64 ± 0.33		3.77 ± 0.55	0.752 ± 0.091			17.0 ± 2.9	1.76 ± 0.12	0.435 ± 0.065	1.40 ± 0.33	0.94 ± 0.34	0.88 ± 0.29	0.397 ± 0.048	0.126 ± 0.013	3.45 ± 0.24
18.23 ± 0.36		2.49 ± 0.49	0.75 ± 0.11			13.4 ± 2.4	1.43 ± 0.10	0.506 ± 0.065	1.56 ± 0.36	1.02 ± 0.37	0.79 ± 0.18	0.463 ± 0.058		2.60 ± 0.18
16.74 ± 0.41		1.73 ± 0.39	0.48 ± 0.10			7.1 ± 1.3	1.192 ± 0.085	0.501 ± 0.065	1.71 ± 0.35	1.19 ± 0.36	0.55 ± 0.18	0.476 ± 0.059		1.78 ± 0.12
15.18 ± 0.45		1.39 ± 0.29	0.32 ± 0.11			2.84 ± 0.71	1.074 ± 0.076	0.562 ± 0.058	1.60 ± 0.37	1.01 ± 0.37	0.37 ± 0.19	0.420 ± 0.03		1.011 ± 0.070
13.46 ± 0.51		3.92 ± 0.32					0.925 ± 0.065	0.472 ± 0.048	1.10 ± 0.19	0.60 ± 0.20	0.44 ± 0.23	0.346 ± 0.038		0.488 ± 0.034
11.60 ± 0.59							0.649 ± 0.045	0.344 ± 0.034	0.64 ± 0.13	0.28 ± 0.14	0.34 ± 0.17	0.230 ± 0.027		0.1152 ± 0.0087
9.46 ± 0.70		1.95 ± 0.18					0.332 ± 0.023	0.133 ± 0.015	0.17 ± 0.10		0.20 ± 0.17	0.090 ± 0.016		0.0286 ± 0.0036
8.23 ± 0.77		1.69 ± 0.17					0.176 ± 0.013				0.149 ± 0.094			
6.85 ± 0.88		1.23 ± 0.13					0.0611 ± 0.0073				0.078 ± 0.053			

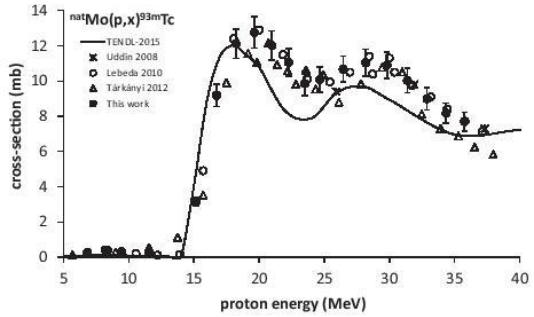

Fig. 1a. Cross-sections for the ^{nat}Mo(p,x)^{93m}Tc reactions compared with previously published data [14,15,20] and prediction of the TALYS code adopted from the TENDL-2015 library [39].

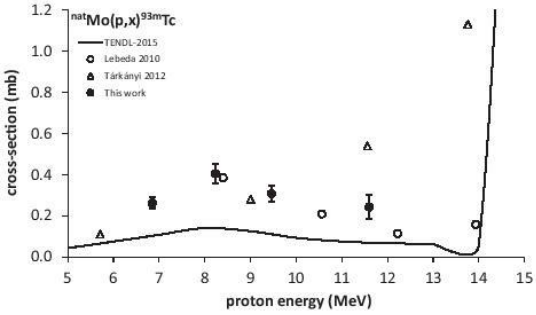

Fig. 1b. Cross-sections for the ^{nat}Mo(p,x)^{93m}Tc reactions compared with previously published data [15,20] and prediction of the TALYS code adopted from the TENDL-2015 library [39] for the low energy region, where it is formed solely in the ^{92}Mo(p,γ) reaction until ca 13.8 MeV.

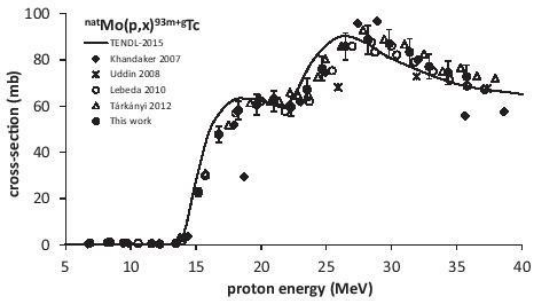

Fig. 2a. Cumulative cross-sections for the ^{nat}Mo(p,x)$^{93m+g}$Tc reactions compared with previously published data [13–15,20] and prediction of the TALYS code adopted from the TENDL-2015 library [39].

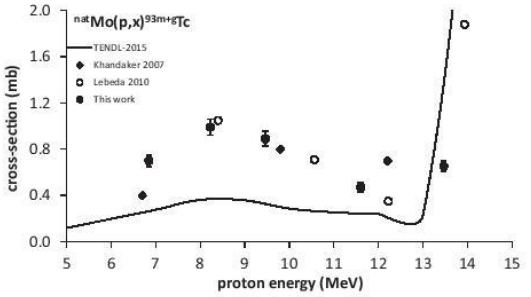

Fig. 2b. Cumulative cross-sections for the ^{nat}Mo(p,x)$^{93m+g}$Tc reactions compared with previously published data [13,15,20] and prediction of the TALYS code adopted from the TENDL-2015 library [39] for the low energy region, where it is formed solely in the ^{92}Mo(p,γ) reaction until ca 13.8 MeV.

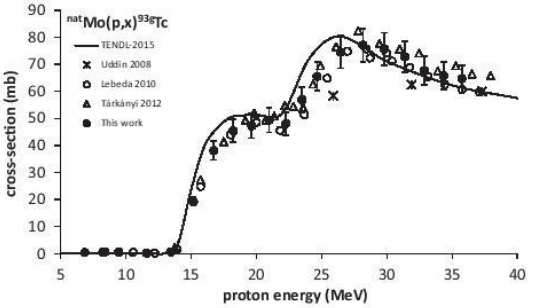

Fig. 3a. Cross-sections for the ^{nat}Mo(p,x)^{93g}Tc reactions compared with previously published data [14,15,20] and prediction of the TALYS code adopted from the TENDL-2015 library [39].

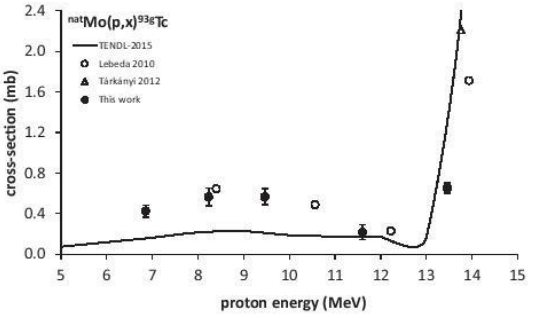

Fig. 3b. Cross-sections for the ^{nat}Mo(p,x)^{93g}Tc reactions compared with previously published data [15,20] and prediction of the TALYS code adopted from the TENDL-2015 library [39] for the low energy region, where it is formed solely in the ^{92}Mo(p,γ) reaction until ca 13.8 MeV.

interference-free 1 868.68 keV gamma line. Since ^{94m}Tc does not decay at all via isomeric transition, activities of both metastable and ground states are entirely independent.

The cross-sections for the ^{nat}Mo(p,x)^{94g}Tc reactions were measured by Kormali et al. (1976) [1], Bonardi et al. (2002) [8], Khandaker et al. (2007) [13], Lebeda and Pruszyński (2010) [15], Alharbi et al. (2011) [16,17] and Tárkányi et al. (2012) [20]. Our new data correspond well with the cross-sections in Refs. [15,20], while the data in Ref. [1] are significantly lower for $E_p > 15$ MeV. The data of Refs. [8,16,17] are slightly higher and a few points in Ref. [13] are significantly lower, although the rest is consistent with our measurement (see Fig. 4). The TENDL-2015 prediction agrees with the measured course of the excitation function, but remarkably overestimates the experimental data.

Our data for the formation of ^{94m}Tc are consistent with the previously published values of Uddin et al. (2008) [14], Lebeda and Pruszyński (2010) [15] and Tárkányi et al. (2012) [20]. A few points in Ref. [20] for $E_p > 28$ MeV are somewhat higher, but they are also burdened with higher uncertainty. The prediction adopted from the TENDL-2015 library suggests significantly lower cross-sections than the experimental evidence and also much less pronounced maximum around 16 MeV (Fig. 5) [39].

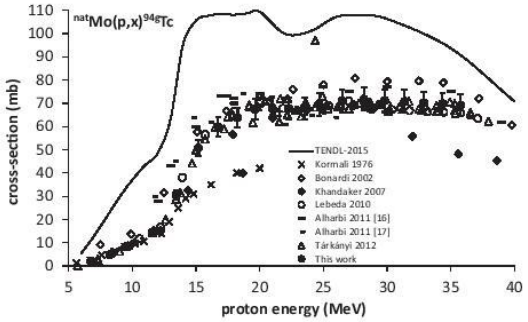

Fig. 4. Cross-sections for the ^{nat}Mo(p,x)^{94g}Tc reactions compared with previously published data [14,15,20] and prediction of the TALYS code adopted from the TENDL-2015 library [39].

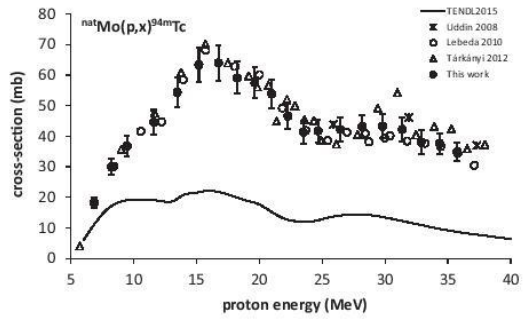

Fig. 5. Cross-sections for the ^{nat}Mo(p,x)^{94m}Tc reactions compared with previously published data [14,15,20] and prediction of the TALYS code adopted from the TENDL-2015 library [39].

3.2.3. Cross-sections for the ^{nat}Mo(p,x)^{95g} and ^{nat}Mo(p,x)^{95m}Tc reactions

Activity of ^{95g}Tc was calculated via its 765.79 keV gamma line. Results are displayed on Fig. 6. Our data show the best agreement with those published by Khandaker et al. (2007) [13] and our previous measurement [15], however, all the published cross-sections are relatively consistent. Data of Bonardi et al. (2002) [8] and some data of Khandaker et al. (2006) [11] are slightly higher than the data of the present work. On the other hand, data of Uddin et al.

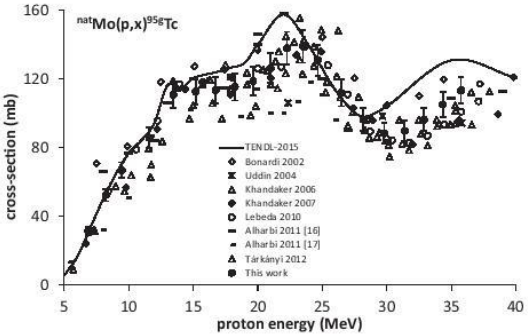

Fig. 6. Cross-sections for the ^{nat}Mo(p,x)^{95g}Tc reactions compared with previously published data [8,10,11,13,15–17,20] and prediction of the TALYS code adopted from the TENDL-2015 library [39].

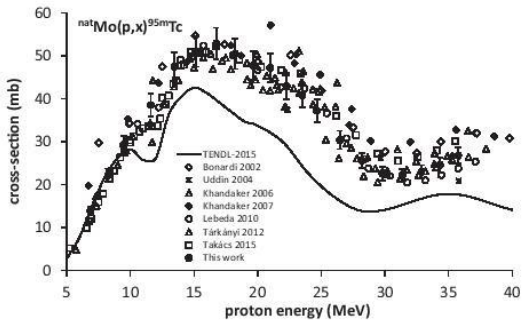

Fig. 7. Cross-sections for the ^{nat}Mo(p,x)^{95m}Tc reactions compared with previously published data [8,10,11,13,15,20,22] and prediction of the TALYS code adopted from the TENDL-2015 library [39].

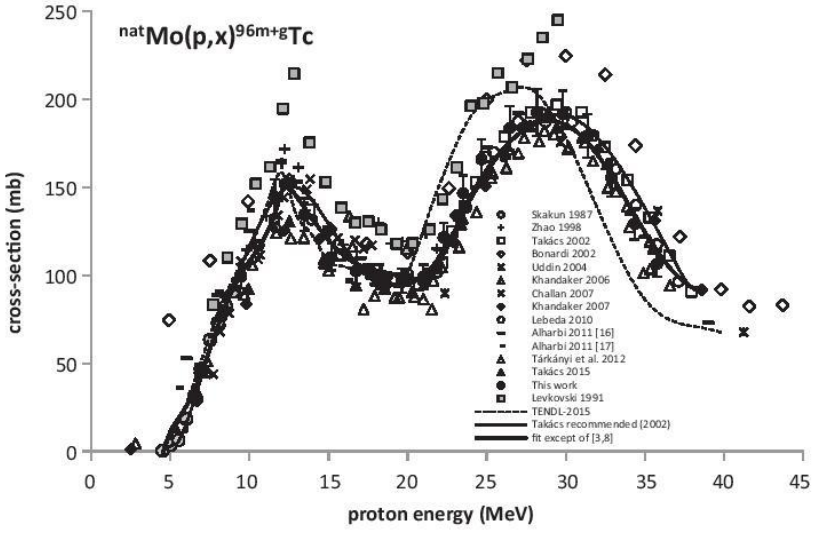

Fig. 8. Cross-sections for the ^{nat}Mo(p,x)$^{96m+g}$Tc reactions compared with previously published data [2–4,7,8,10–17,20,22] and prediction of the TALYS code adopted from the TENDL-2015 library [39]. Polynomial fit of all the experimental data up to 40 MeV except of Refs. [3,8] is displayed as well.

(2004) [10], Alharbi et al. (2011) [17] and Tárkányi et al. (2012) [20] are in general more scattered and lower than our data. This time, we observed cross-sections that were also somewhat higher in the energy region above 30 MeV in contrast to the data in Refs. [13,15]. This fact may be related to the monitoring reaction data used in Refs. [13,15] that seem to be less reliable in this energy region. Theoretical model agrees well with the experiment except slightly higher predicted values in the energy region of 15–24 MeV and 30–40 MeV.

Activity of ^{95m}Tc was calculated using its 204.12 keV gamma line. Obtained cross-sections for production of ^{95m}Tc (Fig. 7) fit well with our previous measurement [15] and Tárkányi et al. (2012) [20]. Cross-sections published by Khandaker et al. (2006, 2007) [11,13] agree with our data for $E_p < 23$ MeV, and then start to be significantly higher. Recent data of Takács et al. (2015) [22] correspond with our data as well, but for the $E_p > 22$ MeV they are slightly higher. Values of Bonardi et al. (2002) [8] are systematically higher than our cross-sections and the three data points of Uddin et al. (2004) [10] in the measured energy region are rather scattered similarly to the data for ^{95g}Tc. TENDL-2015 shows the same trend as the experiments, but its prediction is significantly lower for $E_p > 10$ MeV and indicates pronounced minimum at 12 MeV (Fig. 7) than is not observed in the experimental data.

3.2.4. Cross-sections for the ^{nat}Mo(p,x)$^{96m+g}$Tc reactions

Cross-sections for the reactions leading to $^{96m+g}$Tc were calculated using its 778.22 keV gamma line after the total decay of ^{96m}Tc and interfering ^{96}Nb. A minor interference due to the 777.92 keV gamma line of ^{99}Mo (intensity 4.28% per decay) was corrected. All the results are displayed on Fig. 8. There is a good agreement between the excitation function provided by TENDL-2015 and the measurements. However, the experimental data covering the second peak of the excitation function are slightly shifted to higher energies in contrast to the prediction of TENDL-2015.

Measurements of Skakun et al. (1987) [2], Takács et al. (2002) [7], Khandaker et al. (2007) [13], Lebeda and Pruszyński (2010) [15] and Takács et al. (2015) [22] (except the values around the first maximum) are in a good agreement with our data. Cross-sections of Levkovski (1991) [3] and Bonardi et al. (2002) [8] are obviously systematically higher than the rest of the published material. Data of Zhao et al. (1998) [4] and of Challan et al. (2007) [12] are higher for $E_p > 14$ MeV as well as data of Alharbi et al. (2011) [16,17] for $E_p < 10$ MeV, in contrast, data of Tárkányi et al. (2012) [20] are on average lower for $E_p > 10$ MeV. Data of Uddin et al. (2004) [10] and Khandaker et al. (2006) [11] seem to be shifted to higher energies in comparison to our measurement. On Fig. 8 we show also the polynomial fit of all the measured cross-sections except Levkovski (1991) [3] and Bonardi et al. (2002) [8]. The Levkovski data agree relatively well with the majority of the measurements if decreased for ca 20%. It confirms the conclusions of Ref. [7]. We would like to note that the part of the data in Ref. [20] that were adopted from the experiment in Ref. [7] were excluded in order to avoid their duplication. Our preliminary proposal of the recommended cross-sections for this nuclear reaction as a proton beam monitor as well as the derived thick target yields are displayed in Table 4.

3.2.5. Cross-sections for the ^{nat}Mo(p,x)^{97m}Tc reactions

After the decay of all the measurable activation products except ^{95m}Tc, we detected in the spectra well distinguished peak with energy of 96.50 keV, belonging to the only emitted, weak gamma line of ^{97m}Tc. Its net peak area was corrected for the mean attenuation in the foils, but this accounted for the activity increase of only 1.1%.

The measured cross-sections together with the prediction adopted from TENDL-2015 are displayed on Fig. 9. Theoretical model follows well the shape of the experimental excitation function including the slight increase for $E_p > 30$ MeV due to the contribution of the ^{100}Mo(p,4n) reaction. However, starting from

Table 4
Recommended cross-sections and thick target yields for the ^{nat}Mo(p,x)$^{96m+g}$Tc, ^{100}Mo(p,2n)^{99m}Tc and ^{100}Mo(p,x)^{99}Mo reactions.

E_p (MeV)	^{nat}Mo(p,x)$^{96m+g}$Tc		^{100}Mo(p,2n)^{99m}Tc		^{100}Mo(p,x)^{99}Mo	
	σ (mb)	Y (MBq/μAh)	σ (mb)	Y (MBq/μAh)	σ (mb)	Y (MBq/μAh)
5.0	11.3	0.0189				
5.5	18.7	0.0728				
6.0	25.7	0.156				
6.5	34.6	0.276				
7.0	45.8	0.444				
7.5	58.5	0.674				
8.0	71.3	0.974	14.7	0.00		
8.5	83.1	1.347	36.3	2.04		
9.0	93.2	1.791	63.8	6.30		
9.5	101.4	2.299	94.4	13.32		
10.0	108.2	2.867	125.3	23.48		
10.5	114.7	3.490	154.3	36.89		
11.0	122.4	4.175	179.5	53.45	2.15	0.012
11.5	132.7	4.935	200.1	72.92	2.83	0.033
12.0	146.3	6.204	215.6	94.90	4.81	0.069
12.5	150.3	6.746	226.4	119.0	7.68	0.130
13.0	144.4	7.708	233.0	144.7	11.5	0.226
13.5	138.1	8.656	236.3	171.7	16.2	0.370
14.0	131.7	9.586	237.5	199.7	21.7	0.573
14.5	125.6	10.50	237.4	228.5	28.1	0.848
15.0	119.9	11.39	236.9	258.0	35.1	1.205
15.5	115.0	12.26	236.4	288.1	42.8	1.656
16.0	111.0	13.12	236.2	318.9	50.8	2.212
16.5	107.9	13.97	236.0	350.4	59.3	2.881
17.0	105.6	14.82	235.5	382.5	67.9	3.670
17.5	103.9	15.67	233.9	415.1	76.5	4.587
18.0	102.8	16.53	230.4	448.1	85.1	5.635
18.5	101.9	17.40	224.3	481.0	93.6	6.818
19.0	101.0	18.27	215.1	513.5	101.7	8.135
19.5	100.0	19.16	202.4	545.0	109.4	9.588
20.0	98.9	20.05	186.5	574.8	116.7	11.17
20.5	98.2	20.95	167.9	602.5	123.4	12.89
21.0	98.5	21.86	147.8	627.6	129.5	14.73
21.5	100.9	22.81	130.7	650.1	135.0	16.68
22.0	107.3	24.14	114.4	670.3	139.9	18.75
22.5	114.0	24.87	99.6	688.2	144.1	20.93
23.0	126.2	26.07	86.6	704.0	147.7	23.20
23.5	136.5	27.40	75.6	718.0	150.7	25.56
24.0	145.3	28.85	66.5	730.5	153.2	28.00
24.5	153.1	30.41	58.9	741.7	155.1	30.51
25.0	159.9	32.08	52.8	751.8	156.5	33.08
25.5	166.0	33.83	47.8	761.0	157.6	35.72
26.0	171.5	35.68	43.8	769.6	158.4	38.41
26.5	176.2	37.60	40.4	777.6	158.9	41.15
27.0	180.2	39.61	37.7	785.1	159.2	43.94
27.5	183.4	41.68	35.5	792.2	159.5	46.77
28.0	185.8	43.81	33.9	799.0	159.6	49.64
28.5	187.3	46.00	32.7	805.7	159.8	52.55
29.0	187.7	48.22	31.7	812.2	160.0	55.50
29.5	187.2	50.47	30.9	818.6	160.2	58.49
30.0	185.5	52.74	30.3	825.0	160.6	61.53
30.5	182.8	55.01	30.0	831.3	161.0	64.61
31.0	179.0	57.27	29.7	837.7	161.6	67.74
31.5	174.2	59.50	29.5	844.1	162.1	70.91
32.0	168.5	61.68	29.4	850.5	162.7	74.14
32.5	162.1	63.82	29.1	857.0	163.3	77.41
33.0	155.1	65.89	28.7	863.4	163.8	80.74
33.5	147.6	67.89	28.2	869.9	164.1	84.10
34.0	139.9	69.81	27.3	876.2	164.3	87.51
34.5	132.1	71.65	26.2	882.4	164.3	90.96
35.0	124.6	73.40	24.8	888.4	164.0	94.45
35.5	117.4	75.07	23.1	894.0	163.5	97.96
36.0	110.9	76.66	21.2	899.3	162.8	101.5
36.5	105.1	78.18	19.3	904.2	162.1	105.0
37.0	100.1	79.64	17.6	908.7	161.5	108.6
37.5	96.1	81.05	16.5	912.8	161.2	112.2
38.0	93.0	82.42	16.3	916.9	161.7	115.9

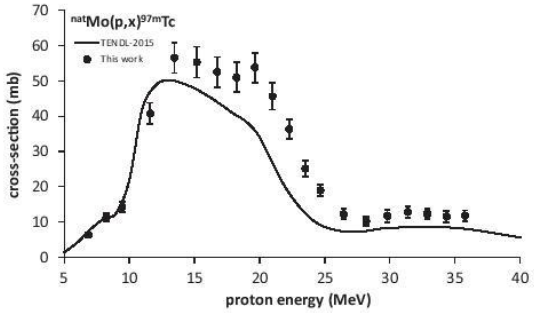

Fig. 9. Cross-sections for ^{nat}Mo(p,x)^{97m}Tc reactions and prediction of the TALYS code adopted from the TENDL-2015 library [39].

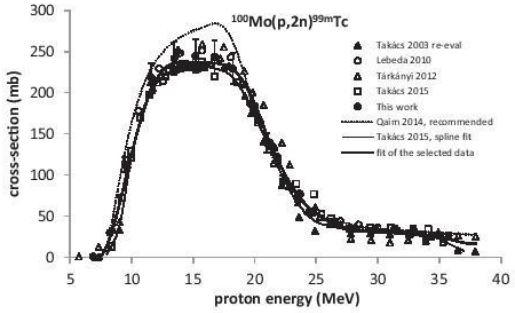

Fig. 10b. Polynomial fit of the selected cross-sections for ^{100}Mo(p,2n)^{99m}Tc reaction [9,15,20,22,this work] compared with recommended data of Qaim et al. [28] and spline fit [9,22].

ca 13 MeV, TENDL-2015 underestimates slightly the measured data. As far as we know, it is the first reported measurement of this excitation function.

3.2.6. Cross-sections for the ^{nat}Mo(p,x)^{99m}Tc, i.e. for the ^{100}Mo(p,2n)^{99m}Tc reaction

Activity of ^{99m}Tc born in the irradiated foils was calculated via its 140.51 keV gamma line. Contribution of ^{99}Mo and ^{90}Nb was corrected as described in the Section 2.3. All the data were converted to isotopic cross-sections on ^{100}Mo (cf. Introduction) and are displayed together with previous measurements and the TENDL-2015 prediction on Fig. 10a.

Apparently, present measurement shows the best agreement with Takács et al. from 2003 [9] (we use re-evaluated data adopted from Takács et al., 2015 [22]), Lebeda and Pruszyński (2010) [15], Tárkányi et al. (2012) [20] and Takács et al. (2015) [22]. Cross-sections of Lagunas-Solar et al. (1999) [5] and Challan et al. (2007) [12] are significantly higher and those of Levkovski (1991) [3], Gagnon et al. (2011) [18] and Manenti et al. (2014) [21] are somewhat higher than our data. On the other hand, rather lower values are provided by Scholten et al. (1999) [6], Khandaker et al. (2007) [13] and Alharbi et al. (2011) [16]. The large scattering of the measurements around the maximum is difficult to explain. It could cause an improper correction of interferences, particularly if the spectra were recorded later after the EOB. In contrast,

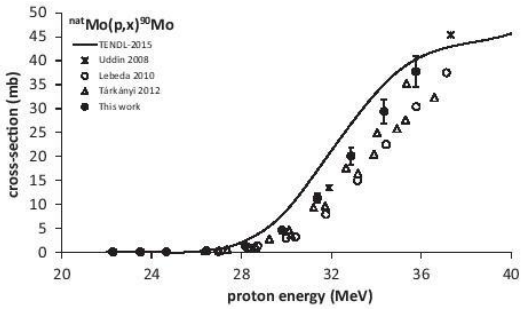

Fig. 11. Cross-sections for ^{nat}Mo(p,x)^{90}Mo reactions compared with previously published data [14,15,20] and prediction of the TALYS code adopted from the TENDL-2015 library [39].

scattering of the data above 30 MeV may be explained by an increasing uncertainty of the measured ^{99m}Tc activity due to the corrections for the growing number and relative contribution of the interferences with proton beam energy (cf. Section 2.3). Theoretical model starts to underestimate all the experimental data for $E_p > 14$ MeV.

On Fig. 10b we show polynomial fit of the selected cross-sections [9,15,20,22 and this work] together with the first

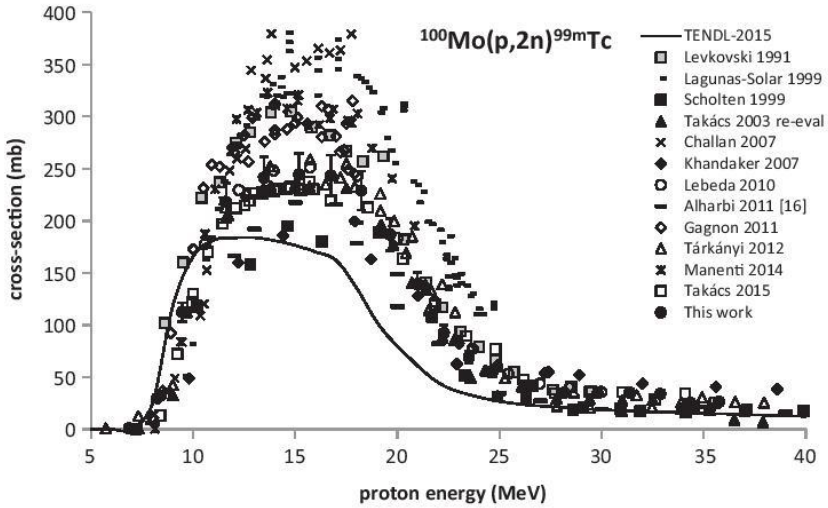

Fig. 10a. Cross-sections for ^{100}Mo(p,2n)^{99m}Tc reaction compared with previously published data [3,5,6,9,12,13,15,16,18,20–22] and prediction of the TALYS code adopted from the TENDL-2015 library [39].

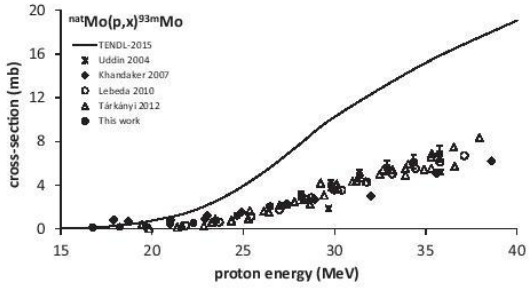

Fig. 12. Cross-sections for ^{nat}Mo(p,x)^{93m}Mo reactions compared with previously published data [10,13,15,20] and prediction of the TALYS code adopted from the TENDL-2015 library [39].

recommended data provided by Qaim et al. (2014) [28] and spline fit of the data in Refs. [9,22] as given in Ref. [22]. The selected data were processed with the great care regarding both activity measurements and interference corrections. Moreover, they are well consistent and comprise enough points for a good fit (altogether 131 cross-section values covering the energy interval of 5.7–38.0 MeV). Although any selection has also subjective aspects, we propose the cross-sections and derived thick target yields summarized in Table 4 as recommended data for the cyclotron production of ^{99m}Tc. They are very close to the fit in Ref. [22], but for $E_p < 20$ MeV they are naturally lower than the recommended data proposed by Qaim et al. [28] due to the different data selection.

3.2.7. Cross-sections for the ^{nat}Mo(p,x)^{90}Mo reactions

Activity of ^{90}Mo was calculated via its 257.34 keV gamma line. The derived cross-sections are displayed on Fig. 11 together with

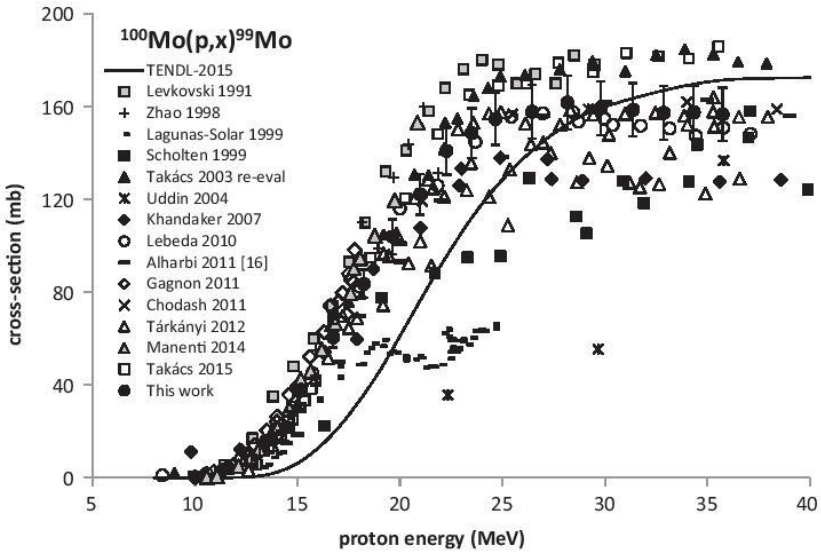

Fig. 13a. Cross-sections for ^{100}Mo(p,x)^{99}Mo reactions compared with previously published data [3–6,9,10,13,15,16,18–22] and prediction of the TALYS code adopted from the TENDL-2015 library [39].

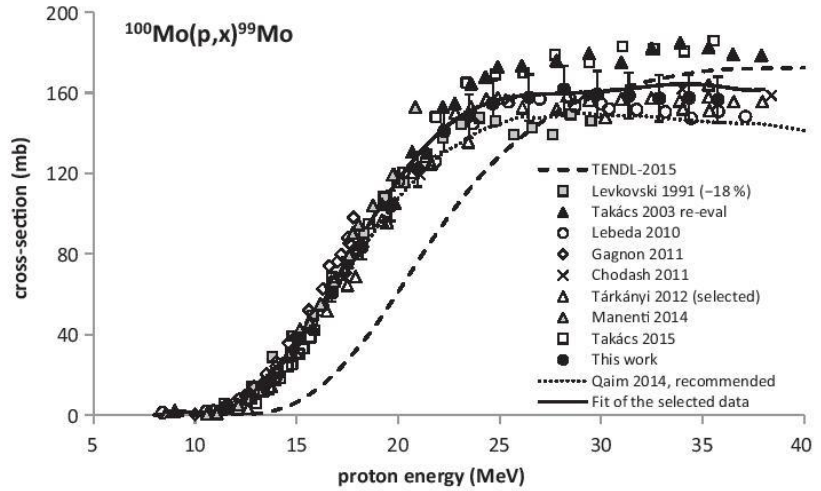

Fig. 13b. Polynomial fit of the selected cross-sections for ^{100}Mo(p,x)^{99}Mo reactions [3,9,10,15,18–22] compared with the recommended data of Qaim et al. [28] and prediction of the TENDL-2015 library [39].

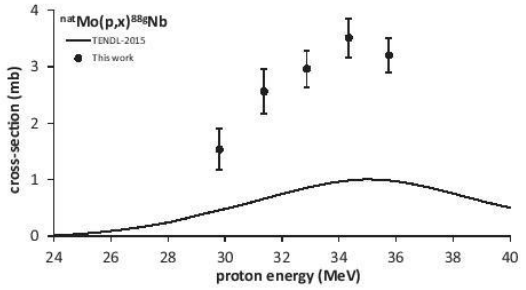

Fig. 14. Cross-sections for ^{nat}Mo(p,x)^{88g}Nb reactions compared with the prediction of the TALYS code adopted from the TENDL-2015 library [39].

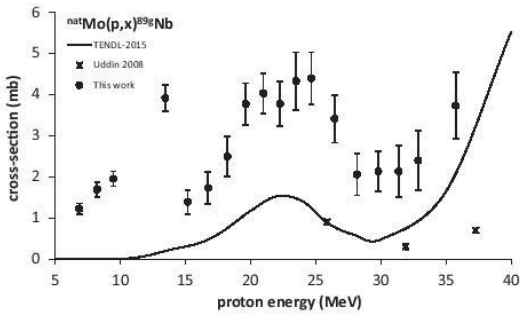

Fig. 15. Cross-sections for ^{nat}Mo(p,x)^{89g}Nb reactions compared with previously published data [14] and prediction of the TALYS code adopted from the TENDL-2015 library [39].

the previously published data of Uddin et al. (2008) [14], our previous measurement in 2010 [15] and Tárkányi et al. (2012) [20], and prediction provided by the TENDL-2015 library. The latter is in very good agreement with the data we present now, slightly overestimating them for E_p = 26–35 MeV. Both points of Uddin et al. (2008) [14] as well as roughly a half of the Tárkányi's data [20] are in excellent agreement with the current measurement, while our previous measurement [15] and the rest of the Tárkányi's data [20] are lower. Precise quantification of ^{90}Mo is relevant for appropriate correction of the ^{99m}Tc activity for the contribution of ^{90}Mo/^{90}Nb generator to the 141 keV net peak area.

The radionuclide may originate also from the decay of very short-lived ^{90m}Tc ($T_{½}$ = 8.7 s) and ^{90g}Tc ($T_{½}$ = 49.2 s) born in the ^{92}Mo(p,3n) reaction (threshold 33.37 MeV). Regarding this fact, the measured cross-sections are cumulative for E_p > 33.37 MeV. The contribution of this indirect production seems to be negligible even for the highest measured energy point (TENDL-2015 predicts total cross-section of only 0.243 mb at 35 MeV for this reaction).

3.2.8. Cross-sections for the ^{nat}Mo(p,x)^{93m}Mo reactions

The short-lived isomer ^{93m}Mo was quantified via its 684.69 keV gamma line. The ground state ^{93g}Mo is not measurable due to its long half-life (4000 a). The isomer is formed solely in the nuclear reactions indicated in the Table 1, because neither ^{93m}Tc, nor ^{93g}Tc decays to it. The measured cross-sections are displayed on Fig. 12 together with the prediction taken from TENDL-2015.

Data of Khandaker et al. (2007) [13] are higher than our data until ca 22 MeV, while for E_p > 30 MeV they are lower being similar to those of Uddin et al. (2004) [10]. Our previous measurement [15] and data of Tárkányi et al. (2012) [20] are in a good agreement with the present measurement, being on average slightly lower. The TENDL-2015 prediction overshoots more than twice all the available experimental data.

3.2.9. Cross-sections for the ^{nat}Mo(p,x)^{99}Mo, i.e. for the ^{100}Mo(p,x)^{99}Mo reactions

Activity of ^{99}Mo was calculated via its interference-free 739.50 keV gamma line. It is cumulative regarding the decay of ^{99m}Nb ($T_{½}$ = 2.6 min) and ^{99g}Nb ($T_{½}$ = 15 s) from 14 MeV, but this contribution seems to be minor. The derived cross-sections are displayed on Fig. 13a. Almost all of the published experimental data indicate similar shape of the excitation function, but they remarkably differ from each other in absolute values. Cross-sections provided by Lagunas-Solar et al. (1999) [5] and by Uddin et al. (2004) [10] are significantly lower than the other experimental data, and data of Scholten et al. (1999) [6] are on average not only somewhat lower, but also much more scattered than observed in other experiments. Data of Levkovski (1991) [3] and Zhao et al. (1998) [4] are higher than our data in the whole measured region, data of Takács et al. (2003) [9], Manenti (2014) [21] and Gagnon et al. (2011) [18] are very close to our data, the latter two being slightly higher, but the cross-sections of Takács et al. (2003) [9] are apparently higher than our measurement for E_p > 20 MeV. The recent measurement of Takács et al. (2015) [22] resembles re-evaluated data of Takács et al. (2003) [9,22], but it suggests lower data for E_p < 16 MeV. We observed very good agreement with our previous measurement [15], Chodash et al. (2011) [19] and some data in Tárkányi et al. (2012) [20] (it contains several data sets from various experiments). Cross-sections in Khandaker et al. (2007) [13] and Alharbi et al. (2011) [16] are somewhat lower, but the first two points of the former work are surprisingly higher than all the data in this region.

Prediction adopted from the TENDL-2015 library agrees relatively well with the measured data, but it is shifted for ca 4 MeV to higher energy.

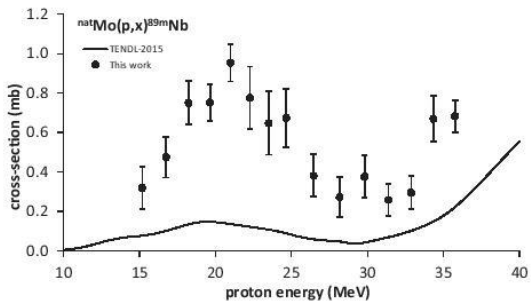

Fig. 16. Cross-sections for ^{nat}Mo(p,x)^{89m}Nb reactions compared with the prediction of the TALYS code adopted from the TENDL-2015 library [39].

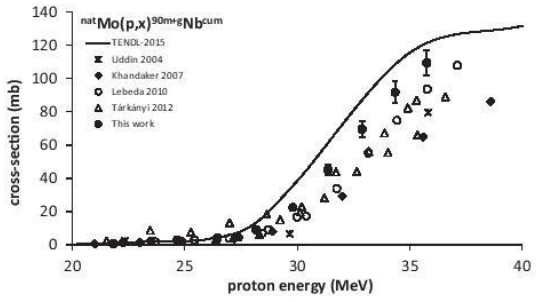

Fig. 17. Cross-sections for ^{nat}Mo(p,x)$^{90m+g}$Nb^{cum} reactions cumulative regarding ^{90}Mo decay compared with previously published data [10,13,15,20] and prediction of the TALYS code adopted from the TENDL-2015 library [39].

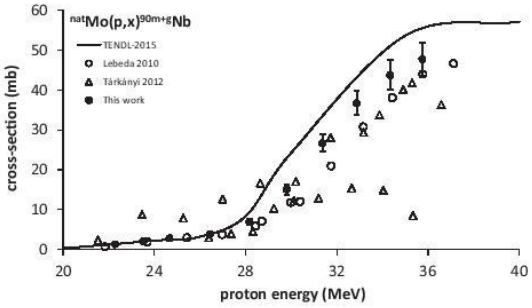

Fig. 18. Cross-sections for ^{nat}Mo(p,x)$^{90m+g}$Nb reactions compared with previously published data [15,20] and prediction of the TALYS code adopted from the TENDL-2015 library [39].

We have, therefore, selected experimental cross-sections [3,9,10,15,18–22] for the construction of the recommended data. For these purposes, we decreased Levkovski's data [3] by 18%, used re-evaluated data of Takács et al. [9] given in Ref. [22] and selected only some data sets from Tárkányi et al. [20] similarly to Takács et al. [22]. Altogether 194 data points in the energy range of 8.4–38.0 MeV were used for the polynomial fit. The data selection, their fit and recommendation provided by Qaim et al. in 2014 [28] are displayed on Fig. 13b. The recommended cross-sections derived from the fit as well as the calculated thick target yields for the ^{100}Mo(p,x)^{99}Mo reactions are summarized in Table 4.

3.2.10. Cross-sections for the ^{nat}Mo(p,x)^{88g}Nb and ^{nat}Mo(p,x)^{88m}Nb reactions

The short-lived ground state ^{88g}Nb and isomeric state ^{88m}Nb were detected only in a few foils irradiated with the highest beam energy, the latter only in a single foil corresponding to 35.75 MeV energy point. The isomer decays directly to ^{88}Zr via β^+ and EC. They are born practically only in the ^{92}Mo(p,αn) reaction. No indirect formation is possible in the studied energy range.

Activity of the ^{88g}Nb was quantified using its dominant 1057.1 keV gamma line that was corrected in one case for the interfering ^{88m}Nb, while the activity of ^{88m}Nb was deduced from its interference-free 450.6 keV gamma line (cf. Table 1). The obtained cross-sections for the ground state are displayed on Fig. 14 and compared with the prediction of TENDL-2015. The model suggests significantly lower cross-sections than observed in the experiment. No measured data were published previously.

The only measured cross-section for ^{88m}Nb at 35.75 MeV was equal to 2.61 ± 0.45 mb, being roughly twice the predicted value from TENDL-2015. Since the single point does not show any trend, it is neither included in Table 3, nor displayed on a separate figure.

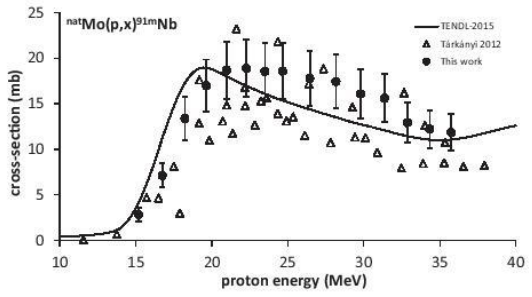

Fig. 19. Cross-sections for ^{nat}Mo(p,x)^{91m}Nb reactions compared with previously published data [20] and prediction of the TALYS code adopted from the TENDL-2015 library [39].

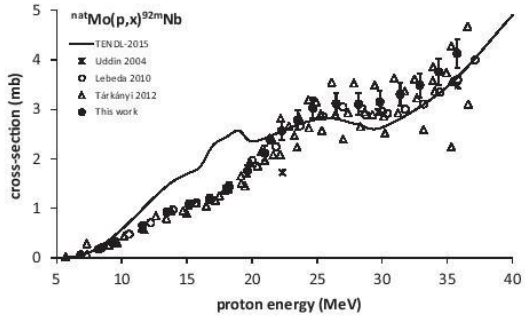

Fig. 20. Cross-sections for ^{nat}Mo(p,x)^{92m}Nb reactions compared with previously published data [10,15,20] and prediction of the TALYS code adopted from the TENDL-2015 library [39].

3.2.11. Cross-sections for the ^{nat}Mo(p,x)^{89g}Nb and ^{nat}Mo(p,x)^{89m}Nb reactions

Activity of ^{89g}Nb was calculated using its dominant, interference-free 1627.2 keV gamma line that has relatively low intensity. Due to this fact and the short half-life, the peak could be measured only in the spectra taken shortly after the EOB in larger distances sample-detector and its area was burdened with larger uncertainties. The radionuclide is born solely in the nuclear reactions (indicated in the Table 1), because the isomeric state ^{89m}Nb decays by β^+ and EC directly to ^{89}Zr.

The obtained cross-sections are displayed on Fig. 15. They follow trend of the predicted excitation function adopted from TENDL-2015 except of the prominent maximum observed only in the experiment around 13.5 MeV, but the prediction is significantly lower. The only available previous measurement of Uddin et al. (2008) [14] for this excitation function provides three points in the measured proton energy range that are all several times lower than our data.

Isomer ^{89m}Nb was quantified via its dominant, well measurable 588.0 keV gamma line. The measured cross-sections are displayed on Fig. 16. They follow the trend as suggested in TENDL-2015, but the predicted values are several times lower than data observed in the experiment. No previous measurement was found in the literature in the studied proton energy range.

3.2.12. Cross-sections for the ^{nat}Mo(p,x)$^{90m+g}$Nb^{cum} and ^{nat}Mo(p,x)$^{90m+g}$Nb reactions

Activity of $^{90m+g}$Nb was determined via its interference-free 1129.22 keV gamma line. It is cumulative regarding ^{90}Mo for proton energy exceeding ca 25 MeV, and this contribution becomes

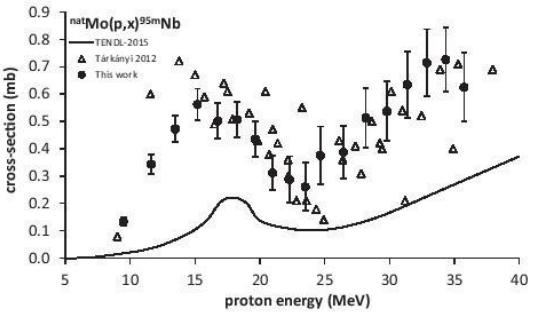

Fig. 21. Cross-sections for ^{nat}Mo(p,x)^{95m}Nb reactions compared with previously published data [20] and prediction of the TALYS code adopted from the TENDL-2015 library [39].

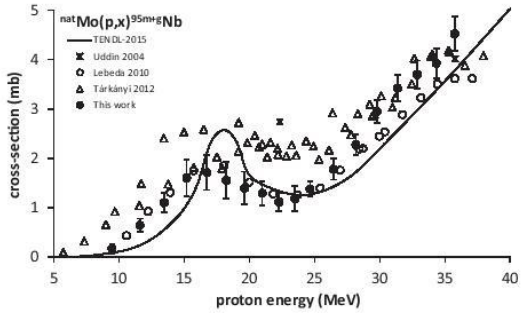

Fig. 22. Cross-sections for ^{nat}Mo(p,x)$^{95m+g}$Nb reactions compared with previously published data [10,15,20] and prediction of the TALYS code adopted from the TENDL-2015 library [39].

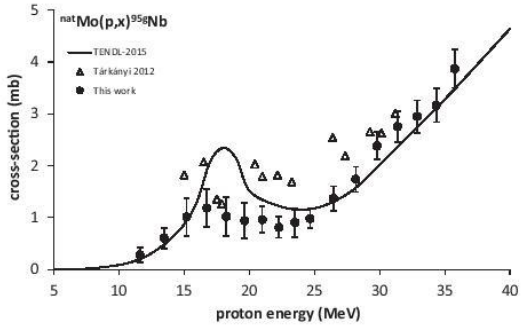

Fig. 23. Cross-sections for ^{nat}Mo(p,x)^{95g}Nb reactions compared with previously published data [20] and prediction of the TALYS code adopted from the TENDL-2015 library [39].

significant with increasing energy. Cumulative activity of $^{90m+g}$Nb^{cum} was measured after the total decay of ^{90}Mo. The respective cross-sections are displayed on Fig. 17 together with previously published data [10,13,15,20] and prediction of the TALYS code [39]. All the experimental data except few points of Tárkányi et al. (2012) [20] are lower than our new data, particularly those of Uddin et al. (2004) [10], Khandaker et al. (2007) [13] and some from rather scattered data in Ref. [20]. The prediction of the TENDL-2015 follows well the course of our data, but exceeds them slightly for $E_p > 28$ MeV.

The cross-sections for the direct formation of $^{90m+g}$Nb in the nuclear reactions on ^{nat}Mo were derived from the data for ^{90}Mo (cf. Section 3.2.7) and the formula (2). Thus obtained cross-sections are anyhow cumulative regarding very short-lived ^{90m}Nb ($T_{½}$ = 18.8 s) and ^{90m2}Nb ($T_{½}$ = 6.19 ms). The data corrected for the ^{90}Mo decay are displayed together with the prediction of TENDL-2015 and two data sets of Lebeda and Pruszyński (2010) [15] and Tárkányi et al. (2012) [20] on Fig. 18. The works [15,20] provide only cumulative cross-sections for $^{90m+g}$Nb^{cum} and for ^{90}Mo. Thus the data for direct formation of $^{90m+g}$Nb were derived from them using the formula (2). Cross-sections in Ref. [15] as well as some data sets in Ref. [20] agree well with our measurement, being on average slightly lower, but some data sets in Ref. [20] significantly differ, showing rather large scattering. Our data follow well the prediction taken from the TENDL-2015 library, being only somewhat lower in the energy range of 28–36 MeV.

3.2.13. Cross-sections for the ^{nat}Mo(p,x)^{91m}Nb reactions

The long-lived isomer ^{91m}Nb was detected in spectra of many foils after the decay of the radionuclides with half-life shorter than 5 days. Its activity was calculated via its 1204.67 keV gamma line that is interference-free, but has also very low intensity of 2%. It resulted together with its half-life in higher uncertainties of the measured cross-sections. Formation of ^{91g}Nb was not observed due to its long half-life (680 a), as well as formation of ^{91m2}Nb ($T_{½}$ = 3.76 μs). Isomer ^{91m}Nb may be born also indirectly in the decay of ^{91m2}Nb, ^{91}Mo ($T_{½}$ = 15.49 min), ^{91m}Mo ($T_{½}$ = 64.6 s) that are additionally decay products of ^{91}Tc ($T_{½}$ = 3.14 min) and ^{91m}Tc ($T_{½}$ = 3.3 min). The cross-sections are, therefore, in principle cumulative, although the contribution of the indirect formation seems to be minor taking into account decay schemes of these radionuclides, cf. Ref. [35].

Our data as well as the only existing previous measurement of Tárkányi et al. (2012) [20] and results of TALYS model [39] are shown on Fig. 19. In general, our data follow the trend of TENDL-2015 library and are slightly lower for $E_p < 21$ MeV and slightly higher for $E_p > 21$ MeV. The Tárkányi's data are again rather scattered and except few points in general lower than both our results and TENDL-2015.

3.2.14. Cross-sections for the ^{nat}Mo(p,x)^{92m}Nb reactions

The ^{92}Nb nucleus has long-lived ($T_{½} = 3.47 \times 10^7$ a) unmeasurable ground state. Its isomer, ^{92m}Nb, is however, well visible in all the foils of both stacks. Activity of ^{92m}Nb was quantified via its dominant 934.44 keV gamma line after the decay of shorter-lived activities in the foils.

The obtained cross-sections are displayed on Fig. 20. They are in a very good agreement with previously reported measurements of Uddin et al. (2004) [10], Lebeda and Pruszyński (2010) [15] and Tárkányi et al. (2012) [20] except some scattered points in Ref. [20] in the energy range 25–36 MeV. Prediction of the TENDL-2015 reflects the shape of the experimental data only partially – it seems to be slightly shifted to lower energies and sug-

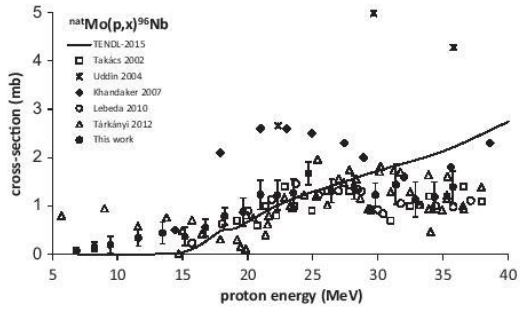

Fig. 24. Cross-sections for ^{nat}Mo(p,x)^{96}Nb reactions compared with previously published data [7,10,13,15,20] and prediction of the TALYS code adopted from the TENDL-2015 library [39].

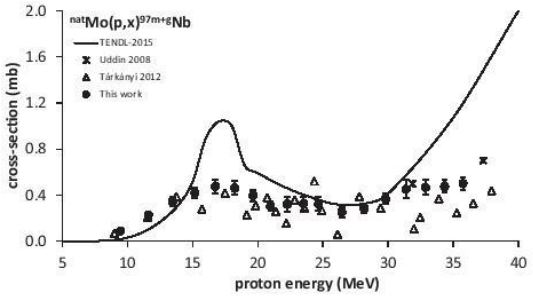

Fig. 25. Cross-sections for ^{nat}Mo(p,x)$^{97m+g}$Nb reactions compared with previously published data [14,20] and prediction of the TALYS code adopted from the TENDL-2015 library [39].

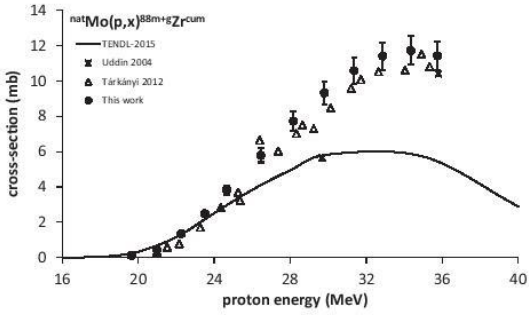

Fig. 26. Cumulative cross-sections for ^{nat}Mo(p,x)$^{88m+g}$Zr^{cum} reactions compared with previously published data [10,20] and prediction of the TALYS code adopted from the TENDL-2015 library [39].

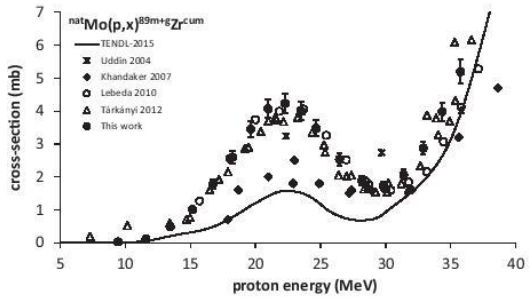

Fig. 27. Cross-sections for ^{nat}Mo(p,x)$^{89m+g}$Zr^{cum} reactions compared with previously published data [10,13,15,20] and prediction of the TALYS code adopted from the TENDL-2015 library [39].

gests small maximum at 19 MeV that is missing in all the published data.

3.2.15. Cross-sections for the ^{nat}Mo(p,x)^{95m}Nb, ^{nat}Mo(p,x)$^{95m+g}$Nb and ^{nat}Mo(p,x)^{95g}Nb reactions

Activity of ^{95m}Nb was calculated using its 235.69 keV gamma line and cumulative activity of $^{95m+g}$Nb via 765.80 keV gamma line after the total decay of ^{95m}Nb. The net peak area of the 765.80 keV gamma line of ^{95g}Nb was corrected for the interfering ^{95g}Tc in transient equilibrium with its parent ^{95m}Tc (isomeric transition probability is only 3.88 ± 0.32%, cf. Ref. [35]). It somewhat increases the data uncertainty. Cross-sections for the direct formation of the ground state ^{95g}Nb were deduced from the formula (2) using

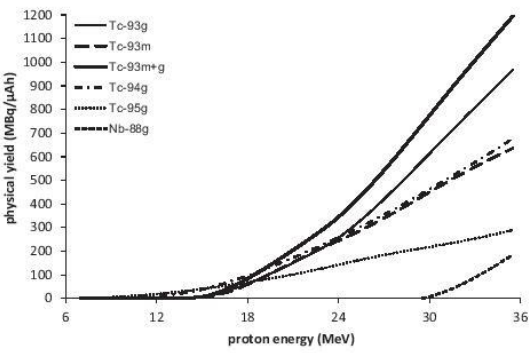

Fig. 28. Physical thick target yields for ^{93g}Tc, ^{93m}Tc, $^{93m+g}$Tc, ^{94g}Tc, ^{95g}Tc and ^{88g}Nb born in ^{nat}Mo(p,x) reactions.

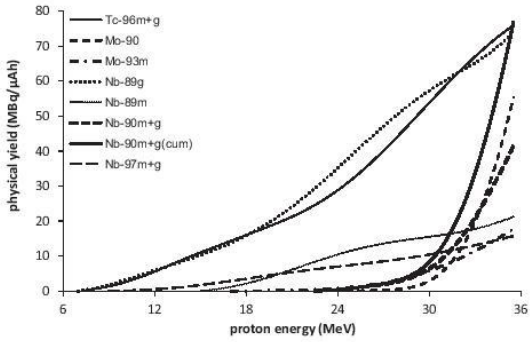

Fig. 29. Physical thick target yields for $^{96m+g}$Tc, ^{90}Mo, ^{93m}Mo, ^{89g}Nb, ^{89m}Nb, $^{90m+g}$Nb, $^{90m+g}$Nb^{cum} and $^{97m+g}$Nb born in ^{nat}Mo(p,x) reactions.

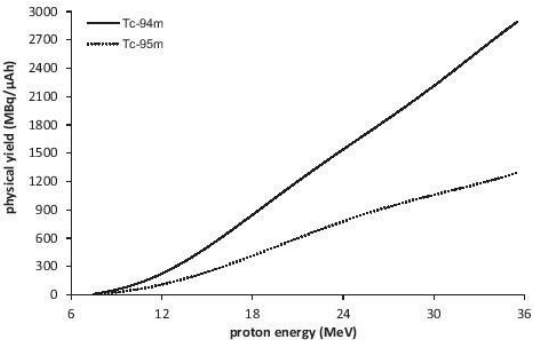

Fig. 30. Physical thick target yields for ^{94m}Tc and ^{95m}Tc born in ^{nat}Mo(p,x) reactions.

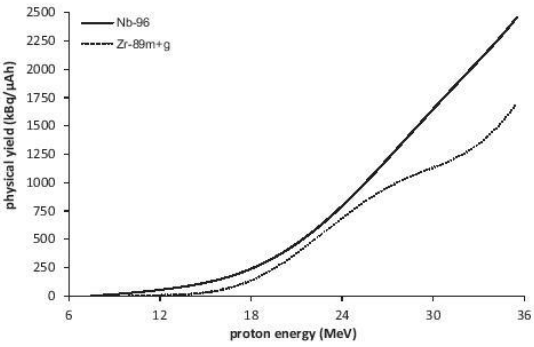

Fig. 31. Physical thick target yields for ^{96}Nb and $^{89m+g}$Zr born in ^{nat}Mo(p,x) reactions.

the value of ^{95m}Nb isomeric transition probability $f = 94.4 \pm 0.6\%$ adopted from Ref. [35].

Data for the formation of isomer ^{95m}Nb are displayed on Fig. 21. They are generally in a good agreement with the values provided by Tárkányi et al. (2012) [20], the latter are, however, again more scattered. The TENDL-2015 library provides similar course of the excitation function, but suggests significantly lower cross-sections than observed in the experiments.

Cumulative cross-sections for $^{95m+g}$Nb are in a very good agreement with our previous measurement [15], being somewhat higher from $E_p = 30$ MeV. In contrast, data of Uddin et al. (2004) [10] and Tárkányi et al. (2012) [20] are significantly higher in the energy range of 5–27 MeV. The forecast adopted from the

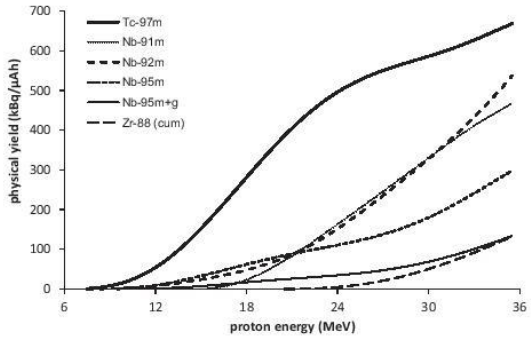

Fig. 32. Physical thick target yields for ^{97m}Tc, ^{91m}Nb, ^{92m}Nb, ^{95m}Nb, $^{95m+g}$Nb and ^{88}Zr born in ^{nat}Mo(p,x) reactions.

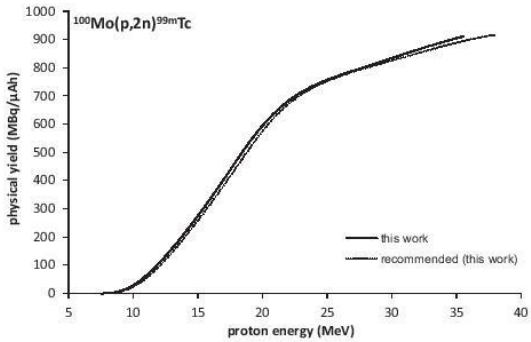

Fig. 33. Physical thick target yield for ^{99m}Tc born in ^{100}Mo(p,2n)^{99m}Tc reaction.

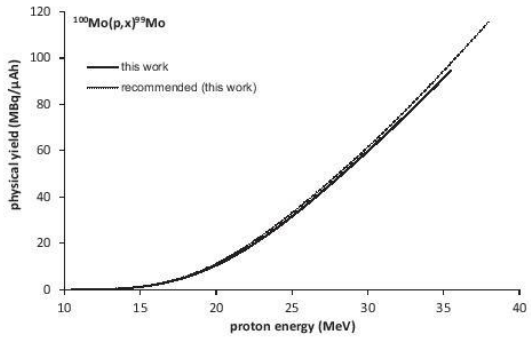

Fig. 34. Physical thick target yield for ^{99}Mo born in ^{100}Mo(p,x)^{99}Mo reactions.

TENDL-2015 library describes well the course of our data, but again assumes more prominent maximum around 18 MeV, cf. Fig. 22.

The cross-sections for formation of ^{95g}Nb are shown on Fig. 23 together with the data of Tárkányi et al. (2012) [20] deduced from the published cross sections for ^{95}Nb and $^{95m+g}$Nb using the formula (2). The results of Ref. [20] are on average systematically higher than our data. Prediction of TALYS model adopted from the TENDL-2015 library [39] describes well the course of cross-sections measured in this work except more prominent maximum at 18 MeV.

3.2.16. Cross-sections for the ^{nat}Mo(p,x)^{96}Nb reactions

This radionuclide decays to the same stable product as ^{96g}Tc, and shares with it almost all the emitted gamma lines that however differ in intensity. For measuring ^{96}Nb activity we chose the 568.87 keV gamma line that was corrected for the contribution of ^{96g}Tc emitting the same gamma line with much lower intensity, cf. Table 1 (the final effect is larger due to the difference in activities of ^{96}Tc and ^{96}Nb, increasing thus also the overall uncertainty).

Measured cross-sections are displayed on Fig. 24. Our data are in relatively good agreement with Takács et al. (2002) [7], Lebeda and Pruszyński (2010) [15] and Tárkányi et al. (2012) [20]. Data of Uddin et al. (2004) [10], Khandaker et al. (2007) [13] as well as prediction of the TALYS model code [39] are significantly higher compared to our measurement.

3.2.17. Cross-sections for the ^{nat}Mo(p,x)$^{97m+g}$Nb reactions

Relatively short-lived activity of ^{97g}Nb was measured using its 657.94 keV gamma line. The activity is cumulative regarding the short-lived isomer ^{97m}Nb ($T_{½}$ = 58.7 s) that decays entirely via isomeric transition to the ground state. Both nuclei are born mainly in the ^{100}Mo(p,α) reaction until ca 30 MeV, when ^{98}Mo(p,2p) reaction starts to contribute to their formation more significantly.

The results are shown on Fig. 25. Our data show general agreement with those of Uddin et al. (2008) [14] and some data of Tárkányi et al. (2012) [20], but one half of the data in Ref. [20] is significantly lower than our cross-sections. The TENDL-2015 prediction [39] suggests more pronounced maximum of the ^{100}Mo(p,α) reaction at 17 MeV and also steeper increase of the ^{98}Mo(p,2p) reaction cross-sections between 30 and 40 MeV than the experimental data.

3.2.18. Cross-sections for the ^{nat}Mo(p,x)$^{88m+g}$Zr^{cum} reactions

Formation of the long-lived ^{88g}Zr comprises contribution of the recently discovered short-lived isomer ^{88m}Zr ($T_{½}$ = 1.32 μs, IT 100%) and is also cumulative with respect to the short-lived precursors ^{88}Nb ($T_{½}$ = 14.55 min) and ^{88m}Nb ($T_{½}$ = 7.78 min). Activity of ^{88g}Zr was determined via its 392.87 keV gamma line after the decay of the shorter-lived radionuclides.

The obtained cross-sections are displayed on Fig. 26 together with the prediction of TENDL-2015 and two published data sets of Uddin et al. (2004) [10] and Tárkányi et al. (2012) [20]. There is very good agreement between our data and Ref. [20]. From the two points in Ref. [10], the one at 29.7 MeV is significantly lower. The TENDL-2015 library complies with the trend of the experimental data, but it underestimates them from ca 25 MeV.

3.2.19. Cross-sections for the ^{nat}Mo(p,x)$^{89m+g}$Zr^{cum} reactions

The cumulative activity of $^{89m+g}$Zr comprises contribution from the decay of ^{89g}Nb and ^{89m}Nb. It was calculated using the 909.15 keV gamma line of ^{89g}Zr after the total decay of its precursors. The measured and previously published data as well as the prediction of TENDL-2015 are shown on Fig. 27.

The measured cross-sections agree quite well with the data of Lebeda and Pruszyński (2010) [15] and Tárkányi et al. (2012) [20]. Data of Khandaker et al. (2007) [13] and TENDL-2015 [39] are obviously lower. The three points of Uddin et al. (2004) [10] do not show any specific trend, but they might be shifted to higher energies due to the larger energy uncertainty, because they are deduced from the last foils of the stack irradiated with 67 MeV protons (similar is true for all data in Ref. [10] in this energy range).

3.3. Thick target yields

Thick target yields were calculated for all the radionuclides found in the irradiated foils using the fitted experimental data and stopping power of protons in molybdenum in the measured energy range. It means that almost all the thick target yields (except, e.g. ^{88g}Nb) could be calculated for the proton beam energy leaving the target at the practical threshold of the nuclear reactions

resulting in a particular radionuclide. We, however, show only cumulative yields – independent yield is usually of no practical use. The calculated yields are summarized in Figs. 28–32. In the following two paragraphs, we discuss thoroughly the yields for ^{99m}Tc and ^{99}Mo on ^{100}Mo that are displayed separately on Figs. 33 and 34.

3.3.1. Thick target yield for formation of ^{99m}Tc

The thick target yield of the ^{100}Mo(p,2n)^{99m}Tc reaction was deduced from the fit of cross-sections measured in this work and the fit of the selected experimental data shown on Fig. 10b. Calculated yields based on both fits are displayed on Fig. 33 and numerical values of the latter fit are also summarized in Table 4. As apparent from Fig. 33, the difference of both fits is negligible. The yield is significantly dependent on the beam energy in the range available in the most widespread compact cyclotrons for medical radionuclides production. Assuming the proton beam energy leaving the target to be equal to 10 MeV, beam current 500 μA and irradiation time 6 h, we get the following EOB activities: 710 GBq (E_{in} = 16.5 MeV), 923 GBq (E_{in} = 18.0 MeV), 1.07 TBq (E_{in} = 19.0 MeV) and 1.55 TBq (E_{in} = 24.0 MeV). In the calculation, we took into account also the contribution of ^{99}Mo decay to the EOB activity of ^{99m}Tc due to its decay during the irradiation. These values are only somewhat lower than previous estimates based on more "optimistic" cross-sections (and also isotopic abundance of ^{100}Mo) in Refs. [15] or [28], and negligibly higher than the last work focused on ^{99m}Tc production data [22].

3.3.2. Thick target yield for formation of ^{99}Mo

The thick target yield of the ^{100}Mo(p,x)^{99}Mo reactions was also deduced from the fit of both cross-sections measured in this work and of the selected experimental data shown on Fig. 13b. Results of the calculation are displayed on Fig. 34 and the yields based on recommended cross-sections are given in Table 4. The difference of both fits is small, cf. Fig. 34. The yield is rather low for routine production of ^{99}Mo on commercially available compact cyclotrons (81.4 GBq for E_{in} = 24.0 MeV, beam current 500 μA and irradiation time 6 h). The recent measurement of Chodash et al. (2011) [19] suggests that the cross-sections for the ^{100}Mo(p,x)^{99}Mo reactions are almost constant in the energy interval 25–50 MeV, i.e. large-scale production may be possible on highly enriched ^{100}Mo using e.g. dedicated linear accelerators. Anyhow, in this case one must take into account that the product will have low specific activity. It means that production of ^{99}Mo/^{99m}Tc generators should have "central" character followed by distribution of ^{99m}Tc itself and would require efficient recovery of ^{100}Mo from the generators. Moreover, the production suggested in [19] assumes beam current as high as 5 mA at 50 MeV protons to be degraded to 10–20 MeV. It corresponds to the heat input of 150–200 kW in the target – it is obviously great technological challenge regarding the efficient cooling.

Taking all the above mentioned into account, we consider direct, decentralized production of ^{99m}Tc on an existing network of compact medical cyclotrons closer to reality rather than centralized production of ^{99}Mo via ^{100}Mo(p,x) reactions on dedicated, high-current accelerators.

4. Conclusion

Cross-sections of ^{nat}Mo(p,x) reactions resulting in formation of ^{93g}Tc, ^{93m}Tc, $^{93m+g}$Tc, ^{94g}Tc, ^{94m}Tc, ^{95g}Tc, ^{95m}Tc, $^{96m+g}$Tc, ^{97m}Tc, ^{99m}Tc, ^{90}Mo, ^{93m}Mo, ^{99}Mo, ^{88g}Nb, ^{88m}Nb, ^{89g}Nb, ^{89m}Nb, $^{90m+g}$Nb, $^{90m+g}$Nb^{cum}, ^{91m}Nb, ^{92m}Nb, ^{95g}Nb, ^{95m}Nb, $^{95m+g}$Nb, ^{96}Nb, $^{97m+g}$Nb, $^{88m+g}$Zr^{cum} and $^{89m+g}$Zr^{cum} were measured in the proton energy range of 6.9–35.8 MeV. All the data were compared with previously published values and prediction of the TALYS nuclear reaction model code adopted from the TENDL-2015 library. As far as we know, the cross-sections for the ^{nat}Mo(p,x)^{97m}Tc, ^{88g}Nb, ^{88m}Nb and ^{89m}Nb have never been measured previously in this energy region. The thick target yields were deduced from the experimental cross-sections for all the radionuclides.

In the case of ^{nat}Mo(p,x)$^{96m+g}$Tc, ^{100}Mo(p,2n)^{99m}Tc and ^{100}Mo(p,x)^{99}Mo reactions, we selected published experimental data in order to propose recommended cross-sections and thick target yields. We believe that our data, together with several recently published measurements, will allow for reliable modeling accelerator-based production of ^{99m}Tc and ^{99}Mo, for final establishing ^{nat}Mo as a proton beam monitor using the ^{nat}Mo(p,x)$^{96m+g}$ Tc reaction and also provide sound cross-sections relevant for e.g. thin layer activation and as a feedback for the nuclear reaction model codes.

Acknowledgement

The authors are grateful to the crew of the U-120 M cyclotron for the irradiations and to Dr. Petr Hanč and Anton Cvíčela for the help with the gamma spectra measurements. The work was supported by the IAEA Coordinated Research Project "*Nuclear Data for Charged-Particle Monitor Reactions and Medical Isotope Production*" under the contract no. 17461 and by the Czech Academy of Sciences under the NPI research plan AV0Z10480505. The irradiations were carried out at the CANAM infrastructure of the NPI CAS Řež supported through MEYS project no. LM2011019.

References

[1] S.M. Kormali, D.L. Swindle, E.A. Schweikert, Charged particle activation of medium Z. II. Proton excitation functions, J. Radioanal. Nucl. Chem. 31 (2) (1976) 437–450.
[2] E.A. Skakun, V.S. Batij, Y.N. Rakivnenko, O.A. Rastrepin, Excitation functions and isomeric ratios for the interaction of protons of less than 9-MeV with Zr and Mo isotopes, Sov. J. Nucl. Phys. 46 (1987) 17–24.
[3] V.N. Levkovski, Middle Mass Nuclides (A = 40–100) Activation Cross-sections by Medium Energy (E = 10–50 MeV) Protons and Alpha Particles (Experiment and Systematics), Inter-vesi, Moscow, 1991.
[4] W. Zhao, W. Yu, X. Han, H. Lu, Excitation functions of reactions from d + Ti, d + Mo, p + Ti and p + Mo, in: Communication of Nuclear Data Progress No. 19, INDC(CPR)-044/L, China Nuclear Data Center. Atomic Energy Press, Beijing, 1998, pp. 17–20.
[5] M.C. Lagunas-Solar, Accelerator production of ^{99m}Tc with proton beams and enriched ^{100}Mo targets, in: IAEA-TECDOC-1065, IAEA, Vienna, 1999, pp. 87–112.
[6] B. Scholten, R.M. Lambrecht, M. Cogneau, Ruiz H. Vera, Excitation functions for the cyclotron production of ^{99m}Tc and ^{99}Mo, Appl. Radiat. Isot. 51 (1) (1999) 69–80.
[7] S. Takács, F. Tarkányi, M. Sonck, A. Hermanne, Investigation of the ^{nat}Mo(p,x)^{96mg}Tc nuclear reaction to monitor proton beams: New measurements and consequences on the earlier reported data, Nucl. Instrum. Methods Phys. Res. B 198 (3–4) (2002) 183–196.
[8] M. Bonardi, C. Biratari, F. Groppi, E. Sabbioni, Thin-target excitation functions, cross-sections and optimised thick-target yield for ^{nat}Mo(p, xn)$^{94g,95m,95g,96(m+g)}$Tc nuclear reactions induced by protons from threshold up to 44 MeV. No carrier added radiochemical separation and quality control, Appl. Radiat. Isot. 57 (5) (2002) 617–635.
[9] S. Takács, Z. Szűcs, F. Tárkányi, A. Hermanne, M. Sonck, Evaluation of proton induced reactions on ^{100}Mo: new cross sections for production of ^{99m}Tc and ^{99}Mo, J. Radioanal. Nucl. Chem. 257 (1) (2003) 195–201.
[10] M.S. Uddin, M. Hagiwara, F. Tárkányi, F. Ditrói, M. Baba, Experimental studies on the proton-induced activation reactions of molybdenum in the energy range 22–67 MeV, Appl. Radiat. Isot. 60 (6) (2004) 911–920.
[11] M.U. Khandaker, A.K.M.M.H. MeazeKim, K. Kim, D. Son, G. Kim, Y.S. Lee, Measurements of the proton-induced reaction cross-sections of ^{nat}Mo by using the MC50 cyclotron at the Korea institute of radiological and medical sciences, J. Kor. Phys. Soc. 48 (4) (2006) 821–826.
[12] M.B. Challan, M.N.H. Comsan, M.A. Abou-Zeid, Thin target yields and EMPIRE-II predictions on the accelerator production of technetium-99m, J. Nucl. Radiat. Phys. 2 (2007) 1–12.
[13] M.U. Khandaker, M.S. Uddin, K.S. Kim, Y.S. Lee, G.N. Kim, Measurement of cross-sections for the (p,xn) reactions in natural molybdenum, Nucl. Instrum. Methods Phys. Res. B 262 (2) (2007) 171–181.

[14] M.S. Uddin, M. Baba, Proton-induced activation cross-sections of the short-lived radionuclides formation on molybdenum, Appl. Radiat. Isot. 66 (2) (2008) 208–214.
[15] O. Lebeda, M. Pruszyński, New measurement of excitation functions for (p,x) reactions on ^{nat}Mo with special regard to the formation of ^{95m}Tc, $^{96m+g}$Tc, ^{99m}Tc and ^{99}Mo, Appl. Radiat. Isot. 68 (12) (2010) 2355–2365.
[16] AA. Alharbi, A. Azzam, M. McCleskey, B> Roeder, A. Spiridon, E. Simmons, V.Z. Goldberg, A. Banu, L. Trache, R.E. Tribble, Medical radioisotopes production: a comprehensive cross-section study for the production of Mo and Tc radioisotopes via proton induced nuclear reactions on ^{nat}Mo. In: Prof. Nirmal Singh (Ed.), Radioisotopes – Applications in Bio-Medical Science, ISBN: 978-953-307-748-2, 2011.
[17] A.A. Alharbi, J. Alzahrani, J. Azzam, Activation cross-section measurements of some proton induced reactions on Ni, Co and Mo for proton analysis (PAA) purposes, Radiochim. Acta 99 (12) (2011) 763–770.
[18] K. Gagnon, F. Bénard, M. Kovacs, T.J. Ruth, P. Schaffer, J.S. Wilson, S.A. McQuarrie, Cyclotron production of ^{99m}Tc: Experimental measurement of the ^{100}Mo(p,x)^{99}Mo, ^{99m}Tc and ^{99g}Tc excitation functions from 8 to 18 MeV, Nucl. Med. Biol. 38 (8) (2011) 907–916.
[19] P. Chodash, C.T. Angell, J. Benitez, E.B. Norman, M. Pedretti, H. Shugart, E. Swanberg, R. Yee, Measurement of excitation functions for the ^{nat}Mo(d, x)^{99}Mo and ^{nat}Mo(p,x)^{99}Mo reactions, Appl. Radiat. Isot. 69 (10) (2011) 1447–1452.
[20] F. Tárkányi, F. Ditrói, A. Hermanne, S. Takács, A.V. Ignatyuk, Investigation of activation cross-sections of proton induced nuclear reactions on ^{nat}Mo up to 40 MeV: new data and evaluation, Nucl. Instrum. Methods Phys. Res. B 280 (1) (2012) 45–73.
[21] S. Manenti, U. Holzwarth, M. Loriggiola, L. Gini, J. Esposito, F. Groppi, F. Simonelli, The excitation functions of ^{100}Mo(p,x)^{99}Mo and ^{100}Mo(p,2n)^{99m}Tc, Appl. Radiat. Isot. 94 (2014) 344–348.
[22] S. Takács, A. Hermanne, F. Ditrói, F. Tárkányi, M. Aikawa, Reexamination of cross sections of the ^{100}Mo(p,2n)^{99m}Tc reaction, Nucl. Instrum. Methods Phys. Res. B 347 (1) (2015) 26–38.
[23] The supply of medical radioisotopes. An Economic Study of the Molybdenum-99 Supply Chain. OECD-NEA report no. 6967, 2010, ISBN 978-92-64-99149-1.
[24] R. van Noorden, The medical testing crisis, Nature 504 (12) (2013) 202–204.
[25] K. Gagnon, Cyclotron production of technetium-99m PhD thesis, University of Alberta, 2012.
[26] J. Esposito, G. Vecchi, G. Pupillo, A. Taibi, L. Uccelli, A. Boschi, M. Gambaccini, Evaluation of ^{99}Mo and ^{99m}Tc productions based on a high-performance cyclotron, Sci. Technol. Nucl. Installations (2013) 14. Article ID 972381.
[27] F. Bénard, K.R. Buckley, T.J. Ruth, S.K. Zeisler, J. Klug, V. Hanemaayer, M. Vuckovic, X. Hou, A. Celler, J.-P. Appiah, J. Valliant, M.S. Kovacs, P. Schaffer, Implementation of multi-curie production of ^{99m}Tc by conventional medical cyclotrons, J. Nucl. Med. 55 (6) (2014) 1–6.
[28] S.M. Qaim, S. Sudár, B. Scholten, A.J. Koning, H.H. Coenen, Evaluation of excitation functions of ^{100}Mo(p,d+pn)^{99}Mo and ^{100}Mo(p,2n)^{99m}Tc reactions: estimation of long-lived Tc-impurity and its implication on the specific activity of cyclotron-produced ^{99m}Tc, Appl. Radiat. Isot. 85 (2) (2014) 101–113.
[29] M. Fikrle, J. Kučera, F. Šebesta, Preparation of ^{95m}Tc radiotracer, J. Radioanal. Nucl. Chem. 286 (3) (2010) 661–663.
[30] F. Ditrói, F. Tárkányi, F. Takács, Wear measurement using radioactive tracer technique based on proton, deuteron and alpha-particle induced nuclear reactions on molybdenum, Nucl. Instrum. Methods Phys. Res. B 290 (1) (2012) 30–38.
[31] M. Berglund, M.E. Wieser, Isotopic compositions of the elements 2009 (IUPAC technical report), Pure Appl. Chem. 83 (2) (2011) 397–410.
[32] S.Y.F. Chu, L.P. Ekström, R.B. Firestone, The Lund/LBNL nuclear data search, 1999. Available at the web page <http://ie.lbl.gov/toi/>.
[33] M. Čihák, O. Lebeda, J. Štursa, Beam dynamic simulation in the isochronous cyclotron U-120M, in: Proceedings of the Eighteenth International Conference on Cyclotrons and their Applications, CYCLOTRONS 2007, Giardini Naxos, Italy, 2007.
[34] J.F. Ziegler, M.D. Ziegler, J.P. Biersack, SRIM2010 Code, Available at URL <http://www.srim.org/>.
[35] NuDat 2.6, National Nuclear Data Center, Brookhaven National Laboratory, 2012. Available at URL <www.nndc.bnl.gov/nudat2/>.
[36] V.P. Chechev, M.-M. Bé, Radioactive equilibrium: ^{99}Mo/^{99m}Tc decay characteristics, Appl. Radiat. Isot. 87 (2014) 132–136.
[37] B. Pritychenko, A. Sonzogni, Q-value calculator, NNDC, Brookhaven National Laboratory. Available from URL <http://www.nndc.bnl.gov/qcalc>.
[38] J. Frána, Program DEIMOS32 for gamma-ray spectra evaluation, J. Radioanal. Nucl. Chem. 257 (3) (2003) 583–587.
[39] A.J. Koning, D. Rochman, S.C. van der Marck, J. Kopecky, J.Ch. Sublet, S. Pomp, H. Sjostrand, R. Forrest, E. Bauge, H. Henriksson, O. Cabellos, S. Goriely, J. Leppanen, H. Leeb, A. Plompen, R. Mills, TALYS-based evaluated nuclear data library. Available from URL <http://www.talys.eu/tendl-2015>.
[40] K. Gul, A. Hermanne, M.G. Mustafa, F.M. Nortier, P. Obložinský, S.M. Qaim, B. Scholten, Yu. Shubin, S. Takács, F. Tárkányi, Z. Zhuang, Charged particle cross-section database for medical radionuclide production: diagnostic radionuclides and monitor reactions, in: IAEA-TECDOC-1211, IAEA, Vienna, 2001. Update available from URL: <www.nds.iaea.org/medical/>.

Publikácia II

Červenák J., Lebeda O.

Measurement of cross-sections of proton-induced nuclear reactions on ^{197}Au focused on the production of the theranostic pair ^{197m,g}Hg

Nucl. Instrum. Methods Phys. Res. B 458 (2019) 118-125
https://doi.org/10.1016/j.nimb.2019.08.006

Nuclear Inst. and Methods in Physics Research B 458 (2019) 118–125

Contents lists available at ScienceDirect

Nuclear Inst. and Methods in Physics Research B

journal homepage: www.elsevier.com/locate/nimb

Measurement of cross-sections of proton-induced nuclear reactions on ^{197}Au focused on the production of the theranostic pair ^{197m,g}Hg

Jaroslav Červenák, Ondřej Lebeda*

Nuclear Physics Institute of the CAS, Husinec-Řež 130, 250 68 Řež, Czech Republic

ARTICLE INFO

Keywords:
^{197m}Hg
^{197g}Hg
Theranostic pair
Cross-sections
Proton activation
Gold target

ABSTRACT

We measured cross-sections of the nuclear reactions ^{197}Au(p,x)^{197m}Hg, ^{197g}Hg, ^{195m}Hg, ^{195g}Hg, ^{196m2}Au, $^{196m1+g}$Au, $^{194m+g}$Au in the energy range of 6.4–35.3 MeV having used stacked-foil technique with high purity gold foils. The results were compared with previously published data and with prediction of the TALYS nuclear reaction model code adopted from the TENDL-2017 library. Thick target yields were deduced from the measured data. Production of the theranostic isomeric pair ^{197m,g}Hg is thoroughly discussed.

1. Introduction

The isomers of ^{197}Hg, ^{197m}Hg (23.8 h) and ^{197g}Hg (64.14 h), form an interesting theranostic radionuclide pair for imaging and therapy [1]. While the shorter-lived ^{197m}Hg emits a dominant 134 keV γ-line suitable for imaging via Single Photon Emission Computed Tomography (SPECT) as well as high energy conversion electrons (150, 119 and 82 keV) and Auger electrons (7.6 keV) promising for therapy of small tumours and metastases, the longer-lived ground state provides 77.35 keV gamma line, 77.58 keV X-$K_{\beta 3}$, 77.98 keV X-$K_{\beta 1}$ rays and 68.81 keV X-$K_{\alpha 1}$ rays appropriate for the SPECT imaging and also therapeutic conversion electrons (63 keV) together with Auger electrons (7.4 keV) [1,2]. Moreover, it is easy to shield even larger activities of the pair due to the absence of high energy γ-rays. Finally, chemistry of mercury, as a metal element, enables labelling reactions using appropriate chelators [3].

In contrast to the reactor-produced mercury radioisotopes that suffer from low specific activity, production of ^{197m,g}Hg by protons or deuterons on naturally monoisotopic ^{197}Au allows to obtain almost carrier-free product. Rapid and efficient separation of mercury radioisotopes from the gold target results in high radionuclidic purity and high-specific activity of ^{197m,g}Hg suitable for labelling. It eliminates risk related to chemical toxicity of the mercury itself that stopped interest in the reactor-produced Hg radioisotopes.

For reliable and well-controlled production of ^{197m,g}Hg, precise knowledge of the excitation functions for their formation is necessary. Moreover, the EOB isomeric ratio of ^{197m}Hg/^{197g}Hg depends not only on the particle energy, irradiation and cooling times, but also on the projectile inducing the nuclear reaction leading to their formation. In general, deuteron-induced reactions provide higher isomeric cross-section ratio *m/g* compared to proton-induced reactions. This ratio for a given particle and a particular production target is a function of the incident beam energy and its loss in the target, i.e. of its thickness (see Section 3.4 Thick target yields).

Due to the few available experimental data sets that are not always consistent, we decided to re-measure excitation functions of proton-induced nuclear reactions on gold up to 35.3 MeV proton energy available on the cyclotron U-120 M at the Nuclear Physics Institute, Řež. For the same reason, the deuteron-induced excitation functions were re-measured up to 20 MeV and the results will be reported in a separate article.

2. Experimental

2.1. Target and irradiation

Two stacks consisting of ^{197}Au foils (99.9%, 7 μm thick, Goodfellow, Great Britain) interleaved with ^{nat}Ti foils (99.6% 11.0 μm thick, AlfaAesar, USA) and Cu degraders (55.9 and 10.6 μm thick, Goodfellow, Great Britain) were irradiated on the external proton beam line of the cyclotron U-120 M at the Nuclear Physics Institute of the Czech Academy of Sciences (CAS). The stacks were placed in a Faraday-cup-like holder. Precise thickness of each foil was determined by weighing. The beam energy loss and straggling was calculated with use of the program SRIM2008 [4].

The first stack of foils contained 13 Au targets and 14 Ti monitors

* Corresponding author.
E-mail address: lebeda@ujf.cas.cz (O. Lebeda).

https://doi.org/10.1016/j.nimb.2019.08.006
Received 23 June 2019; Received in revised form 30 July 2019; Accepted 8 August 2019

interleaved with thicker Cu degraders, and the incident proton energy was set to 35.2 ± 0.2 MeV. The second stack of foils contained 12 Au targets and 12 Ti monitors interleaved with thinner Cu degraders, and the incident proton energy was set to 17.3 ± 0.2 MeV [5]. Each stack was irradiated for 1 h.

Beam current was recorded each second of the irradiation and integrated over the bombardment time t_b. The recorded value of beam current was slightly corrected by reconstruction of the monitoring excitation function ^{nat}Ti(p,x)^{48}V [6].

2.2. Activity measurement

Three energy and efficiency calibrated HPGe detectors (GMX45-Plus, Ortec; GC2019, Canberra and GEM40P4-83-SMP, Ortec) were used for measurement of gamma-ray spectra of the irradiated foils. Their calibration was performed with a set of standards (^{241}Am, ^{152}Eu, ^{137}Cs, ^{133}Ba and ^{60}Co) for various distances sample-detector. The whole energy range for a given distance sample-detector was covered with a polynomial of the fifth degree ($\ln \eta = f(\ln E)$, where η is the detection efficiency and E is the energy of a gamma line). Linear fit was used for photo-peak energies higher than 240 keV.

All the irradiated Au foils were measured several times in order to optimize quantification of radionuclides with various half-lives and intensities of the gamma-lines. All the Ti monitors were measured after ca 16 days in order to avoid the interference from the decay of ^{48}Sc to the activity of ^{48}V. The ^{48}V activity fraction ejected from the monitor to the following Au foil was measured and added to the activity measured in the monitor itself (0.5–3.5% of ^{48}V born in the foil was ejected, depending on the beam energy in the foil). All the acquired spectra were evaluated in the program DEIMOS [7].

The decay data used for the activity calculation were adopted from the NuDat2 database [8] and, if missing, from the Firestone's Table of Isotopes [2]. Q-values and thresholds of the reactions were calculated via Q-calc program online [9]. The decay and nuclear reaction data relevant for the experiment are summarized in Table 1.

2.3. Calculation of cross-sections, their uncertainties, thick target yields and prediction of excitation functions

Cross-sections were calculated using the activation formula (equation (1)):

$$\sigma = \frac{P_\gamma}{I_\gamma \eta t_m} \frac{\lambda t_r}{1 - e^{-\lambda t_r}} e^{\lambda t_c} \frac{Aze}{d\rho N_A I \left(1 - e^{-\lambda t_b}\right)} \quad (1)$$

where σ is cross-section for formation of a radionuclide at the energy in the middle of the foil (cm^2), P_γ is net peak area of the γ-line used for the radionuclide's quantification, I_γ is intensity of this γ-line, η is detection efficiency for this γ-line, t_m is life time of the measurement (h), t_r is real time of measurement (including the dead time) (h), λ is decay constant of a radionuclide (h^{-1}), t_c is time between the EOB and the start of the measurement (h), A is atomic weight of the foil's metal (g/mol), z is proton charge (z = 1), e is elementary charge (1.602177×10^{-19}C), d is foil's thickness (cm), ρ is density of the foil's metal (g/cm^3), N_A is Avogadro's number (6.022137×10^{23} mol^{-1}), I is beam current (A) and t_b is irradiation time (h).

Total cross-section uncertainty was deduced from partial uncertainties of the parameters in the activation formula summarized below:

- detection efficiency for a gamma line selected for the activity calculation (ca 3 %)
- emission probability of a gamma line selected for the activity calculation (usually < 5 %)
- net peak area of a gamma line selected for the activity calculation (< 10 %)
- beam current (ca 6 %)
- foil's thickness (< 2 %)

The obtained cross-sections were compared with previously published data and with theoretical predictions of the TALYS nuclear reaction model code adopted from the TENDL-2017 library [10].

2.4. Interference corrections

The only interference to be corrected was the contribution of parent nuclei decay to daughter nuclei activity in the generator systems formed in the target foils. Activity of a daughter radionuclide born from a parent radionuclide during the irradiation (Eq. (2)) and after EOB (Eq. (3)) was taken into account [11,12].

$$A_2^{EOB} = f \frac{d\rho N_A \sigma I}{Aze} \left(1 - \frac{\lambda_2}{\lambda_2 - \lambda_1} e^{-\lambda_1 t_b} + \frac{\lambda_1}{\lambda_2 - \lambda_1} e^{-\lambda_2 t_b}\right) \quad (2)$$

$$A_2 = f \frac{\lambda_2}{\lambda_2 - \lambda_1} A_1^{EOB} \left(e^{-\lambda_1 t} - e^{-\lambda_2 t}\right) + A_2^{EOB} e^{-\lambda_2 t} \quad (3)$$

3. Results and discussion

3.1. Beam energy and current

The integrated beam current measured in the first stack indicated an average value of 0.574 μA, in the second stack it was 0.622 μA. The reconstructed excitation function of the monitoring reaction ^{nat}Ti(p,x)^{48}V with the recommended cross-sections [6] are displayed in Fig. 1. The slight corrections resulted in the incident beam energies equal to 35.40 MeV and 17.50 MeV, respectively, and in the beam currents equal to 0.567 μA and 0.590 μA, respectively. It is a good agreement that demonstrates the setting of the beam parameters is within the expected uncertainties.

3.2. Measured cross-sections and prediction of excitation functions

The measured cross-sections together with the previously published data and the excitation functions predicted by the TALYS code (TENDL-2017 library) [10] are displayed on Figs. 2–8. The cross-sections obtained in our experiment including their uncertainties are summarized in Table 2.

3.2.1. Cross-sections for the ^{197}Au(p,n)^{197m}Hg

The activity of ^{197m}Hg was calculated from the net peak area of its 133.98 keV γ-line (33.5% per decay). All the previously published data were corrected with the use of the currently adopted emission probabilities of the radiation used by the authors for quantification of the cross-sections, if possible. The data we measured are in a very good agreement with data of Vandenbosch and Huizenga (1960) [13], Szelecsényi et al. (1997, 2007) [14,15] and Elmaghraby et al. (2010) [16]. The best agreement was observed with recent results of Ditrói et al. (2016) [17]. Hansen's et al. (1962) [18] and Gritsyna's et al. (1963) [19] data show the same course of the excitation function as the rest of the experimental data, they are, however, slightly higher and lower respectively when compared to our data. Moreover, Gritsyna's data seem to be shifted towards lower energies. The largest difference was observed between our data and the cross-sections provided by Satheesh et al. (2012) [20]. Their data seem to overestimate significantly the remaining experimentalists; moreover, they are rather scattered. Theoretical model is in an excellent agreement with our data up to ca 11 MeV. All the authors, including us, observed then a sharp maximum around 11.8 MeV; in contrast, the TALYS predicts much slower gradual decrease of the excitation function with another maximum.

Table 1
Data for the investigated radionuclides. *Q*-values and thresholds for the isomeric nuclei need to be lowered by the energy level of the isomer. *Q*-values for reactions where composed particles are emitted need to be increased by the particle binding energy (d = np + 2.225 MeV, t = p2n + 8.482 MeV, ^{3}He = 2pn + 7.718 MeV, α = 2p2n + 28.296 MeV). Energies and intensities of gamma lines used for quantification are in bold. Uncertainties in the last digits are given in italics.

Radionuclide Spin	Half-life	Reaction	Q (MeV)	Threshold (MeV)	E_γ (keV)	I_γ (%)
^{195m}Hg 13/2+	41.6 h *8*	^{197}Au(p,3n)	−17.051	17.139	261.75 *4*	31 *3*
					387.87 *5*	2.18 *18*
					560.27 *4*	**7.1**
^{195g}Hg 1/2−	10.53 h *3*				180.11 *4*	1.95 *24*
					207.10 *4*	1.6 *3*
					585.13 *5*	2.04 *25*
					599.66 *4*	1.83 *22*
					779.80 *5*	**7.0**
					1111.04 *10*	1.48 *22*
^{197m}Hg 13/2+	23.8 h *1*	^{197}Au(p,n)	−1.382	1.389	**133.98 *5***	**33.5**
					164.97 *7*	0.262
					279.01 *5*	6
^{197g}Hg 1/2−	64.14 h *5*				**191.437 *10***	**0.632 *21***
					268.78 *5*	0.0393 *19*
^{194g}Au 1−	38.02 h *10*	^{197}Au(p,p3n)	−23.142	23.260	293.548 *7*	10.58 *15*
					328.464 *6*	**60.4 *8***
					645.152 *9*	2.34 *3*
					948.310 *9*	2.28 *3*
					1104.044 *10*	2.14 *3*
					1175.353 *11*	2.11 *3*
					1468.882 *15*	6.61 *11*
					1886.89 *6*	2.23 *18*
					1924.225 *22*	2.19 *9*
^{196m2}Au 12−	9.6 h *1*	^{197}Au(p,pn)	−8.072	8.114	137.69 *3*	1.3 *4*
					147.81 *2*	**43.5**
					168.37 *2*	7.8 *5*
					188.27 *3*	30.0 *15*
					285.49 *7*	4.4 *5*
					316.19 *5*	3.0 *3*
^{196g}Au 2−	6.1669 d *6*				333.03 *5*	22.9 *9*
					355.73 *5*	**87**
					426.10 *8*	6.6
					129.79 *2*	2.90 *21*

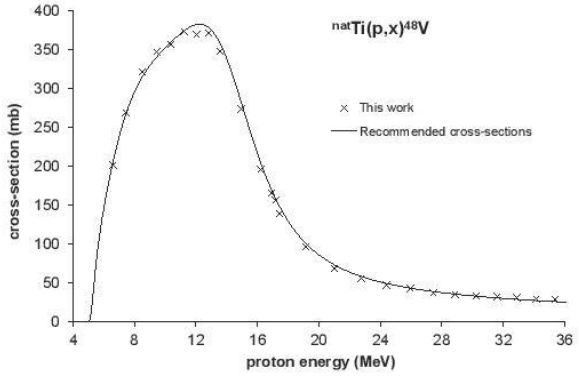

Fig. 1. Reconstruction of the recommended excitation function of the ^{nat}Ti(p,x)^{48}V reactions [6] from the ^{48}V activity measured in the Ti monitors in both stacks of foils.

3.2.2. Cross-sections for the ^{197}Au(p,n)^{197g}Hg

The activity of the ground state ^{197g}Hg was calculated from its strongest γ-line 191.44 keV that has rather low intensity of 0.632% per decay. The activity was corrected for the contribution of ^{197m}Hg decay as described in the Section 2.4. The experimental data for the excitation function of the ^{197}Au(p,n)^{197g}Hg reaction are the most scattered from all the studied reactions. This can be due to the fact that majority of the authors used for the ^{197g}Hg quantification the 77.35 keV gamma line that interferes with two X-rays (77.58 keV and 77.98 keV) of different intensities. It is, therefore, very difficult to apply any correction. Only the data of Elmaghraby et al. (2010) [16] were corrected as they used the 191.44 keV γ-line for evaluation. Our data are again in the best agreement with Ditrói et al. (2016) [17], although these cross-sections are slightly higher in the energy region of 13–17 MeV (Ditrói et al. used the same γ-line and intensity for evaluation as we did). The data of Hansen et al. (1962) [18] and Gritsyna et al. (1963) [19] follow almost perfectly the theoretical prediction, being systematically lower than our measurement, while those of Vandenbosch and Huizenga (1960) [13] are shifted towards higher energies. Even though the remaining data sets [18,20–22] have similar shape, their cross-sections are higher or even significantly higher and in the case of Thomas and Bartolini (1967) [21] and Chodil et al. (1967) [22], their points are quite scattered as well. Schery's et al. (1974) [23] point is a little lower than our excitation function. Theoretical model fits perfectly with our data up to 9 MeV and in the energy region over 20 MeV. Between 9 and 20 MeV, the prediction follows the shape of the experimental data, but shows lower values.

3.2.3. Cross-sections for the ^{197}Au(p,3n)^{195m}Hg

The activity of ^{195m}Hg was calculated using its 560.27 keV γ-line with the intensity of 7.1% per decay. Experimental cross-sections for the ^{197}Au(p,3n)^{195m}Hg reaction are quite consistent, all of them follow the same trend. The best agreement with our data can be found with the results of Michel et al. (1997) [24]. The remaining data sets

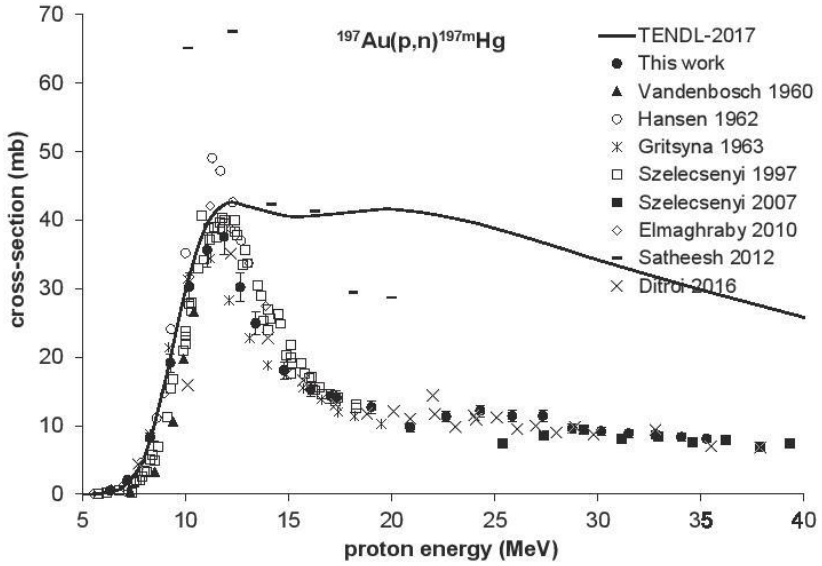

Fig. 2. Cross-sections for the ^{197}Au(p,n)^{197m}Hg reaction.

[15,17,25,26] show lower cross-section values, and there is a good agreement among them. Ditrói's et al. (2016) [17] data are slightly scattered in the energy region up to 24 MeV, nevertheless they are the second closest cross-sections to our measurement (the scattering seems to be due to combing data from the two experiments at different cyclotrons). Theoretical prediction has a steeper increase than the experimental data and the maximum of the excitation function is approximately 10% higher compared to our results; for projectile energies exceeding 29 MeV, the prediction is in an excellent agreement with our results, and with the data of Michel et al. [24] and Ditrói et al. [17].

3.2.4. Cross-sections for the ^{197}Au(p,3n)^{195g}Hg

Cross-sections of ^{195g}Hg were calculated using its 779.80 keV γ-line with the emission probability of 7.0% per decay. The activity was corrected for the contribution of ^{195m}Hg decay (see Section 2.4.). Our results are in very good agreement with the data of Ditrói et al. (2016) [17] even though they show the same scattering in the energy region up to 24 MeV as in the case of their cross-sections for formation of ^{195m}Hg. Nagame's et al. (1990) [26] cross-sections seem to be systematically lower. The single cross-section point around maximum provided by Bonardi and Birattari (1984) [25] agrees well with our measurement, while another single value published by Gusakow et al. (1960) [27] overestimates significantly the data measured in this energy region. Theoretical prediction should be shifted to higher energies (ca 3 MeV) and its values multiplied by ca 1.35 in order to agree well with the experimental data.

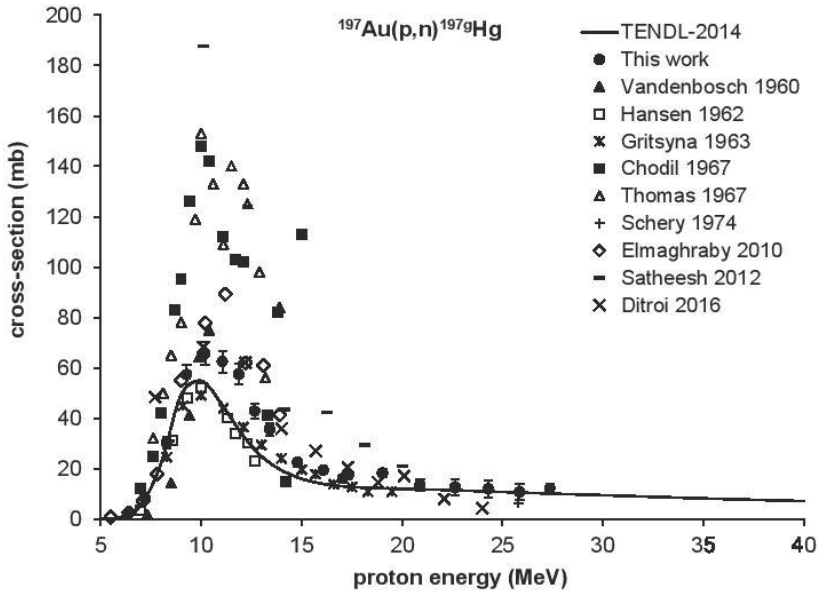

Fig. 3. Cross-sections for the ^{197}Au(p,n)^{197g}Hg reaction.

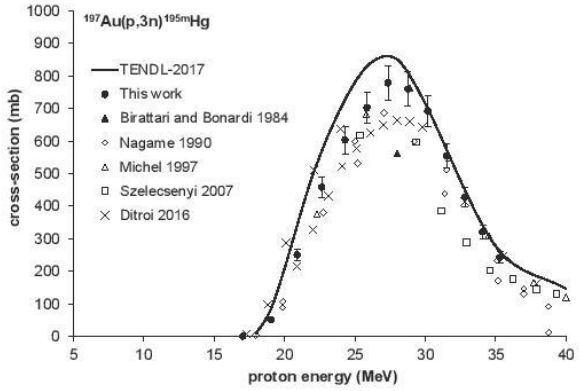

Fig. 4. Cross-sections for the ^{197}Au(p,3n)^{195m}Hg reaction.

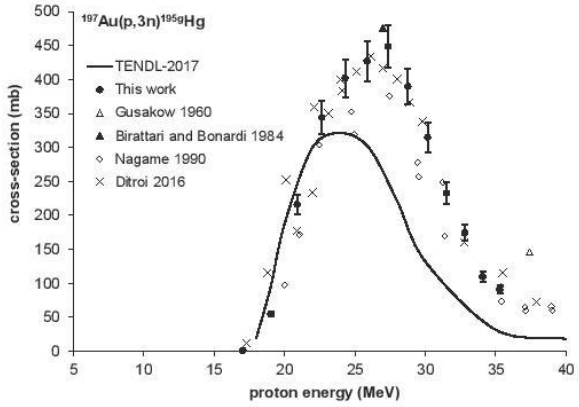

Fig. 5. Cross-sections for the ^{197}Au(p,3n)^{195g}Hg reaction.

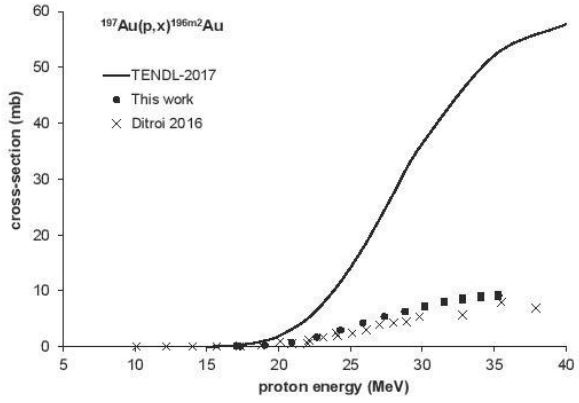

Fig. 6. Cross-sections of proton-induced reactions on gold leading to ^{196m2}Au.

3.2.5. Cross-sections for the $^{197}Au(p,x)^{196m2}Au$

The activity of ^{196m2}Au was calculated using its 147.81 keV γ-line with 43.5% intensity. The only available experimental cross-section data for formation of ^{196m}Au were those of Ditroi et al. (2016) [17]. They agree with our results very well up to 25 MeV, while for higher energies, Ditroi's cross-sections start to be systematically lower. The TALYS prediction overestimates by far all the experimental data, although its shape corresponds with them.

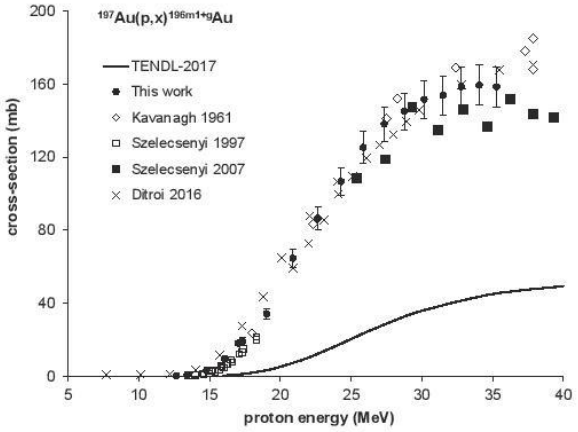

Fig. 7. Cross-sections of proton-induced reactions on gold leading to $^{196m1+g}$Au.

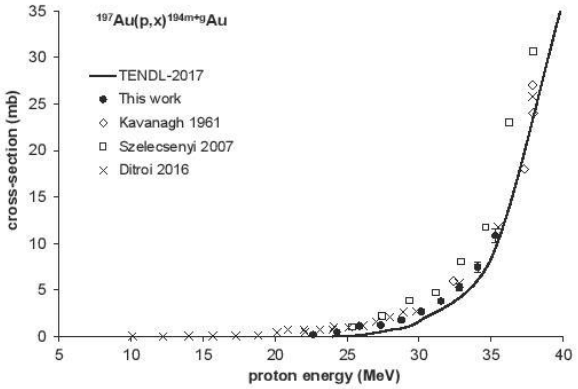

Fig. 8. Cross-sections of proton-induced reactions on gold leading to $^{194m+g}$Au.

3.2.6. Cross-sections for the $^{197}Au(p,x)^{196m1+g}Au$

The cross-sections of $^{196m1+g}$Ag are based on its intense 355.73 keV γ-line (emission probability of 87% per decay). The activity was corrected for the contribution of ^{196m2}Au decay (cf. 2.4), but it is cumulative regarding the short-lived isomer ^{196m1}Au ($T_{½}$ = 8.1 s). In the 10–30 MeV energy interval, all the four available experimental data sets [14,15,17,28] are in a good agreement with each other and with our measurement. For the energies exceeding 30 MeV, the experimental data start to be less consistent and more scattered. TENDL-2017 underestimates significantly the measured excitation functions in the whole energy region.

3.2.7. Cross-sections for the $^{197}Au(p,x)^{194m+g}Au$

The activity of ^{194g}Ag was calculated from its 328.464 keV γ-line with intensity of 60.4%. It is cumulative regarding its isomeric state ^{194m}Au that decays solely to its ground state via isomeric transition with half-life of 600 ms. All the experimental data sets [15,17,28] show the same trend as our cross-sections, however, data of Szelecsényi et al. [15] seem to be systematically higher. The TALYS prediction slightly underestimates the measured data almost in the whole energy range.

3.3. Isomeric cross-section ratios

Isomeric cross-section ratios for the three isomeric pairs found in the target were calculated from the measured cross-sections and compared with experimental isomeric ratios calculated from the cross-sections

Table 2
Measured cross-sections data for formation of Hg and Au radioisotopes in the ^{197}Au(p,x) reactions.

E_p (MeV)	σ (mb)						
	^{197m}Hg	^{197g}Hg	^{195m}Hg	^{195g}Hg	^{196m2}Au	$^{196m1+g}$Au	$^{194m+g}$Au
35.29 ± 0.20	8.10 ± 0.56		243 ± 17	90.6 ± 6.3	9.18 ± 0.63	158 ± 11	10.84 ± 0.76
34.07 ± 0.20	8.33 ± 0.58		321 ± 22	109.7 ± 7.6	9.02 ± 0.62	159 ± 11	7.48 ± 0.53
32.81 ± 0.20	8.72 ± 0.61		428 ± 29	174 ± 12	8.52 ± 0.59	158 ± 11	5.27 ± 0.38
31.51 ± 0.21	8.85 ± 0.62		554 ± 38	233 ± 16	7.99 ± 0.55	154 ± 11	3.81 ± 0.28
30.17 ± 0.21	9.20 ± 0.64		693 ± 48	315 ± 22	7.32 ± 0.51	152 ± 10	2.68 ± 0.20
28.77 ± 0.22	9.57 ± 0.67		760 ± 52	390 ± 27	6.32 ± 0.44	145 ± 10	1.78 ± 0.14
27.35 ± 0.22	11.45 ± 0.79	12.1 ± 2.1	779 ± 54	449 ± 31	5.40 ± 0.37	138.1 ± 9.5	1.23 ± 0.10
25.86 ± 0.23	11.42 ± 0.79	10.7 ± 3.4	703 ± 48	427 ± 29	4.25 ± 0.29	125.2 ± 8.7	1.12 ± 0.10
24.30 ± 0.23	12.16 ± 0.84	12.0 ± 3.3	603 ± 42	402 ± 28	2.97 ± 0.21	106.5 ± 7.5	0.480 ± 0.056
22.65 ± 0.24	11.31 ± 0.78	12.5 ± 3.0	458 ± 32	344 ± 24	1.72 ± 0.12	86.4 ± 6.1	0.226 ± 0.041
20.90 ± 0.25	9.77 ± 0.67	13.5 ± 2.2	250 ± 17	216 ± 15	0.781 ± 0.060	64.5 ± 5.0	
19.03 ± 0.27	12.70 ± 0.87	15.7 ± 1.7	51.6 ± 2.4	54.5 ± 1.1	0.254 ± 0.021	34.0 ± 2.9	
17.32 ± 0.20	14.2 ± 1.0	17.4 ± 1.2			0.0188 ± 0.022	18.9 ± 2.2	
17.04 ± 0.28	14.3 ± 1.0	16.0 ± 1.7	0.56 ± 0.19	1.12 ± 0.44	0.134 ± 0.010	17.9 ± 1.3	
16.08 ± 0.20	15.3 ± 1.1	19.4 ± 1.4				9.56 ± 0.66	
14.79 ± 0.21	18.1 ± 1.2	22.5 ± 1.6				3.28 ± 0.23	
13.41 ± 0.22	24.9 ± 1.7	35.6 ± 2.5				0.607 ± 0.043	
12.66 ± 0.23	30.2 ± 2.1	42.8 ± 3.0				0.186 ± 0.015	
11.87 ± 0.23	37.6 ± 2.6	57.4 ± 4.0					
11.05 ± 0.24	35.6 ± 2.4	62.5 ± 4.4					
10.19 ± 0.25	30.3 ± 2.1	65.7 ± 4.6					
9.27 ± 0.26	19.2 ± 1.3	57.3 ± 4.0					
8.28 ± 0.27	8.27 ± 0.57	30.2 ± 2.1					
7.19 ± 0.30	2.07 ± 0.14	8.34 ± 0.63					
6.35 ± 0.32	0.504 ± 0.037	2.02 ± 0.21					

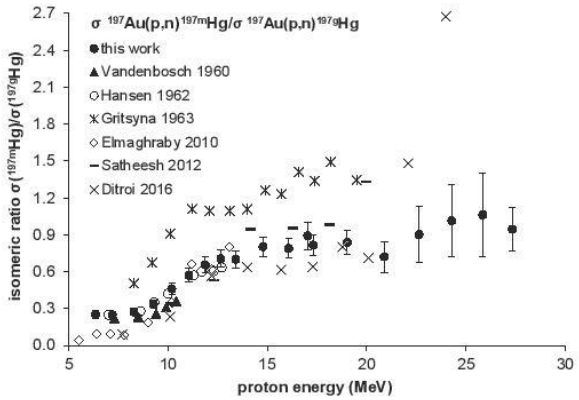

Fig. 9. Isomeric cross-section ratio for the formation of ^{197m}Hg/^{197g}Hg.

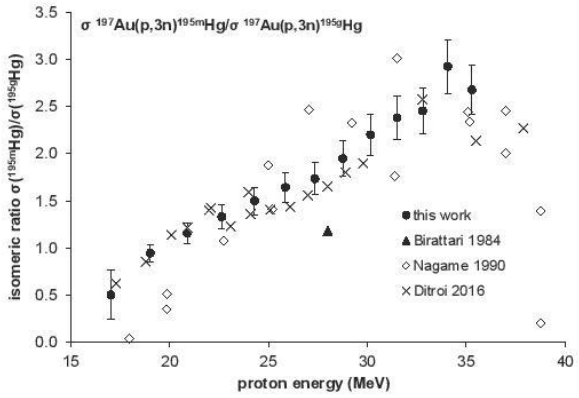

Fig. 10. Isomeric cross-section ratio for the formation of ^{195m}Hg/^{195g}Hg.

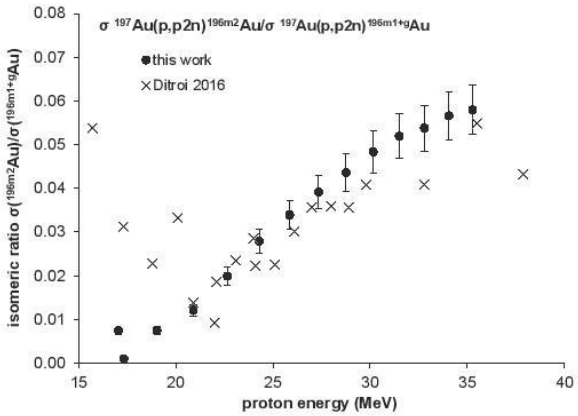

Fig. 11. Isomeric cross-section ratio for the formation of ^{196m2}Au/$^{196m1+g}$Au.

provided by the other authors. The comparison is displayed on the Figs. 9–11 and discussed below.

3.3.1. Isomeric cross-section ratio for formation of ^{197m}Hg/^{197g}Hg

All the data follow approximately the same trend. Gritsyna's et al. (1963) [19] data overestimate the rest of other experimental data in the whole measured energy range. All the remaining data are in an acceptable agreement with ours up to 20 MeV, where Ditrói's et al. (2016) [17] and Elmaghraby's et al. (2010) [16] data start to be remarkably higher. In general, the cross-section ratio *m/g* increases with energy, exceeding 0.8 around 15 MeV and at ca 25 MeV reaching its maximum value of 1.06.

3.3.2. Isomeric cross-section ratio for formation of ^{195m}Hg/^{195g}Hg

Ditrói's et al. (2016) [17] data are in a very good agreement with ours. Nagame's et al. (1990) [26] values follow roughly the same trend, but they are too scattered. The only point of Bonardi and Birattari (1984) [25] seems to underestimate the other three data sets. The ratio

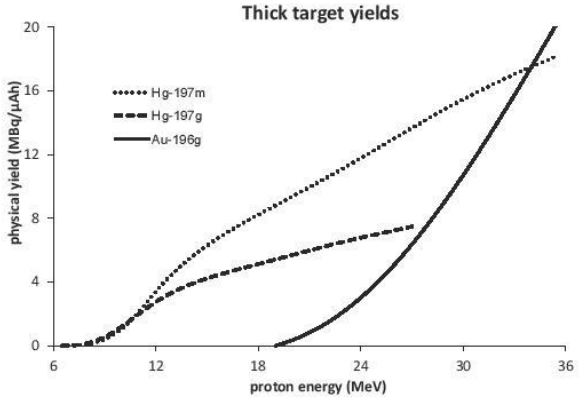

Fig. 12. Physical thick target yields for ^{197m}Hg, ^{197g}Hg and $^{196m1+g}$Au.

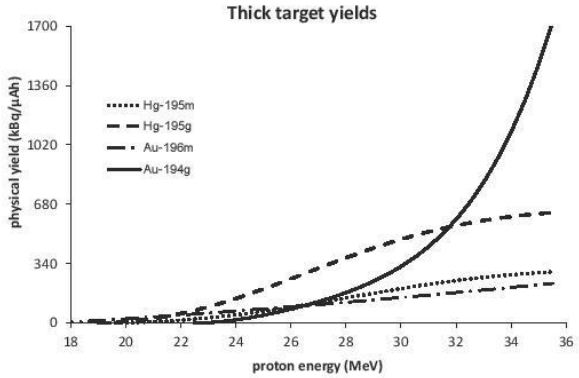

Fig. 13. Physical thick target yields for ^{195m}Hg, ^{195g}Hg, ^{196m2}Au and $^{194m+g}$A.

m/g increases quite rapidly with the proton energy from 0.5 at 17 MeV to almost 3 around 35 MeV.

3.3.3. Isomeric cross-section ratio for formation of ^{196m2}Au/$^{196m1+g}$Au

The isomeric cross-section ratio that can be calculated in this case is the ratio of measurable cross-section for *m2* state and sum of cross-sections for the formation of *m1* state ($T_{½}$ = 8.1 s, J_{π} = 5+) and the ground state. Ditrói's et al. (2016) [17] data show large scattering, although in general follow the same trend as our *m2/(m1 + g)* cross-section ratio. The ratio *m2/(m1 + g)* increases rapidly with energy, however, formation of the ground state is remarkably enhanced compared to both isomeric pairs of the mercury radioisotopes discussed above.

3.4. Thick target yields

Thick target yields were calculated for all the radionuclides quantified in the experiment. The experimental cross-section data were fitted with one or two polynomial fits and integrated using the stopping power of protons in gold [4] in order to obtain thick target yields. The deduced yields are displayed on the Figs. 12 and 13.

3.4.1. Thick target yields for formation of ^{197m}Hg and ^{197g}Hg

With beam energies below 17 MeV (threshold for formation of ^{195m}Hg/^{195g}Hg, cf. Table 1 and Figs. 4 and 5), it is possible to obtain ^{197m}Hg/^{197g}Hg without any measurable radionuclidic impurities just by chemical separation of mercury from Au target, and the product is practically carrier-free except traces of stable ^{196}Hg produced in the ^{197}Au(p,2n) reaction (E_{thr} = 8.21 MeV).

The ^{197m}Hg/^{197g}Hg activity ratio at the EOB for e.g. 10 h long irradiation may vary between ca 1.1 to ca 1.8 using various beam energy losses (incident 12–24 MeV, leaving energy 8–20 MeV). Shortening the bombardment time to 5 h increases this ratio to 2.0. Further shortening brings only minor effect, while the available activity drops significantly. Avoiding formation of ^{195m}Hg/^{195g}Hg, one may vary the ^{197m}Hg/^{197g}Hg activity ratio at the EOB actually between 1.1 and 1.8, producing several GBq of both isomers in 10 h with 100 μA proton beam. In all the cases, the contribution of ^{197m}Hg decay to the EOB activity of ^{197g}Hg during the irradiation was taken into account.

The evolution of the ^{197m}Hg/^{197g}Hg activity ratio in time post-EOB must be considered before administration of this theranostic pair. For therapeutic application, enhanced formation of ^{197m}Hg is desirable, for diagnostic a vice versa, cf. [1].

4. Conclusion

In this work, we presented new experimental cross-sections for the proton-induced reactions on ^{197}Au resulting in ^{197m}Hg, ^{197g}Hg, ^{195m}Hg, ^{195g}Hg, ^{196m2}Au, $^{196m1+g}$Au and $^{194m+g}$Au in the energy range of 6.4–35.3 MeV. Some of the previously published data (^{197m}Hg, ^{197g}Hg) were corrected to the currently adopted γ-line intensities before comparing them to our results. All the experimental data were compared with the theoretical prediction of cross-sections of the TALYS nuclear reaction model adopted from the TENDL-2017 online library. The isomeric ratios for the three isomeric pairs found in the target were calculated, as well as thick target yields for all the radionuclides quantified in the experiment. Possible ways for modifying the EOB activity ratio for the theranostic pair ^{197m}Hg/^{197g}Hg were shortly discussed.

Declaration of Competing Interest

None

Acknowledgement

The work was supported from ERDF/ESF project "CANAM-OP" of the Ministry of Education, Youth and Sports of the Czech Republic (No. CZ.02.1.01/0.0/0.0/16_013/0001812).

References

[1] R. Freudenberg, R. Apolle, M. Walther, H. Hartmann, J. Kotzerke, Molecular imaging using the theranostic agent $^{197(m)}$Hg: phantom measurements and Monte Carlo simulations, Eur. J. Nucl. Med. Mol. Imaging 5 (15) (2018), https://doi.org/10.1186/s40658-018-0216-9.
[2] S.Y.F. Chu, L.P. Ekström, R.B. Firestone, The Lund/LBNL nuclear data search, 1999. Available at the web page < http://ie.lbl.gov/toi/ > .
[3] M. Walther, S. Preusche, S. Bartel, G. Wunderlich, R. Freudenberg, J. Steinbach, H.-J. Pietzsch, Theranostic mercury: $^{197(m)}$Hg with high specific activity for imaging and therapy, Appl. Radiat. Isot. 97 (2015) 177–181, https://doi.org/10.1016/j.apradiso.2015.01.001.
[4] J.F. Ziegler, M.D. Ziegler, J.P. Biersack, SRIM2010 Code, Available at URL < http://www.srim.org/ > .
[5] M. Čihák, O. Lebeda, J. Štursa, Beam dynamic simulation in the isochronous cyclotron U-120M, Proceedings of the eighteenth international conference on cyclotrons and their applications, CYCLOTRONS 2007, Giardini Naxos, (2007).
[6] K. Gul, A. Hermanne, M.G. Mustafa, F.M. Nortier, P. Obložinský, S.M. Qaim, B. Scholten, Yu Shubin, S. Takács, F. Tárkányi, Z. Zhuang, Charged particle cross section database for medical radionuclide production: diagnostic radionuclides and monitor reactions, IAEA-TECDOC-1211, IAEA, Vienna, (2001) Update available from URL: < www.nds.iaea.org/medical/ > .
[7] J. Frána, Program DEIMOS32 for gamma-ray spectra evaluation, J. Radioanal. Nucl. Chem. 257 (3) (2003) 583–587, https://doi.org/10.1023/A:1025448800782.
[8] NuDat 2.6, National Nuclear Data Center, Brookhaven National Laboratory, 2012. Available at URL < www.nndc.bnl.gov/nudat2/ > .
[9] B. Pritychenko, A. Sonzogni, Q-value calculator, NNDC, Brookhaven National Laboratory. Available from URL < http://www.nndc.bnl.gov/qcalc > .
[10] A.J. Koning, D. Rochman, S.C. van der Marck, J. Kopecky, J.Ch. Sublet, S. Pomp, H. Sjostrand, R. Forrest, E. Bauge, H. Henriksson, O. Cabellos, S. Goriely, J. Leppanen, H. Leeb, A. Plompen, R. Mills, TALYS-based evaluated nuclear data library. Available from URL < http://www.talys.eu/tendl-2017 > .
[11] O. Lebeda, V. Lozza, P. Schrock, J. Štursa, K. Zuber, Excitation functions of proton-

induced reactions on natural Nd in the 10–30 MeV energy range, and production of radionuclides relevant for double-β decay, Phys. Rev. C 85 (1) (2012), https://doi.org/10.1103/PhysRevC.85.014602.
[12] J. Červenák, O. Lebeda, Experimental cross-sections for proton-induced reaction on ^{nat}Mo, Nucl. Inst. Methods in Phys Res. B 380 (2016) 32–49, https://doi.org/10.1016/j.nimb.2016.05.006.
[13] R. Vandenbosch, J.R. Huizenga, Isomeric cross-section ratios for reactions producing the isomeric pair $Hg^{197,197m}$, Phys. Rev. 120 (4) (1960) 1313–1318, https://doi.org/10.1103/PhysRev. 120.1313.
[14] F. Szelecsényi, S. Takács, A. Fenyvesi, Z. Szücs, F. Tárkányi, S.-J. Heselius, J. Bergman, E. Boothe, Study of the ^{197}Au(p, pn)$^{196m1,\ m2,\ g}$Au and ^{197}Au(p, n)^{197m}Hg reactions and their application for proton beam monitoring in radioisotope production, Conf. Nucl. Data Sci. Techn., Trieste 2 (1997) 1483.
[15] F. Szelecsényi, G.F. Steyn, Z. Kovács, T.N. Van Der Walt, Application of Au + p nuclear reactions for proton beam monitoring up to 70 MeV, Conf. Nucl. Data Sci. Technology, Nice 2 (2007) 1259.
[16] E.K. Elmaghraby, K.F. Hassan, H. Omara, Z.A. Saleh, Production of the mercury-197 through proton induced reaction on gold, Appl. Radiat. Isot. 68 (12) (2010) 1694–1698, https://doi.org/10.1016/j.apradiso.2010.04.009.
[17] F. Ditrói, F. Tárkányi, S. Takács, A. Hermanne, Activation cross sections of proton induced nuclear reactions on gold up to 65 MeV, Appl. Radiat. Isot. 113 (2016) 96–109, https://doi.org/10.1016/j.apradiso.2016.04.020.
[18] L.F. Hansen, R.C. Jopson, H. Mark, C.D. Swift, Ta^{181}(p, n)W^{181} and Au^{197}(p, n) Hg^{197} excitation functions between 4 and 13 MeV, Nucl. Phys. 30 (1962) 389–398, https://doi.org/10.1016/0029-5582(62)90062-7.
[19] V. Gritsyna, A. Klyucharev, V. Remaev, L. Reshetova, Ratio of the cross sections for formation of the isomer and ground states of nuclei in the (p, n) reaction at energies from the threshold to 20 MeV, J. Exptl. Theoret. Phys. 17 (1963) 1186–1189.
[20] B. Satheesh, M.M. Musthafa, B.P. Singh, R. Prasad, Study of isomeric cross-section ratio and pre-equilibrium fraction in proton and alpha particle induced nuclear reactions on ^{197}Au, Int. Journal of Modern Physics, Part E 21 (6) (2012) 12, https://doi.org/10.1142/S0218301312500590 1250059.
[21] R.G. Thomas, W. Bartolini, Neutron production in Ag, Ta, Au, Pt, and Pb by the interaction of 7.5-14-MeV protons, Phys. Rev. 159 (4) (1967) 1022–1028, https://doi.org/10.1103/PhysRev.159.1022.
[22] G. Chodil, R.C. Jopson, H. Mark, C.D. Swift, R.G. Thomas, M.K. Yates, (p,n) and (p,2n) cross sections on nine elements between 7.0 and 15.0 MeV, Nucl. Phys. A 93 (1967) 648–672, https://doi.org/10.1016/0375-9474(67)90312-0.
[23] S.D. Schery, D.A. Lind, H.W. Fielding, C.D. Zafiratos, The (p, n) reaction to the isobaric analogue state of high-Z elements at 25.8 MeV, Nucl. Phys. A 234 (1) (1974) 109–129, https://doi.org/10.1016/0375-9474(74)90382-0.
[24] R. Michel, R. Bodemann, H. Busemann, R. Daunke, M. Gloris, H.-J. Lange, B. Klug, A. Krins, I. Leya, M. Lüpke, S. Neumann, H. Reinhardt, M. Schnatz-Büttgen, U. Herpers, Th. Schiekel, F. Sudbrock, B. Holmqvist, H. Condé, P. Malmborg, M. Suter, B. Dittrich-Hannen, P.-W. Kubik, H.-A. Synal, D. Filges, Cross sections for the production of residual nuclides by low- and medium-energy protons from the target elements C, N, O, Mg, Al, Si, Ca, Ti, V, Mn, Fe, Co, Ni, Cu, Sr, Y, Zr, Nb, Ba and Au, Nucl. Instrum. Methods Phys. Res. Section B 129 (2) (1997) 153–193, https://doi.org/10.1016/S0168-583X(97)00213-9.
[25] M. Bonardi, C. Birattari, Excitation functions for the Au(p,3n)^{195g,195m}Hg nuclear reactions and ^{195m}Hg, ^{195g}Hg/^{195m}Au generator yields, Int. J. Appl. Radiat. Isot. 35 (6) (1984) 564, https://doi.org/10.1016/0020-708x(84)90187-x.
[26] Y. Nagame, K. Sueki, S. Baba, H. Nakahara, Isomeric yield ratios in proton-, ^{3}He-, and alpha-particle-induced reactions on ^{197}Au, Phys. Rev. C 41 (3) (1990) 889–897, https://doi.org/10.1103/physrevc.41.889.
[27] M. Gusakow, Y. Legoux, H. Sergolle, Spallation reaction (p, n + p),(p,2n + p) and (p,3n) on gold. Production effective cross section at variation proton energy, Comptes Rendus De L'Academie Des Sciences 251 (1960) 70.
[28] T.M. Kavanagh, R.E. Bell, Cross-sections of (p,pxn) reactions in Au-197, Canad. J. Phys. 39 (8) (1961) 1172–1183, https://doi.org/10.1139/p61-132.

Publikácia III

Lebeda O., Červenák J.

Measurement of deuteron-induced nuclear reactions cross-sections on ^{197}Au and on ^{nat}Cu focused on the theranostic $^{197m,g}Hg$

Nucl. Instrum. Methods Phys. Res. B 461 (2019) 105-113
https://doi.org/10.1016/j.nimb.2019.09.034

Nuclear Inst. and Methods in Physics Research B 461 (2019) 105–113

Contents lists available at ScienceDirect

Nuclear Inst. and Methods in Physics Research B

journal homepage: www.elsevier.com/locate/nimb

Measurement of deuteron-induced nuclear reactions cross-sections on ^{197}Au and on ^{nat}Cu focused on the theranostic ^{197m,g}Hg

Ondřej Lebeda*, Jaroslav Červenák

Nuclear Physics Institute of the CAS, Husinec-Řež 130, 250 68 Řež, Czech Republic

ARTICLE INFO

Keywords:
^{197m}Hg
^{197g}Hg
Theranostic radionuclides
Cross-sections
Deuteron reactions
Gold target

ABSTRACT

Theranostic ^{197m,g}Hg of high specific activity may be produced by proton or deuteron activation of gold. The particle choice affects the isomeric ratio. In order to compare both projectiles, we re-measured cross-sections of the nuclear reactions ^{197}Au(d,x)^{197m}Hg, ^{197g}Hg, ^{198m}Au, ^{198g}Au, ^{196m2}Au, $^{196m1+g}$Au in the energy range of 8.3–19.7 MeV having employed usual stacked-foil method. The obtained values were compared with previously measured data and with prediction of the TALYS nuclear reaction model code adopted from the TENDL-2017 library. Experimental data were used for calculation of the thick target yields. The yields for the isomeric pair ^{197m,g}Hg were confronted with those for recently re-measured proton-induced reactions. We also provide a new data set for the reaction ^{nat}Cu(d,x)^{63}Zn.

1. Introduction

The isomers of ^{197}Hg, ^{197m}Hg (23.8 h) and ^{197g}Hg (64.14 h), represent an interesting theranostic radionuclide [1]. Each of them emits both imaging and therapeutic radiation, the former dominates in the decay of the ground state, while the latter in the decay of the metastable state [1,2]. Easy shielding allows for safe handling and transport of large activities, and well-known mercury chemistry offers several approaches, how to attach it to organic molecules [3]. High-specific activity ^{197m,g}Hg may be produced in the ^{197}Au(p,n) or ^{197}Au(d,2n) nuclear reactions, avoiding thus the issues related to the chemical toxicity of the element present in the reactor-produced mercury radioisotopes.

We have recently re-measured the excitation functions of the ^{197}Au (p,x) nuclear reactions and showed that the isomeric activity ratio *m/g* at the EOB may vary between 1.1 and 1.8, while keeping the yield of both at acceptable levels [4]. In the present work, we focused on the precise re-measurement of the deuteron-induced nuclear reactions on ^{197}Au up to 19.7 MeV deuteron energy available on the cyclotron U-120M at the Nuclear Physics Institute, Řež. As a "by-product" of the study, we employed the activation of the thin Cu degraders to measure new data for the ^{nat}Cu(d,x)^{63}Zn nuclear reaction that is potentially interesting for the beam monitoring.

2. Experimental

2.1. Target and irradiation

One stack composed of thirteen gold foils (99.9%, 7 μm thick, Goodfellow) interleaved with fourteen ^{nat}Ti foils (99.8%, 11.0 μm thick, AlfaAesar) and sixteen ^{nat}Cu degraders (10.6 μm thick, Goodfellow) was bombarded with deuterons on the external beam line of the cyclotron U-120M at the Nuclear Physics Institute of the Czech Academy of Sciences (CAS) in a Faraday-cup-like holder for one hour.

The areal density of the target nuclei in each foil was measured by weighing and the deuteron energy loss and straggling was determined with use of the program SRIM2008 [5]. The incident deuteron energy was set to 19.8 ± 0.2 MeV [6]. Beam current was recorded each second and integrated over the bombardment time t_b. The incident beam energy and recorded value of the beam current was slightly corrected by reconstruction of the monitoring excitation function ^{nat}Ti (d,x)^{48}V [7].

2.2. Activity measurement

Three energy and efficiency calibrated γ-ray spectrometers

* Corresponding author.
E-mail address: lebeda@ujf.cas.cz (O. Lebeda).

https://doi.org/10.1016/j.nimb.2019.09.034
Received 16 August 2019; Received in revised form 19 September 2019; Accepted 19 September 2019

Table 1
Data for the quantified radionuclides. *Q*-values for isomeric nuclei need to be lowered by the energy level of the isomer. *Q*-values for reactions where composed particles are emitted need to be increased by binding energy of the particle (d = np + 2.225 MeV, t = p2n + 8.482 MeV, ^{3}He = 2pn + 7.718 MeV, α = 2p2n + 28.296 MeV). Energies and intensities of gamma lines used for quantification of a radionuclide's activity are in bold. Uncertainties in the last digits are displayed in italics.

Radionuclide Spin	Half-life	Reaction	Q (MeV)	Threshold (MeV)	E_γ (keV)	I_γ (%)
^{197m}Hg 13/2+	23.8 h *1*	^{197}Au(d,2n)	−3.606	3.643	**133.98 *5***	**33.5**
					164.97 *7*	0.262
					279.01 *5*	6
^{197g}Hg 1/2−	64.14 h *5*				**191.437 *10***	**0.632 *21***
					268.78 *5*	0.0393 *19*
^{196m2}Au 12−	9.6 h *1*	^{197}Au(d,p2n)	−10.291	10.402	137.69 *3*	1.3 *4*
					147.81 *2*	**43.5**
					168.37 *2*	7.8 *5*
					188.27 *3*	30.0 *15*
					285.49 *7*	4.4 *5*
					316.19 *5*	3.0 *3*
^{196g}Au 2−	6.1669 d *6*				333.03 *5*	22.9 *9*
					355.73 *5*	**87**
					426.10 *8*	6.6
					129.79 *2*	2.90 *21*
^{198m}Au 12−	2.272 d *16*	^{197}Au(d,p)	4.288	0	97.21 *5*	69 *5*
					180.31 *5*	49 *5*
					204.10 *6*	39 *5*
					214.89 *5*	**77.3**
					333.82 *15*	18 *4*
^{198g}Au 2−	2.6941 d *2*				**411.80205 *17***	**95.62**
					675.8836 *7*	0.805 *5*
^{48}V	15.9735 d *25*	^{47}Ti(d,n)	4.605	0	944.130 *4*	7.870 *7*
		^{48}Ti(d,2n)	−7.022	7.317	**983.525 *4***	**99.98 *4***
		^{49}Ti(d,3n)	−15.164	15.788	**1312.106 *8***	**98.2 *3***
^{46}Sc	83.79 d *4*	^{48}Ti(d,α)	3.979	0	**889.277 *3***	**99.984 *1***
		^{49}Ti(d,αn)	−4.163	4.334	**1120.545 *4***	**99.987 *1***
		^{50}Ti(d,α2n)	−15.102	15.711		
^{63}Zn	38.47 min *5*	^{63}Cu(d,2n)	−6.373	6.577	**669.62 *5***	**8.20 *32***
					962.06 *4*	**6.50 *40***

equipped with HPGe detectors (GMX45-Plus, Ortec; GC2019, Canberra and GEM40P4-83, Ortec) were used for identification and quantification of the radionuclides in the activated foils. The calibration was performed with a set of standards (^{241}Am, ^{152}Eu, ^{137}Cs, ^{133}Ba and ^{60}Co) for various distances sample-detector (150, 200, 400, 600, 1000 and 1600 mm). The whole energy range for a given distance sample-detector was covered with a polynomial of the fifth degree ($\ln \eta = f(\ln E)$, where η is detection efficiency and E is the energy of a gamma line). Linear fit was used for the γ-ray energies higher than 240 keV. The true coincidence correction was negligible for all the used sample-detector distances.

The activated gold foils were measured four or five times at various distances sample-detector in order to optimize quantification of radionuclides with various half-lives and intensities of the γ-lines. The Ti monitors were measured a month post EOB in order to avoid the interference from the emissions of ^{48}Sc to the activity of ^{48}V. The ^{48}V and ^{46}Sc activity fractions ejected from the monitor to the following Au foil were measured and added to the activity measured in the monitor itself (1.4–3.2% of ^{48}V and 2.5–3.9% of ^{46}Sc born in the foils was ejected, depending on the beam energy in the foil). The acquired γ-ray spectra were evaluated in the program DEIMOS [8].

The decay data used for the activity calculations and the nuclear reaction data relevant for the experiment are summarized in Table 1. The decay data were adopted from the NuDat2 database [9] and from the Firestone's Table of Isotopes [2]. Q-values and thresholds of the reactions were calculated via Q-calc program online [10].

2.3. Calculation of cross-sections, their uncertainties, thick target yields and prediction of excitation functions

Cross-sections were deduced from the activation formula (Eq. (1)):

$$\sigma = \frac{P_\gamma}{I_\gamma \eta t_m} \frac{\lambda t_r}{1 - e^{-\lambda t_r}} e^{\lambda t_c} \frac{Aze}{d\rho N_A I \left(1 - e^{-\lambda t_b}\right)}, \quad (1)$$

where σ is cross-section for formation of a radionuclide at the energy in the middle of the foil (cm^2), P_γ is net peak area of the γ-line used for the radionuclide's quantification, I_γ is intensity of this γ-line, η is detection efficiency for this γ-line, t_m is life time of the measurement (h), t_r is real time of the measurement (including the dead time) (h), λ is decay constant of a radionuclide (h^{-1}), t_c is cooling time between the EOB and the start of the measurement (h), A is atomic weight of the foil's metal (g/mol), z is deuteron charge (z = 1), e is elementary charge (1.602177×10^{-19}C), d is foil's thickness (cm), ρ is density of the foil's metal (g/cm^3), N_A is Avogadro's number (6.022137×10^{23} mol^{-1}), I is beam current (A) and t_b is irradiation time (h).

Total relative cross-section uncertainty was calculated as the square root of the sum of the squares of partial relative uncertainties of the parameters in the activation formula summarized below:

- detection efficiency for a gamma line selected for the activity calculation (ca 3%)
- emission probability of a gamma line used in the activity calculation

(usually < 5%)
- net peak area of a gamma line selected for the activity calculation (< 10%)
- beam current (ca 6%)
- foil's thickness (< 2%)

The measured cross-sections obtained in this work were compared with previously published data and with theoretical prediction of the TALYS nuclear reaction model code adopted from the TENDL-2017 library [11].

2.4. Interference corrections

In the measured γ-ray spectra, no interferences in the sense of overlapping peaks energy occurred, and the only interference to be taken into account was the contribution of the isomeric parent nuclei decay to daughter nuclei ground state activity in the generator systems formed in the target foils. The measured activity of the daughter ground state was decreased by the activity due to decay of a parent radionuclide during the irradiation (Eq. (2)) and after the EOB (Eq. (3)) in order to obtain the ground state activity formed directly in the nuclear reaction [12,13].

$$A_2^{EOB} = f\frac{d\rho N_A \sigma I}{Aze}\left(1 - \frac{\lambda_2}{\lambda_2 - \lambda_1}e^{-\lambda_1 t_b} + \frac{\lambda_1}{\lambda_2 - \lambda_1}e^{-\lambda_2 t_b}\right) \quad (2)$$

$$A_2 = f\frac{\lambda_2}{\lambda_2 - \lambda_1}A_1^{EOB}(e^{-\lambda_1 t} - e^{-\lambda_2 t}) + A_2^{EOB}e^{-\lambda_2 t} \quad (3)$$

3. Results and discussion

3.1. Beam energy and current

The reconstruction of the monitoring reaction ^{nat}Ti(d,x)^{48}V excitation function using the recommended cross-sections [7] is displayed in Fig. 1. We also reconstructed the excitation function for the formation of ^{46}Sc born in the Ti foils in parallel with ^{48}V (see Fig. 2) and compared the cross-sections with the recent fit of the available experimental data [14]. Reconstruction of the ^{nat}Ti(d,x)^{48}V monitoring reaction resulted in a slight correction of the incident beam energy (19.8 → 20.0 MeV) and of the recorded beam current (0.553 → 0.568 μA). These minor corrections show that the beam parameters are close to the primary settings, being within the estimated uncertainties.

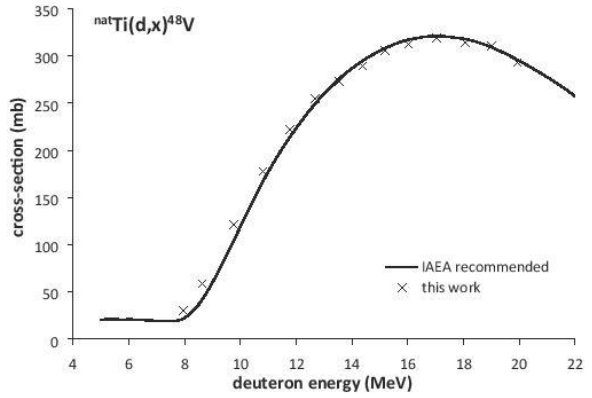

Fig. 1. Reconstructed excitation function of the monitoring reaction ^{nat}Ti(d,x)^{48}V.

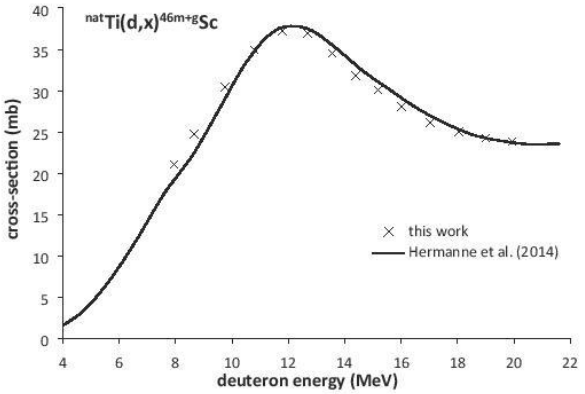

Fig. 2. Excitation function of the proposed monitoring reaction ^{nat}Ti(d,x)$^{46m+g}$Sc – our data in comparison with the fit of Hermanne et al. (2014) [14].

3.2. Measured cross-sections and prediction of excitation functions

The measured cross-sections together with the previously published data and the excitation functions predicted by TALYS code (TENDL-2017 library) [11] are displayed in Figs. 3–12. Previously measured cross-sections were corrected for the difference between the emission probabilities of the radiation used by the authors for the evaluation, and the currently adopted values. Detailed description of the applied corrections is provided for ^{197m}Hg and particularly for ^{197g}Hg, where the available experimental data are too discrepant if taken as published. Other corrections were straightforward. The cross-sections obtained in our experiment including the uncertainties are summarized in Tables 2 and 3.

3.2.1. Cross-sections for the ^{nat}Cu(d,x)^{63}Zn reactions

The presence of thin copper degraders (10.6 μm) in the stack naturally suggested to exploit their activation and investigate their monitoring potential. After disassembling the irradiated target, the copper foils were immediately measured on a separate γ-ray spectrometer in order to quantify the activity of the short-lived ^{63}Zn. The deduced cross-sections calculated with use of both prominent γ-lines accompanying the decay of ^{63}Zn are summarized in Table 2 and displayed in Fig. 3. They can be assigned solely to the ^{63}Cu(d,2n)^{63}Zn nuclear reaction, because the (d,4n) reaction on the second stable Cu isotope, ^{65}Cu, has threshold of 24.95 MeV [10]. The data in Table 3 are, therefore, independent elemental cross-sections that can be easily converted to independent isotopic cross-sections dividing them by the ^{63}Cu abundance in ^{nat}Cu (0.6915). Agreement between the activities of ^{63}Zn calculated via both emitted γ-rays is very good, well within the expected uncertainties, although the quantification via the 662.62 keV γ-line seems to provide systematically slightly higher values than that via the 962.06 keV γ-line.

Previously measured data up to 20 MeV [15–17] are scarce and inconsistent. The single point of Bartell et al. (1950) is probably shifted to higher energy (the last foil in the stack irradiated with 194 MeV deuterons), data of Fulmer and Williams (1970) are systematically larger, and the recently provided cross-sections of Takács et al. (2006) show the best agreement with our results, but almost all are shifted to higher values. In contrast, prediction of the excitation function adopted from the TENDL-2017 library up to 14 MeV agrees almost perfectly with our measurement, but then decreases faster to lower amplitudes. The reaction has potential as a deuteron monitoring reaction, but more independent experiments are necessary to propose recommended cross-section for it.

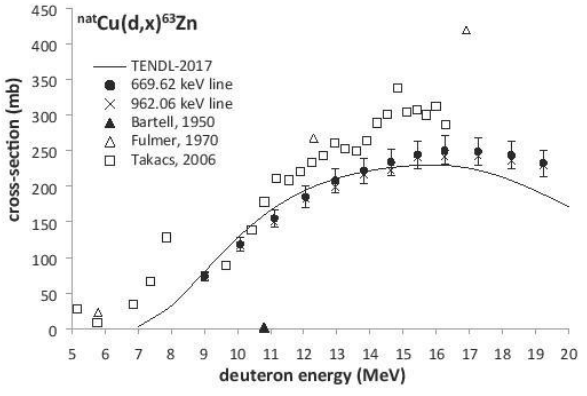

Fig. 3. Cross-sections of the possible monitoring reaction $^{nat}Cu(d,x)^{63}Zn$ – our values in comparison with the previously published data [15–17] and the TALYS prediction taken from the TENDL-2017 library in the measured energy range.

3.2.2. Cross-sections for the $^{197}Au(d,2n)^{197m}Hg$

Isomer ^{197m}Hg was quantified via its dominant 133.98 keV γ-line (33.5% per decay) and the cross-sections are displayed in Fig. 4. Our results agree well with practically all the previously reported measurements of Vandenbosch and Huizenga (1960) [18], Chevarier et al. (1970) [19], Khrisanfov et al. (1973) [20], Long et al. (1985) [21], Wenrong and Hanlin (1989) [22], Tárkányi et al. (2011) [23] and Tárkányi et al. (2015) [24]. The published data in Fig. 4 were corrected for the minor differences in the emission probability of the 133.98 keV γ-line used by their authors for the quantification of ^{197m}Hg activity – 0.338 [18], 0.313 [19] and 0.341 [21,22]. The cross-sections of [20] were used as published, because the authors don't provide the emission probabilities they used. The data of [24] seem to be shifted towards higher energies, probably the effect of the increased uncertainty in the last foils of a long stack irradiated with 50 MeV deuterons. The data of [18,19] are slightly higher for the energies following the maximum of the excitation function. The TALYS prediction overestimates all the experimental data almost twice at the maximum position and suggests slower, more regular decrease of the excitation function around 20 MeV, overestimating the experimental data by a factor of three.

3.2.3. Cross-sections for the $^{197}Au(d,2n)^{197g}Hg$

The ground state ^{197g}Hg was quantified via its γ-line 191.44 keV (low intensity of 0.632% per decay) and its activity was corrected for

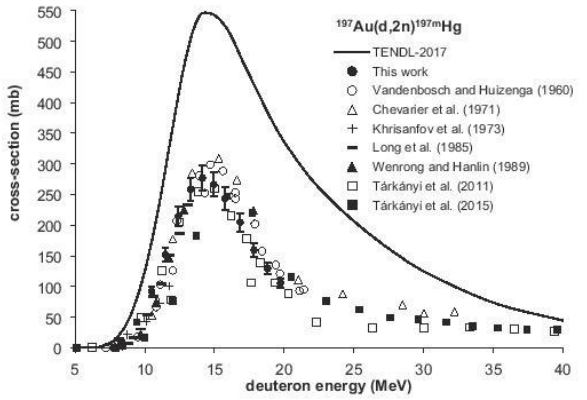

Fig. 4. Cross-sections of the $^{197}Au(d,2n)^{197m}Hg$ reaction – the measured values in comparison with the previously published data [18–24] and the TALYS prediction adopted from the TENDL-2017 library.

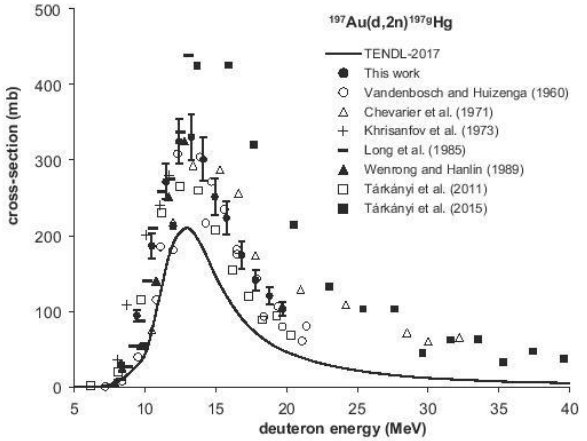

Fig. 5. Cross-sections of the $^{197}Au(d,2n)^{197g}Hg$ reaction – the measured values in comparison with the previously published data [18–24] and the TALYS prediction adopted from the TENDL-2017 library.

the contribution of ^{197m}Hg decay as described in the Section 2.4. Results are displayed in Fig. 5. The originally most scattered data sets were brought into better agreement with use of detailed corrections. The measurements of Vandenbosch and Huizenga [18], Chevarier et al. [19] and Long et al. [21] were slightly corrected for the difference in the 77 keV peak emission probability used by the authors (0.283, 0.313, 0.306) and the sum of the emission probabilities of the contributing γ-line 77.35 keV of ^{197g}Hg and interfering Au X-rays ($K_{\beta 3}$, $K_{\beta 1}$ and $K_{\beta 5}$) adopted from [2] that is equal to 0.316. The data of Wenrong and Hanlin [22] were corrected for the lower emission probability of the 190.44 keV line they used (0.49%). Moreover, the authors of the last two publications [23,24] confirmed in personal communication that the tabulated cross-sections for the formation of ^{197g}Hg were actually calculated as $\sigma_g + f\sigma_m$, where f is the transition probability of the ^{197m}Hg to the ground state (0.914). The same seems to be true for the works [21,22]. After deducing the σ_g itself, we found much better agreement with the data of [21–23] except the last point of [21]. In contrast, the cross-sections of [19,24] exceed remarkably our data from the maximum forward and seem to be slightly shifted towards higher energies. In the case of [24], it may be again partly due to the effect of the long stack and high incident beam energy. Prediction of TALYS underestimates practically all the reported data by roughly one third at the

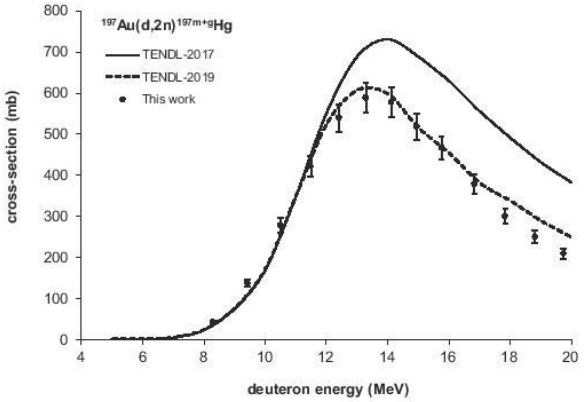

Fig. 6. Cross-sections of the $^{197}Au(d,2n)^{197m+g}Hg$ reaction – the sum of the measured cross-sections for the formation of the metastable state and the ground state in comparison with the TALYS prediction adopted from the TENDL-2017 and recently released TENDL-2019 library.

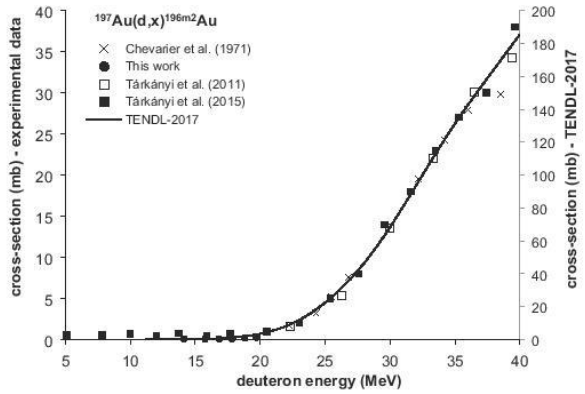

Fig. 7. Cross-sections of the ^{197}Au(d,p2n)^{196m2}Au reaction – the measured values in comparison with the previously published data [19,23,24] and the TALYS prediction adopted from the TENDL-2017 library.

maximum, although the shape of the excitation function is similar to the experimental data.

A recent paper of Sudár and Qaim [25] has demonstrated that the isomeric cross-section ratio is strongly affected by the $\Theta_{eff}/\Theta_{rig}$ parameter of the spin cut-off factor and it is mass number dependent. As it is not reflected in the TALYS code, we also compared the simple sum of the measured cross-sections and predicted cross-sections for the formation of the metastable and the ground states, see Fig. 6. The result shows significantly better agreement between TALYS and the experimental data, particularly if compared with recently released TENDL-2019. However, it is true only for the ^{197}Au(d,2n) reaction – neither summing of *m* and *g* states cross-sections, nor using TENDL-2019 data results in better agreement between experiment and theory in the case of the ^{197}Au(d,p2n) and ^{197}Au(d,p) reactions treated below.

3.2.4. Cross-sections for the ^{197}Au(d,p2n)^{196m2}Au

The longer-lived isomer of ^{196}Au – ^{196m2}Au – was measured via its 147.81 keV γ-line with high intensity of 43.5%. The deduced cross-sections are shown in Fig. 7 – all the experimental data [19,23,24] seem to agree very well, and the TENDL-2017 perfectly follows their shape, but the predicted amplitude is five times higher (note the extra axis). However, detail of the data below 25 MeV displayed in Fig. 8 illustrates large disagreement between our experiment and data of Tárkányi et al. [24]. It doesn't seem to be explained by a simple energy shift, and rather suggests energy straggling and/or possible contamination of the last foils with highly activated foils during disassembly of the stack.

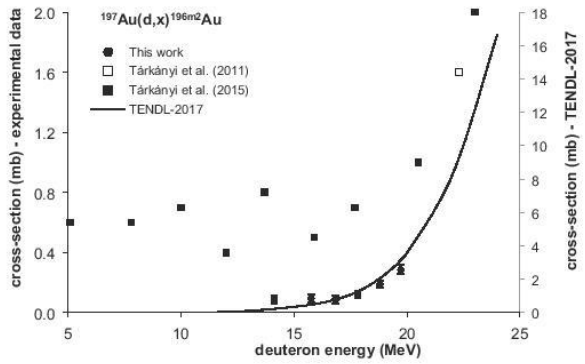

Fig. 8. Cross-sections of the ^{197}Au(d,p2n)^{196m2}Au reaction – detail illustrating rather large scattering of the available experimental data for the projectile's energy below 20 MeV.

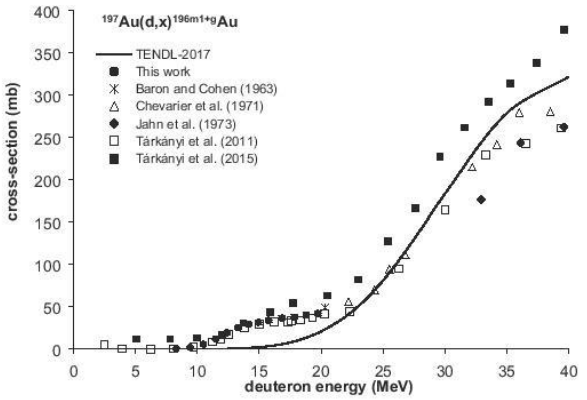

Fig. 9. Cross-sections of the ^{197}Au(d,p2n)$^{196m1+g}$Au reaction – the measured values in comparison with the previously published data [19,23–26] and the TALYS prediction adopted from the TENDL-2017 library.

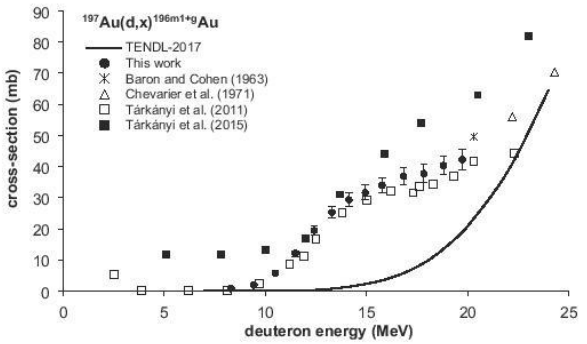

Fig. 10. Cross-sections of the ^{197}Au(d,p2n)$^{196m1+g}$Au reaction – detail illustrating rather large scattering of the available experimental data for the projectile's energy below 20 MeV.

3.2.5. Cross-sections for the ^{197}Au(d,p2n)$^{196m1+g}$Au

The cross-sections for the formation of ^{196g}Au were deduced from the measurement of its dominant 355.73 keV γ-line (emission probability of 87% per decay). Although the activity of the ground state was corrected for the small contribution of ^{196m2}Au decay (cf. 2.4), the cross-sections are definitely cumulative regarding the short-lived

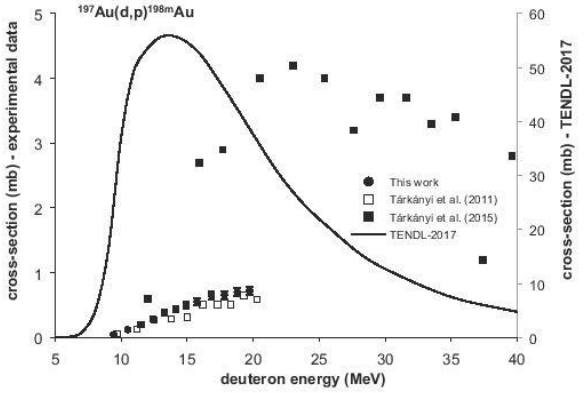

Fig. 11. Cross-sections of the ^{197}Au(d,p)^{198m}Au reaction – the measured values in comparison with the previously published data [23,24] and the TALYS prediction adopted from the TENDL-2017 library.

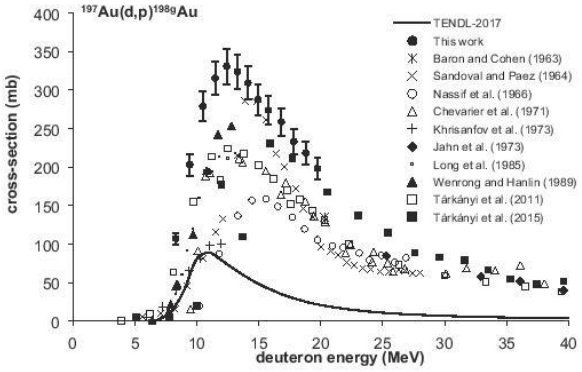

Fig. 12. Cross-sections of the ^{197}Au(d,p)^{198g}Au reaction – the measured values in comparison with the previously published data [19–28] and the TALYS prediction adopted from the TENDL-2017 library.

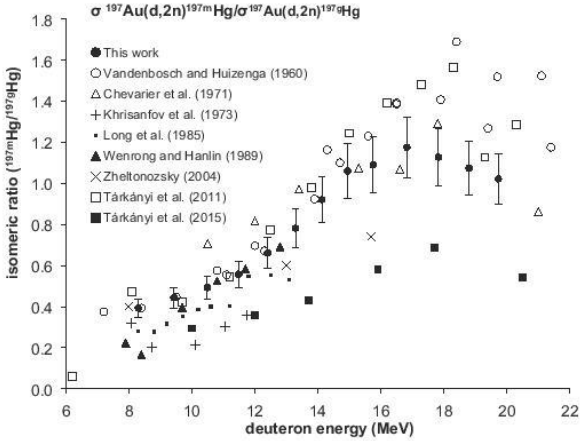

Fig. 13. Isomeric cross-section ratios for the formation of ^{197m}Hg and ^{197g}Hg in the ^{197}Au(d,2n) reaction.

Table 2
Cross-sections for the ^{nat}Cu(d,x)^{63}Zn reactions measured in this work.

E_d (MeV)	σ (mb) for ^{nat}Cu(d,x)^{63}Zn	
	via 669.62 keV	via 962.06 keV
19.22 ± 0.22	232 ± 18	229 ± 17
18.26 ± 0.25	244 ± 19	236 ± 17
17.26 ± 0.28	249 ± 20	243 ± 18
16.25 ± 0.31	251 ± 20	242 ± 18
15.43 ± 0.34	244 ± 19	241 ± 18
14.63 ± 0.37	234 ± 19	222 ± 16
13.81 ± 0.40	222 ± 18	217 ± 16
12.95 ± 0.44	208 ± 17	199 ± 15
12.06 ± 0.48	185 ± 15	182 ± 13
11.11 ± 0.53	155 ± 12	150 ± 11
10.08 ± 0.59	118.3 ± 9.4	116.8 ± 8.6
9.01 ± 0.66	73.7 ± 5.9	74.0 ± 5.4

isomer ^{196m1}Au ($T_{½}$ = 8.1 s), i.e. the data are related to $^{196m1+g}$Au. Results are displayed in Fig. 9. In general, the prediction of TENDL-2017 follows the course of all the available experimental data [19,23,24,26,27], however, in the region below 20 MeV significantly underestimates them, as obvious from the detail of the excitation function (see Fig. 10). Our results agree very well with the work of Tárkányi et al. [23] obtained with similar incident energy, while the data of their later work [24] from the single bombardment of a long stack with 50 MeV incident deuteron energy differ again from our cross-sections, being remarkably larger except two points.

3.2.6. Cross-sections for the ^{197}Au(d,p)^{198m}Au

The activity of the isomer ^{198m}Au was determined via its prominent 214.89 keV γ-line (emission probability of 77.3% per decay). The deduced cross-sections are displayed in Fig. 11. From the only two other published data sets [23,24], our data agree very well with the earlier work [23], while the recent [24] provides several times higher cross-section values. The cause of this discrepancy was suggested in the above Sections 3.2.4 and 3.2.5. The TENDL-2017 prediction is by an order of magnitude higher than measured values, and it doesn't correspond to the experimental data neither in the maximum position, nor in the shape.

3.2.7. Cross-sections for the ^{197}Au(d,p)^{198g}Au

The activity of the ground state ^{198g}Au was determined via its prominent 411.80 keV γ-line (emission probability of 95.62% per decay). Contribution of the isomeric state ^{198m}Au to the activity of the ground state is negligible. The measured cross-sections are displayed in Fig. 12. There are plenty of reported data available [19–24,26–29]. Although the activity of ^{198g}Au is easy to quantify precisely and its decay data are well established for decades, the experimental material is surprisingly scattered. Our cross-sections are systematically higher than all the other data sets except few points of Sandoval and Paez (1964) [28] and Tárkányi et al. (2015) [24]. The published data agree more or less in the shape, just Nassif et al. (1963) [29] and Sandoval

Table 3
Cross-sections for formation of Hg and Au radionuclides in the ^{197}Au(d,x) reactions measured in this work.

E_d (MeV)	σ (mb)					
	^{197m}Hg	^{197g}Hg	^{196m2}Au	$^{196m1+g}$Au	^{198m}Au	^{198g}Au
19.73 ± 0.21	105.6 ± 7.9	103.4 ± 9.7	0.285 ± 0.031	42.3 ± 3.2	0.720 ± 0.063	198 ± 14
18.80 ± 0.23	129.4 ± 9.7	121 ± 12	0.188 ± 0.025	40.3 ± 3.0	0.699 ± 0.063	218 ± 15
17.83 ± 0.26	159 ± 12	141 ± 14	0.120 ± 0.019	37.8 ± 2.8	0.655 ± 0.059	234 ± 16
16.83 ± 0.29	205 ± 15	174 ± 18	0.085 ± 0.028	36.8 ± 2.8	0.656 ± 0.061	259 ± 18
15.76 ± 0.33	244 ± 18	224 ± 22	0.093 ± 0.028	34.0 ± 2.6	0.547 ± 0.052	274 ± 19
14.94 ± 0.36	267 ± 20	252 ± 25		31.6 ± 2.4	0.496 ± 0.048	288 ± 20
14.13 ± 0.39	277 ± 21	301 ± 29	0.088 ± 0.027	29.3 ± 2.2	0.443 ± 0.045	310 ± 21
13.29 ± 0.42	258 ± 19	331 ± 31		25.2 ± 1.9	0.382 ± 0.042	324 ± 22
12.41 ± 0.46	215 ± 16	325 ± 29		19.5 ± 1.5	0.290 ± 0.037	331 ± 23
11.48 ± 0.51	151 ± 11	271 ± 24		12.07 ± 0.91	0.198 ± 0.033	315 ± 22
10.49 ± 0.56	92.0 ± 6.9	187 ± 16		5.71 ± 0.43	0.121 ± 0.025	279 ± 19
9.43 ± 0.63	42.0 ± 3.2	94.7 ± 7.9		1.93 ± 0.15	0.046 ± 0.010	203 ± 14
8.30 ± 0.71	11.89 ± 0.89	30.2 ± 2.7		0.819 ± 0.063		107.5 ± 7.5

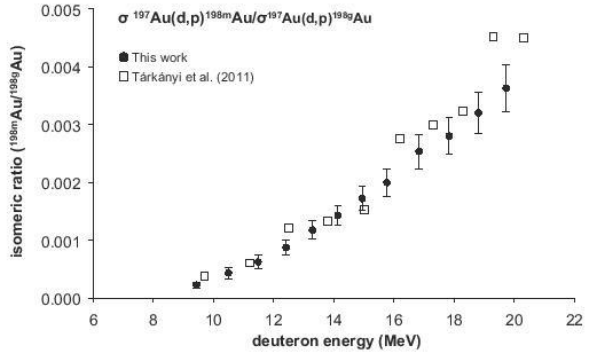

Fig. 14. Isomeric cross-section ratios for the formation of ^{198m}Au and ^{198g}Au in the ^{197}Au(d,p) reaction.

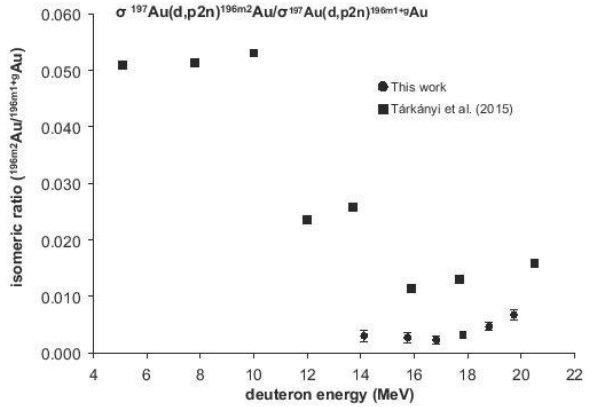

Fig. 15. Isomeric cross-section ratios for the formation of ^{196m2}Au and $^{196m1+g}$Au in the ^{197}Au(d,p2n) reactions.

and Paez (1964) [28] show the maximum at the slightly higher energy (1.5–2.5 MeV). There is definitely not a single cause of the described discrepancies, and their explanation would probably result in mere conjectures. TENDL-2017 underestimates almost all the published data, predicts maximum at the energy lower for 1.5 MeV compared to majority of the experimental data and shows less steep decrease of the excitation function.

3.3. Isomeric cross-section ratios

The isomeric cross-section ratios σ_m/σ_g as a function of energy were calculated for all the three isomeric pairs quantified in the target, including the uncertainties. They are compared with the ratios of the cross-sections provided by the other authors in the Figs. 13–15. The previously published cross-sections were corrected as described above before calculating their ratio. The three ratio values published by Zheltonozhsky et al. (2004) [30] were included among the σ_m/σ_g ratios for the isomeric pair ^{197m}Hg/^{197g}Hg.

3.3.1. Isomeric cross-section ratio for formation of ^{197m}Hg/^{197g}Hg

All the data follow very roughly similar shape, they are, however, rather scattered, viz. Fig. 13. From the available ratios [18–24,30], the best agreement was found with Vandenbosch and Huizenga [18], Wenrong and Hanlin [22] and Tárkányi et al. (2011) [23] up to ca 15 MeV, where the data of [18] and [23] become to be remarkably

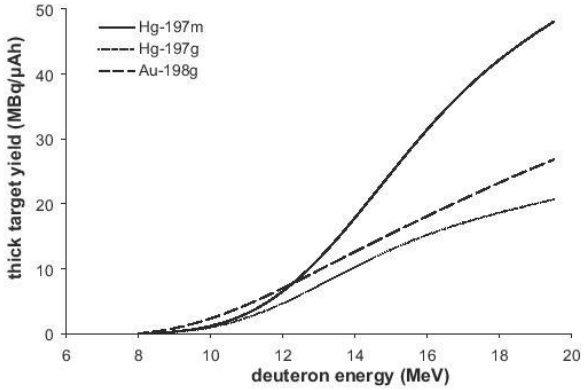

Fig. 16. Thick target yield (production rate) for ^{197m}Hg, ^{197g}Hg and $^{198m+g}$Au.

larger. Fair agreement was found also with the data of Chevarier et al. [19] and the first two points of [29]. Our data suggest gradual growing of the σ_m/σ_g ratio with the maximum of ca 1.18 at 17 MeV.

3.3.2. Isomeric cross-section ratio for formation of ^{198m}Au/^{198g}Au

As obvious from Fig. 14, the only reported data for this isomeric pair are those of Tárkányi et al. (2011) [23]. They agree very well in both the shape and the magnitude with our data, showing steady increase in the measured energy range. Formation of the metastable state is obviously suppressed.

3.3.3. Isomeric cross-section ratio for formation of ^{196m2}Au/$^{196m1+g}$Au

In the case of the isotope ^{196}Au, we may measure only the $\sigma_{m2}/\sigma_{m1+g}$ isomeric ratio due to the short half-life of ^{196m1}Au. Like in the case of the ^{198m}Au/^{198g}Au, we found just a single reported data set covering both isomers in the work of Tárkányi et al. (2015) [24]. The data displayed in Fig. 15 clearly reveal remarkable scattering of their data [24]. Our measurement suggests existence of an inconspicuous minimum around 17 MeV. Similarly to ^{198}Au, the formation of the ground state seems to be highly enhanced.

3.4. Thick target yields

We deduced the thick target yields from the measured cross-section for ^{197m}Hg, ^{197g}Hg, ^{198m}Au, ^{198g}Au, ^{196m2}Au, $^{196m1+g}$Au by their fitting with one or two polynomial fits and integrating the fit with use of the stopping power of deuterons in gold [5]. The calculated yields are

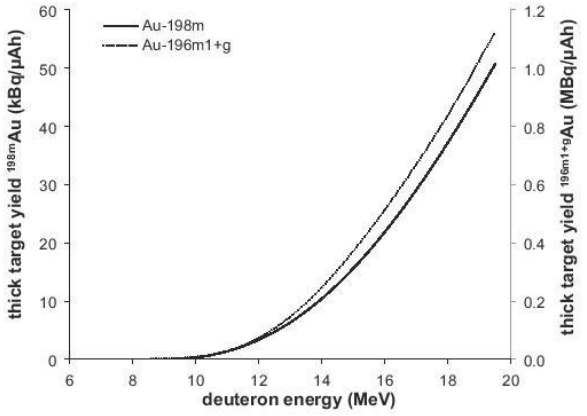

Fig. 17. Thick target yield (production rate) for ^{198m}Au and $^{196m1+g}$Au.

shown in Figs. 16 and 17.

3.4.1. Thick target yields for formation of ^{197m}Hg and ^{197g}Hg

With deuterons, one always produces ^{197m,g}Hg with traces of stable ^{198}Hg and ^{196}Hg. However, the mass of these mercury isotopes originating in the (d,n) and (d,3n) nuclear reactions is comparable to that of ^{197m,g}Hg, and thus negligible regarding chemical toxicity (10 GBq of ^{197m}Hg corresponds to 0.40 μg, and 10 GBq of ^{197g}Hg to 1.1 μg of the metal). Daily average intake of inorganic Hg in the absence of the occupational exposure is in order of several micrograms, usually not exceeding 10 μg/day [31]. WHO estimated a tolerable intake of total mercury to be 2 μg/kg of body weight per day, while the strictest U.S. Environmental Protection Agency (EPA) recommends consuming maximum of 0.1 μg/kg of body weight per day – it is anyhow 5 μg Hg intake for 50 kg person. Like in the case of the proton activation of gold, one may prepare high specific activity ^{197m}Hg/^{197g}Hg free of any radionuclidic impurities just by chemical separation of mercury from an Au target [4].

The ^{197m}Hg/^{197g}Hg activity ratio at the EOB for e.g. 10 h long irradiation may vary between ca 1.1 to ca 2.5 using various beam energy losses (incident 12–19.5 MeV, leaving energy 8–18 MeV). Shorter bombardment time of 5 h enhances this ratio to 2.75. Further shortening brings only small effect, while reducing the EOB activities. One may easily reach the ^{197m}Hg/^{197g}Hg activity ratio of 2.3 at the EOB, producing more than 10 GBq of the ground state in 10 h with 100 μA deuteron beam of 19.5 MeV energy. The contribution of the ^{197m}Hg decay to the EOB activity of ^{197g}Hg during the irradiation was taken into account in the calculations.

In general, deuterons provide higher ^{197m}Hg/^{197g}Hg EOB activity ratio than protons under the comparable bombardment conditions. It is desirable for potential therapeutic applications [1]. Moreover, the thick target yields of both isomers are much larger in the case of the ^{197}Au (d,2n) reaction compared to the ^{197}Au(p,n) reaction – the production rate of ^{197m}Hg/^{197g}Hg for the 19.5 → 8.0 MeV deuterons is 48.0 and 20.3 MBq/μAh, respectively, for the 27 → 6.5 MeV protons it is only 13.7 and 7.5 MBq/μAh, respectively [4].

4. Conclusion

In this work, we provide new experimental data for the deuteron-induced nuclear reactions on ^{197}Au resulting in ^{197m}Hg, ^{197g}Hg, ^{198m}Au, ^{198g}Au, ^{196m2}Au and $^{196m1+g}$Au in the energy range of 8.3–19.7 MeV. Attention was paid to the correction of the previously published data, in particular for the formation of ^{197m}Hg and ^{197g}Hg, for the differences in the γ-line emission probabilities used by the authors, and to the character of the published cross-sections (independent versus cumulative). The experimental material was juxtaposed to the theoretical predictions of the TALYS nuclear reaction model code adopted from the TENDL-2017 online library. The isomeric ratios for the three isomeric pairs found in the target were calculated from the measured cross-sections, and the thick target yields for all the radionuclides quantified in the experiment were deduced. The obtained results demonstrate superiority of deuterons over protons in the production of ^{197m}Hg/^{197g}Hg in terms of the yield and the practically achievable *m/g* activity ratio.

Declaration of Competing Interest

The authors declare that they have no known competing financial interests or personal relationships that could have appeared to influence the work reported in this paper.

Acknowledgement

The work was supported from ERDF/ESF project “CANAM-OP” of the Ministry of Education, Youth and Sports of the Czech Republic (No. CZ.02.1.01/0.0/0.0/16_013/0001812).

References

[1] R. Freudenberg, R. Apolle, M. Walther, H. Hartmann, J. Kotzerke, Molecular imaging using the theranostic agent $^{197(m)}$Hg: phantom measurements and Monte Carlo simulations, Eur. J. Nucl. Med. Mol. Imaging 5 (15) (2018), https://doi.org/10.1186/s40658-018-0216-9.
[2] S.Y.F. Chu, L.P. Ekström, R.B. Firestone, The Lund/LBNL nuclear data search, 1999. Available at the web page < http://ie.lbl.gov/toi/ > .
[3] M. Walther, S. Preusche, S. Bartel, G. Wunderlich, R. Freudenberg, J. Steinbach, H.-J. Pietzsch, Theranostic mercury: $^{197(m)}$Hg with high specific activity for imaging and therapy, Appl. Radiat. Isot. 97 (2015) 177–181, https://doi.org/10.1016/j.apradiso.2015.01.001.
[4] J. Červenák, O. Lebeda, Measurement of cross-sections of proton-induced nuclear reactions on ^{197}Au focused on the production of the theranostic pair ^{197m,g}Hg, Nucl. Inst. Methods in Phys. Res. B (2019), https://doi.org/10.1016/j.nimb.2019.08.006.
[5] J.F. Ziegler, M.D. Ziegler, J.P. Biersack, SRIM2010 Code, Available at URL < http://www.srim.org/ > .
[6] M. Čihák, O. Lebeda, J. Štursa, Beam dynamic simulation in the isochronous cyclotron U-120M, Proceedings of the Eighteenth International Conference on Cyclotrons and their Applications, CYCLOTRONS 2007, (2007) Giardini Naxos, Italy.
[7] K. Gul, A. Hermanne, M.G. Mustafa, F.M. Nortier, P. Obložínský, S.M. Qaim, B. Scholten, Yu. Shubin, S. Takács, F. Tárkányi, Z. Zhuang, Charged particle cross section database for medical radionuclide production: diagnostic radionuclides and monitor reactions, in: IAEA-TECDOC-1211, IAEA, Vienna, 2001. Update available from URL: < www.nds.iaea.org/medical/ > .
[8] J. Frána, Program DEIMOS32 for gamma-ray spectra evaluation, J. Radioanal. Nucl. Chem. 257 (3) (2003) 583–587, https://doi.org/10.1023/A:1025448800782.
[9] NuDat 2.6, National Nuclear Data Center, Brookhaven National Laboratory, 2012. Available at URL < www.nndc.bnl.gov/nudat2/ > .
[10] B. Pritychenko, A. Sonzogni, Q-value calculator, NNDC, Brookhaven National Laboratory. Available from URL < http://www.nndc.bnl.gov/qcalc > .
[11] A.J. Koning, D. Rochman, S.C. van der Marck, J. Kopecky, J.Ch. Sublet, S. Pomp, H. Sjostrand, R. Forrest, E. Bauge, H. Henriksson, O. Cabellos, S. Goriely, J. Leppanen, H. Leeb, A. Plompen, R. Mills, TALYS-based evaluated nuclear data library. Available from URL < http://www.talys.eu/tendl-2017 > .
[12] O. Lebeda, V. Lozza, P. Schrock, J. Štursa, K. Zuber, Excitation functions of proton-induced reactions on natural Nd in the 10–30 MeV energy range, and production of radionuclides relevant for double-β decay, Phys. Rev. C 85 (1) (2012) 12, https://doi.org/10.1103/PhysRevC.85.014602 014602.
[13] J. Červenák, O. Lebeda, Experimental cross-sections for proton-induced reaction on ^{nat}Mo, Nucl. Inst. Methods Phys. Res. B 380 (2016) 32–49, https://doi.org/10.1016/j.nimb.2016.05.006.
[14] A. Hermanne, F. Tárkányi, S. Takács, F. Ditrói, N. Amjed, Excitation functions for production of ^{46}Sc by proton and deuteron beams in ^{nat}Ti: a basis for additional monitor reactions, Nucl. Inst. Methods Phys. Res. B 338 (1) (2014) 31–41, https://doi.org/10.1016/j.nimb.2014.07.026.
[15] F.O. Bartell, A.C. Helmholz, S.D. Softky, D.B. Stewart, Excitation functions for spallation reaction on Cu*, Phys. Rev. 80 (6) (1950) 1006–1010, https://doi.org/10.1103/PhysRev. 80.1006.
[16] C.B. Fulmer, I.R. Williams, Excitation functions for radioactive nucleides produced by deuteron-induced reactions in copper, Nucl. Phys. A 155 (1970) 40–48, https://doi.org/10.1016/0375-9474(70)90077-1.
[17] S. Takács, F. Tárkányi, B. Király, A. Hermanne, M. Sonck, Evaluated activation cross sections of longer-lived radionuclides produced by deuteron-induced reactions on natural copper, Nucl. Inst. Methods Phys. Res. B 251 (1) (2006) 56–65, https://doi.org/10.1016/j.nimb.2006.06.007.
[18] R. Vandenbosch, J.R. Huizenga, Isomeric cross-section ratios for reactions producing the isomeric pair Hg^{197,197m}, Phys. Rev. 120 (4) (1960) 1313–1318, https://doi.org/10.1103/PhysRev. 120.1313.
[19] N. Chevarier, A. Chevarier, A. Demeyer, T.M. Duc, Réactions Induites sur l'Or par des Deutons de 10 a 70 MeV, Journal de Physique 32 (7) (1971) 483–490, https://doi.org/10.1051/jphys:01971003207048300.
[20] Yu.V. Khrisanfov, V.Yu. Padalko, P.P. Zarubin, Excitation functions for ^{197}Au + d reactions, Bull. Russ. Acad. Sci. – Phys. 36 (1973) 580.
[21] X. Long, X. Peng, F. He, Activation cross-sections of Au-197 with deuterons, Inst. of Nucl. Sci. and Technol., Sichuan U. Reports, No. 001, 1985.
[22] Zhao Wenrong, Lu Hanlin, Measurements of cross sections for Au-197(d, x) reaction, Chin. J. Nucl. Med. 11 (2) (1989) 83–88.
[23] F. Tárkányi, F. Ditrói, A. Hermanne, S. Takács, B. Király, H. Yamazaki, M. Baba, A. Mohammadi, A.V. Ignatyuk, Activation cross-sections of deuteron induced nuclear reactions on gold up to 40 MeV, Nucl. Inst. Methods Phys. Res. B 269 (2011) 1389–1400, https://doi.org/10.1016/j.nimb.2011.03.019.
[24] F. Tárkányi, A. Hermanne, F. Ditrói, S. Takács, R. Adam Rebeles, A.V. Ignatyuk, New data on cross-sections of deuteron induced nuclear reactions on gold up to 50 MeV and comparison of production routes of medically relevant Au and Hg radioisotopes, Nucl. Inst. Methods Phys. Res. B 362 (2015) 116–132, https://doi.org/10.1016/j.nimb.2015.09.044.
[25] S. Sudár, S.M. Qaim, Mass number and excitation energy dependence of the $\Theta_{eff}/\Theta_{rig}$ parameter of the spin cut-off factor in the formation of an isomeric pair, Nucl. Phys. A 979 (2018) 113–142, https://doi.org/10.1016/j.nuclphysa.2018.09.039.
[26] N. Baron, B.L. Cohen, Activation cross-section survey of deuteron-induced reactions, Phys. Rev. 126 (6) (1963) 2636–2642, https://doi.org/10.1103/PhysRev. 129.2636.
[27] P. Jahn, H.-J. Probst, A. Djaloeis, W.F. Davidson, C. Mayer-Boericke, Measurement

and interpretation of ^{197}Au-(d, xnyp) excitation functions in the energy range from 25 to 86 MeV, Nucl. Phys. A 209 (2) (1973) 333–347, https://doi.org/10.1016/0375-9474(73)90581-2.
[28] E. Sandoval, E. Paez, Cross section for the Au^{197}(d, p)A^{u19}8 reaction, Phys. Rev. 136 (2B) (1964) 415–417, https://doi.org/10.1103/PhysRev. 136.B415.
[29] S.J. Nassiff, E. Quel, J. Testoni, Excitation function for the reaction Au-197(d, p)Au-198, Nucl. Phys. 88 (2) (1966) 344–348, https://doi.org/10.1016/0029-5582(66)90592-X.
[30] V.A. Zheltonozhsky, V.M. Mazur, Z.M. Bigan, Investigation of the excitation of metastable states of ^{197}Pt and ^{197}Hg in (γ, n) and (d,2n) reactions, Phys. Atomic Nucl. 67 (5) (2004) 875–881.
[31] M. Nordberg, G.F. Nordberg, B.A. Fowler, L. Friberg (Eds.), Handbook on the Toxicology of Metals, third ed., Elsevier, 2007, p. 681 ISBN 978-0-12-369419-3.

Publikácia IV

Lebeda O., Červenák J.

Revised cross-sections for formation of theranostic ^{197m,g}Hg in proton- and deuteron-induced reactions on ^{197}Au

Nucl. Instrum. Methods Phys. Res. B 478 (2020) 85-91
https://doi.org/10.1016/j.nimb.2020.05.014

Nuclear Inst. and Methods in Physics Research B 478 (2020) 85–91

Contents lists available at ScienceDirect

Nuclear Inst. and Methods in Physics Research B

journal homepage: www.elsevier.com/locate/nimb

Revised cross-sections for formation of theranostic ^{197m,g}Hg in proton- and deuteron-induced reactions on ^{197}Au

Ondřej Lebeda*, Jaroslav Červenák

Nuclear Physics Institute of the CAS, Husinec-Řež 130, 250 68 Řež, Czech Republic

ARTICLE INFO

Keywords:
Cross-sections
^{197m}Hg
^{197g}Hg
Data revision
Theranostic radionuclides

ABSTRACT

We have recently re-measured excitation functions of proton- and deuteron-induced nuclear reactions on ^{197}Au focused particularly on theranostic ^{197m,g}Hg. The γ-ray spectra evaluation revealed inconsistency in the γ-line emission probabilities of ^{197m}Hg. Detailed measurements of the separated ^{197m,g}Hg samples resulted in a thorough revision of the ^{197m}Hg decay scheme. In this short summary, we provide cross-sections, isomeric ratios and the yields of ^{197m}Hg and ^{197g}Hg corrected for the new decay data.

1. Introduction

Both isomers of ^{197}Hg have theranostic potential [1]. It motivated us to careful re-measurement of proton- and deuteron-induced reaction cross-sections on ^{197}Au that provide ^{197m,g}Hg with high yield and high specific activity. The results were recently published [2,3]. In the course of the γ-ray spectra evaluation, we noticed large discrepancy in the 134 and 279 keV γ-lines emission probabilities available in the data bases [4,5]. The former peak is associated with the dominant IT transition of ^{197m}Hg, while the latter with its EC decay. We have, therefore, separated ^{197m,g}Hg from thick deuteron-irradiated gold target and subjected its point-like sources to multiple γ-ray spectrometry measurements. Analysis of the acquired spectra allowed for a thorough revision of the ^{197m}Hg decay scheme [6]. Here, we report cross-sections of the ^{197}Au(p,n) and ^{197}Au(d,2n) nuclear reactions corrected for the new decay data, as well as the isomeric ratios and thick target yields. The correction was also applied to the previously published data, wherever possible.

2. Method

The new decay data are summarized in Table 1. The change involves not only γ-line emission probabilities in the decay of ^{197m}Hg, but also the IT/EC branching ratio and slightly ^{197g}Hg half-life. All these data are relevant for the ^{197m}Hg activity calculation and for the correction of the ^{197m}Hg decay contribution to the ^{197g}Hg activity. The raw data obtained in the works [2,3] were, therefore, re-evaluated together with the previously published results according to [6]. In a few cases, we still improve interpretation of several earlier data sets and obtained better agreement among them.

3. Results and discussion

3.1. Cross-sections for the ^{197}Au(p,n)^{197m}Hg reaction

The revised independent isotopic cross-sections for the ^{197}Au (p,n)^{197m}Hg reaction are displayed in Table 2. Fig. 1 shows them in the context of the previously published data [7–13] and prediction of the TALYS code (TENDL-2019 library) [14]. All the previous measurements were also corrected for the difference between the emission probabilities of the radiation used by the authors for the evaluation, and the data in Table 1. In contrast to [2], we were able to rectify the cross-sections of Gritsyna et al. [9] having ascertained that the authors derived the 134-keV emission probability from the IT transition probability 0.97 and conversion coefficient 2.1, i.e. 0.313 per decay. All the experimental data show quite consistent picture, only a few values of Hansen et al. [8] and Gritsyna et al. [9] around maximum seem to be slightly shifted towards higher values. The only work of Satheesh et al. [15] that significantly exceeds other measurements was excluded from the Fig. 1 (cf. Fig. 2 in [2]). The TALYS prediction complies with the experimental data very well up to the maximum, from where it starts to remarkably deviate from them showing very slow decrease.

3.2. Cross-sections for the ^{197}Au(p,n)^{197g}Hg reaction

The revised independent isotopic cross-sections for the ^{197}Au (p,n)^{197g}Hg reaction are displayed in Table 2 and Fig. 2. They are compared with previous works [7–9,12,13,16] and prediction of the TALYS code (TENDL-2019 library) [14]. In the case of the ground state, there is no chance to correct properly the other measurements for the

* Corresponding author.
E-mail address: lebeda@ujf.cas.cz (O. Lebeda).

https://doi.org/10.1016/j.nimb.2020.05.014
Received 3 April 2020; Received in revised form 10 May 2020; Accepted 11 May 2020

Table 1
The previous decay data for the ^{197m}Hg and ^{197g}Hg in Nuclear Data Sheets in black [5] compared with the recently measured values in red [6]. The uncertainties in the last digits are displayed in italics. Gamma lines used for the cross-section evaluation are in bold.

Radionuclide Spin	Half-life	Decay mode Branching ratio	E_γ (keV)	I_γ (%)
^{197m}Hg 13/2+	23.8 h *1*	IT 91.4 % *7* EC 8.6 % *7*	**133.98** *5* 164.97 *7* 279.01 *5*	**33.5** *3* 0.262 *5* 6.1 *5*
	23.82 h *4*	IT 94.69 % *9* EC 5.32 % *9*	**133.79** *5* 164.84 *5* 278.65 *5*	**34.8** *3* 0.2816 *25* 3.79 *4*
^{197g}Hg 1/2−	64.14 h *5* 64.81 h *24*	EC 100 %	**191.437** *10* 268.78 *5*	**0.632** *21* 0.0393 *19*

new decay scheme due to the missing primary data, we have therefore, used them as published. It is naturally reflected in remarkable scattering of the available cross-sections that often don't agree within indicated uncertainties, see Fig. 2. Besides the work of Satheesh et al. [15], we excluded from the comparison also the data of Thomas et al. [17] and Chodil et al. [18] whose experiment measured total cross-section of all the (p,n) and (p,pn) reactions on ^{197}Au via counting emitted neutrons (cf. Fig. 3 in [2]).

3.3. Isomeric cross-section ratios and thick target yields for the ^{197}Au(p,n)^{197m,g}Hg reactions

The isomeric cross-section ratios σ_m/σ_g as a function of energy were calculated including the uncertainties and compared with the cross-section ratios deduced from the previously published data in Figs. 1 and 2 and contained in the work of Sudár and Qaim [19]. As the previously published cross-sections could be corrected properly only for the ^{197m}Hg (see above), thus deduced σ_m/σ_g ratios must be taken with caution and are rather scattered, see Fig. 3. The best agreement we observed with the data of Elmaghraby et al. [12], Ditrói et al [13] (only below 20 MeV) and Sudár and Qaim [19]. Moreover, the ratio σ_m/σ_g for the proton energies beyond 20 MeV is burdened with high uncertainties due to the decreasing counting statistics in the peak of ^{197g}Hg.

Thick target yields for both ^{197m}Hg and ^{197g}Hg were deduced from our experimental cross-sections by fitting them with one or two polynomial fits and integrating the excitation function using the stopping power of protons in gold [20]. The yields are displayed on Fig. 4.

3.4. Cross-sections for the ^{197}Au(d,2n)^{197m}Hg reaction

The corrected cross-sections for the ^{197}Au(d,2n)^{197m}Hg reaction are summarized in Table 3. Their comparison with the published data sets [7,21–26] and with the TALYS prediction adopted from the TENDL-2019 library are displayed on Fig. 5. After the revision of the previous measurements for the new decay scheme, we observe relatively good agreement among the authors, only the data of Chevarier et al. [21] are slightly shifted towards higher values, a few cross-sections of Tárkányi et al. [25] for energies exceeding 17 MeV are lower than expected from the trend of the other data and all the data of Tárkányi et al. [26] seem

Table 2
Cross-sections for the reactions ^{197}Au(p,n)^{197m}Hg and ^{197}Au(p,n)^{197g}Hg corrected for the new decay data displayed in Table 1 [6]

E_p (MeV)	σ (mb) ^{197m}Hg	^{197g}Hg
35.29 ± 0.20	7.80 ± 0.54	
34.07 ± 0.20	8.03 ± 0.56	
32.81 ± 0.20	8.39 ± 0.59	
31.51 ± 0.21	8.53 ± 0.60	
30.17 ± 0.21	8.86 ± 0.62	
28.77 ± 0.22	9.20 ± 0.65	
27.35 ± 0.22	9.53 ± 0.66	13.7 ± 3.7
25.86 ± 0.23	10.98 ± 0.77	10.9 ± 5.2
24.30 ± 0.23	10.10 ± 0.70	13.1 ± 5.2
22.65 ± 0.24	10.89 ± 0.76	12.7 ± 4.6
20.90 ± 0.25	11.68 ± 0.81	13.7 ± 3.3
19.03 ± 0.27	12.23 ± 0.85	15.3 ± 1.9
17.32 ± 0.20	13.66 ± 0.95	17.6 ± 1.4
17.04 ± 0.28	13.79 ± 0.96	16.2 ± 1.8
16.08 ± 0.20	14.74 ± 1.0	19.6 ± 1.7
14.79 ± 0.21	17.4 ± 1.2	22.7 ± 2.3
13.41 ± 0.22	24.0 ± 1.7	35.9 ± 3.3
12.66 ± 0.23	29.0 ± 2.0	43.2 ± 3.0
11.87 ± 0.23	36.2 ± 2.5	58.1 ± 3.9
11.05 ± 0.24	34.3 ± 2.4	63.2 ± 4.5
10.19 ± 0.25	29.1 ± 2.0	66.4 ± 5.3
9.27 ± 0.26	18.4 ± 1.3	57.9 ± 4.5
8.28 ± 0.27	7.95 ± 0.55	30.5 ± 2.4
7.19 ± 0.30	1.99 ± 0.14	10.22 ± 0.88
6.35 ± 0.32	0.475 ± 0.035	2.02 ± 0.26

to be slightly shifted towards higher energies. Prediction of the TALYS code follows well the shape of the experimental data, but absolute values are almost twice larger than average experimental points (note the extra axis for the TALYS predicted cross-sections).

3.5. Cross-sections for the ^{197}Au(d,2n)^{197g}Hg reaction

The cross-sections for the ^{197}Au(d,2n)^{197g}Hg reaction are provided in Table 3 and shown in the context of the previous measurements [7,21–26] and compared to the TALYS prediction adopted from the TENDL-2019 library are displayed on Fig. 6. Again, no actual correction could be applied to the previously measured cross-section due to the missing primary data. The experimental material is more scattered than in the case of the ^{197m}Hg as expected, but except the measurements of Chevarier et al. [21], Tárkányi et al. [26] and last point of Long et al. [23] that seem to be systematically shifted to higher values, fair agreement among the other works was observed. Prediction of TALYS obviously underestimates almost all the experimental values by ca 1/3 at the maximum, but the shape of the excitation function corresponds well to the measurements.

3.6. Isomeric cross-section ratios and thick target yields for the ^{197}Au(d,2n)^{197m,g}Hg reactions

The isomeric cross-section ratios σ_m/σ_g and their uncertainty were calculated from the revised cross-sections and are shown in comparison with the cross-section ratios derived from previously published material and with the isomeric ratios provided directly by Zheltonozhsky et al.

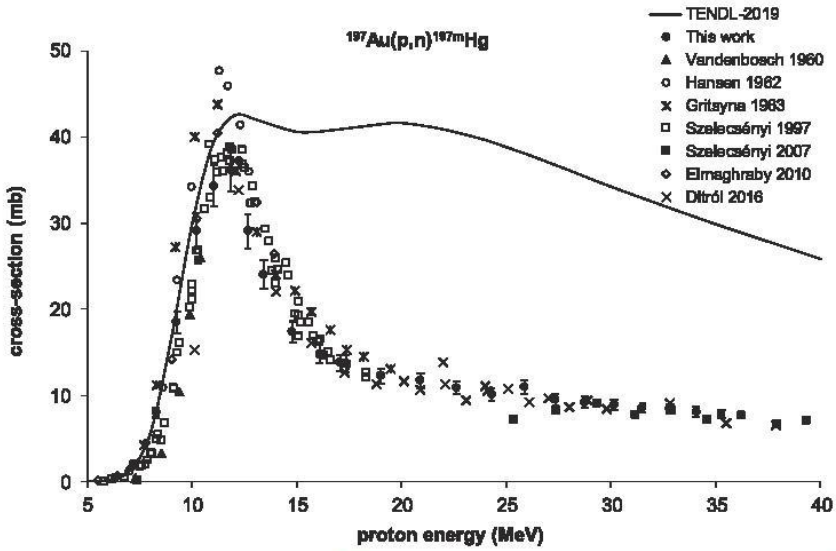

Fig. 1. Cross-sections of the ^{197}Au(p,n)^{197m}Hg reaction – our values in [2] corrected for the new decay data of ^{197m}Hg summarized in Table 1 [6]. The previously published data [7–13] were corrected for the new emission probability of the 134 keV γ-line [6]. TENDL-2019 prediction [14] is displayed, too.

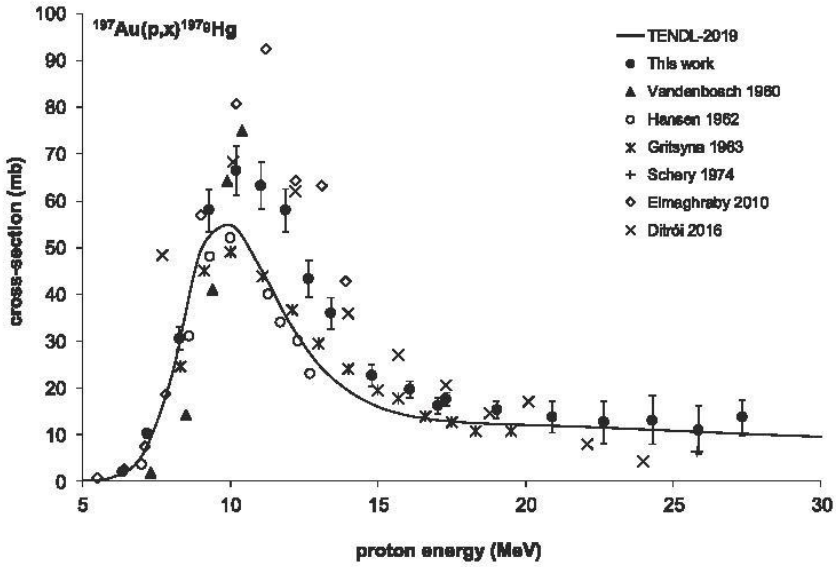

Fig. 2. Cross-sections of the ^{197}Au(p,n)^{197g}Hg reaction – our values corrected for the new decay data of ^{197m}Hg (γ-ray emission probability, half-life, IT branching ratio) and ^{197g}Hg (half-life) summarized in Table 1 [6]. The previous data [7–9,12,13,16] are displayed as published together with the TENDL-2019 prediction [14].

[27] on Fig. 7. As the consequent correction of the ^{197g}Hg cross-sections in previous works is impossible, the calculated ratios σ_m/σ_g are – like in the case of protons – burdened with additional uncertainty. Although the trends are very similar showing a maximum around 17 MeV, absolute values of various authors differ significantly from each other and some are rather scattered.

Thick target yields for both ^{197m}Hg and ^{197g}Hg were deduced from our experimental cross-sections by fitting them with one or two

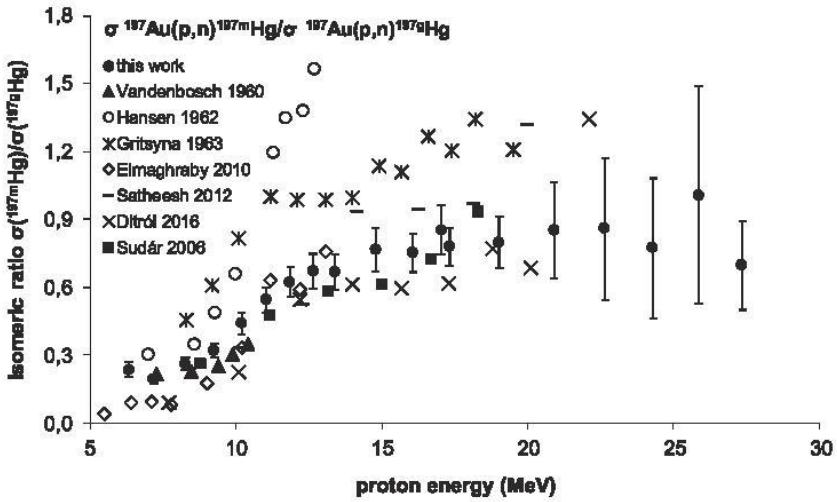

Fig. 3. Isomeric cross-section ratios for the formation of ^{197m}Hg and ^{197g}Hg in the ^{197}Au(p,n) reaction calculated from the corrected cross-sections displayed in Table 2 together with other experimental data (correction of the ^{197g}Hg cross-sections cannot be performed due to missing primary data).

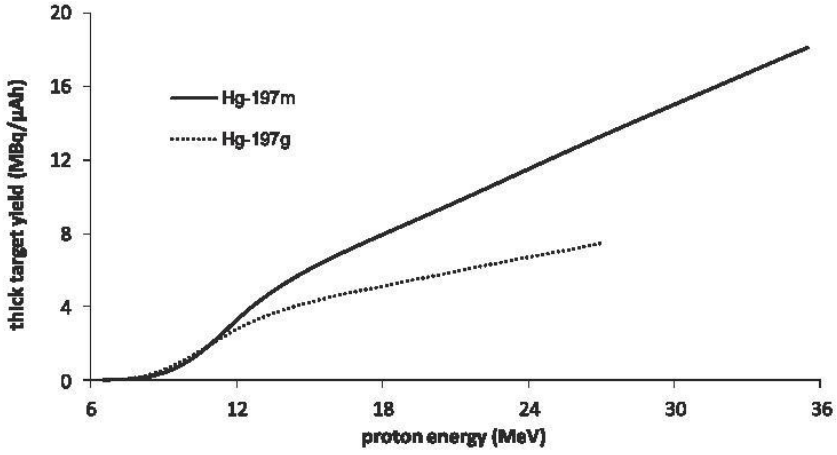

Fig. 4. Thick target yield (production rate) for ^{197m}Hg and ^{197g}Hg in proton activation of gold deduced from the corrected cross-sections displayed in Table 2.

Table 3
Cross-sections for the reactions ^{197}Au(d,2n)^{197m}Hg and ^{197}Au(d,2n)^{197g}Hg corrected for the new decay data displayed in Table 1.

E_d (MeV)	σ (mb) ^{197m}Hg	^{197g}Hg
19.73 ± 0.21	99.8 ± 6.9	104.9 ± 9.5
18.80 ± 0.23	122.3 ± 8.5	122 ± 11
17.83 ± 0.26	151 ± 10	144 ± 14
16.83 ± 0.29	193 ± 13	177 ± 17
15.76 ± 0.33	230 ± 16	227 ± 21
14.94 ± 0.36	250 ± 17	255 ± 24
14.13 ± 0.39	262 ± 18	305 ± 28
13.29 ± 0.42	244 ± 17	334 ± 30
12.41 ± 0.46	203 ± 14	328 ± 28
11.48 ± 0.51	144 ± 10	274 ± 23
10.49 ± 0.56	87.8 ± 6.1	188 ± 16
9.43 ± 0.63	39.8 ± 2.8	95.3 ± 7.8
8.30 ± 0.71	11.52 ± 0.80	30.4 ± 2.7

polynomial fits and integrating the excitation function using the stopping power of deuterons in gold [20]. The yields are displayed on Fig. 8.

3.7. Comparison of proton and deuteron production routes of ^{197m,g}Hg

The discussion of the production of ^{197m,g}Hg in proton- and deuteron-induced reactions on gold in [3] remains true. Deuteron activation results in higher ^{197m}Hg/^{197g}Hg EOB activity ratio than proton activation for optimal production conditions. In this case, deuteron activation is more favourable regarding the yields of both isomers, too – the production rate of ^{197m}Hg and ^{197g}Hg for the 19.5 → 8.0 MeV deuteron beam energy loss is 45.3 and 20.7 MBq/μAh, respectively, for the 27 → 6.5 MeV proton beam energy loss it is only 13.3 and 7.5 MBq/μAh, respectively. Also radionuclidic purity of the deuteron-produced ^{197m,g}Hg is superior to proton-produced, because no ^{195m,g}Hg is formed in the target.

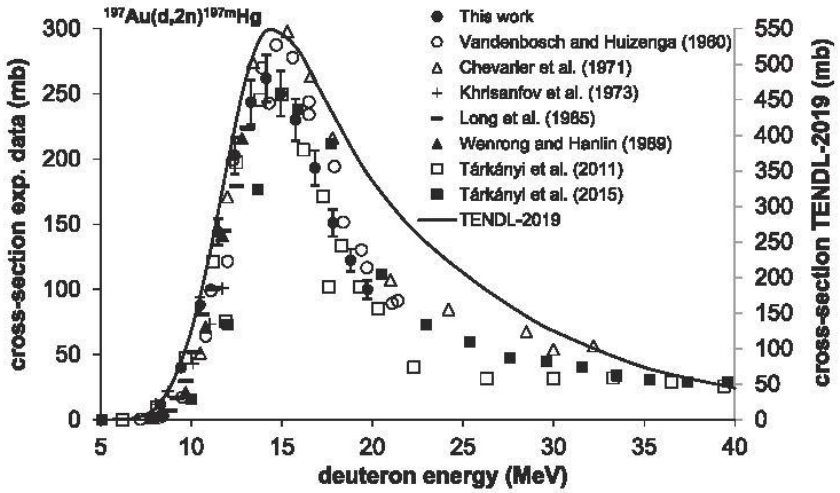

Fig. 5. Cross-sections of the ^{197}Au(d,2n)^{197m}Hg reaction – our values [3] corrected for the new decay data of ^{197m}Hg summarized in Table 1 [6]. The previously published data [7,21–26] were corrected for the new emission probability of the 134 keV γ-line [6]. TENDL-2019 prediction [14] is displayed, too.

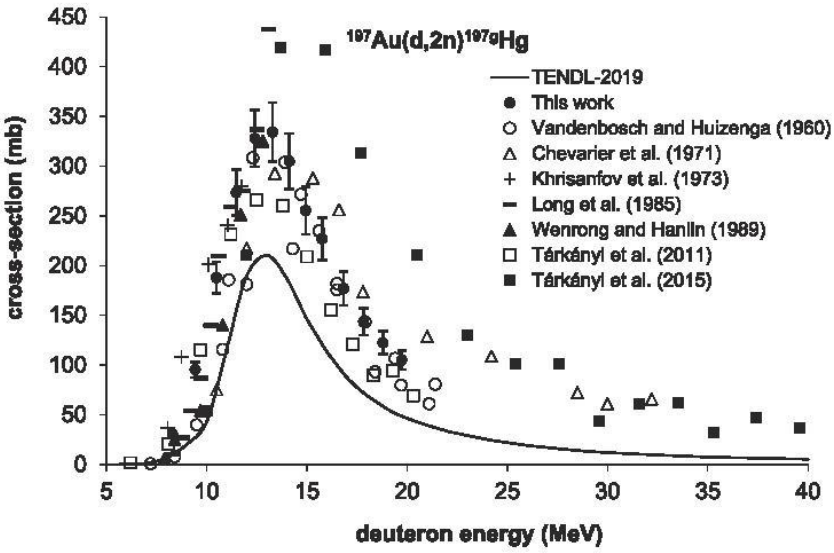

Fig. 6. Cross-sections of the ^{197}Au(d,2n)^{197g}Hg reaction – our values [3] corrected for the new decay data of ^{197m}Hg (γ-ray emission probability, half-life, IT branching ratio) and ^{197g}Hg (half-life) summarized in Table 1 [6]. The previous data [7,21–26] are displayed as published together with the TENDL-2019 prediction [14].

4. Conclusion

We provide cross-sections, isomeric ratios and thick target yields for the ^{197}Au(p,n)^{197m}Hg, ^{197g}Hg and ^{197}Au(d,2n)^{197m}Hg,^{197g}Hg reactions revised for the new decay scheme of ^{197m}Hg. In some cases, we obtained better agreement with the previous experimental data, in particular for ^{197m}Hg formation, where the correction is straightforward. Comparison of the experiment with the theoretical predictions of the TALYS nuclear reaction model code adopted from the TENDL-2019 online library is presented, too. The results confirmed superiority of deuterons over protons in the production of ^{197m}Hg/^{197g}Hg in terms of the yield and achievable *m/g* activity ratio.

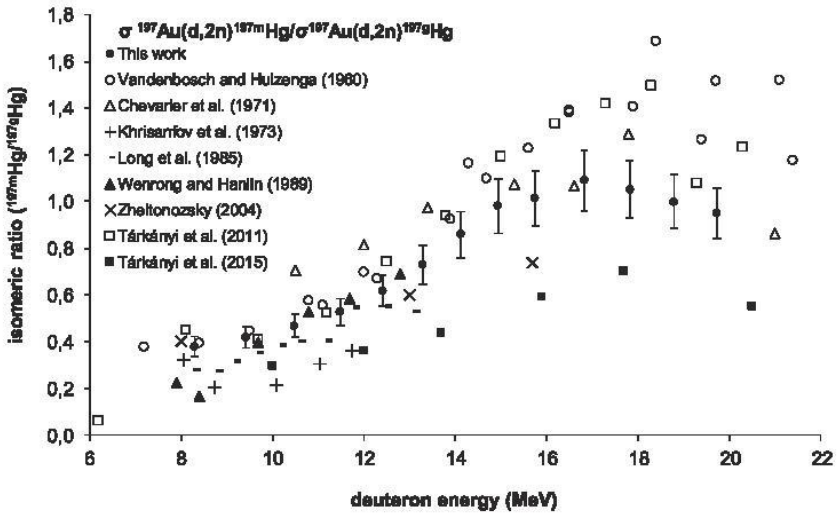

Fig. 7. Isomeric cross-section ratios for the formation of ^{197m}Hg and ^{197g}Hg in the ^{197}Au(d,2n) reaction calculated from the corrected cross-sections displayed in Table 3 together with other experimental data (correction of the ^{197g}Hg cross-sections cannot be performed due to missing primary data).

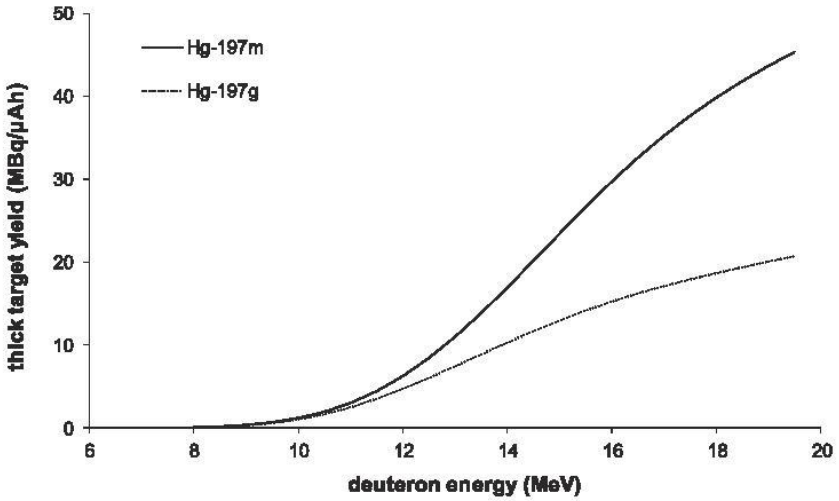

Fig. 8. Thick target yield (production rate) for ^{197m}Hg and ^{197g}Hg in deuteron activation of gold deduced from the corrected cross-sections displayed in Table 3.

CRediT authorship contribution statement

Ondřej Lebeda: Conceptualization, Methodology, Writing - original draft. **Jaroslav Červenák:** Data curation, Writing - review & editing.

Declaration of Competing Interest

The authors declare that they have no known competing financial interests or personal relationships that could have appeared to influence the work reported in this paper.

Acknowledgement

The work was supported from ERDF/ESF project "CANAM-OP" of the Ministry of Education, Youth and Sports of the Czech Republic (No. CZ.02.1.01/0.0/0.0/16_013/0001812).

References

[1] R. Freudenberg, R. Apolle, M. Walther, H. Hartmann, J. Kotzerke, Molecular imaging using the theranostic agent $^{197(m)}$Hg: phantom measurements and Monte Carlo simulations, Eur. J. Nucl. Med. Mol. Imaging 5 (15) (2018), https://doi.org/10.1186/s40658-018-0216-9.

[2] J. Červenák, O. Lebeda, Measurement of cross-sections of proton-induced nuclear reactions on ^{197}Au focused on the production of the theranostic pair ^{197m,g}Hg, Nucl. Inst. Methods in Phys. Res. B. 458 (2019) 118–125, https://doi.org/10.1016/j.nimb.2019.08.006.

[3] O. Lebeda, J. Červenák, Measurement of deuteron-induced nuclear reactions cross-sections on ^{197}Au and on ^{nat}Cu focused on the theranostic ^{197m,g}Hg, Nucl. Inst. Methods in Phys. Res. B. 461 (2019) 105–113, https://doi.org/10.1016/j.nimb.2019.09.034.

[4] NuDat 2.6, National Nuclear Data Center, Brookhaven National Laboratory, 2012. Available at URL < www.nndc.bnl.gov/nudat2/ > .

[5] H. Xiaolong, Z. Chunmey, Nucl. Data Sheets 104 (2005) 283.

[6] O. Lebeda, F.G. Kondev, J. Červenák, Branching ratio and γ-ray emission probabilities in the decay of the $J^{\pi} = 13/2^{+}$ isomer in ^{197}Hg. Nucl. Inst. Methods in Phys, Res. A 959 (2020) 163481, , https://doi.org/10.1016/j.nima.2020.163481.

[7] R. Vandenbosch, J.R. Huizenga, Isomeric cross-section ratios for reactions producing the isomeric pair $Hg^{197,197m}$, Phys. Rev. 120 (4) (1960) 1313–1318, https://doi.org/10.1103/PhysRev.120.1313.

[8] L.F. Hansen, R.C. Jopson, H. Mark, C.D. Swift, Ta^{181}(p,n)^{W18}1 and A^{u19}7(p,n)^{Hg1}97 excitation functions between 4 and 13 MeV, Nucl. Phys. 30 (1962) 389–398, https://doi.org/10.1016/0029-5582(62)90062-7.

[9] V. Gritsyna, A. Klyucharev, V. Remaev, L. Reshetova, Ratio of the cross sections for formation of the isomer and ground states of nuclei in the (p,n) reaction at energies from the threshold to 20 MeV, J. Exptl. Theoret. Phys. 17 (1963) 1186–1189.

[10] F. Szelecsényi, S. Takács, A. Fenyvesi, Z. Szücs, F. Tárkányi, S.-J. Heselius, J. Bergman, E. Boothe, Study of the ^{197}Au(p,pn)$^{196m1, m2, g}$Au and ^{197}Au(p,n)^{197m}Hg reactions and their application for proton beam monitoring in radioisotope production, Conf. On Nucl. Data for Sci. and Techn., Trieste 2 (1997) 1483.

[11] F. Szelecsényi, G.F. Steyn, Z. Kovács, T.N. Van Der Walt, Application of Au + p nuclear reactions for proton beam monitoring up to 70 MeV, Conf. on Nucl. Data for Sci. and Technology, Nice 2 (2007) 1259.

[12] E.K. Elmaghraby, K.F. Hassan, H. Omara, Z.A. Saleh, Production of the mercury-197 through proton induced reaction on gold, Appl. Radiat. Isot. 68 (12) (2010) 1694–1698, https://doi.org/10.1016/j.apradiso.2010.04.009.

[13] F. Ditrói, F. Tárkányi, S. Takács, A. Hermanne, Activation cross sections of proton induced nuclear reactions on gold up to 65 MeV, Appl. Radiat. Isot. 113 (2016) 96–109, https://doi.org/10.1016/j.apradiso.2016.04.020.

[14] A.J. Koning, D. Rochman, S.C. van der Marck, J. Kopecky, J.Ch. Sublet, S. Pomp, H. Sjostrand, R. Forrest, E. Bauge, H. Henriksson, O. Cabellos, S. Goriely, J. Leppanen, H. Leeb, A. Plompen, R. Mills, TALYS-based evaluated nuclear data library. Available from URL < http://www.talys.eu/tendl-2019 > .

[15] B. Satheesh, M.M. Musthafa, B.P. Singh, R. Prasad, Study of isomeric cross-section ratio and pre-equilibrium fraction in proton and alpha particle induced nuclear reactions on ^{197}Au, Int. J. Mod. Phys., Part E 21(12) (6) (2012) 1250059, https://doi.org/10.1142/S0218301312500590.

[16] S.D. Schery, D.A. Lind, H.W. Fielding, C.D. Zafiratos, The (p,n) reaction to the isobaric analogue state of high-Z elements at 25.8 MeV, Nucl. Phys. A 234 (1) (1974) 109–129, https://doi.org/10.1016/0375-9474(74)90382-0.

[17] R.G. Thomas, W. Bartolini, Neutron production in Ag, Ta, Au, Pt, and Pb by the interaction of 7.5-14-MeV protons, Phys. Rev. 159 (4) (1967) 1022–1028, https://doi.org/10.1103/PhysRev.159.1022.

[18] G. Chodil, R.C. Jopson, H. Mark, C.D. Swift, R.G. Thomas, M.K. Yates, (p,n) and (p,2n) cross sections on nine elements between 7.0 and 15.0 MeV, Nucl. Phys. A 93 (1967) 648–672, https://doi.org/10.1016/0375-9474(67)90312-0.

[19] S. Sudár, S.M. Qaim, Cross sections for the formation of ^{195}Hg$^{m, g}$, ^{197}Hg$^{m, g}$, and ^{196}A$^{m, g}$ in α and ^{3}He-particle induced reactions on Pt: Effect of level density parameters on the calculated isomeric cross-section ratio, Phys. Rev. C 73 (2006) 034613, , https://doi.org/10.1103/PhysRevC.73.034613.

[20] J.F. Ziegler, M.D. Ziegler, J.P. Biersack, SRIM2010 Code, Available at URL < http://www.srim.org/ > .

[21] N. Chevarier, A. Chevarier, A. Demeyer, T.M. Duc, Réactions Induites sur l'Or par des Deutons de 10 a 70 MeV, Journal de Physique 32 (7) (1971) 483–490, https://doi.org/10.1051/jphys:01971003207048300.

[22] Yu.V. Khrisanfov, V.Yu. Padalko, P.P. Zarubin, Excitation functions for ^{197}Au + d reactions, Bull. Russian Academy of Sciences – Physics 36 (1973) 580.

[23] X. Long, X. Peng, F. He, Activation cross-sections of Au-197 with deuterons, Inst. of Nucl. Sci. and Technol., Sichuan U. Reports, No. 001, 1985.

[24] Wenrong Zhao, Hanlin Lu, Measurements of cross sections for Au-197(d,x) reaction, Chinese J. of Nuclear Medicine 11 (2) (1989) 83–88.

[25] F. Tárkányi, F. Ditrói, A. Hermanne, S. Takács, B. Király, H. Yamazaki, M. Baba, A. Mohammadi, A.V. Ignatyuk, Activation cross-sections of deuteron induced nuclear reactions on gold up to 40 MeV, Nucl. Inst. Methods Phys. Res. B 269 (2011) 1389–1400, https://doi.org/10.1016/j.nimb.2011.03.019.

[26] F. Tárkányi, A. Hermanne, F. Ditrói, S. Takács, R. Adam Rebeles, A.V. Ignatyuk: New data on cross-sections of deuteron induced nuclear reactions on gold up to 50 MeV and comparison of production routes of medically relevant Au and Hg radioisotopes, Nucl. Inst. Methods Phys. Res. B 362 (2015) 116–132. doi: 10.1016/j.nimb.2015.09.044.

[27] V.A. Zheltonozhsky, V.M. Mazur, Z.M. Bigan, Investigation of the Excitation of Metastable States of ^{197}Pt and ^{197}Hg in (γ, n) and (d,2n) Reactions, Physics of Atomic Nuclei 67 (5) (2004) 875–881.

Publikácia V

Lebeda O., Kondev F. G., Červenák J.

Branching ratio and γ-ray emission probabilities in the decay of the $J^{\pi}=13/2^{+}$ isomer in ^{197}Hg

Nucl. Instrum. Methods Phys. Res. A 959 (2020) 163481
https://doi.org/10.1016/j.nima.2020.163481

Nuclear Inst. and Methods in Physics Research, A 959 (2020) 163481

Contents lists available at ScienceDirect

Nuclear Inst. and Methods in Physics Research, A

journal homepage: www.elsevier.com/locate/nima

Branching ratio and γ-ray emission probabilities in the decay of the $J^{\pi} = 13/2^{+}$ isomer in ^{197}Hg

O. Lebeda [a], F.G. Kondev [b,*], J. Červenák [a]

[a] Nuclear Physics Institute, Czech Academy of Sciences, Husinec-Řež 130, 250 68 Řež, Czech Republic
[b] Physics Division, Argonne National Laboratory, Argonne, Lemont 60439, USA

ARTICLE INFO

Keywords:
Radioactivity
^{197g}Hg
^{197m}Hg
γ ray emission probabilities
Branching ratio
Half-life

ABSTRACT

Gamma rays following the decay of the ^{197g}Hg and ^{197m}Hg radionuclides were measured using chemically-purified sources and a planar HPGe detector. In the case of ^{197m}Hg, precise values of 94.68 (9)% and 5.32 (9)% were determined for the IT and EC branches, respectively, the latter found to differ significantly from previously published data. The half-lives of ^{197g}Hg and ^{197m}Hg were also measured as 64.81 (24) h and 23.82 (4) h.

1. Introduction

The structure of low-lying levels in ^{197}Hg is well known from various spectroscopy studies (see Ref. [1] and references therein). The ground state, ^{197g}Hg ($J^{\pi} = 1/2^{-}$), decays via an electron capture (EC) to low-spin $J^{\pi} = 1/2^{+}$ and $3/2^{+}$ levels in the daughter ^{197}Au nucleus. A long-lived isomeric state, ^{197m}Hg ($J^{\pi} = 13/2^{+}$, E = 298 keV), is known to exhibit both internal transition (IT) and EC decays, the latter directly populating the $J^{\pi} = 11/2^{-}$, E = 409-keV isomer ($T_{1/2}$ = 7.73 (6) s [1]) in ^{197}Au, as shown in Fig. 1.

There is a continuing interest in the decay properties of ^{197g}Hg and ^{197m}Hg since both radionuclides have potential for theranostic medical applications [2]. However, significant differences were observed in the activity of ^{197m}Hg depending whether γ rays associated with the IT decay branch (134-keV γ ray) or the EC one (279-keVγ ray) were used for its quantification in recent excitation function measurements of proton- and deuteron-induced reactions [3,4], thus implying inconsistencies in the presently adopted nuclear data for this radionuclide.

The determination of the IT and EC branching ratio of ^{197m}Hg is not straight forward and it requires a detailed knowledge of the decay scheme and a range of complementary nuclear structure information, such as γ-ray emission probabilities, multipolarities, M1+E2 mixing ratios and total electron conversion coefficients. Earlier, branching ratios were recommended in both ENSDF [1,5,6] and the Table of Isotopes [7,8], but the values varied over the years, since they were based on the nuclear data known at the time of publication.

In this paper, we report on new measurements of the emission probabilities for γ rays that follow the decay of ^{197m}Hg. Precise values for the IT and EC branching intensities were determined and the latter was found to differ significantly from the previously published data. The half-lives of ^{197g}Hg and ^{197m}Hg were also measured with a high precision.

2. Experimental methods

2.1. Radionuclide production and source preparation

The radionuclides were produced by deuteron activation of a water-cooled, high-purity (99.99%, Safina, Czech Republic) ^{197}Au target that had a diameter of 10 mm and a thickness of 60 μm. The target was irradiated for 1.5 h with a 19 MeV, 6.5 μA deuteron beam provided by the U-120M cyclotron of the Nuclear Physics Institute of the Czech Academy of Science.

A chemical separation of mercury radionuclides from gold ones, including ^{198}Au, that was produced in the ^{197}Au(d, p) reaction, was performed after the irradiation was completed. The target was dissolved in aqua regia prepared from 525 μl of 30% HCl and 175 μl of 65% HNO_3 (purity TraceSelect, Sigma-Aldrich). A 300 μl of 6M HCl was added to the final solution, which was then loaded into a column filled with LN resin (TRISKEM, France). The column was prepared by soaking 3.6 g of LN resin for 15 min in 6M HCl. It was then transferred to a 10 ml Eppendorf pipette tip plugged with glass wool and rinsed slowly with 30 ml of 6M HCl. Altogether 15 fractions of 1 ml volume each were collected and their relative activities were measured using an ionizing chamber (BqMetr4, Empos, Czech Republic). It was found that the ^{197g}Hg and ^{197m}Hg activities were eluted almost entirely (>95%) in the fractions 8 and 9. All fractions were also sampled and measured

* Corresponding author.
E-mail address: kondev@anl.gov (F.G. Kondev).

https://doi.org/10.1016/j.nima.2020.163481
Received 16 December 2019; Received in revised form 15 January 2020; Accepted 20 January 2020
Available online 21 January 2020
0168-9002/

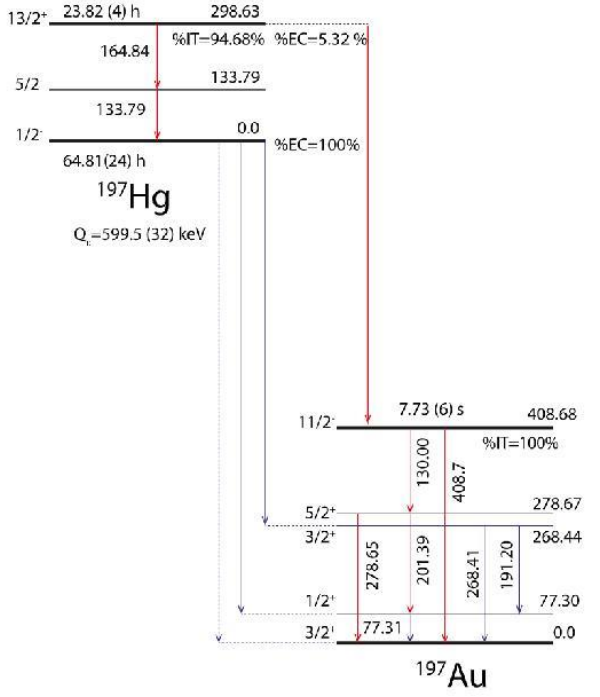

Fig. 1. Decay schemes of ^{197g}Hg and ^{197m}Hg. The level and γ ray energies, as well as the half-lives and %IT and %EC branching ratios are from the present work. The Q_γ value is from Ref. [9], while the J^π values, the half-life and % IT of ^{197m}Au are from Ref. [11].

Table 1
Gamma-ray energies and emission probabilities determined in the present work, together with the transition multipolarities, mixing ratios and total conversion electron coefficients used to determine the EC and IT branching ratios of ^{197m}Hg.

$E_\gamma(\Delta E_\gamma)^a$ (keV)	$I_\gamma(\Delta I_\gamma)^a$ (rel. units)	$I_\gamma(\Delta I_\gamma)^b$ (%)	Mult. [1]	$\delta(\Delta\delta)^c$	$\alpha_T(\Delta\alpha_T)$ [10]
^{197m}Hg; %IT = 94.68 (9)%					
133.79 (5)	1000 (6)	34.8 (3)	E2		1.705 (24)
164.84 (5)	8.09 (5)	0.2816 (26)	M4		337 (5)
^{197m}Hg; %EC = 5.32 (9)%					
77.31 (5)	0.410 (16) [d]	0.0143 (6)	M1+E2	−0.352 (11)	4.14 (10)
130.00 (5)	4.92 (4)	0.1713 (21)	E3		29.9 (4)
201.39 (5)	1.55 (5)	0.0540 (18)	E2		0.366 (5)
278.65 (5)	108.8 (6)	3.79 (4)	M1+E2	−0.40 (4)	0.368 (9)
408.7 (1)	0.164 (16)	0.0057 (6)	M4		3.87 (5)
^{197g}Hg; %EC = 100%					
77.31 (5)	1000 (10)				
191.20 (5)	28.4 (3)				
268.41 (5)	1.97 (5)				

[a] Determined in the present work, unless otherwise stated.
[b] Determined in the present work using the new %EC and %IT branches.
[c] See Table 2 for details.
[d] Determined in the present work from I_γ^{tot}(77.31-keV γ ray) = I_γ^{tot}(201.39-keV γ ray).

with a γ-ray spectrometer equipped with a HPGe detector (GMX45Plus, Ortec, U.S.A.) at the distance of 600 mm. No traceable activity of ^{198}Au was observed in any of the fractions, indicating a good separation of Hg from the Au radionuclides. Two sources with a diameter of 5 mm each were prepared by evaporating 25 µl from the strongest fraction on a thin filtration paper, which were sealed between two 150 µm thick polyethylene foils. These sources were used in γ-ray spectroscopy measurements aimed at determining the half-lives of ^{197g,m}Hg and the relative γ-ray emission probabilities following their decays.

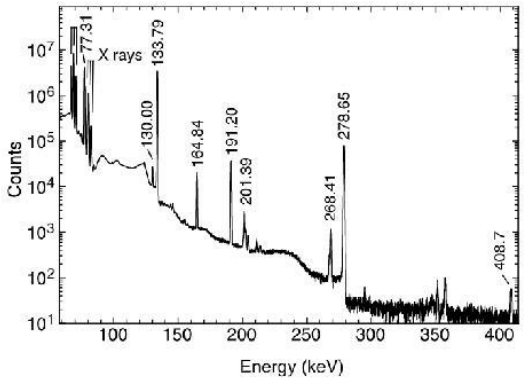

Fig. 2. Gamma-ray spectrum of ^{197g}Hg and ^{197m}Hg measured with the planar HPGe detector (Canberra, GL0515R) at a distance of 200 mm.

2.2. Measurements

One of the two sources was measured with a γ-ray spectrometer comprising of a planar HPGe detector (Canberra, GL0515R) at a distance of 200 mm from the detector, which had an energy resolution (full width at half maximum (FWHM)) of 0.5 keV at E_γ = 81 keV. The results from these measurements were used to determine the emission probabilities of γ-rays following the decays of ^{197g}Hg and ^{197m}Hg. The other source was used in a set of singles measurements using a planar HPGe detector (Canberra, GL0515R) located at a fixed distance of 120 mm from the source. The activities were followed for approximately 232 h and the results were used to determine the half-lives of ^{197g}Hg and ^{197m}Hg. The HPGe spectrometers were carefully calibrated for energy and efficiency with a set of ^{241}Am (489.3 kBq, combined standard uncertainty 0.4%), ^{133}Ba (75.77 kBq, combined standard uncertainty 0.5%) and ^{152}Eu (477.2 kBq, combined standard uncertainty 0.6%) standards that were provided by the Czech Metrology Institute, Prague. The nuclear data for the standard radionuclides were taken from Ref. [11].

The analysis of the γ-ray spectra was carried out with the $gf3$ program of the RADWARE spectroscopy package [12]. The basic parameters, such as peak shape and FWHM as a function of the γ-ray energy, were determined from the calibration sources spectra, and were fixed during the fitting procedure. A parallel analysis using the GENIE2000 software [13] was also carried out and the results were found to be consistent with those obtained using the $gf3$ program.

3. Results and discussion

The γ-ray spectrum that was used to determine the relative γ-ray emission probabilities in the decays of ^{197g}Hg and ^{197m}Hg is shown in Fig. 2. Measured γ-ray energies and emission probabilities are presented in Table 1, together with values for the transition multipolarities, M1+E2 mixing ratios (δ) and total electron conversion coefficients (α_T). Given the assigned γ-ray transition multipolarities, the α_T values were determined using the *BrICC* code [10] and for γ rays of a mixed M1+E2 multipolarity they were calculated as:

$$\alpha_T(M1+E2) = \frac{\alpha_I(M1) + \delta^2\alpha_I(E2)}{1+\delta^2} \quad (1)$$

where α_T(M1) and α_T(E2) are the total conversion coefficient for pure M1 and E2 multipolarities, respectively. The δ values for the 77.31-keV and 278.65-keV γ rays were obtained from a least-squares fit to the available experimental data, presented in Table 2, using the *bricemixing* program [29].

The quoted uncertainties in the γ-ray emission probabilities represent one standard deviation and these were obtained from the quadratic

Table 2
Experimental data, including K, L and total electron conversion coefficient, sub-shell electron ratios and mixing ratios from $\gamma\gamma(\theta)$ measurements, used to determine the M1+E2 mixing ratios for the 278.65-keV and 77.31-keV γ rays.

278.65-keV γ ray	Reference	77.31-keV γ ray	Reference
$\alpha_K = 0.29$ (3)	[14]	$\alpha_T = 4.37$ (10)	[15]
$\delta = -0.41$ (4)	[16]	$\alpha_L = 2.46$ (26)	[17]
$\delta = -0.33$ (9)	[18]	M1/M2/M3 = 100/44 (4)/0.41 (4)	[19]
$\delta = -0.40$ (4)	[20]	L1/L2/L3 = 100/44 (3)/35 (2)	[19]
$\delta = -0.39$ (2)	[21]	L1/L2/L3 = 100/51 (1)/37 (1)	[22]
$\alpha_K = 0.32$ (4)	[23]	L1/L2/L3 = 100/44 (4)/32 (2)	[24]
K/L = 4.8 (5)	[25]	L1/L2/L3 = 100/42 (7)/35 (8)	[26]
L1/L2/L3 = 100/17.9 (27)/4.8 (7)	[27]	$\delta = -0.352$ (5)	[28]

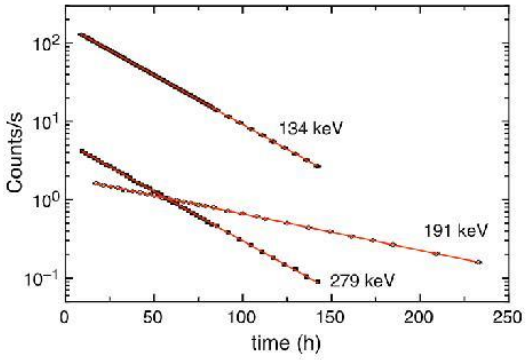

Fig. 3. Activities for the 133.79-keV and 278.65-keV γ rays (^{197m}Hg), and 191.20-keV γ ray (^{197g}Hg) as a function of time after irradiation.

Table 3
Comparison between the measured in the present work EC and IT branching ratios and the absolute γ ray emission probabilities for the 133.79 keV and 278.65 keV γ rays with previously published values.

EC (%)	IT (%)	I_γ(133.79 keV γ ray) (%)	I_γ(278.65 keV γ ray) (%)	Reference
5.32 (9)	94.68 (9)	34.8 (3)	3.79 (4)	Present work
8.6 (7)	91.4 (7)	33.5 (3)	6.1 (5)	NDS2005 [1,30]
8.6 (7)	91.4 (7)	33.5 (3)	6.1 (5)	NDS1995 [5,30]
7.0 (7)	93.0 (7)	34 (4)	5.0 (7)	NDS1991 [6,27]
7.0 (7)	93.0 (7)	34 (4)	5.0 (7)	TOI1999 [8,27]
6.5 (10)	93.5 (10)	34.3 (5)	5.4 (4)	TOI1978 [7,31]
8.6 (7)	91.4 (7)	33.5		NUDAT [32]
8.6 (7)	91.4 (7)	33.9 (3)	6.1 (5)	ENDF/BVIII.0 [33]
8.6 (7)	91.4 (7)	33.5 (3)	6.1 (5)	JEFF3.3 [34]

sum of individual uncertainties that arise from the statistics of the full-energy peaks, relative detector efficiency (~0.5%), dead-time corrections (~0.2%), and peak/background modeling (~0.2%). Using the established decay scheme of ^{197m}Hg, shown in Fig. 1, and the data presented in Table 1, the %EC and %IT branching intensities of ^{197m}Hg can be determined from:

$$\%EC/\%IT = \frac{I_\gamma^{tot}(130.00\gamma) + I_\gamma^{tot}(408.7\gamma)}{\frac{1}{2}(I_\gamma^{tot}(133.79\gamma) + I_\gamma^{tot}(164.84\gamma))} \quad (2)$$

$$\%EC + \%IT = 100 \quad (3)$$

where $I_\gamma^{tot} = I_\gamma \times (1 + \alpha_T)$ is the total γ-ray emission probability and I_γ is the relative γ-ray emission probability (column 2 of Table 1). Comparison between the presently determined EC and IT branching ratio for ^{197m}Hg with results from previous evaluations is presented in Table 3. It should be pointed out that the deduced in the present work EC = 5.32 (9)% differs significantly from that of 8.6 (7)%, recommended in the most-recent ENSDF evaluation [1] that is based on the value reported in Ref. [30]. Similarly, the absolute γ-ray emission probability for the 278.65-keV γ rays is approximately a factor of two smaller compared to that recommended in Ref. [1]. Somewhat different branching intensities were reported in the earlier ENSDF evaluation [6], adopted also in the latest edition of the Table of Isotopes [8], which are based only on the γ-ray emission probabilities measured in Ref. [27] and the known at that time values for δ and α_L. The values published in the earlier version of Table of Isotopes [7] were based on the γ-ray emission probabilities reported in Ref. [31].

The general purpose databases, such as ENDF [33] and JEFF [34], use the most-recent data recommended in ENSDF [1], although there is a small discrepancy in the absolute γ-ray emission probability for the 133.79-keV γ ray that is quoted in Ref. [33] as 33.9 (3)%. Controversially, while the data for the EC decay of ^{197m}Hg are included in the ENSDF database [1], they are missing in NUDAT [32], which is frequently used by the applications community and considered as a "friendly face"of ENSDF. In addition, the value for the absolute emission probability of the 133.79-keV γ ray is given without an uncertainty in NUDAT [32], which is misleading.

The half-lives of ^{197g}Hg and ^{197m}Hg were determined by measuring the net-peak areas as a function of time for the strongest γ rays that follow their decay. The corresponding time spectra are shown in Fig. 3. The statistical uncertainties of the net-peak areas ranged between 0.11 and 2.5%, while the systematic uncertainties were estimated to be ~1% and included contributions from geometrical efficiency corrections (~0.6%), the peak/background modeling (~0.2%) and dead-time corrections (~0.2%). The half-life of ^{197m}Hg was determined as 23.82 (4) h and 23.81 (6) h by fitting the net-peak areas of the 133.79-keV and 278.65-keV γ rays, respectively, as a function of time with a single exponential decay curve. The presently determined value is consistent with that of 23.8 (1) h recommended in the most-recent ENSDF evaluation [1], but it is more precise. The half-life of ^{197g}Hg was determined from a two exponential fit to the net-peak area of the 191.20-keV γ ray as a function of time and by fixing the half-life of ^{197m}Hg to 23.82 (4) h. The obtained value of 64.81 (24) h in the present work is somewhat larger compared to that of 64.14 (5) h that is recommended in the most-recent ENSDF evaluation [1], which is based on the yet unpublished data reported in Ref. [35].

In summary, the decays of ^{197g}Hg and ^{197m}Hg were studied by means of γ-ray spectroscopy counting of chemically-purified radioactive sources with a planar HPGe detector. Accurate emission probabilities were measured for γ rays that followed the decays of these radionuclides. The IT and EC branching intensities of ^{197m}Hg were determined and the latter were found to differ significantly from previously published values. The half-lives of ^{197g}Hg and ^{197m}Hg were also measured with a high precision.

Declaration of competing interest

The authors declare that they have no known competing financial interests or personal relationships that could have appeared to influence the work reported in this paper.

CRediT authorship contribution statement

O. Lebeda: Data curation, Funding acquisition, Investigation, Methodology, Project administration, Resources, Software, Supervision, Writing - review & editing. **F.G. Kondev:** Investigation, Methodology, Software, Visualization, Writing - original draft, Writing - review & editing. **J. Červenák:** Data curation, Investigation, Methodology.

Acknowledgments

This work was supported by the U.S. Department of Energy, Office of Nuclear Physics, under Contract No. DE-AC02-06CH11357 and by the ERDF/ESF project CANAM-OP of the Ministry of Education, Youth and Sports of the Czech Republic (No. CZ.02.1.01/0.0/0.0/16_013/0001812). The authors wish to express their gratitude to Dr. Kameník for his help in the production of the sources and with the γ-ray spectra acquisition.

References

[1] H. Xiaolong, Z. Chunmey, Nucl. Data Sheets 104 (2005) 283.
[2] R. Prendenberg, R. Apolle, M. Walther, H. Hartmann, J. Kotzerke, Eur. J. Nucl. Med. Mol. Imaging 5 (15) (2018).
[3] J. Červenák, O. Lebeda, Nucl. Instrum. Methods Phys. Res. B 458 (2019) 118.
[4] O. Lebeda, J. Červenák, Nucl. Instrum. Methods Phys. Res. B 461 (2019) 105.
[5] C. Zhou, Nucl. Data Sheets 76 (1995) 399.
[6] C. Zhou, Nucl. Data Sheets 62 (1991) 433.
[7] C. Michael Lederer, Virginia S. Shirley (Eds.), Table of Isotopes, seventh ed., Wiley, New York, 1978.
[8] R.B. Firestone, S.Y. Frank Chu, C.M. Baglin (Eds.), Table of Isotopes 8th Edition: 1999 Update, Wiley, New York, 1999.
[9] M. Wang, G. Audi, F.G. Kondev, W.J. Huang, S. Naimi, X. Xu, Chin. Phys. C 41 (2017) 030003.
[10] T. Kibéi, T.W. Burrows, T. M.B. Trzhaskovskaya, C.W. Nestor Jr., Nucl. Instrum. Methods Phys. Res. A 589 (2008) 202.
[11] Update of X Ray and Gamma Ray Decay Data StandArds for Detector Calibration and Other Applications, STI/PUB/1287 v. 2, International Atomic Energy Agency, 2007.
[12] D.C. Radford, Nucl. Instrum. Methods Phys. Res. A 361 (1995) 297.
[13] GENIE2000 basic spectroscopy software, https://www.mirion.com/products/genie-2000-basic-spectroscopy-software.
[14] R. Joly, J. Brunner, J. Halter, O. Huber, Helv. Phys. Acta 28 (1955) 403.
[15] D.J. Erickson, L.D. Roberts, J.W. Burton, J.O. Thomson, Phys. Rev. B 3 (1971) 2180.
[16] M. Martin, P. Marmier, J. de Boer, Helv. Phys. Acta 31 (1958) 435.
[17] S. Bhuloka Reddy, D. Sudhakara Reddy, K.L. Narasimham, B.V. Thirumala Rao, V. Lakshminarayana, Curr. Sci. 45 (1976) 791.
[18] F.K. McGowan, P.H. Stelson, Phys. Rev. 109 (1958) 901.
[19] V.Y. Padalko, P.P. Zarubin, Y.V. Khrisanfov, Bull. Acad. Sci. USSR, Phys. Ser. 36 (1973) 2217.
[20] F.K. McGowan, W.T. Milner, R.L. Robinson, P.H. Stelson, Ann. Phys. 63 (1971) 549.
[21] A.E. Stuchbery, L.D. Wood, H.H. Bolotin, C.E. Doran, I. Morrison, A.P. Byrne, G.J. Lampard, Nuclear Phys. A 486 (1988) 374.
[22] D. Krpić, R. Stepić, I. Bikit, J. Milanović, R. Vukanović, Z. Phys. 243 (1971) 452.
[23] F. Smend, W. Weirauch, W.-D. Schmidt-Ott, A. Flammersfeld, Z. Phys. 191 (1966) 1.
[24] L.J. van Heerden, D. Reitmann, H. Schneider, Nuovo Cimento 11 (1959) 167.
[25] R.P. Sharma, H.L. Nielsen, Nuclear Phys. A 152 (1970) 401.
[26] A. Backlin, S.G. Malmskog, Ark. Fys. 34 (1967) 59.
[27] Z. Plajner, I. Řezanka, A. Špalek, J. Prána, M. Josovič, M. Fišer, Czech. J. Phys. B 20 (1970) 917.
[28] H. Prosser, F.E. Wagner, G. Wortmann, G.M. Kalvius, R. Wäppling, Hyp. Inter. 1 (1975) 25.
[29] T. Kibédi, Private communication, https://www-nds.iaea.org/public/ensdf_pgm.
[30] N. Chakravarty, S.S. Rattan, R.J. Singh, A. Ramaswami, Radiochim. Acta 61 (1993) 9.
[31] A.J. Haverfield, H.T. Easterday, J.M. Hollander, Nuclear Phys. 64 (1965) 379.
[32] NUDAT databases at www.nndc.bnl.gov, 2019, (Retrieval on 17 November 2019).
[33] ENDF databases at www.nndc.bnl.gov, 2019, (Retrieval on 17 November 2019).
[34] JEFF3.3 database at www.oecd-nea.org/dbdata/jeff/jeff33/, 2019, (Retrieval on 17 November 2019.
[35] J.S. Eldridge, W.S. Lyon, ORNL-3889, 1966, p. 49.

Publikácia VI

Červenák J., Lebeda O.

New cross-section data for proton-induced reactions on ^{nat}Ti and ^{nat}Cu with special regard to the beam monitoring

Submitted into: Nucl. Instrum. Methods Phys. Res. B
Submitted manuscript NIMB-S-20-00521

New cross-section data for proton-induced reactions on ^{nat}Ti and ^{nat}Cu with special regard to the beam monitoring

Jaroslav Červenák, Ondřej Lebeda
Nuclear Physics Institute of the CAS, Husinec-Řež 130, 250 68 Řež, Czech Republic

Abstract
Excitation functions of the reactions ^{nat}Ti(p,x)^{48}V, ^{43}Sc, ^{44g}Sc, ^{44m}Sc, $^{46m+g}$Sc, ^{47}Sc, ^{48}Sc and ^{nat}Cu(p,x)^{62}Zn, ^{63}Zn, ^{65}Zn, ^{61}Cu, $^{58m+g}$Co were measured in the energy interval of 6.4–36.0 MeV (titanium) and 7.3–35.9 MeV (copper) with use of stacked-foil technique and off-line γ-ray spectrometry. The results were compared with previously published experimental data and with prediction of the nuclear reaction model code TALYS adopted from the TENDL-2019 online library. Thick target yields were calculated from the obtained cross-sections. Finally, we fit the selected experimental data sets for the ^{nat}Ti(p,x)^{48}V and ^{nat}Cu(p,x)^{62,63,65}Zn reactions and compare the results with the IAEA recommended cross-sections.

1. Introduction

Nuclear reactions of heavy charged particles on metals easily available as thin foils of even thickness and forming well measurable radionuclides are suitable for cyclotron beam monitoring. Among them, proton-induced reactions on aluminium, titanium and copper resulting in sodium, vanadium, scandium, zinc and cobalt isotopes are the most widespread. For such a purpose, precise knowledge of their excitation functions is inevitable. Reasonable amount of sound experimental data is required for construction of recommended cross-sections for the beam monitoring [1], and more independent measurements contribute to their reliability and gradual improvement.

We have, therefore, carefully re-measured excitation functions of proton-induced reactions on titanium and copper. Part of these unpublished data was already provided in a private communication for deducing recommended cross-sections [1]. In this work, we present complete experimental material.

2. Experimental

2.1 Target and irradiation

The cross-sections were measured using well-established stacked foil method followed by off-line γ-ray spectrometry. Two stacks of metal foils were irradiated on the external proton beam of cyclotron U-120M in the Nuclear Physics Institute of the CAS. Both stacks contained ten ^{nat}Mo foils (99.9 %, 19.3 μm thick, Goodfellow, GB), ten ^{nat}Cu foils (99.9 %, 10.6 μm thick, Goodfellow, GB), eleven ^{nat}Ti foils (99.6 %, 11.0 μm thick, Alfa Aesar, USA) and some ^{nat}Cu foils (55.9 μm thick) acting as energy degraders where needed.

Both stacks were placed in a Faraday-cup-like target holder and irradiated for one hour. The incident proton beam energy was deduced from the precise beam orbit position measurement [2]. Proton energy in the centre of each foil in the stack was calculated using stopping power of protons in the foil material using the code SRIM [3]. Beam current was kept constant during irradiation, recorded each second and integrated over the bombardment time t_b.

2.2 Activity measurement

The stacks were disassembled soon after the end of bombardment (EOB), and single foils were measured on energy and efficiency calibrated HPGe detectors (GMX45-Plus, Ortec and GC2019, Canberra). The calibration was performed using a set of standards (^{241}Am, ^{152}Eu, ^{137}Cs, ^{133}Ba and ^{60}Co) provided by the Czech Institute of Metrology with combined standard uncertainties varying from 0.4 % to 1.0 %. Detection efficiency curves were obtained for various distances sample to detector ranging from 150 mm to 1 600 mm. A polynomial of the 5th degree was used to fit the logarithm of efficiency versus the logarithm of energy. For the γ-ray energies exceeding 240 keV, a linear fit was used.

Each foil was measured three to six times in order to optimize quantification of radionuclides with various half-lives. The acquired γ-ray spectra were evaluated using the program DEIMOS32 [4]. The decay data (half-lives, γ-ray energies and their emission probabilities) were taken from the online database NuDat2 [5]. Nuclear reaction energies and thresholds were calculated using an online calculator Q-calc [6]. All these data for all the radionuclides identified in the irradiated target are summarized in Table 1.

2.3 Calculation of cross-sections, their uncertainties, thick target yields and prediction of excitation functions

Cross-sections were calculated using the activation formula (equation 1):

$$\sigma = \frac{P_\gamma}{I_\gamma \eta t_m} \frac{\lambda t_r}{1 - e^{-\lambda t_r}} e^{\lambda t_c} \frac{Aze}{d\rho N_A I (1 - e^{-\lambda t_b})}, \quad (1)$$

where σ is cross-section for formation of a radionuclide at the energy in the middle of the foil (cm^2), P_γ is net peak area of a γ-line used for the radionuclide's quantification, I_γ is emission probability of this γ-line per decay, η is detection efficiency for this γ-line, t_m is life time of the measurement (h), t_r is real time of measurement (including the dead time) (h), t_c is time between the EOB and the start of the measurement (h), A is atomic weight of the foil's metal (g/mol), z is proton charge (z = 1), e is elementary charge (1.602177×10^{-19} C), d is foil's thickness (cm), ρ is density of the foil's metal (g/cm^3), N_A is Avogadro's number (6.022137×10^{23} mol^{-1}), I is beam current (A), λ is decay constant of the radionuclide (h^{-1}) and t_b is bombardment time (h).

Total cross-section uncertainty was calculated as a square root of a sum of squares of the relative uncertainties of the particular quantities appearing in the activation formula:

- detection efficiency for a γ-line selected for activity calculation (max. 3 %)
- emission probability of a γ-line selected for activity calculation (usually < 5 %)
- net peak area of a γ-line selected for activity calculation (0.1–10 %)
- beam current (ca 6 %)
- foil's thickness (< 2 %)

The measured cross-sections were compared with previously published values and with prediction of the TALYS nuclear reaction model code adopted from TENDL-2019 library [7].

2.4 Interference treatment

The radionuclides ^{48}V and ^{48}Sc decay to the same product (^{48}Ti) and their most intense γ-lines have the same energy. The activity of ^{48}Sc was, therefore, calculated using its 1037.52-keV line absent in the ^{48}V decay scheme, while the activity of ^{48}V was measured after practically complete decay of ^{48}Sc (ca 15–20 days post EOB, see Table 1).

In the generator system ^{44m}Sc/^{44g}Sc, the activity of the daughter radionuclide born from the parent radionuclide during the irradiation (equation 2) and after EOB (equation 3) was calculated.

$$A_2^{EOB} = f\frac{d\rho N_A \sigma I}{Aze}\left(1 - \frac{\lambda_2}{\lambda_2 - \lambda_1}e^{-\lambda_1 t_b} + \frac{\lambda_1}{\lambda_2 - \lambda_1}e^{-\lambda_2 t_b}\right) \quad (2)$$

$$A_2 = f\frac{\lambda_2}{\lambda_2 - \lambda_1}A_1^{EOB}\left(e^{-\lambda_1 t_c} - e^{-\lambda_2 t_c}\right) + A_2^{EOB}e^{-\lambda_2 t_c}, \quad (3)$$

where f is transition probability of the parent to the daughter radionuclide, λ_1 represent the decay constant of the parent radionuclide (h^{-1}) and λ_2 represent the decay constant of the daughter radionuclide (h^{-1}), other symbols have the above-mentioned meaning.

The contribution of ^{44m}Sc decay was subtracted from the measured activity of ^{44g}Sc in order to obtain its amount born directly in proton-induced reactions. For a more detailed description, cf. [8,9].

3. Results and discussion

3.1 Beam energy and current

Proton beam energy deduced from the precisely measured beam orbit position was 36.00 ± 0.30 MeV and 21.35 ± 0.30 MeV respectively for the 1st and 2nd stack of foils. The beam current obtained from continuous recording of the proton beam was 1.230 μA for the 1st stack and 0.5078 μA for the 2nd stack of foils. These values were used for calculation of cross-sections without any further correction and their estimated uncertainty was 6 %. The data obtained from both irradiations are well consistent providing smooth curves without any visible "break" between the stacks (cf. Figs. 2–18).

3.2 Measured activities, cross-sections and predicted excitation functions

All measured cross-sections are summarised in Tables 2 and 3. The excitation functions and cross-sections are discussed in the following paragraphs and shown in Figs. 2–18 together with previously published experimental data and theoretical predictions of the TALYS nuclear reaction model code adopted from the TENDL-2019 online library.

3.2.1 Recoiled atoms

We measured activity of radioisotopes recoiled from titanium foils onto the following copper foils and added it to the activity measured in the original titanium foil. Activity of the recoiled atoms for scandium isotopes varied in the interval of 1.5–4.5 %. Percentage of the recoiled ^{48}V activity is shown in Fig. 1. It increases almost linearly from 0.8 to 2.2 % for energies up to 20 MeV, then the increase becomes significantly less pronounced and the values vary between 2.1 and 2.6 % for energies up to 36 MeV.

3.2.2 Cross-sections for $^{nat}Ti(p,x)^{48}V$ reactions

The activity of ^{48}V was evaluated as the mean activity calculated via its most intense 983.525 keV and 1312.106 keV γ-lines after the complete decay of ^{48}Sc, as described in the Section 2.4. The experimental data [10–27] are shown in Fig. 2 and are rather consistent except a few data sets. Data of Walton et al. 1976 [13] are scattered in the energy region of 25–40 MeV and data of Jung et al. 1991 [18] and Khandaker et al. 2009 [24] seem to be shifted towards higher energies by 1–2 MeV. Theoretical prediction of cross-sections [7] overestimates their values in the energy interval of 5–15 MeV (the peak region), but the shape of the excitation function is practically identical with the experimental observations.

The selected data [10,16,17,19,20,22,23,25 and this work] are shown in Fig. 3 and comparison of their polynomial fit with the theoretical model and IAEA recommended data [1] is shown in Fig. 4 and in Table 4. It agrees very well with the IAEA recommended cross-sections, the only remarkable difference regards the shape and position of the maximum of the function – the IAEA fit suggests smooth, more symmetric shape of the peak, its maximum occurs at ca 1.5 MeV lower. In this aspect, our fit corresponds more with the TENDL-2019 prediction values.

3.2.3 Cross-sections for $^{nat}Ti(p,x)^{43}Sc$ reactions

Calculation of ^{43}Sc activity was performed using its 372.9 keV γ-line with intensity of 22.5 %. All previously published data [14,19,23,24,27] shown in Fig. 5 are consistent except a few points of Khandaker et al. 2009 [24] that seem to be shifted systematically to higher values. Prediction of the TENDL-2019 library [7] for the energy region below 30 MeV shows two maxima that are observed also in the experimental material, although the first maximum underestimates the experiments, while the second one overestimates them. For energies exceeding 30 MeV, theoretical model forecasts more rapid and steeper increase of the excitation function.

3.2.4 Cross-sections for $^{nat}Ti(p,x)^{44g}Sc$ reactions

Cross-sections of ^{44g}Sc were calculated using its prominent 1157.020 keV γ-line with intensity of 99.9 %. Contribution of ^{44m}Sc decay to ^{44g}Sc activity was corrected as described in the Section 2.4. The experimental data [14,19,23,24] are shown in Fig. 6 and are consistent up to approximately 27 MeV, where our values starts to be slightly lower than the cross-sections of Michel et al. 1978 [14] and Khandaker et al. 2009 [24]. The TENDL-2019 values [7] are in a good agreement with our data up to 30 MeV, where the model predicts a quicker decrease of cross-sections.

3.2.5 Cross-sections for $^{nat}Ti(p,x)^{44m}Sc$ reactions

Activity of ^{44m}Sc was evaluated using its 271.241 keV γ-line with intensity of 86.7 %. Experimental cross-sections [11,14,15,17,19,20,23,24,27] for reactions leading to ^{44m}Sc displayed in Fig. 7 are in a fairly good agreement with each other within their uncertainties. Theoretical prediction of the TALYS code [7] underestimates the experimental values in the region of the second, more pronounced peak (E_p > 22 MeV).

3.2.6 Cross-sections for $^{nat}Ti(p,x)^{46m+g}Sc$ reactions

Evaluation of $^{46m+g}$Sc activity was performed using its 889.277 keV γ-line with intensity of 99.9840 %. Calculated cross-sections are in fact cumulative and include the contribution of the short-lived isomer ^{46m}Sc with half-life of 18.75 s that decays solely via isomeric transition to the ground state.

Experimental data [11,17,24,27,28] shown in Fig. 8 are all in a good agreement, although Khandaker's et al. 2009 data [24] seem to be systematically higher (2–4 mb) in the energy region of 4–27 MeV. IAEA's recommended cross sections [1] are practically identical to Hermanne's et al. 2014 [28] fit of their experimental cross-section points. Even though our values agree well with IAEA's and Hermanne's fit in the energies up to 30 MeV, in the higher energy region, our cross-sections are slightly higher, and they indicate a steeper increase. Theoretical prediction underestimates the measurements in the energy region of 15–30 MeV but matches them very well for $E_p > 31$ MeV.

3.2.7 Cross-sections for $^{nat}Ti(p,x)^{47}Sc$ reactions

Cross-sections of ^{47}Sc were calculated using its 159.381 keV γ-line with intensity of 68.3 %. All the experimental data [11,14,15,17,19,20,23,24,27] shown in Fig. 9 provide quite consistent picture overlapping each other within indicated uncertainties, except the cross-sections of Brodzinski et al. 1971 [11]. Theoretical model [7] predicts a steeper increase of the excitation function, a maximum that is slightly shifted to higher energies and ca 1.6 times higher than the experimental data.

3.2.8 Cross-sections for $^{nat}Ti(p,x)^{48}Sc$ reactions

Activity of ^{48}Sc is based on its non-interfering 1037.522 keV γ-line with intensity of 97.6 %. Experimental cross-sections [11,14,17,20,24,27] displayed in Fig. 10 follow all the same trend without significant discrepancies except one outlying point of Brodzinsky et al. 1971 [11]. Theoretical prediction of the TENDL-2019 library [7] agrees with the measured data quite well but overestimates the experimental values in the energy region of 27–40 MeV almost 1.5 times.

3.2.9 Cross-sections for $^{nat}Cu(p,x)^{62}Zn$ reactions

Cross-sections of ^{62}Zn were evaluated using its 596.56 keV γ-line with intensity of 26.0 %. This γ-line was chosen because of the best statistics of the counts in the photopeak in the γ-ray spectra. Activity of ^{62}Zn calculated from this γ-line was systematically lower by 2.36 ± 0.78 % in comparison to the one calculated from the 548.35 keV γ-line (intensity of 15.3 %).

The available experimental material [20–22,29–42] is recapitulated in Fig. 11. Our data are in a very good agreement with data of Mills et al. 1992 [34], Szelecsényi et al. 2001 [21], Takács et al. 2002 [22] and Jost et al. 2013 [41]. The only measurements that exceed significantly (sometimes even more than twice) the other published cross-sections are those of Williams et al. 1967 [30] and Aleksandrov et al. 1987 [32] (excluded from Fig. 11). Theoretical prediction of TALYS model code [7] describes well the shape of the experimental data but the maximum of the excitation function is slightly shifted towards lower energies (by ca 1 MeV) and shows 1.6 times lower values.

Data selection [20,21,24,29,34,36,37,40–42 and this work] together with their polynomial fit are reported in Fig. 12. The cross-sections resulting from the fit are summarized in Table 4. The fit is in a very good agreement with the IAEA recommended cross-sections [1].

3.2.10 Cross-sections for $^{nat}Cu(p,x)^{63}Zn$ reactions

Activity of ^{63}Zn was deduced from the net peak area of its 669.62 keV γ-line with intensity of 8.2 % because its photopeak had the lowest uncertainty of the net-peak-area in the acquired γ-ray spectra. The activities calculated using this γ-line were systematically higher by 2.7 ± 1.7 % higher compared to the ones deduced from the 962.06 keV line with intensity of 6.5 %.

The published cross-sections [12,21,22,31–34,38,40,43–48] displayed in Fig. 13 represent a consistent body with a few exceptions (data sets of Barrandon et al. 1975 [12] and Alexandrov et al. 1987 [32] that clearly overestimate other measured values). Selected data [21,22,38,31,34,40,43–47] and this work are displayed in Fig. 14 and the cross-sections of their polynomial fit are summarized in Table 4. The fit doesn't practically differ from the IAEA recommended cross-sections [1], only the maximum of our selection is shifted by ca 1 MeV to higher energies.

Theoretical prediction [7] corresponds with the experimental data in its shape but seems to be shifted to lower energies by ca 1–2 MeV and shows approximately 1.4 times lower cross-section values in the peak region.

3.2.11 Cross-sections for $^{nat}Cu(p,x)^{65}Zn$ reactions

Evaluation of ^{65}Zn activity was based on its 1115.539 keV γ-line with intensity of 50.04 %. Experimental data [12,21,22,27,36,38,40,42,44–47,49–51] together with IAEA recommended cross-sections [1] and the theoretical prediction of cross-sections [7] are shown in Fig. 15. Obviously, all the data follow the same trend with a minimal scattering. The minor exception represents the work of Garrido et al. 2016 [27], whose data seem to be slightly shifted towards higher energies. This is the reason why the values of his work were skipped from the data selection for the fit/recommended cross-sections (Fig. 16, Table 4). Our fit of the selected data copies perfectly the IAEA recommended values in the whole energy range. Theoretical prediction of TALYS reaction model code follows the same shape as the experimental data, however it seems to be shifted to lower energies by ca 1 MeV and its maximum shows higher values by ca 20 mb.

3.2.12 Cross-sections for $^{nat}Cu(p,x)^{61}Cu$ reactions

Cross-sections of ^{61}Cu were calculated from the net peak area of 282.956 keV γ-line with intensity of 12.9 % and 656.008 keV γ-line with intensity of 9.8 %. The data obtained using the above given intensities provided consistent cross-section values that differ on average by 2.25 %. When using the intensities from the online library NuDat 2.6 [5] (282.956 keV, 12.2 %; 656.008 keV, 10.8 %), the cross-sections differ systematically by 14.04 ± 0.14 % (higher values for 282.956 keV γ-line). This demonstrates a significant inconsistency in the published emission probabilities that moved us to the decay data revision that will be published later.

The cross-sections based on the 282.956 keV γ-line (12.9 %) are displayed in Fig. 17. Experimental data [20,27,30-32,34,38,42,52,53] show similar shape of the excitation function and their scattering may be partly due to the decay data discrepancies. Only cross-sections of Williams et al. 1967 [30] are clearly too low for proton energies exceeding 30 MeV. Data of Aleksandrov et al. 1987 [32] and Yashima et al. 2003 [53] follow the same trend as the remaining experimental data but they seem to be shifted to lower energies by ca 4 MeV. Theoretical model [7] is in a fair agreement with experimental data up to ca 33 MeV, and then it starts to decrease more rapidly compared to them.

3.2.13 Cross-sections for $^{nat}Cu(p,x)^{58m+g}Co$ reactions

Activity of ^{58g}Co was calculated from the net peak area of its prominent 810.7593 keV γ-line with intensity of 99.450 %. The measured cross-sections are cumulative with regard to the low-energy-level metastable state ^{58m}Co with a half-life of 9.10 h. This isomer emits only single γ-line with energy of 24.889 keV and intensity of 0.0379 % and is thus practically invisible for the detectors used in this experiment. The activity of the ground state was calculated from the spectra acquired after the complete decay of the isomer.

The results, in the context of the previously published data [27,31,42,50,52,53,54], are shown in Fig. 18. The experimental material is consistent except the works of Greenwood et al. 1984 [54] and Yashima et al. 2003 [53] that significantly overestimate the other data sets. The IAEA recommended cross sections [1] agree with the selected experimental data within uncertainties. In contrast, the prediction of the TENDL-2019 [7] underestimates the measured data approximately twice in the energy interval 30–40 MeV.

3.3 Thick target yields

Thick target yields were calculated for all the quantified radionuclides. The experimental cross-section data were fitted with one or two polynomials and integrated using the stopping power of protons in titanium or copper. The deduced thick target yields are displayed in Figs. 19–24.

4. Conclusion

In this paper, we present new measurement of excitation functions for the $^{nat}Ti(p,x)^{48}V$, ^{43}Sc, ^{44g}Sc, ^{44m}Sc, $^{46m+g}Sc$, ^{47}Sc, ^{48}Sc reactions in the energy range 6.4–36.0 MeV, and for the $^{nat}Cu(p,x)^{62}Zn$, ^{63}Zn, ^{65}Zn, ^{61}Cu, $^{58m+g}Co$ reactions in the energy range of 7.3–35.9 MeV. Our cross-sections were compared with previously published experimental data and with prediction of the nuclear reaction model code TALYS adopted from the TENDL-2019 online library. We calculated thick target yields for all the radionuclides listed above.

In case of $^{nat}Ti(p,x)^{48}V$ and $^{nat}Cu(p,x)^{62}Zn$, ^{63}Zn, ^{65}Zn reactions, we selected the most reliable published experimental data, fitted them with simple polynomials and compared the results with the recently up-dated IAEA recommended cross-sections. The differences are marginal for the $^{nat}Cu(p,x)^{62}Zn$, ^{63}Zn, ^{65}Zn reactions. In the excitation function of $^{nat}Ti(p,x)^{48}V$ reaction, we, however, noticed an interesting disagreement around the excitation function maximum: while our fit is "beveled" from the side of lower energies, the IAEA fit suggests quite symmetric shape of the peak.

We noticed significant inconsistency in the published intensities of the ^{61}Cu γ-lines that initiated decay scheme revision that is to be published in a separate work.

Acknowledgement

The authors are grateful to the crew of the U-120M cyclotron for the irradiations and to Dr. Petr Hanč and Anton Cvíčela for the help with the γ-ray spectra measurements. The work was supported by the IAEA Coordinated Research Project "*Nuclear Data for Charged-Particle Monitor Reactions and Medical Isotope Production*" under the contract no. 17461, by the Czech Academy of Sciences under the NPI research plan AV0Z10480505 and the irradiations were carried out at the CANAM infrastructure of the NPI CAS Řež supported through MEYS project no. LM2011019.

References

[1] A. Hermanne, A.V. Ignatyuk, R. Capote, B.V. Carlson, J.W. Engle, M.A. Kellett, T. Kibedi, G. Kim, F.G. Kondev, M. Hussain, O. Lebeda, A. Luca, Y. Nagai, H. Naik, A.L. Nichols, F.M. Nortier, S.V. Suryanarayana, S. Takács, F. Tárkányi, M. Verpelli. *Reference Cross Sections for Charged-particle Monitor Reactions*. Nuclear Data Sheets 148 (special issue), pp. 338–382, 2018. https://doi.org/10.1016/j.nds.2018.02.009

[2] M. Čihák, O. Lebeda, J. Štursa, *Beam dynamic simulation in the isochronous cyclotron U-120M*, in: Proceedings of the eighteenth international conference on cyclotrons and their applications, CYCLOTRONS 2007, Giardini Naxos, Italy, 2007.

[3] Ziegler J.F., Ziegler M.D., Biersack J.P.: SRIM2010 Code. Available at URL <http://www.srim.org/>

[4] J. Frána: *Program DEIMOS32 for gamma-ray spectra evaluation*. J. Radioanal. Nucl. Chem. 257(3), pp. 583–587, 2003. https://doi.org/10.1023/A:1025448800782.

[5] NuDat 2.6. National Nuclear Data Center, Brookhaven National Laboratory, 2012. Available at URL <www.nndc.bnl.gov/nudat2/>.

[6] B. Pritychenko, A. Sonzogni, Q-value calculator, NNDC, Brookhaven National Laboratory. Available from URL <http://www.nndc.bnl.gov/qcalc>.

[7] A.J. Koning, D. Rochman, S.C. van der Marck, J. Kopecky, J.Ch. Sublet, S. Pomp, H. Sjostrand, R. Forrest, E. Bauge, H. Henriksson, O. Cabellos, S. Goriely, J. Leppanen, H. Leeb, A. Plompen, R. Mills, *TALYS-based evaluated nuclear data library*. Available from URL <http://www.talys.eu/tendl-2019>.

[8] O. Lebeda, V. Lozza, P. Schrock, J. Štursa, K. Zuber, Excitation functions of proton-induced reactions on natural Nd in the 10–30 MeV energy range, and production of radionuclides relevant for double-β decay, Phys. Rev. C 85 (1) (2012) 014602, https://doi.org/10.1103/PhysRevC.85.014602

[9] J. Červenák, O. Lebeda, Experimental cross-sections for proton-induced reaction on ^{nat}Mo, Nucl. Inst. Methods Phys. Res. B 380 (2016) 32–49, https://doi.org/10.1016/j.nimb.2016.05.006

[10] Tanaka S., Furukawa M.: *Excitation Functions for (p,n) Reactions with Titanium, Vanadium, Chromium, Iron and Nickel Up to 14 MeV,* Journal of the Physical Society of Japan Vol. 14, p. 1269, 1959

[11] Brodzinski R.L., Rancitelli L.A., Cooper J.A., Wogman N.A.: *High-Energy Proton Spallation of Titanium,* Physical Review, Part C, Nuclear Physics Vol. 4, p. 1250, 1971

[12] Barrandon J.N., Debrun J.L., Kohn A., Spear R.H.: *A Study of the Main Radioisotopes Obtained by Irradiation of Ti,V,Cr,Fe,Ni,Cu and Zn with Protons From 0 to 20 MeV,* Nuclear Instrum.and Methods in Physics Res. Vol. 127, p. 269, 1975

[13] Walton J.R., Heymann D., Yaniv A., Edgerley D., Rowe M.W.: *Cross Sections For He and Ne Isotopes in Natural Mg, Al, and Si, He Isotopes in Ca-F(2),Ar Isotopes in Natural Ca and Radionuclides in Natural Al, Si, Ti, Cr and Stainless Steel Induced by 12 to 45 MeV Protons,* Journal of Geophysical Research Vol. 81, p. 5689, 1976

[14] Michel R., Brinkmann G., Weigel H., Herr W.: *Proton-Induced Reactions on Titanium with Energies Between 13 and 45 MeV,* Journal of Inorganic and Nuclear Chemistry Vol. 40, p. 1845, 1978

[15] Michel R., Brinkmann G.: *On the Depth-Dependent Production of Radionuclides (A between 44 and 59) By Solar Protons in Extraterrestial Matter,* Journal of Radioanalytical Chemistry Vol. 59, Issue 2, p. 467, 1980

[16] West, Jr. H.I., Lanier R.G., Mustafa M.G.: *Excitation functions for the nuclear reactions on titanium leading to the production of ^{48}V, ^{44}Sc and ^{47}Sc, by proton, deuteron and triton irradiations at 0-35 MeV,* Physical Review C Vol. 42, p. 683, 1990

[17] Fink D., Sisterson J., Vogt S., Herzog G., Klein J., Middleton R., Koehler A., Magliss A.: *Production of ^{41}Ca and K, Sc and V short-lived isotopes by the irradiation of Ti with 35 to 150 MeV protons: applications to solar cosmic ray studies,* Nucl. Instrum. Methods in Physics Res., Sect. B Vol. 52, p. 601, 1990

[18] Jung P.: *Cross sections for the production of helium and long-living radioactive isotopes by protons and deuterons,* Conf. on Nucl. Data for Sci. and Technol., Juelich, p. 352, 1991

[19] Kopecky P., Szelecsenyi F., Molnar T., Mikecz P., Tarkanyi F.: *Excitation functions of (p,xn) reactions on ^{nat}Ti: monitoring of bombarding proton beams,* Applied Radiation and Isotopes Vol. 44, p. 687, 1993

[20] Michel R., Bodemann R., Busemann H., Daunke R., Gloris M., Lange H.-J., Klug B., Krins A., Leya I., Luepke M., Neumann S., Reinhardt H., Schnatz-Buettgen M., Herpers U., Schiekel Th., Sudbrock F., Holmqvist B., Conde H., Malmborg P., Suter M., Dittrich-Hannen B., Kubik P.-W., Sinal H.-A., Filges D.: *Cross sections for the production of residual nuclides by low- and medium-energy protons from the target elements C, N, O, Mg, Al, Si, Ca, Ti, V, Mn, Fe, Co, Ni, Cu, Sr, Y, Zr, Nb, Ba and Au,* Nucl. Instrum. Methods in Physics Res., Sect. B Vol. 129, p. 153, 1997

[21] Szelecsenyi F., Tarkanyi F., Takacs S., Hermanne A., Sonck M., Shubin Yu., Mustafa M.G., Youxiang Z.: *Excitation function for the $^{nat}Ti(p,x)^{48}V$ nuclear process: Evaluation and new measurements for practical applications,* Nucl. Instrum. Methods in Physics Res., Sect. B Vol. 174, p. 47, 2001

[22] Takacs S., Tarkanyi F., Sonck M., Hermanne A.: *New cross sections and intercomparison of proton monitor rections on Ti, Ni and Cu,* Nucl. Instrum. Methods in Physics Res., Sect. B Vol. 188, p. 106, 2002

[23] Zarie K., Al-Hammad N., Azzam A.: *Experimental study of excitation functions of some proton induced reactions on ^{nat}Ti for beam monitoring purpos,* Radiochimica Acta Vol. 94, p. 795, 2006

[24] Khandaker M.U., Kim K., Lee M.W., Kim K.S., Kim G.N., Cho Y.S., Lee Y.O.: *Investigations of the $^{nat}Ti(p,x)^{43,44m,44g,46,47,48}Sc$,$^{48}V$ nuclear processes up to 40 MeV,* Applied Radiation and Isotopes Vol. 67, p. 1348, 2009

[25] Bennett M.E., Mayorov D.A., Chapkin K.D., Alfonso M.C., Werke T.A., FoldenIii C.M.: *Measurement of the $^{nat}Lu(p,x)^{175}Hf$ excitation function,* Nucl. Instrum. Methods in Physics Res., Sect.B Vol. 276, p. 62, 2012

[26] Zherebchevsky V. I., Alekseev I. E., Gridnev K. A., Krymov E. B., Lazareva T. V., Maltsev N. A., Panin R. B., Prokofyev N. A., Torilov S. Y., Shtamburg A. I.: *The study of the nuclear reactions for the production of antimony isotopes,* Izv. Rossiiskoi Akademii Nauk, Ser.Fiz. Vol. 80, Issue 8, p. 975, 2016

[27] Garrido E., Duchemin C., Guertin A., Haddad F., Michel N., Metivier V.: *New excitation functions for proton induced reactions on natural titanium, nickel and copper up to 70 MeV,* NIMB Vol. 383, p. 191, 2016

[28] Hermanne A., Tarkanyi F., Takacs S., Ditroi F., Amjed N.: *Excitation functions for production of ^{46}Sc by deuteron and proton beams in ^{nat}Ti: A basis for additional monitor reactions,* Nucl. Instrum. Methods in Physics Res., Sect. B Vol. 338, p. 31, 2014

[29] Cohen B.L., Newman E.: *(p,pn) and (p,2n) cross sections in medium weight elements,* Physical Review Vol. 99, p. 718, 1955

[30] Williams I.R., Fulmer C.B.: *Excitation Functions For Radioactive Isotopes Produced By Protons Below 60 MeV on Al, Fe, and Cu,* Physical Review Vol. 162, p. 1055, 1967

[31] Gruetter A.: *Excitation functions for radioactive isotope produced by proton bombardment of Cu and Al in the energy range of 16 to 70 MeV,* Nuclear Physics, Section A Vol. 383, p. 98, 1982

[32] Aleksandrov V.N., Semyonova M.P., Semyonov V.G.: *Excitation functions for radionuclides produced by (p,x)-reactions of copper and nickel,* Atomnaya Energiya Vol. 62, p. 411, 1987

[33] Levkovski V.N.: *Activation cross sections for the nuclides of medium mass region (A = 40–100) with protons and a -particles at medium (E = 10–50 MeV) energies. (Experiment and systematics),* Inter-Vesi, Moscow, 1991

[34] Mills S.J., Steyn G.F., Nortier F.M.: *Experimental and Theoretical Excitation Functions of Radionuclides Produced in Proton Bombardment of Copper Up to 200 MeV,* Applied Radiation and Isotopes Vol. 43, p. 1019, 1992

[35] Hermanne A., Szelecsenyi F., Sonck M., Takacs S., Tarkanyi F., van den Winkel P.: *New Cross Section Data on ^{68}Zn(p,2n)^{67}Ga and ^{nat}Zn(p,xn)^{67}Ga Nuclear Reactions for the Development of a Reference Data Base,* Journal of Radioanalytical and Nuclear Chemistry Vol. 240, p. 623, 1999

[36] Uddin M.S., Hagiwara M., Tarkanyi F., Ditroi F., Baba M.: *Experimental studies on the proton-induced activation reactions of molybdenum in the energy range 22-67 MeV,* Applied Radiation and Isotopes Vol. 60, Issue. 6, p. 911, 2004

[37] Buthelezi E.Z., Nortier F.M., Schroeder I.W.: *Excitation functions for the production of ^{82}Sr by proton bombardment of ^{nat}Rb at energies up to 100 MeV,* Applied Radiation and Isotopes Vol. 64, p. 915, 2006

[38] Al-Saleh F.S., Al-Harbi A.A., Azzam A.: *Excitation functions of proton induced nuclear reactions on natural copper using a medium-sized cyclotron,* Radiochimica Acta Vol. 94, p. 391, 2006

[39] Khandaker M.U., Uddin M.S., Kim K.S., Lee Y.S., Kim G.N.: *Measurement of cross-sections for the (p,xn) reactions in natural molybdenum,* Nucl. Instrum. Methods in Physics Res., Sect. B Vol. 262, p. 171, 2007

[40] Siiskonen T., Huikari J., Haavisto T., Bergman J., Heselius S.-J., Lill J.-O., Lonnroth T., Perajarvi K.: *Excitation functions of proton-induced reactions in ^{nat}Cu in the energy range 7–17 MeV,* Applied Radiation and Isotopes Vol. 67, p. 2037, 2009

[41] Jost C.U., Griswold J.R., Bruffey S.H., Mirzadeh S., Stracener D.W., Williams C.L.: *Measurement of cross sections for the ^{232}Th(p,4n)^{229}Pa reaction at low proton energies,* Conf. proceedings by Am. Inst. of Phys. No. 1525, p. 520, 2013

[42] Shahid M., Kim K., Naik H., Zaman M., Yang S.C., Kim G.N.: *Measurement of excitation functions in proton induced reactions on natural copper from their threshold to 43 MeV,* Nucl. Instrum. Methods in Physics Res., Sect. B Vol. 342, p. 305, 2015

[43] Howe H.A.: *(p,n) cross sections of copper and zinc,* Physical Review Vol. 109, p. 2085, 1958

[44] Johnson C.H., Galonsky A., Inskeep C.N.: *Cross sections for (p,n) reactions in intermediate-weight nuclei,* Progress Report ORNL-2910, p. 25, 1960

[45] Wing J. and Huizenga J.R.: *(p,n) cross-sections of ^{51}V, ^{52}Cr, ^{63}Cu, ^{65}Cu, ^{107}Ag, ^{109}Ag, ^{111}Cd, ^{114}Cd and ^{139}La from 5 to 10.5 MeV,* Physical Review Vol. 128, p. 280, 1962

[46] Hansen L.F., Albert, R.D.: Statistical theory predictions for 5 to 11 MeV (p,n) and (p,p′) nuclear reactions in ^{51}V, ^{59}Co, ^{63}Cu, ^{65}Cu, and ^{103}Rh, Physical Review Vol. 128, p. 291, 1962

[47] Collé R., Kishore R., Cumming J.B.: *Excitation functions for (p,n) reactions to 25 MeV on ^{63}Cu, ^{65}Cu and ^{107}Ag,* Physical Review C Vol. 9, p. 1819, 1974

[48] Yoshizawa Y., Noma H., Horiguchi T., Katoh T., Amemiya S., Itoh M., Hisatake K., Sekikawa M., Chida K.: *Isotope separator on-line at INS FM cyclotron,* Nuclear Instrum.and Methods in Physics Res. Vol. 134, Issue 1, p. 93, 1976

[49] Dmitriev P.P., Konstantinov I.S., Krasnov N.N.: *Excitation function for the $^{65}Cu(p,n)^{65}Zn$ reaction,* Atomnaya Energiya Vol. 24, p. 279, 1968

[50] Kopecky P.: *Proton beam monitoring via the $Cu(p,x)^{58}Co$, $^{63}Cu(p,2n)^{62}Zn$ and $^{65}Cu(p,n)^{65}Zn$ reactions in copper,* International J. Applied Radiation Isotopes Vol. 36, p. 657, 1985

[51] Kuhnhenn J.: *Thin target cross sections for proton-induced production of radionuclides from lead and bismuth over the proton energy range from 9 to 71 MeV,* Thesis, 2001

[52] Graves S. A., Ellison P. A. Barnhart T. E., Valdovinos H. F., Birnbaum E. R.Nortier F. M., Nickles R. J., Engle J. W.: *Nuclear excitation functions of proton-induced reactions (E_p=35-90 MeV) from Fe, Cu and Al,* NIMB Vol. 386, p. 44, 2016

[53] Yashima H., Uwamino Y., Sugita H., Nakamura T., Ito S., Fukumura A.: *Projectile dependence of radioactive spallation products induced in copper by high-energy heavy ions,* Physical Review, Part C, Nuclear Physics Vol. 66, p. 044607, 2002

[54] Greenwood L.R., Smither R.K.: *Measurement of Cu spallation cross sections at IPNS,* U.S. Dept. of Energy, Fusion Energy Series Vol. 18, No. 0046, p. 11, 1984

Table 1 Data for the investigated radionuclides. *Q*-values for isomeric nuclei have to be lowered by the energy level of the isomer. *Q*-values and threshold energies for reactions where composed particles are emitted have to be increased by binding energy of the particle (d = np + 2.225 MeV, t = p2n + 8.482 MeV, ^{3}He = 2pn + 7.718 MeV, α = 2p2n + 28.296 MeV). Energies of gamma lines used for quantification of each particular radionuclide are in bold. Uncertainties of the half-lives, gamma line energies and their intensities in the last valid digits are given in italics.

radionuclide	half-life	E_γ (keV)	I_γ (%)	contributing reactions	*Q*-value (MeV)	E_{thr} (MeV)
^{48}V	15.9735 d *25*	944.130 *4*	7.870 *7*	^{47}Ti(p,γ)	6.829	0
		983.525 *4*	**99.98 *4***	^{48}Ti(p,n)	-4.797	4.898
		1312.106 *8*	98.2 *3*	^{49}Ti(p,2n)	-12.940	13.206
		2240.396 *6*	2.333 *13*	^{50}Ti(p,3n)	-23.879	24.361
^{43}Sc	3.891 h *12*	**372.9 *3***	**22.5**	^{46}Ti(p,2p2n)	-31.370	32.058
				^{47}Ti(p,2p3n)	-40.251	41.115
				^{48}Ti(p,2p4n)	-51.878	52.968
				^{49}Ti(p,2p5n)	-60.020	61.256
^{44m}Sc	58.61 h *10*	**271.241 *10***	**86.7 *3***	^{46}Ti(p,2pn)	-21.671	22.146
				^{47}Ti(p,2p2n)	-30.552	31.208
				^{48}Ti(p,2p3n)	-42.179	43.065
^{44g}Sc	3.97 h *4*	**1157.020 *15***	**99.9 *4***	^{49}Ti(p,2p4n)	-50.321	51.357
				^{50}Ti(p,2p5n)	-61.260	62.496
^{46g}Sc	83.79 d *4*	**889.277 *3***	**99.9840 *10***	^{47}Ti(p,2p)	-10.465	10.689
				^{48}Ti(p,2pn)	-22.092	22.556
		1120.545 *4*	99.9870 *10*	^{49}Ti(p,2p2n)	-30.234	30.856
				^{50}Ti(p,2p3n)	-41.173	42.004
^{47}Sc	3.3492 d *6*	**159.381 *15***	**68.3 *4***	^{48}Ti(p,2p)	-11.445	11.686
				^{49}Ti(p,2pn)	-19.587	19.991
				^{50}Ti(p,2p2n)	-30.527	31.142
^{48}Sc	43.67 h *9*	175.361 *5*	7.48 *10*	^{49}Ti(p,2p)	-11.348	11.582
		983.526 *12*	100.1 *6*			
		1037.522 *12*	**97.6 *7***	^{50}Ti(p,2pn)	-22.288	22.737
		1312.120 *12*	100.1 *7*			
^{62}Zn	9.186 h *13*	**548.35 *11***	**15.3 *14***	^{63}Cu(p,2n)	-13.265	13.478
		596.56 *13*	26.0	^{65}Cu(p,4n)	-31.092	31.575
^{63}Zn	38.47 min *5*	**669.62 *5***	**8.2**	^{63}Cu(p,n)	-4.149	4.215
		962.06 *4*	6.5 *4*	^{65}Cu(p,3n)	-21.975	22.316
^{65}Zn	243.93 d *9*	**1115.539 *2***	**50.04 *10***	^{65}Cu(p,n)	-2.134	2.167
^{61}Cu	3.333 h *5*	**282.956 *10***	**12.9 *26***	^{63}Cu(p,p2n)	-19.738	20.054
		656.008 *10*	9.8 *20*	^{65}Cu(p,p4n)	-37.565	38.148
^{58}Co	70.86 d *6*	**810.7593 *20***	**99.450**	^{63}Cu(p,3p3n)	-44.524	45.238

Table 2 Measured cross-sections data for ^{nat}Ti(p,x) reactions

E_p (MeV)	σ (mb)						
	^{48}V	^{43}Sc	^{44g}Sc	^{44m}Sc	$^{46m+g}$Sc	^{47}Sc	^{48}Sc
35.97 ± 0.30	28.2 ± 1.9	6.50 ± 0.47	32.1 ± 2.5	16.0 ± 1.1	41.4 ± 2.8	21.6 ± 1.4	0.905 ± 0.064
34.57 ± 0.33	29.5 ± 2.0	5.26 ± 0.39	35.2 ± 2.7	16.7 ± 1.1	34.3 ± 2.3	22.7 ± 1.5	0.829 ± 0.059
33.10 ± 0.35	31.0 ± 2.1	3.90 ± 0.30	38.1 ± 2.9	17.2 ± 1.1	26.8 ± 1.8	24.3 ± 1.6	0.766 ± 0.054
31.61 ± 0.38	32.2 ± 2.2	2.95 ± 0.24	40.3 ± 3.1	16.8 ± 1.1	20.0 ± 1.3	24.8 ± 1.6	0.689 ± 0.049
30.04 ± 0.42	33.8 ± 2.3	3.11 ± 0.24	41.9 ± 3.2	15.6 ± 1.0	14.75 ± 0.99	24.3 ± 1.6	0.652 ± 0.046
28.43 ± 0.46	35.9 ± 2.4	3.35 ± 0.25	39.8 ± 3.0	13.85 ± 0.91	11.36 ± 0.77	22.1 ± 1.5	0.607 ± 0.043
26.72 ± 0.50	40.3 ± 2.6	3.17 ± 0.24	35.6 ± 2.7	11.80 ± 0.78	9.89 ± 0.67	19.1 ± 1.3	0.501 ± 0.036
24.95 ± 0.55	45.4 ± 3.1	2.99 ± 0.23	28.7 ± 2.1	9.33 ± 0.62	8.68 ± 0.58	15.8 ± 1.1	0.402 ± 0.029
23.79 ± 0.58	49.9 ± 3.3	3.06 ± 0.23	21.8 ± 1.6	7.25 ± 0.48	7.86 ± 0.53	13.54 ± 0.90	0.333 ± 0.024
22.58 ± 0.61	55.7 ± 3.8	2.85 ± 0.22	14.0 ± 1.1	4.74 ± 0.31	6.82 ± 0.46	11.08 ± 0.74	0.258 ± 0.019
22.09 ± 0.63	57.2 ± 3.9	2.77 ± 0.21	11.02 ± 0.84	3.81 ± 0.26	6.32 ± 0.44	10.30 ± 0.71	0.239 ± 0.018
21.31 ± 0.30	64.7 ± 4.4	2.54 ± 0.19	5.05 ± 0.38	1.96 ± 0.13	5.41 ± 0.37	8.28 ± 0.56	0.147 ± 0.022
19.98 ± 0.33	79.9 ± 5.4	2.66 ± 0.21	2.72 ± 0.21	1.201 ± 0.082	4.73 ± 0.32	6.23 ± 0.42	0.084 ± 0.016
18.59 ± 0.36	104.2 ± 7.1	3.22 ± 0.24	3.24 ± 0.24	1.191 ± 0.083	4.02 ± 0.28	4.05 ± 0.27	0.053 ± 0.016
17.13 ± 0.40	151 ± 10	3.57 ± 0.26	3.97 ± 0.29	1.204 ± 0.084	3.43 ± 0.23	2.32 ± 0.16	
15.59 ± 0.44	232 ± 16	3.60 ± 0.26	4.08 ± 0.30	1.016 ± 0.072	2.41 ± 0.17	1.304 ± 0.091	
13.91 ± 0.50	343 ± 23	3.20 ± 0.23	3.67 ± 0.26	0.750 ± 0.055	1.73 ± 0.12	0.880 ± 0.063	
12.10 ± 0.57	379 ± 26	2.42 ± 0.18	2.80 ± 0.20	0.433 ± 0.032	1.158 ± 0.082	0.576 ± 0.042	
10.04 ± 0.67	363 ± 25	1.172 ± 0.084	1.367 ± 0.097	0.166 ± 0.014	0.541 ± 0.041	0.287 ± 0.021	
8.86 ± 0.73	338 ± 23	0.357 ± 0.027	0.578 ± 0.047	0.062 ± 0.023	0.292 ± 0.027	0.138 ± 0.027	
7.57 ± 0.82	275 ± 19	0.0410 ± 0.0080	0.118 ± 0.012	0.0202 ± 0.0072	0.071 ± 0.011	0.0406 ± 0.0084	
6.44 ± 0.91	190 ± 13		0.0116 ± 0.0023			0.0115 ± 0.0038	

Table 3 Measured cross-sections data for ^{nat}Cu(p,x) reactions

E_p (MeV)	σ (mb)					
	^{62}Zn (via 548.35 keV)	^{62}Zn (via 596.56 keV)	^{63}Zn	^{65}Zn	^{61}Cu	$^{58m+g}$Co
35.90 ± 0.30	15.8 ± 1.1	16.2 ± 1.1	53.8 ± 3.8	7.22 ± 0.5	178 ± 41	49.3 ± 3.4
34.49 ± 0.33	18.2 ± 1.3	18.5 ± 1.3	57.0 ± 4.0	7.56 ± 0.52	171 ± 39	41.8 ± 2.9
33.02 ± 0.36	22.3 ±1.5	22.9 ± 1.6	53.9 ± 3.8	8.07 ± 0.56	158 ± 36	32.6 ± 2.2
31.53 ± 0.39	27.3 ± 1.9	28.4 ± 2.0	51.3 ± 3.6	5.52 ± 0.59	133 ± 30	22.8 ± 1.6
29.96 ± 0.42	35.5 ± 2.5	36.6 ± 2.5	46.7 ± 3.3	9.10 ±0.63	103 ± 23	12.49 ± 0.86
28.34 ± 0.46	47.3 ± 3.3	48.4 ± 3.3	39.9 ± 2.8	9.81 ± 0.68	69 ± 16	4.72 ± 0.32
26.62 ± 0.50	60.3 ± 4.2	61.3 ± 4.2	31.6 ± 2.3	10.69 ± 0.74	36.3 ± 8.3	0.948 ± 0.066
24.85 ± 0.55	71.6 ± 5.0	72.4 ± 5.0	23.9 ± 1.7	11.41 ± 0.79	13.7 ± 3.1	0.0774 ± 0.0076
23.69 ± 0.58	73.1 ± 5.1	74.4 ± 5.1	24.6 ± 1.8	12.73 ± 0.88	6.4 ± 1.5	0.0146 ± 0.0028
22.47 ± 0.62	71.6 ± 5.0	72.6 ± 5.0	26.5 ± 1.9	14.21 ± 0.98	3.29 ± 0.79	
21.19 ± 0.30	63.7 ± 4.4	65.4 ± 4.5	32.4 ± 2.3	15.5 ± 1.1		
19.86 ± 0.33	55.9 ± 3.9	57.7 ± 4.0	44.5 ± 3.1	19.6 ± 1.4		
18.46 ± 0.36	45.8 ± 3.2	47.1 ± 3.3	68.3 ± 4.8	27.8 ± 1.9		
16.99 ± 0.40	32.1 ± 2.2	32.5 ± 2.3	110.4 ± 7.7	41.4 ± 2.9		
15.44 ± 0.45	15.8 ± 1.1	16.3 ± 1.1	191 ± 13	69.8 ± 4.8		
13.76 ± 0.50	1.42 ± 0.1	1.52 ± 0.11	301 ± 21	118.0 ± 8.2		
11.93 ± 0.57			320 ± 22	190 ± 13		
9.84 ± 0.68			288 ± 20	213 ± 15		
8.64 ±0.74			256 ± 18	192 ± 13		
7.32 ± 0.84			202 ± 14	159 ± 11		

Table 4 The cross-sections for $^{nat}Ti(p,x)^{48}V$ and $^{nat}Cu(p,x)^{62}Zn$, ^{63}Zn, ^{65}Zn resulting from the polynomial fit of the selected experimental data

E_p (MeV)	$^{nat}Ti(p,x)^{48}V$	$^{nat}Cu(p,x)^{62}Zn$	$^{nat}Cu(p,x)^{63}Zn$	$^{nat}Cu(p,x)^{65}Zn$
	σ (mb)			
3.0				3.54
3.5				14.82
4.0			0.39	31.59
4.5			21.82	51.31
5.0	1.60		57.98	72.61
5.5	70.55		95.64	94.03
6.0	136.34		130.31	114.09
6.5	189.03		160.77	131.79
7.0	231.34		186.95	146.93
7.5	266.04		209.25	160.13
8.0	294.79		228.33	172.42
8.5	318.17		245.05	184.76
9.0	336.22		260.35	197.41
9.5	349.12		275.05	209.70
10.0	357.63		289.64	219.94
10.5	363.18		304.00	225.87
11.0	367.58		317.43	225.31
11.5	372.24		328.61	216.99
12.0	377.33		335.91	201.28
12.5	381.05		337.72	180.45
13.0	379.55		332.73	158.24
13.5	367.99	1.70	320.27	138.39
14.0	343.61	4.17	300.31	122.23
14.5	314.39	7.89	273.43	105.19
15.0	281.42	12.36	240.78	84.31
15.5	246.11	17.23	204.34	74.09
16.0	212.45	22.25	168.35	64.32
16.5	182.70	27.26	142.89	55.39
17.0	157.80	32.16	122.78	47.51
17.5	137.80	36.89	104.73	40.77
18.0	122.12	41.43	88.61	35.14
18.5	109.89	45.76	74.85	30.54
19.0	100.15	49.86	63.55	26.85
19.5	91.99	53.72	54.59	23.91
20.0	84.74	57.30	47.67	21.59
20.5	77.99	60.58	42.43	19.76
21.0	71.61	63.52	38.46	18.28
21.5	65.75	66.05	35.35	17.06
22.0	60.71	68.13	32.80	16.02
22.5	56.84	69.71	30.56	15.11
23.0	54.34	70.73	28.52	14.30
23.5	52.77	71.17	26.71	13.56
24.0	50.30	71.00	25.29	12.88
24.5	48.05	70.22	24.58	12.27
25.0	46.02	68.83	25.00	11.72
25.5	44.20	66.88	25.47	11.25
26.0	42.58	64.41	25.71	10.85
26.5	41.15	61.49	27.57	10.51
27.0	39.90	58.21	30.38	10.25
27.5	38.81	54.66	33.60	10.03
28.0	37.87	50.96	36.88	9.85
28.5	37.06	47.19	39.96	9.69
29.0	36.36	43.46	42.70	9.53
29.5	35.76	39.86	45.03	9.37
30.0	35.23	36.48	46.94	9.19
30.5	34.75	33.36	48.44	8.96
31.0	34.30	30.54	49.59	8.73
31.5	33.87	28.05	50.45	8.48
32.0	33.43	25.87	51.08	8.23
32.5	32.97	23.99	51.54	8.01
33.0	32.46	22.35	51.85	7.82
33.5	31.91	20.92	52.06	7.70
34.0	31.30	19.63	52.16	7.64
34.5	30.63	18.44	52.15	7.63
35.0	29.90	17.33	51.99	7.67
35.5	29.13	16.27	51.66	7.72
36.0	28.32	15.29	51.13	7.72

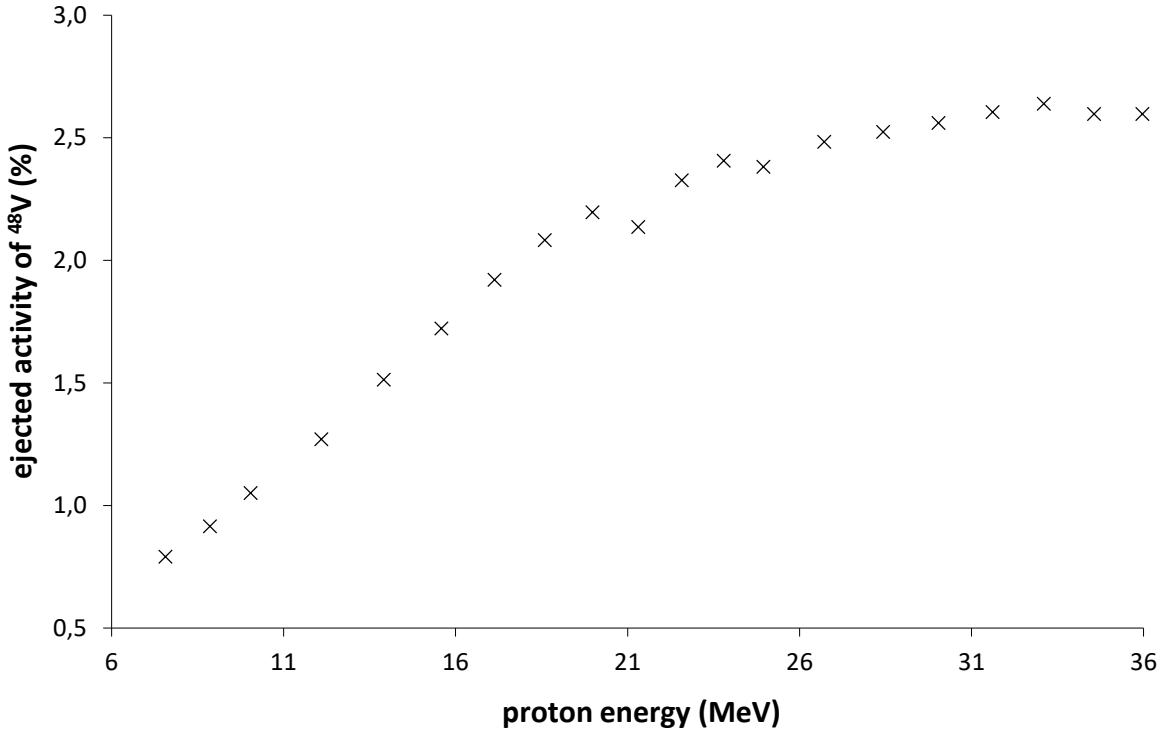

Fig. 1 Activity of ^{48}V recoiled atoms found on the following foil

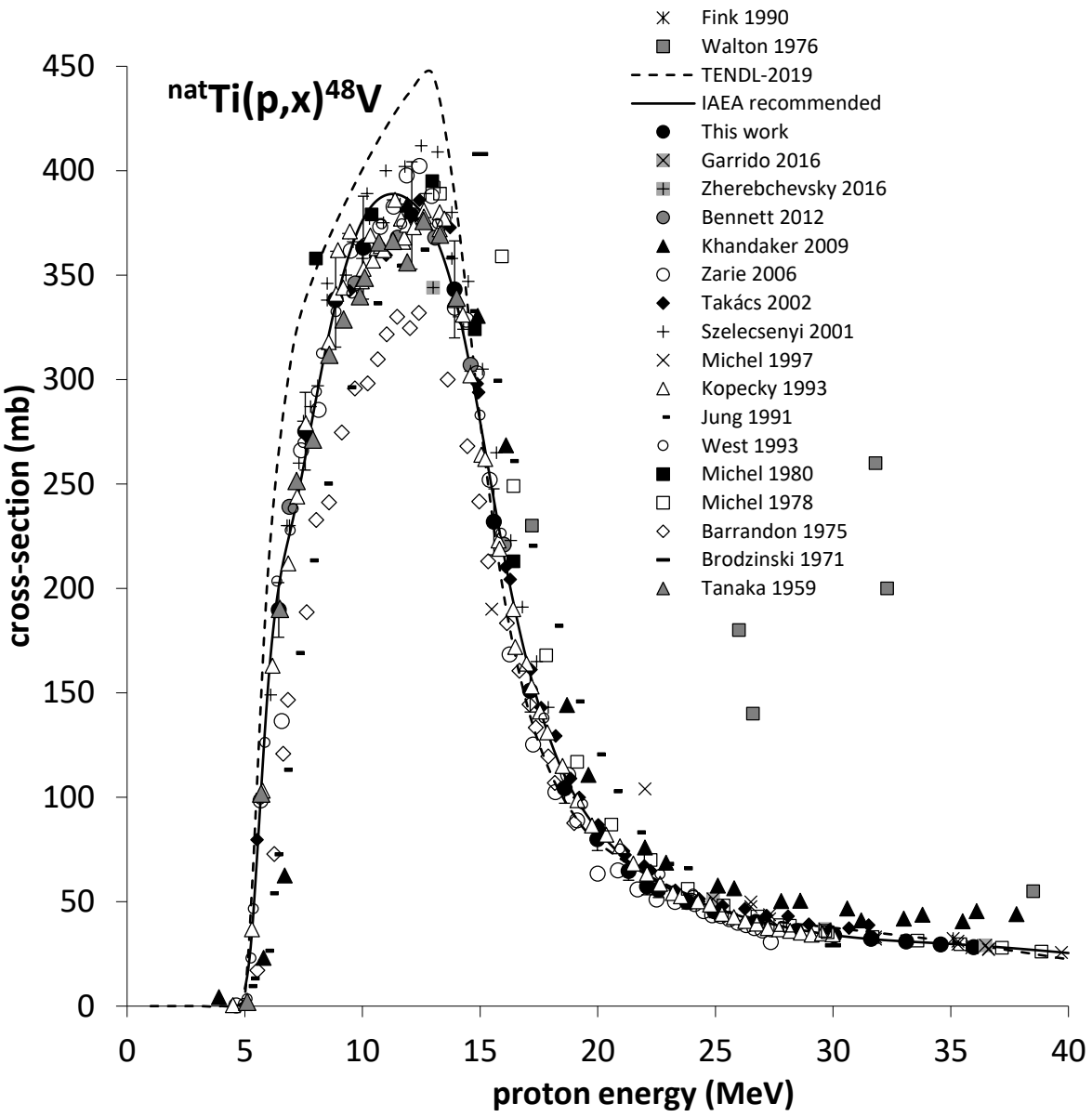

Fig. 2 Cross-sections of reactions $^{nat}Ti(p,x)^{48}V$ – our values in comparison with the previously published data [10-27] and the TALYS prediction taken from the TENDL-2019 library

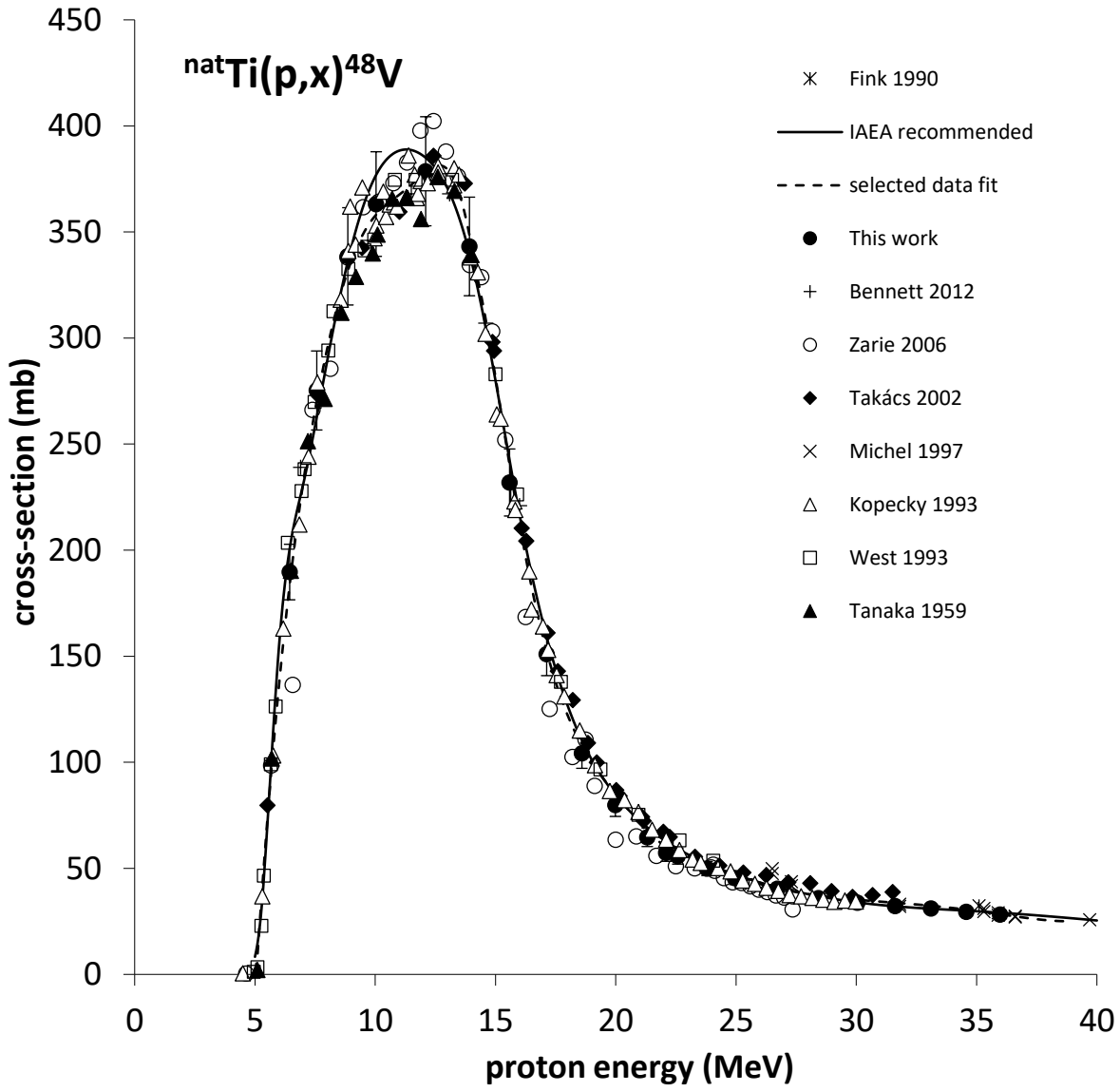

Fig. 3 Selected experimental cross-sections of reactions $^{nat}Ti(p,x)^{48}V$ [10,16,17,19,20,22,23,25]

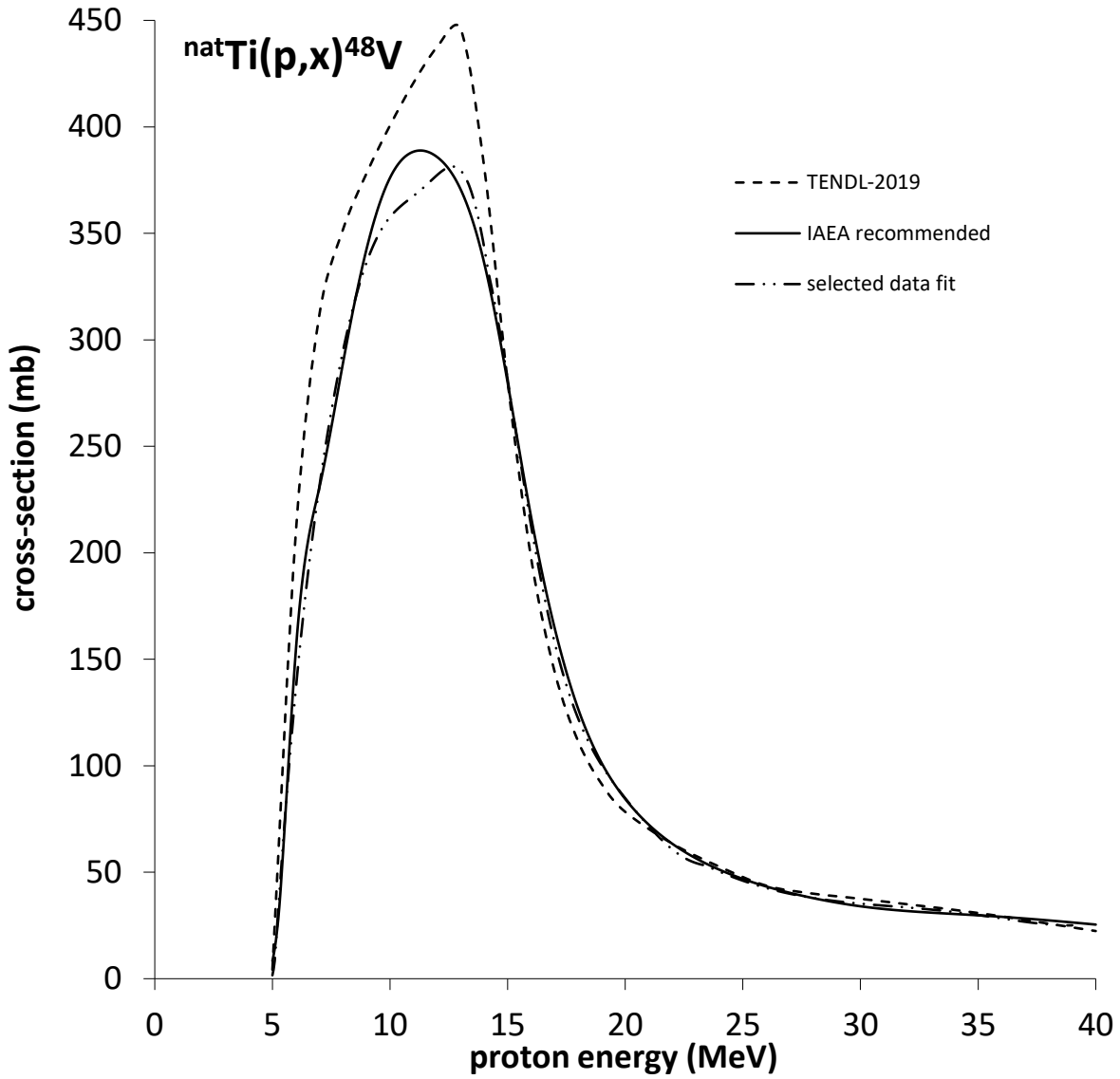

Fig. 4 Comparison of selected cross-section data fit, IAEA recommended cross-sections and TALYS prediction taken from the TENDL-2019 library in the measured energy range of reactions $^{nat}Ti(p,x)^{48}V$

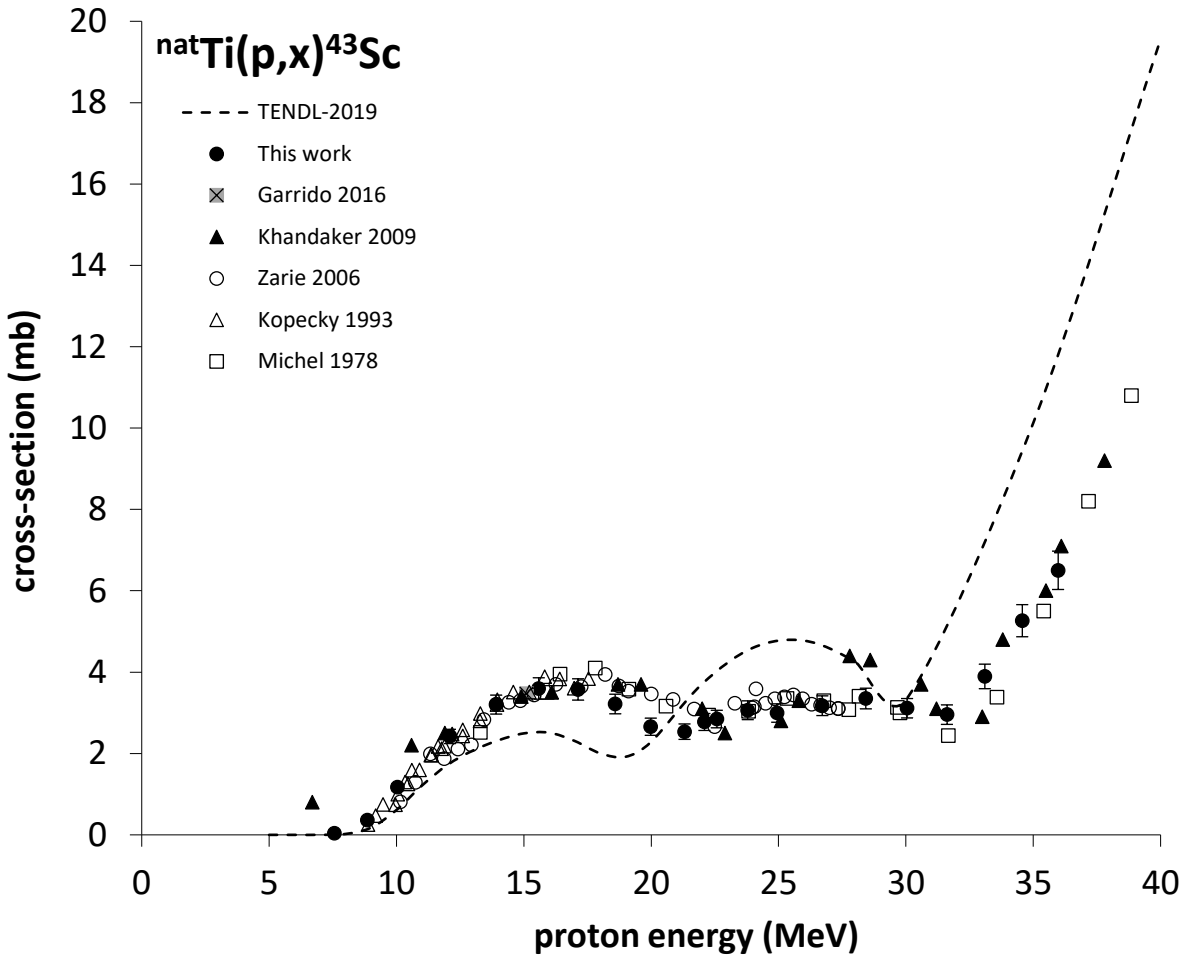

Fig. 5 Cross-sections of reactions $^{nat}Ti(p,x)^{43}Sc$ – our values in comparison with the previously published data [14,19,23,24,27] and the TALYS prediction taken from the TENDL-2019 library

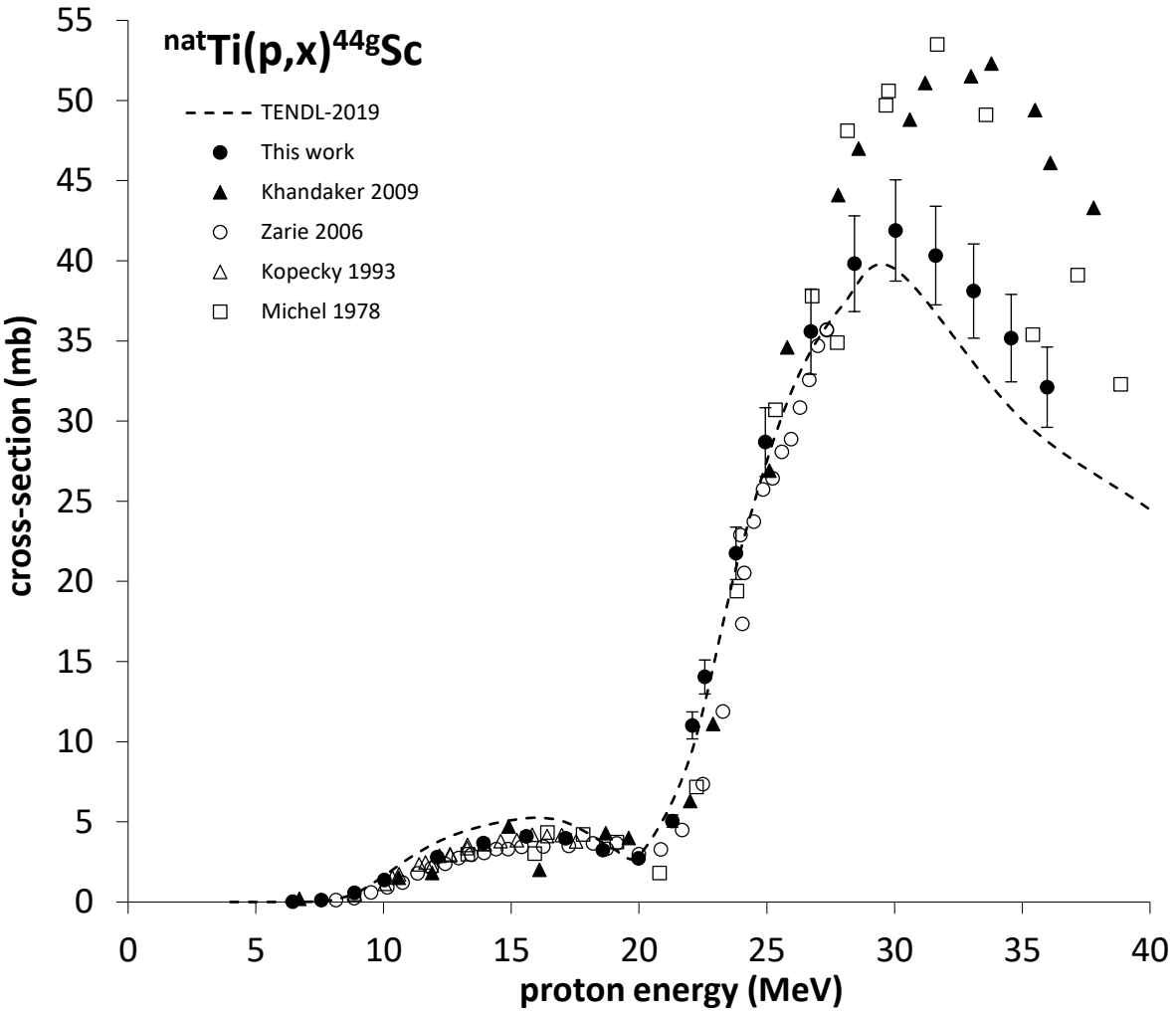

Fig. 6 Cross-sections of reactions $^{nat}Ti(p,x)^{44g}Sc$ – our values in comparison with the previously published data [14,19,23,24] and the TALYS prediction taken from the TENDL-2019 library

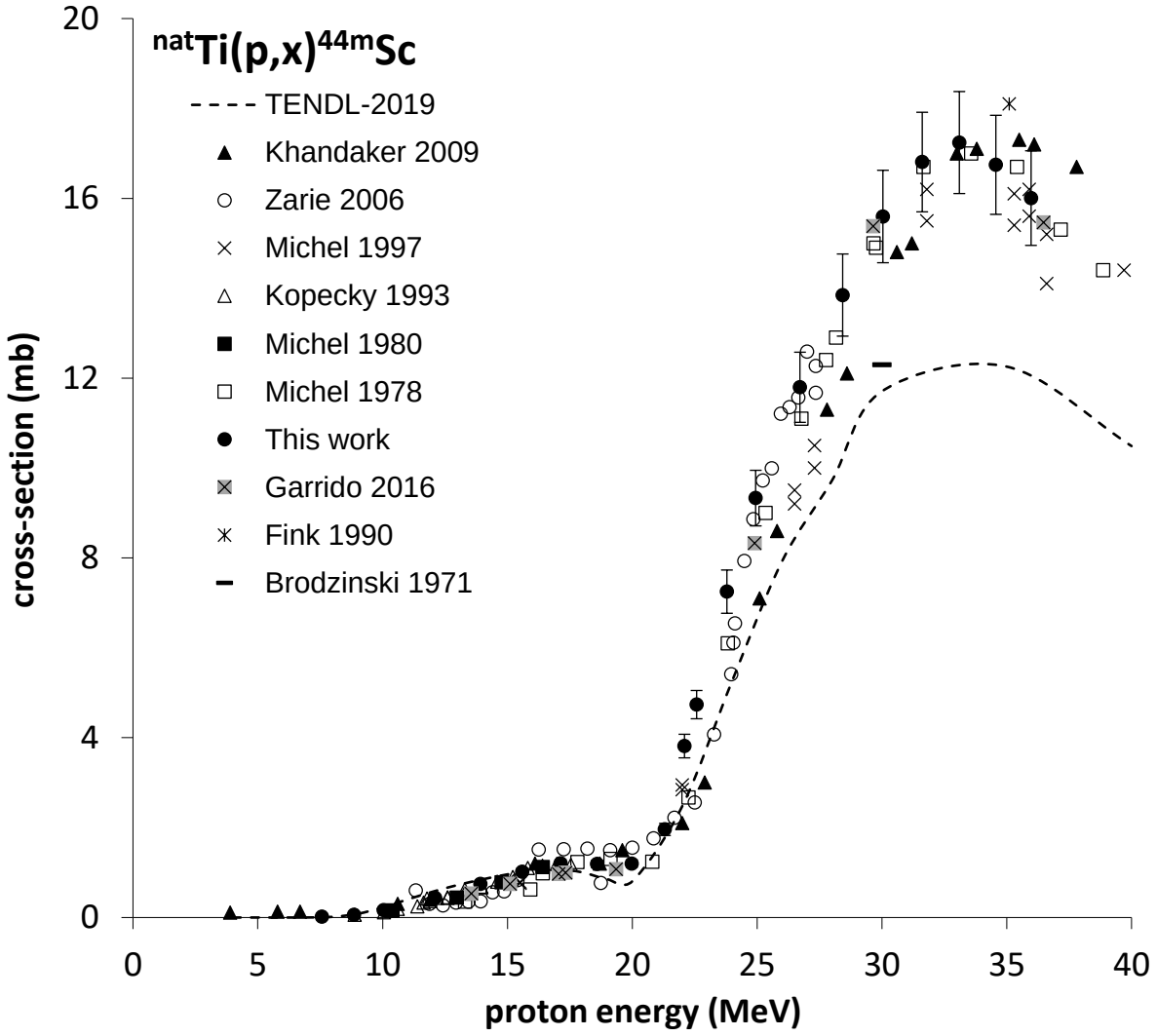

Fig. 7 Cross-sections of reactions $^{nat}Ti(p,x)^{44m}Sc$ – our values in comparison with the previously published data [11,14,15,17,19,20,23,24,27] and the TALYS prediction taken from the TENDL-2019 library

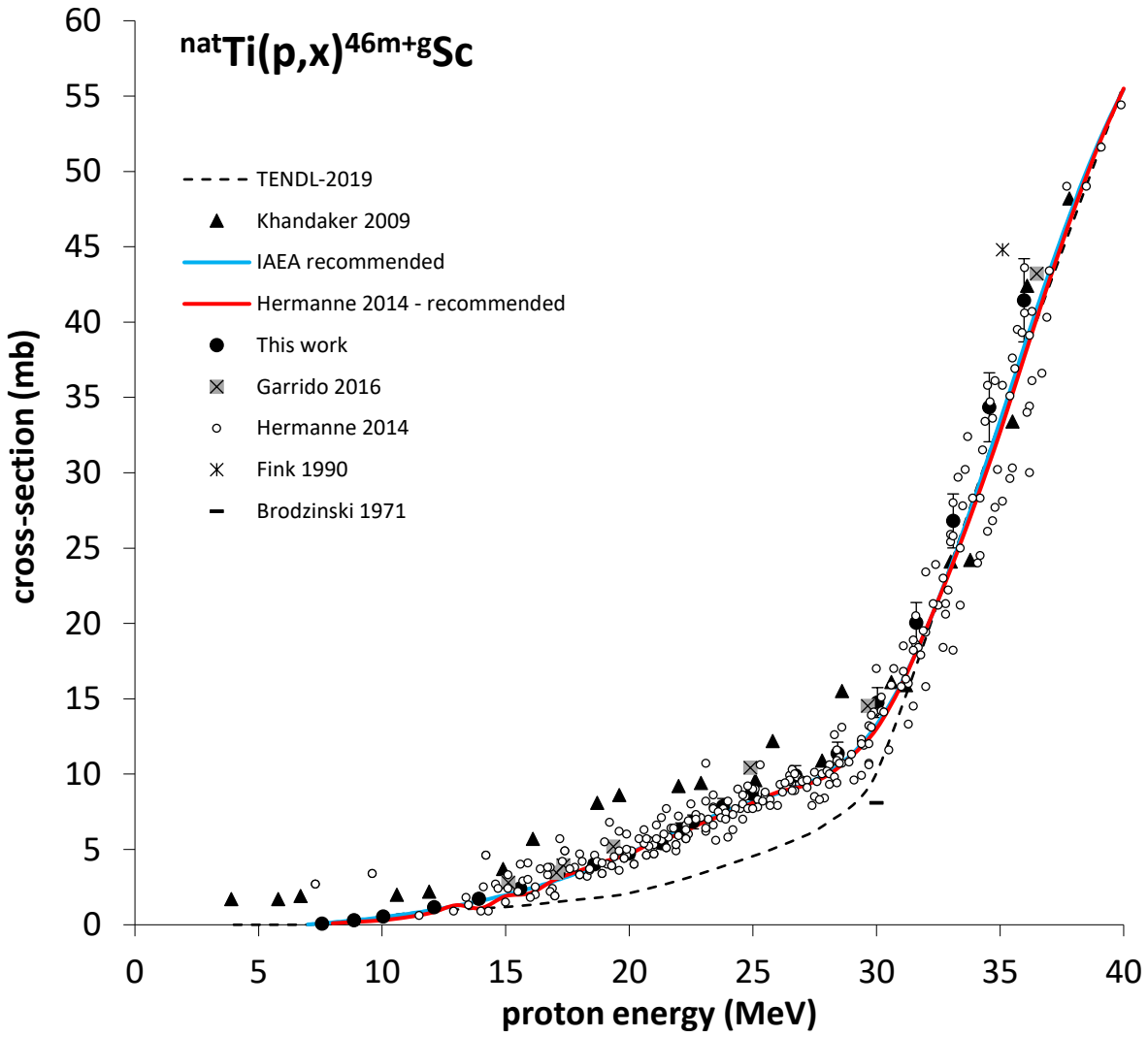

Fig. 8 Cross-sections of reactions ^{nat}Ti(p,x)$^{46m+g}$Sc – our values in comparison with the previously published data [11,17,24,27,28] and the TALYS prediction taken from the TENDL-2019 library

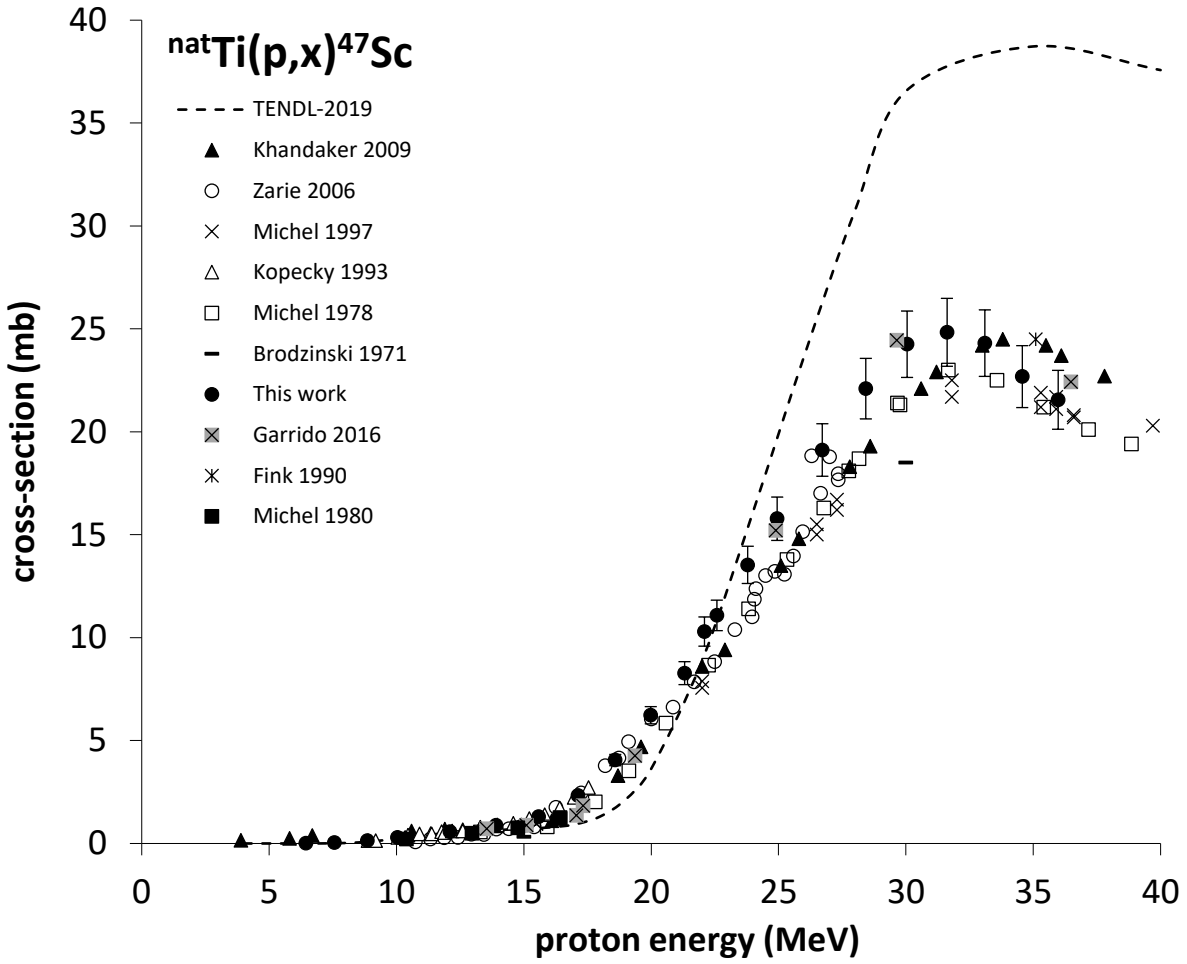

Fig. 9 Cross-sections of reactions ^{nat}Ti(p,x)^{47}Sc – our values in comparison with the previously published data [11,14,15,17,19,20,23,24,27] and the TALYS prediction adopted from the TENDL-2019 library

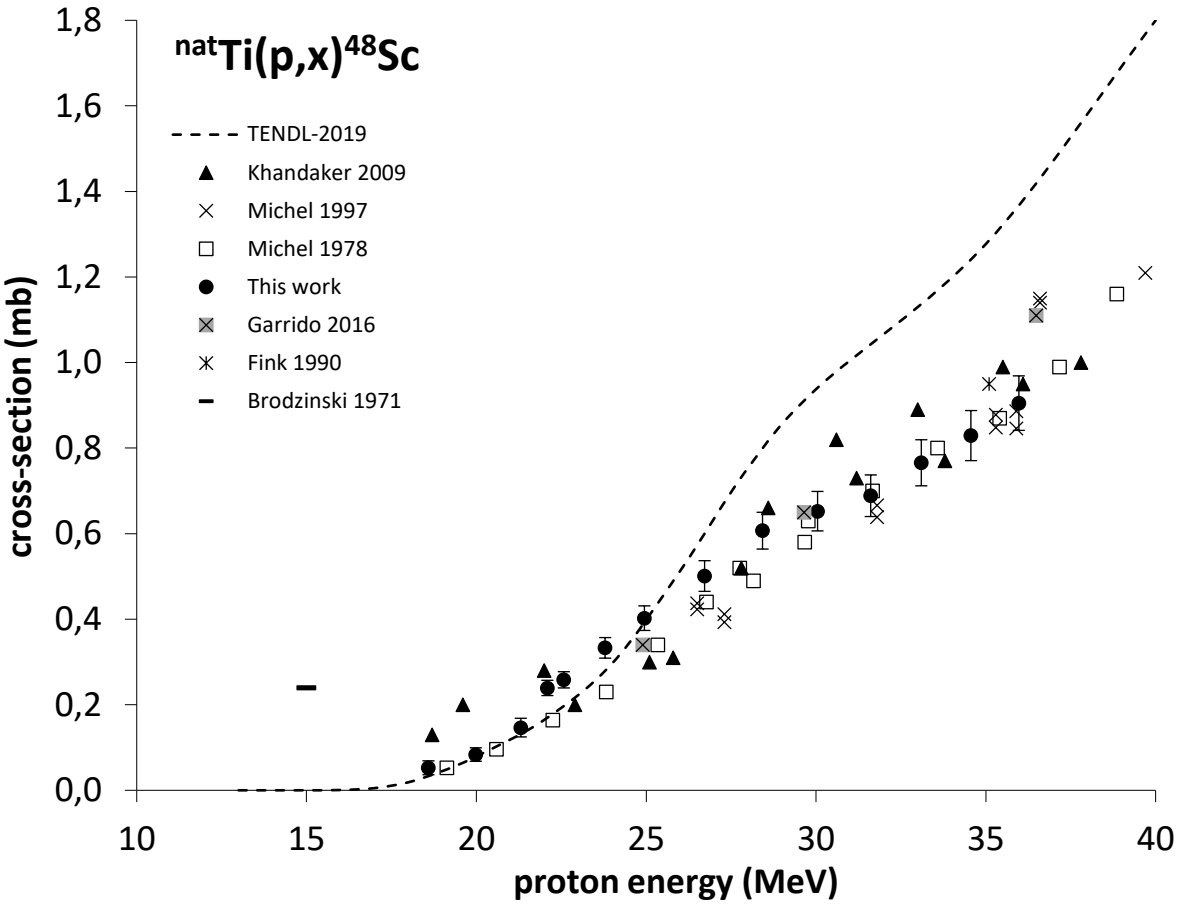

Fig. 10 Cross-sections of reactions $^{nat}Ti(p,x)^{48}Sc$ – our values in comparison with the previously published data [11,14,17,20,24,27] and the TALYS prediction adopted from the TENDL-2019 library

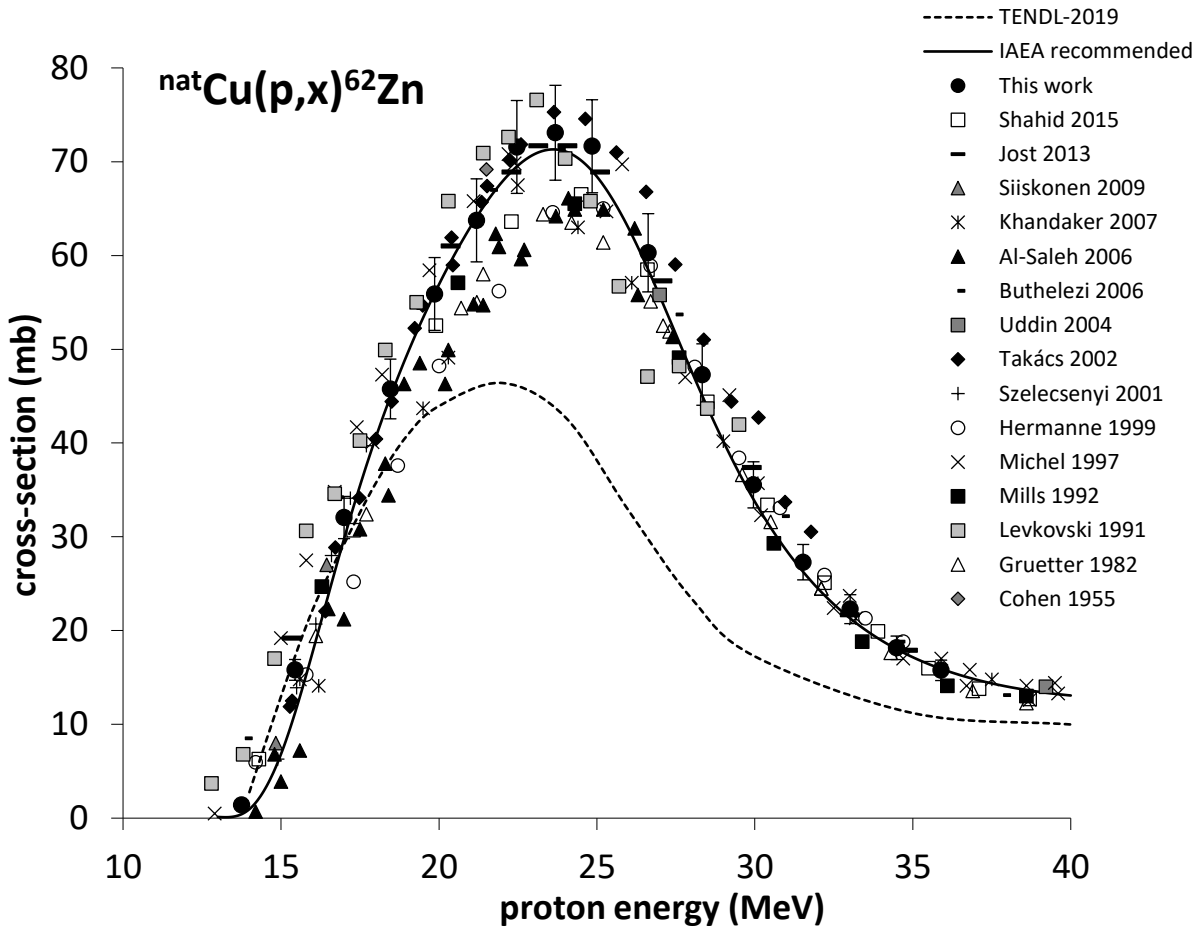

Fig. 11 Cross-sections of reactions $^{nat}Cu(p,x)^{62}Zn$ – our measurement in comparison with the previously published data [20-22,29-42] and the TALYS prediction adopted from the TENDL-2019 library

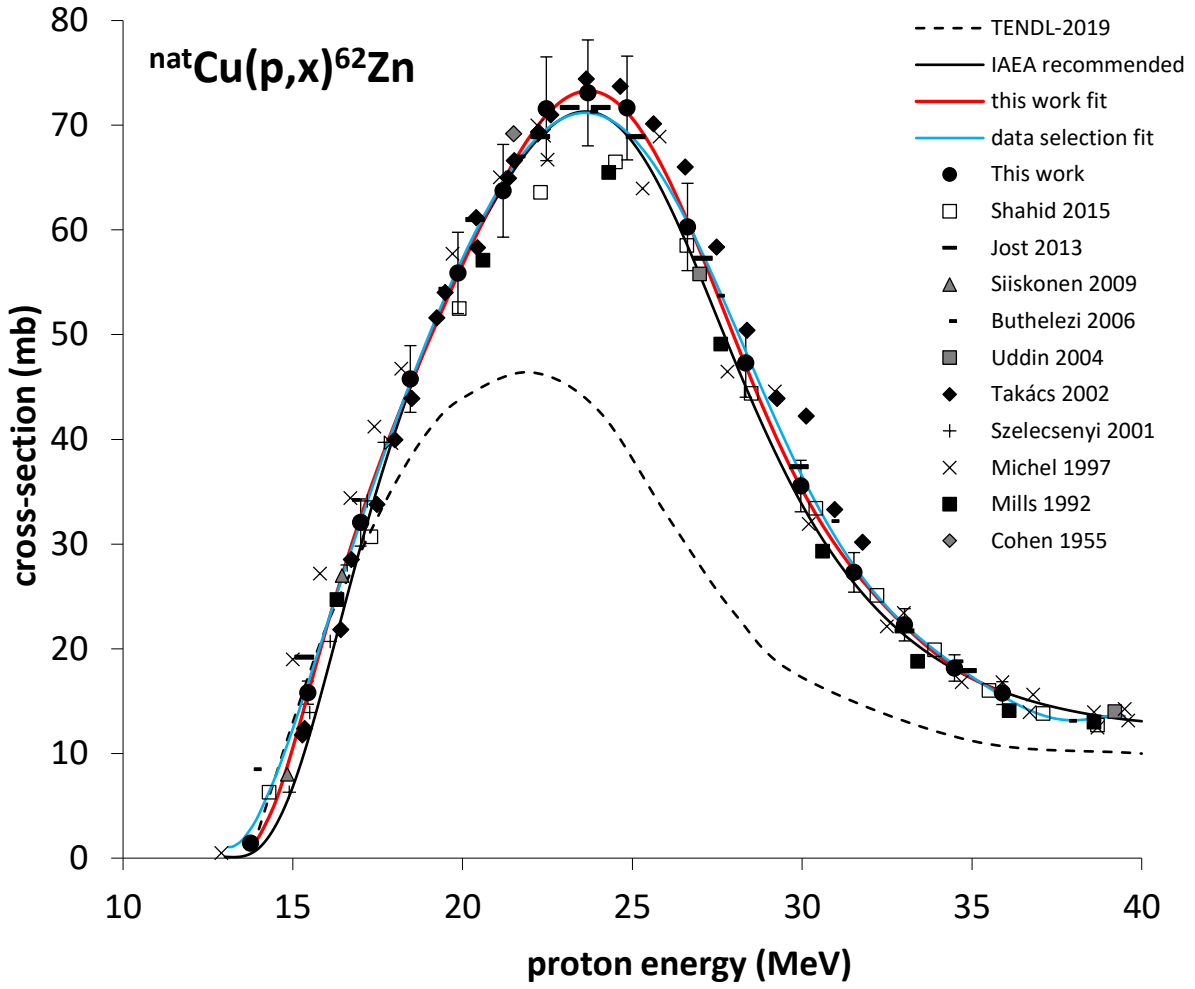

Fig. 12 Selected experimental cross-sections and their fit for reactions $^{nat}Cu(p,x)^{62}Zn$ [20,21,24,29,34,36,37,40-42], TALYS prediction taken from the TENDL-2019 library, IAEA recommended cross-sections

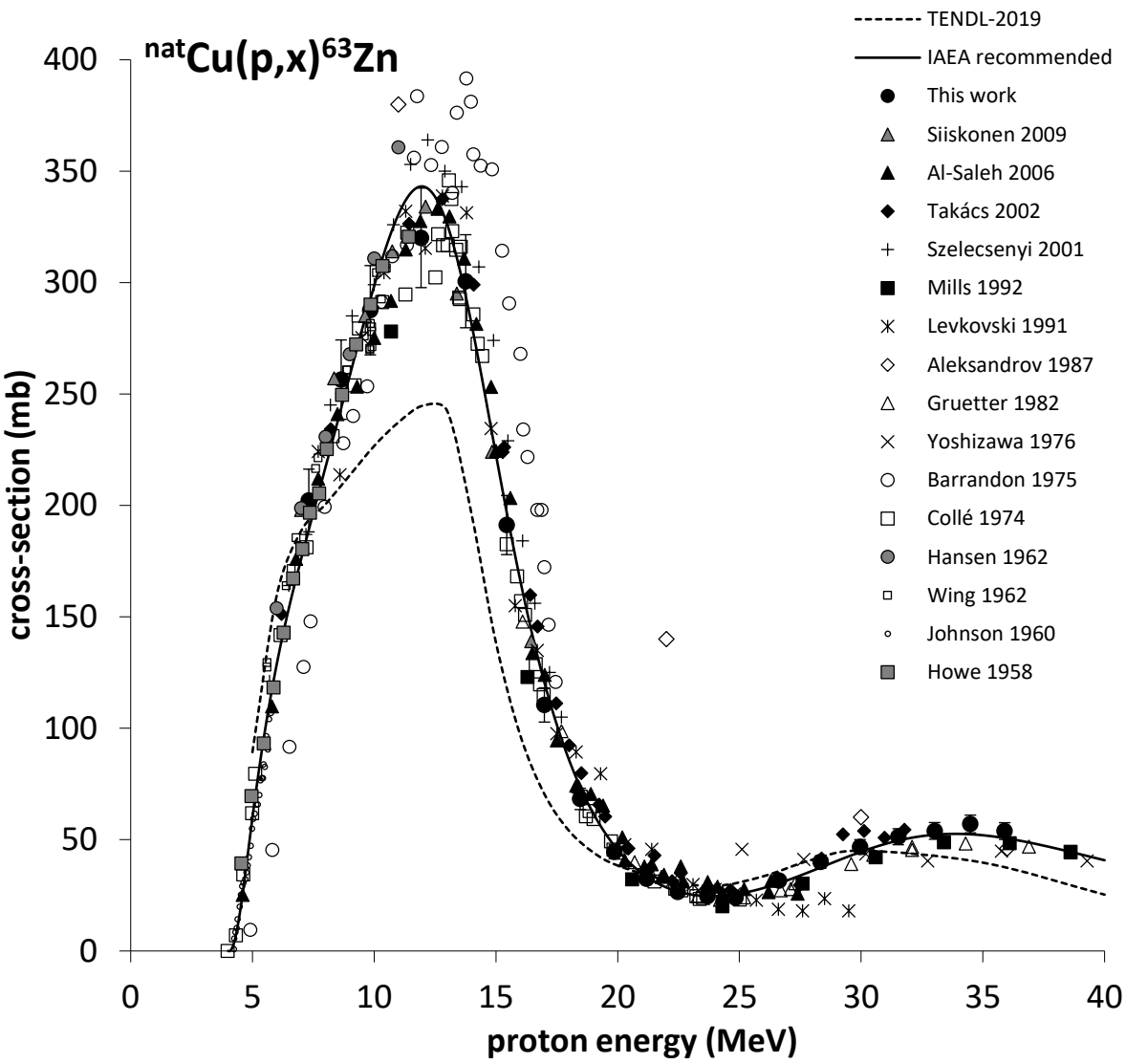

Fig. 13 Cross-sections of reactions $^{nat}Cu(p,x)^{63}Zn$ – our values in comparison with the previously published data [12,21,22,31-34,38,40,43-48] and the TALYS prediction taken from the TENDL-2019 library

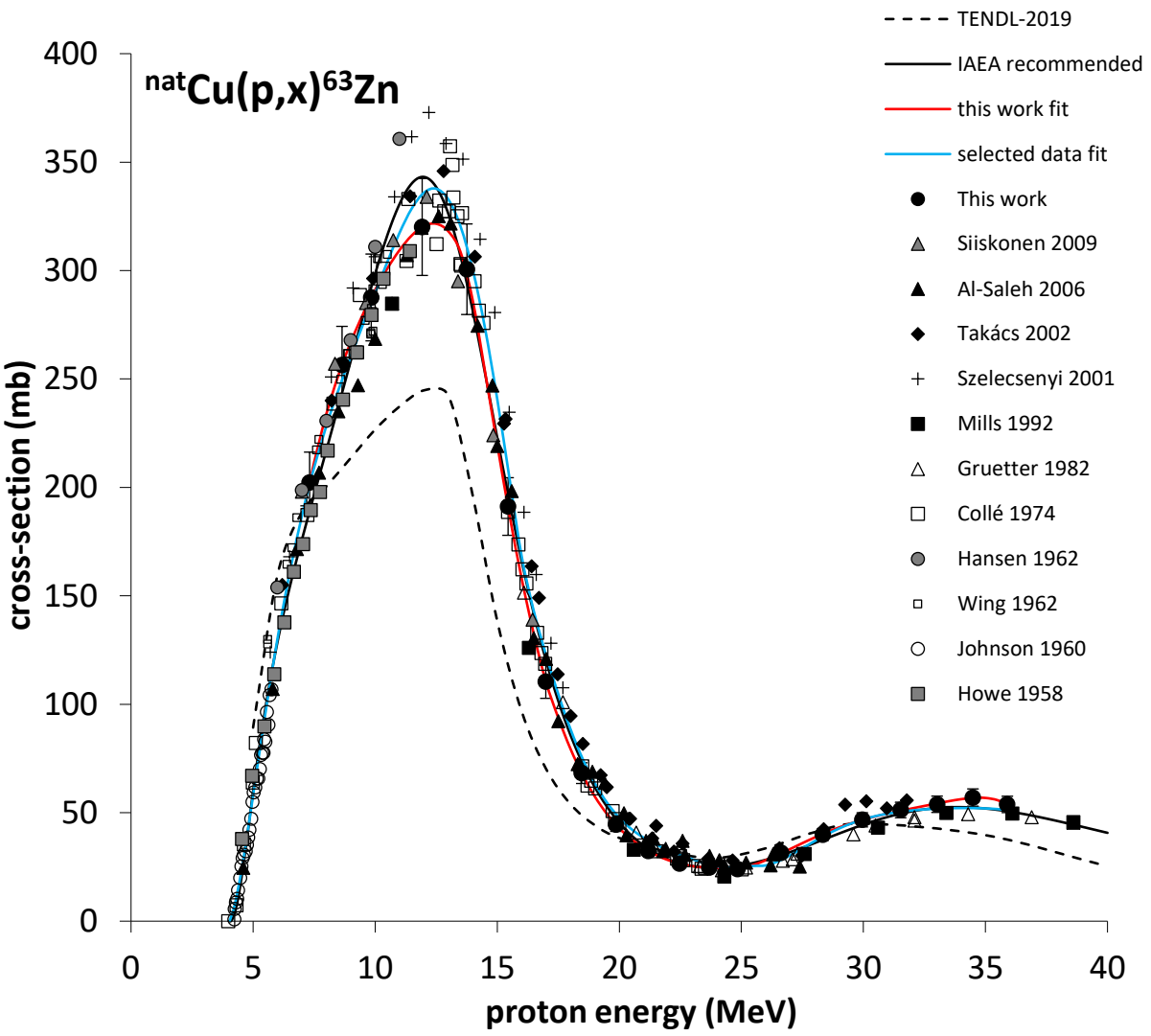

Fig. 14 Selected experimental cross-sections and their fit for reactions $^{nat}Cu(p,x)^{63}Zn$ [21,22,38,31,34,40,43-47], TALYS prediction taken from the TENDL-2019 library, IAEA recommended cross-sections

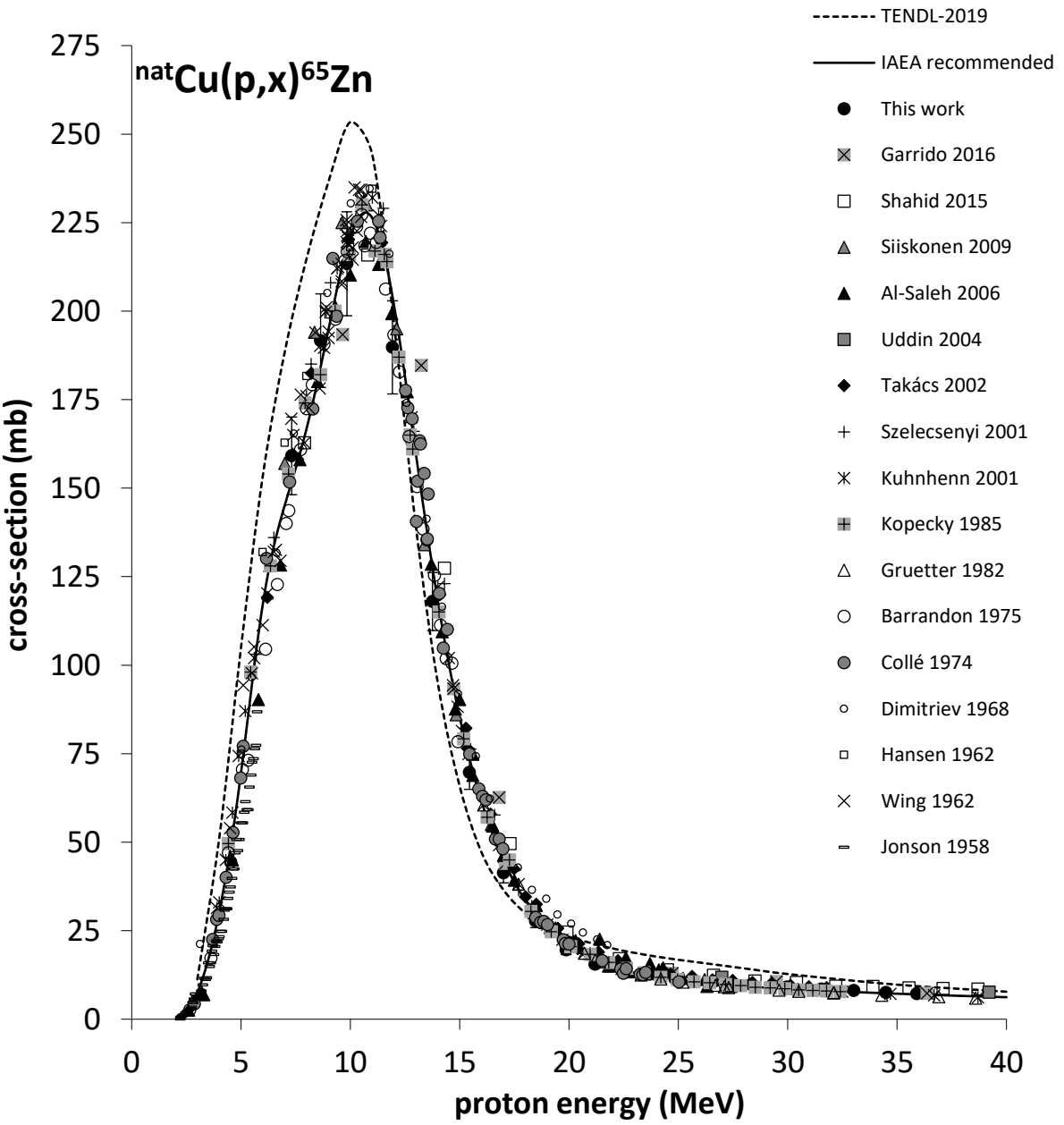

Fig. 15 Cross-sections of reactions $^{nat}Cu(p,x)^{65}Zn$ – our values in comparison with the previously published data [12,21,22,27,36,38,40,42,44-47,49-51] and the TALYS prediction taken from the TENDL-2019 library

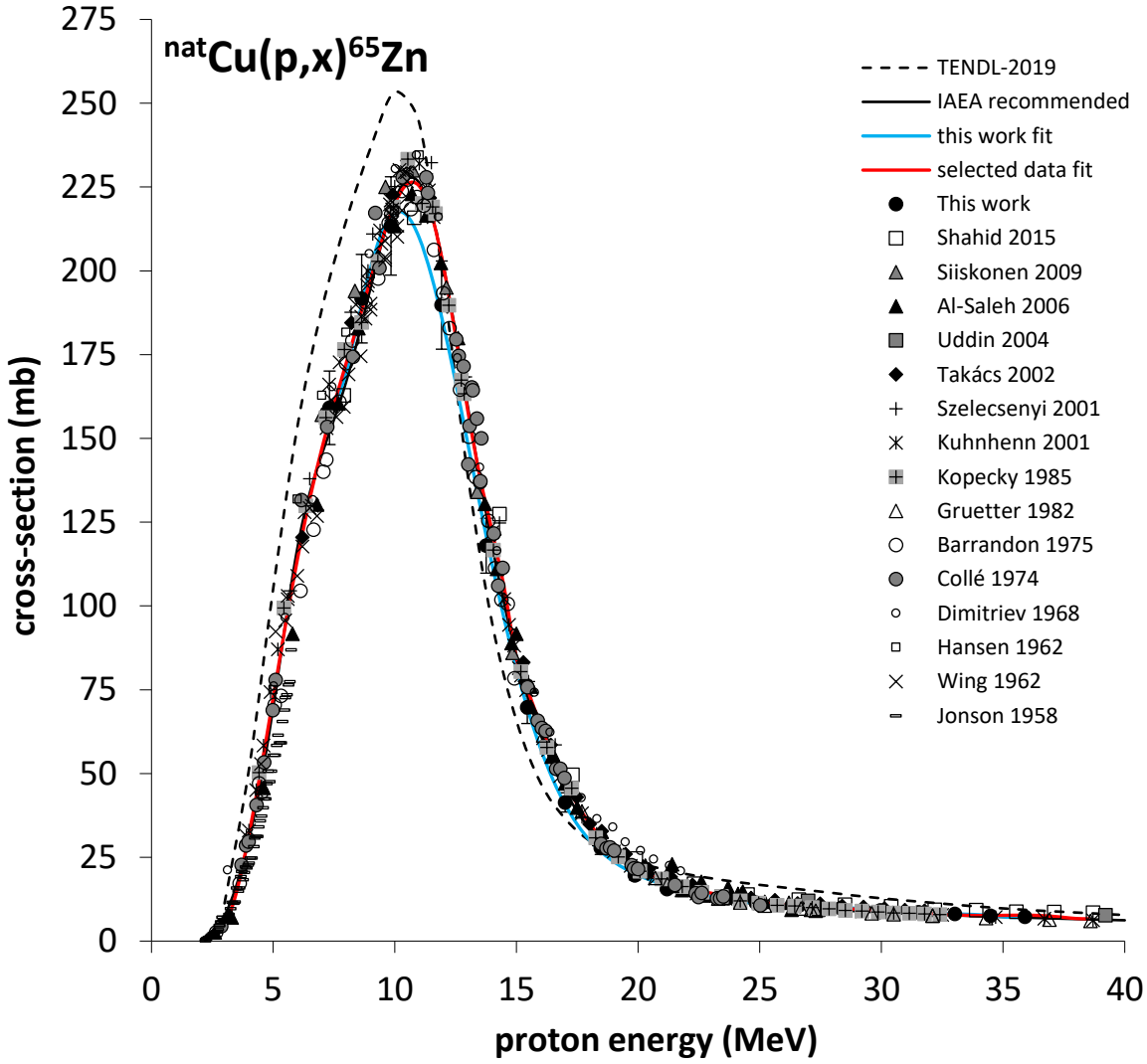

Fig. 16 Selected experimental cross-sections and their fit for reactions $^{nat}Cu(p,x)^{65}Zn$ [12,21,22,36,38,40,42,44-47,49-51], TALYS prediction taken from the TENDL-2019 library, IAEA recommended cross-sections

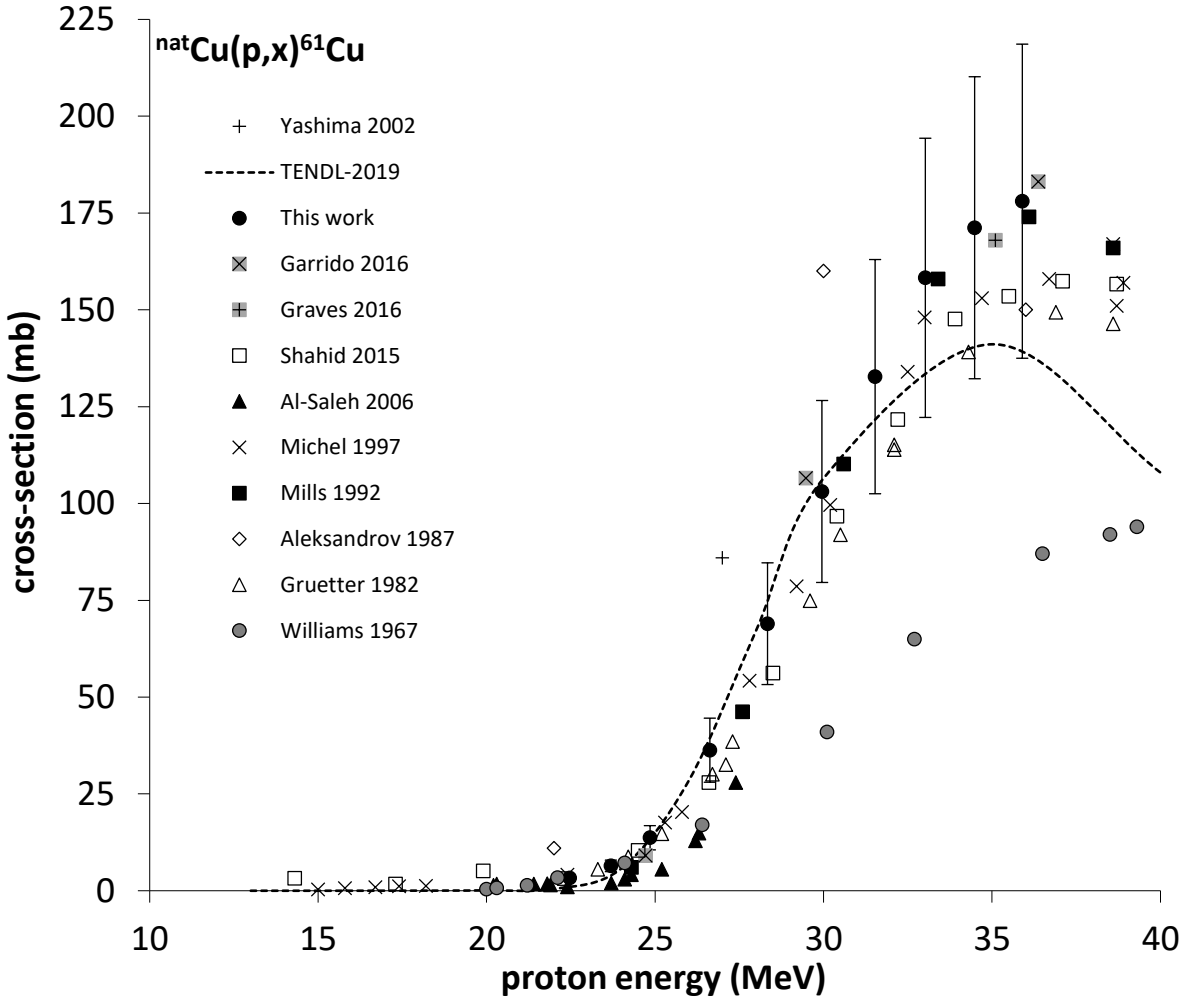

Fig. 17 Cross-sections of reactions $^{nat}Cu(d,x)^{61}Cu$ – our values in comparison with the previously published data [20,27,30-32,34,38,42,52,53] and the TALYS prediction taken from the TENDL-2019 library

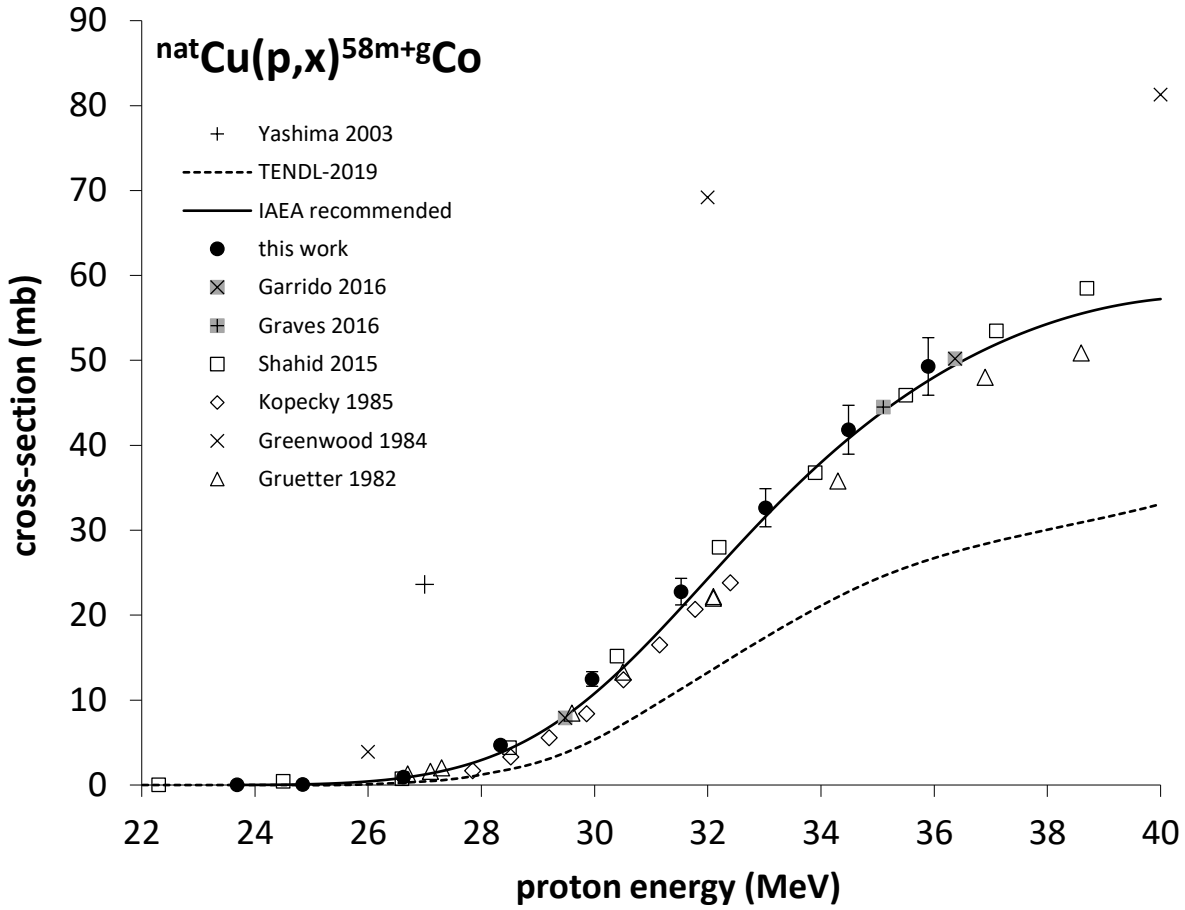

Fig. 18 Cross-sections of reactions $^{nat}Cu(p,x)^{58m+g}Co$ – our values in comparison with the previously published data [27,31,42,50,52,53,54] and the TALYS prediction taken from the TENDL-2019 library

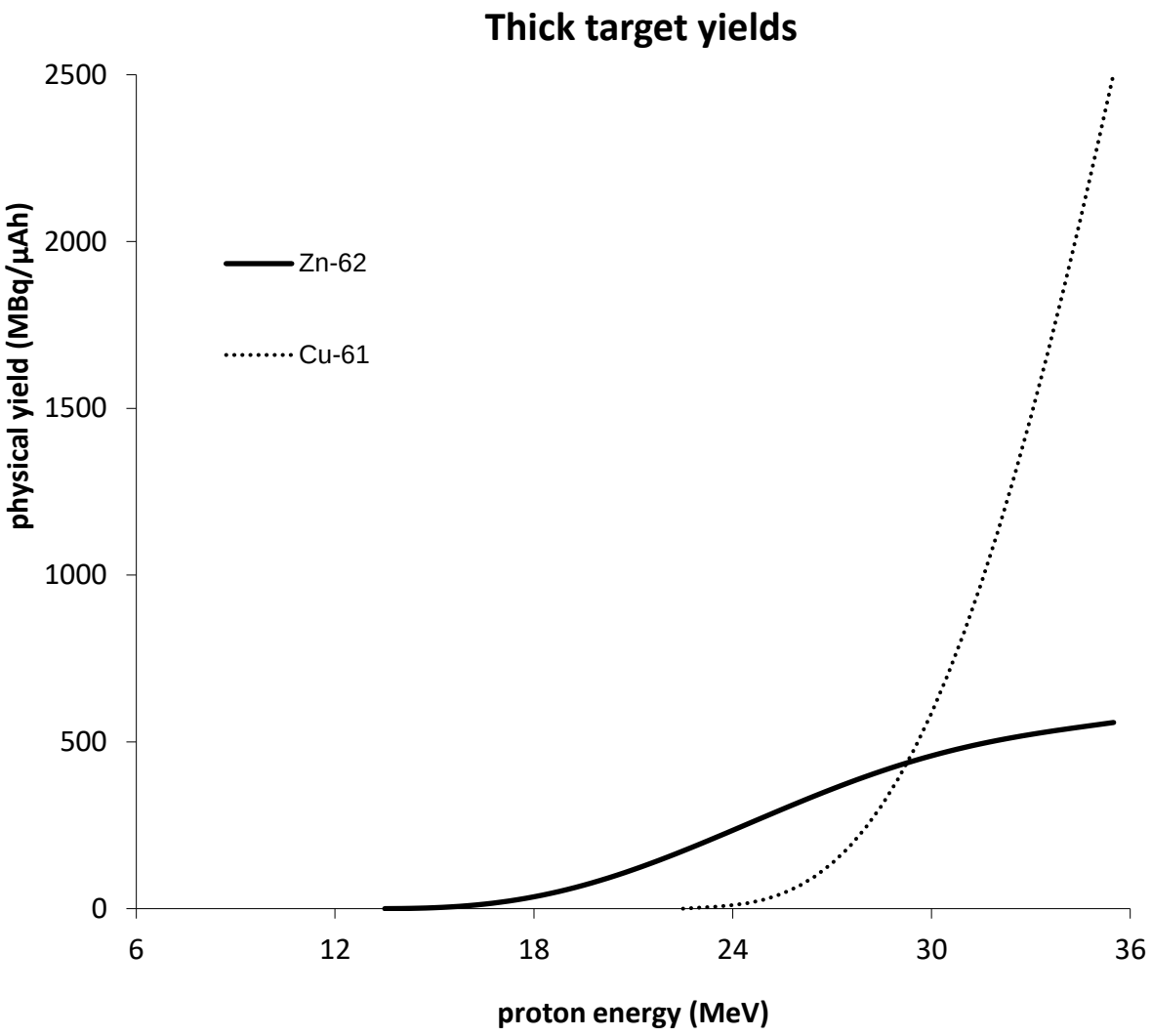

Fig. 19 Thick target yield (production rate) for ^{62}Zn and ^{61}Cu

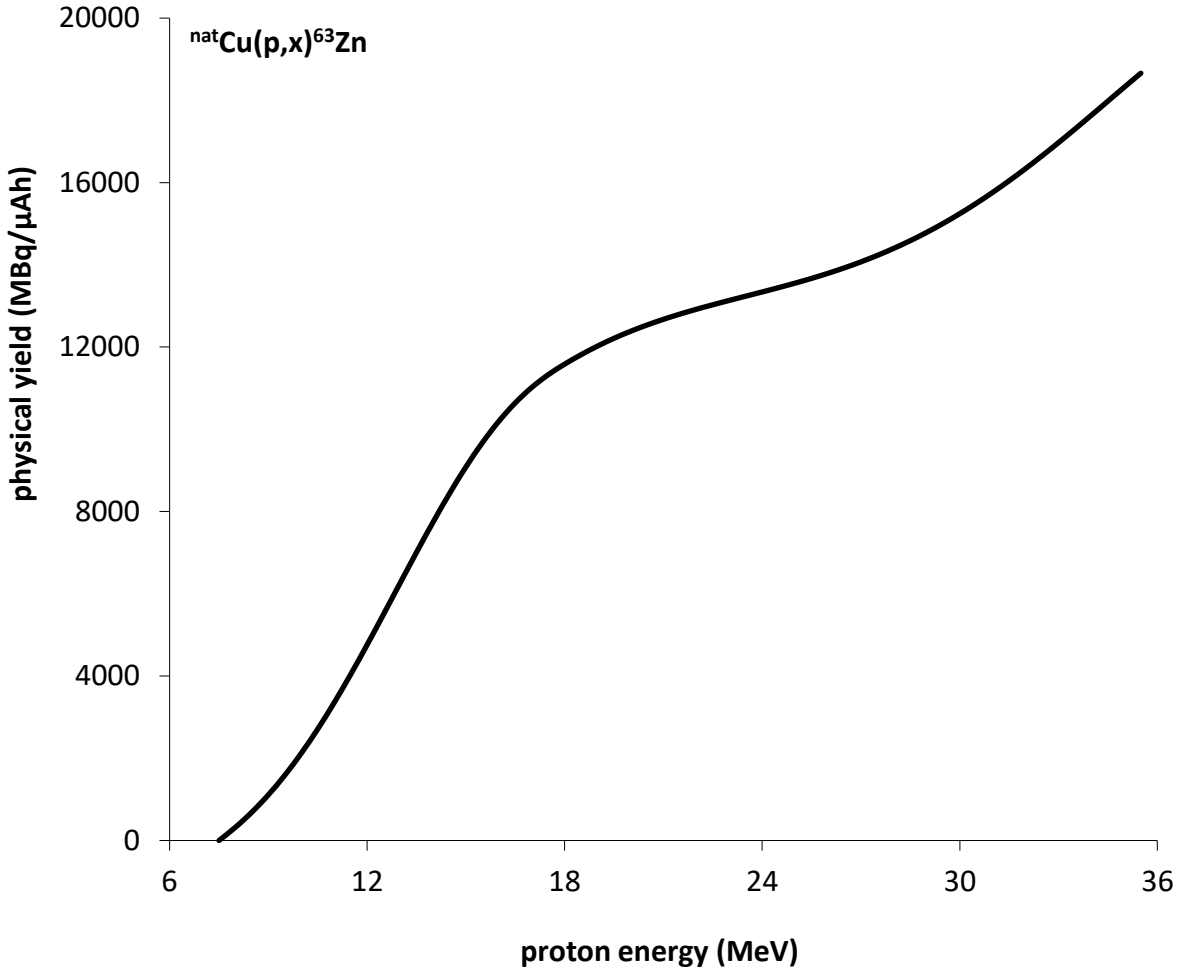

Fig. 20 Thick target yield (production rate) for ^{63}Zn

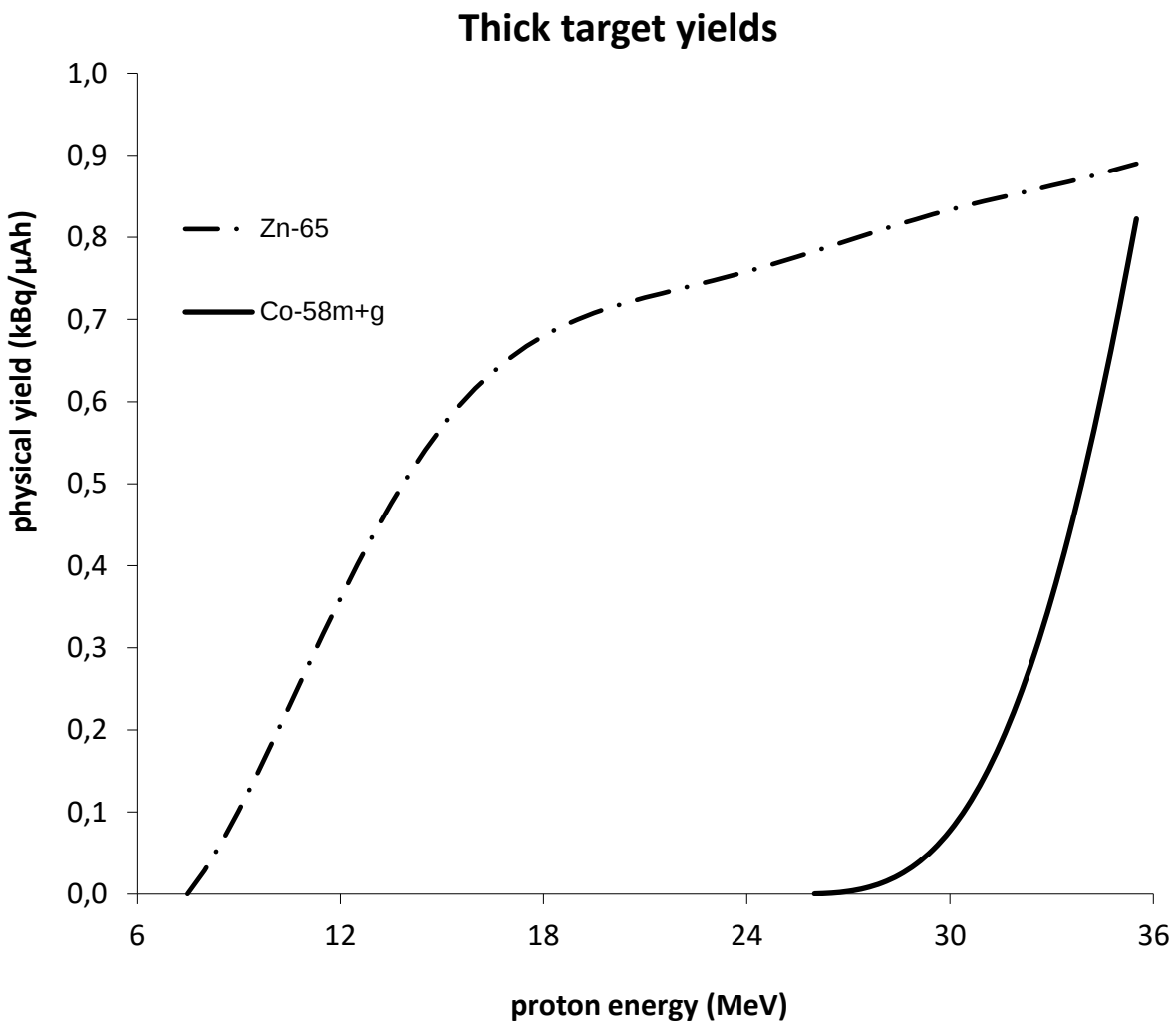

Fig. 21 Thick target yield (production rate) for ^{65}Zn and $^{58m+g}$Co

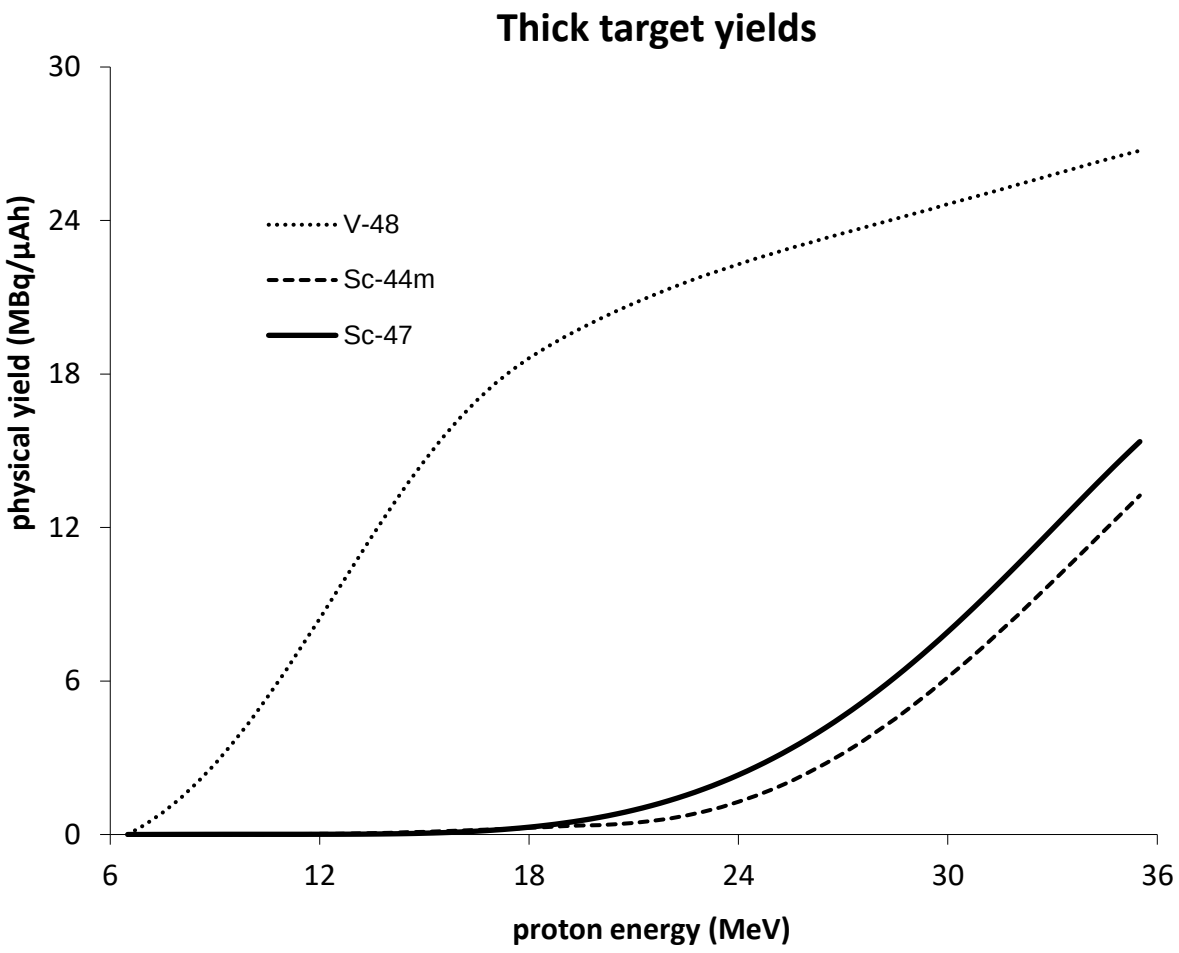

Fig. 22 Thick target yield (production rate) for ^{48}V, ^{44m}Sc and ^{47}Sc

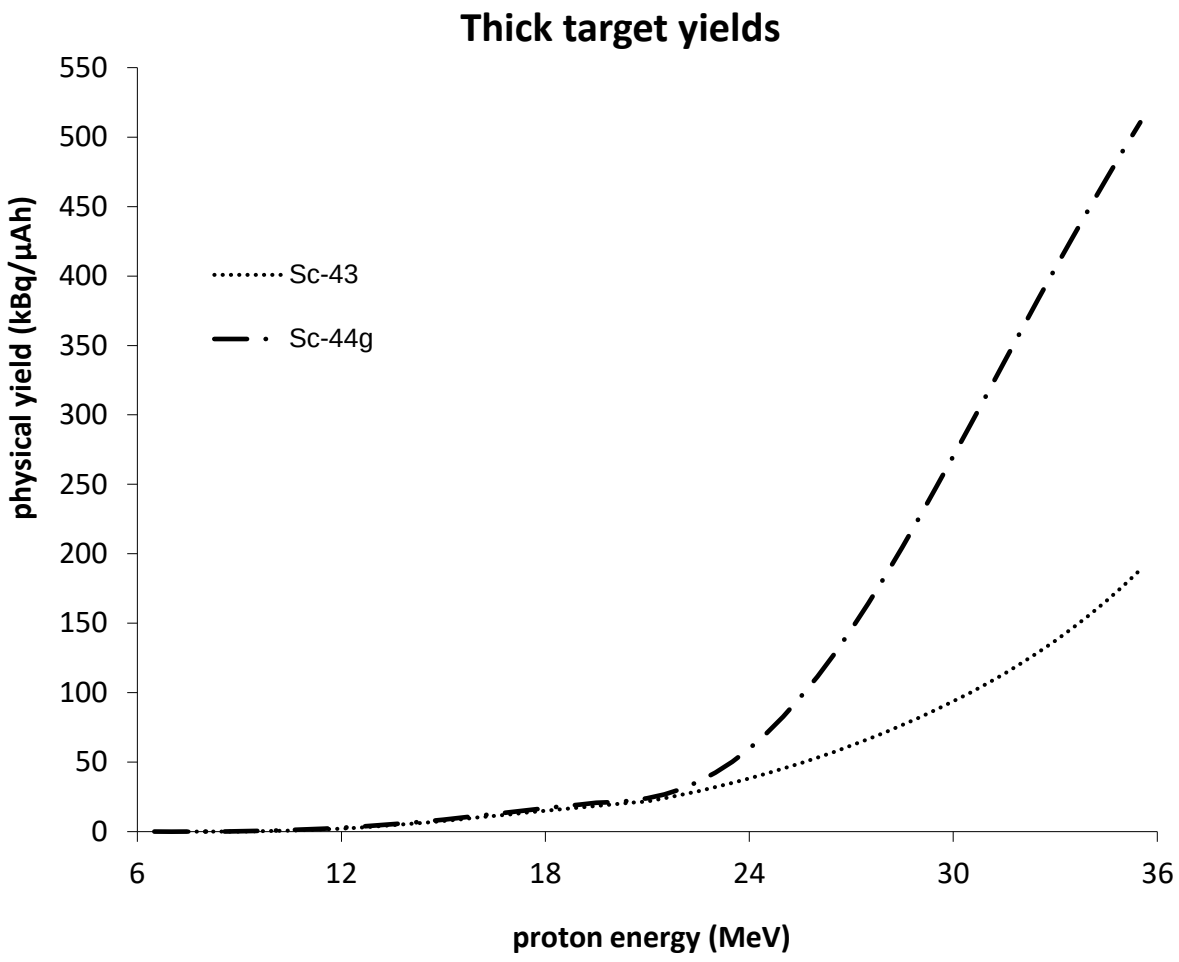

Fig. 23 Thick target yield (production rate) for ^{43}Sc and ^{44g}Sc

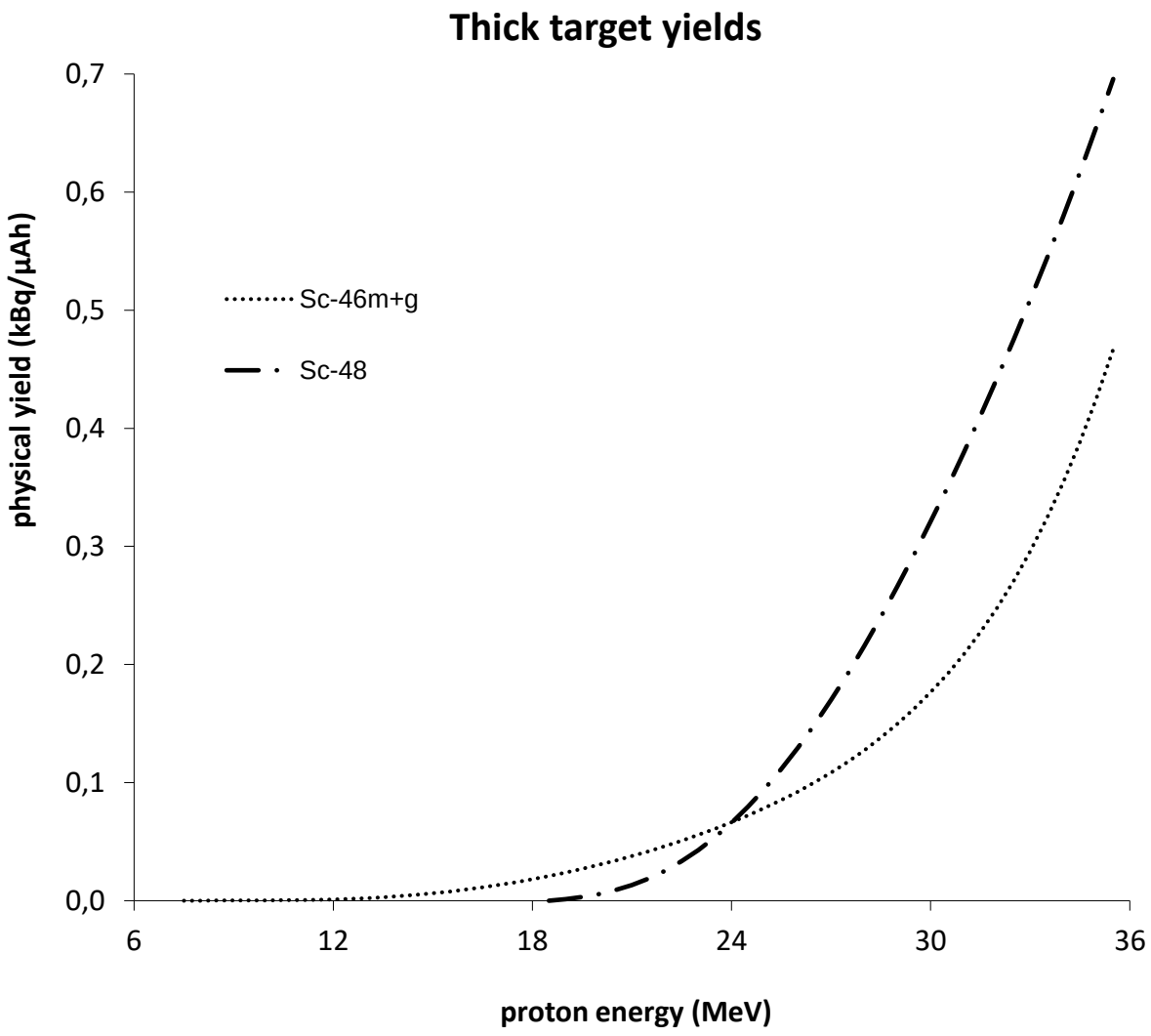

Fig. 24 Thick target yield (production rate) for $^{46m+g}$Sc and ^{48}Sc

7.2 Prehlásenie spoluautorov

Vyjadrenie prof. Ing. Ondřeje Lebedu, Ph.D. k môjmu podielu na príprave a realizácii experimentov, na vyhodnocovaní získaných dát a na písaní publikácií, z ktorých táto práca vychádza.

Agreement of the First/Corresponding Author

I hereby declare my agreement with inclusion of the works:

- Červenák J., Lebeda O., *Experimental cross-sections for proton-induced nuclear reactions on ^{nat}Mo*, Nucl. Instrum. Methods Phys. Res. B 380 (2016) 32–49 doi: doi.org/10.1016/j.nimb.2016.05.006

- Červenák J., Lebeda O., *Measurement of cross-sections of proton-induced nuclear reactions on ^{197}Au focused on the production of the theranostic pair $^{197m,g}Hg$*, Nucl. Instrum. Methods Phys. Res. B 458 (2019) 118–125 doi: 10.1016/j.nimb.2019.08.006

- Lebeda O., Červenák J., *Measurement of deuteron-induced nuclear reactions cross-sections on ^{197}Au and on ^{nat}Cu focused on the theranostic $^{197m,g}Hg$*, Nucl. Instrum. Methods Phys. Res. B 461 (2019) 105–113 doi: 10.1016/j.nimb.2019.09.034

- Lebeda O., Červenák J., *Revised cross-sections for formation of theranostic $^{197m,g}Hg$ in proton- and deuteron-induced reactions on ^{197}Au.* Nucl. Instrum. Methods Phys. Res. B 478 (2020), 85–91. doi: 10.1016/j.nimb.2020.05.014

- Červenák J., Lebeda O., *New cross-section data for proton-induced reactions on ^{nat}Ti and ^{nat}Cu with special regard to the beam monitoring*, Submitted into: Nucl. Instrum. Methods Phys. Res. B, submitted manuscript NIMB-S-20-00521

in the thesis for the degree of Doctor of Philosophy of Jaroslav Červenák. His contribution for these publications was planning the experiments, data acquisition and evaluation, drafting and revision of the manuscripts.

I also declare my agreement with inclusion of the work

- Lebeda O., Kondev F. G., Červenák J., *Branching ratio and γ-ray emission probabilities in the decay of the $J^{\pi}=13/2^{+}$ isomer in ^{197}Hg*, Nucl. Instrum. Methods Phys. Res. A 959 (2020) 163481 doi: 10.1016/j.nima.2020.163481

in the thesis for the degree of Doctor of Philosophy of Jaroslav Červenák. His contribution for this publication was separation of Hg isotopes after the irradiation and samples preparation.

Ondřej Lebeda

6th July 2020